Universitat Autònoma de Barcelona

Localization with OFDM Signals in 5G Systems

Arash Shahmansoori

Localization with OFDM Signals in 5G Systems

Author:

Arash Shahmansoori

Thesis Advisors:
Prof. Gonzalo Seco-Granados
Prof. Henk Wymeersch

This dissertation is submitted for the degree of
Doctor of Philosophy

PhD Program in Electronic and Telecommunication Engineering
Department of Telecommunications and Systems Engineering
Universitat Autònoma de Barcelona

Abstract

A key aspect to design an orthogonal frequency division multiplexing (OFDM) system for combined positioning and high-data-rate communications is to find optimal data and pilot power allocations. Previously, A capacity maximizing design has been investigated for the case of static channels. However, it is logical to consider channel variation for different OFDM symbols due to movement. Joint design of data and pilots with considering the time variations of the channel and correlation between the corresponding channel taps from different OFDM symbols increases the capacity for a given time-delay estimation accuracy. We propose a method for joint design of data and pilots for the time-varying channels. Numerical results approve the improvement in terms of channel capacity for a desired value of time-delay estimation accuracy.

Next, we consider the power allocations for OFDM wireless network localization (WNL). In location-aware wireless networks, mobile nodes (agents) can obtain their positions using range measurements to other nodes with known positions (anchors). Optimal subcarrier power allocation at the anchors reduces positioning error and improves network lifetime and throughput. We present an optimization framework for ergodic and robust subcarrier power allocations in network localization with imperfect knowledge of network parameters based on the fundamental statistical limits. Ergodic and robust power allocations are obtained using semidefinite optimization problems in non-iterative and iterative forms with both unicast and multicast transmissions. Results show that robust and ergodic power allocations provide more accurate localization than non-robust designs under channel and agents positions uncertainty.

Finally, we extend the localization techniques for 5G systems. 5G communications are characterized by large bandwidths, large antenna arrays, and device-to-device communication. We describe why and how these properties are conducive to accurate positioning. We also provide an overview of how 5G technologies have been used for positioning in recent literature. Particularly, millimeter wave and massive multiple-input-multiple-output (MIMO) are considered enabling technologies for future 5G networks. While

their benefits for achieving high-data rate communications are well-known, their potential advantages for accurate positioning are largely undiscovered. We derive fundamental bounds on the position and rotation angle estimation in the presence of clusters for wideband systems. A detection algorithm based on multiple measurement vectors (MMV) matching pursuit is used for the coarse estimation of angle-of-arrival (AOA)/angle-of-departure (AOD) and time-of-arrival (TOA) that are applied for initialization of the estimation phase based on the expectation maximization (EM) with a sequential iterative procedure. The results show the convergence of the estimated parameters to the values obtained by the inverse of Fisher information matrix.

Declaration

I hereby declare that except where specific reference is made to the work of others, the contents of this dissertation are original and have not been submitted in whole or in part for consideration for any other degree or qualification in this, or any other university. This dissertation is my own work and contains nothing which is the outcome of work done in collaboration with others, except as specified in the text and Acknowledgements. This dissertation includes appendices, bibliography, footnotes, tables, equations, and figures.

Acknowledgements

I would like to express my special appreciation and thanks to my advisors Professor Dr. Gonzalo Seco-Granados and Professor Dr. Henk Wymeersch, you have been tremendous mentors for me. I would like to thank you for encouraging my research and for allowing me to grow as a research scientist. Your advice on both research as well as on my career have been priceless. I would also like to thank my committee members for serving as my committee members even at hardship.

This work was financially supported by EU FP7 Marie Curie Initial Training Network MULTI-POS (Multi-technology Positioning Professionals) under grant nr. 316528.

Finally, a special thanks to my family. Words cannot express how grateful I am to my mother and father for all of the sacrifices that you have made on my behalf. Your prayer for me was what sustained me thus far. I would also like to thank all of my friends who supported me in writing, and incented me to strive towards my goal.

Contents

Chapter 1

Localization in 5G: Overview and Challenges

1.1 Introduction

The rapid increase of mobile data volume, the use of smartphones, and the global bandwidth shortage are the main challenges for current wireless networks. At any given location, the maximum available bandwidth for all cellular technologies is 780 MHz with the carrier frequencies ranging from 700 MHz and 2.6 GHz [Rap13]. A tenfold increase of the data rate requires an almost unavoidable increase of the available bandwidth. Given that the goal is to have available a bandwidth on the order of GHz for high data rate communication with low latency and higher localization accuracy, millimeter wave (mm-wave) frequencies are considered as one of the best candidates. Moreover, increasing the bandwidth provides a better time resolution, thereby ensuring the accurate estimation of the TOA that is used for localization. Fig. 1.1 shows that the mm-wave spectrum ranging from 30 GHz to 300 GHz provides more spectrum in bands not previously used in cellular. Particularly, for carrier frequencies $f_c < 6$ GHz the spectrum has a maximum bandwidth $B = 0.555$ GHz, in the centimeter wave (cm-wave) frequencies it is possible to achieve a bandwidth $B = 1.3$ GHz with $f_c = 28$ GHz. In the mm-wave frequencies, we achieve a unlicensed bandwidth $B = 7$ GHz at $f_c = 60$ GHz. Spatial processing techniques relying on massive multiple-input-multiple-output (MIMO) transceivers can also be applied in mm-wave frequencies [Rus13]. Moreover, the spectral allocations in mm-wave frequencies are closer to each other than pieces of spectrum used by the cellular operators nowadays, which are scattered between 700 MHz and 2.6 GHz. This makes mm-wave frequencies more homogenous. Despite the aforementioned advantages, using mm-wave frequencies

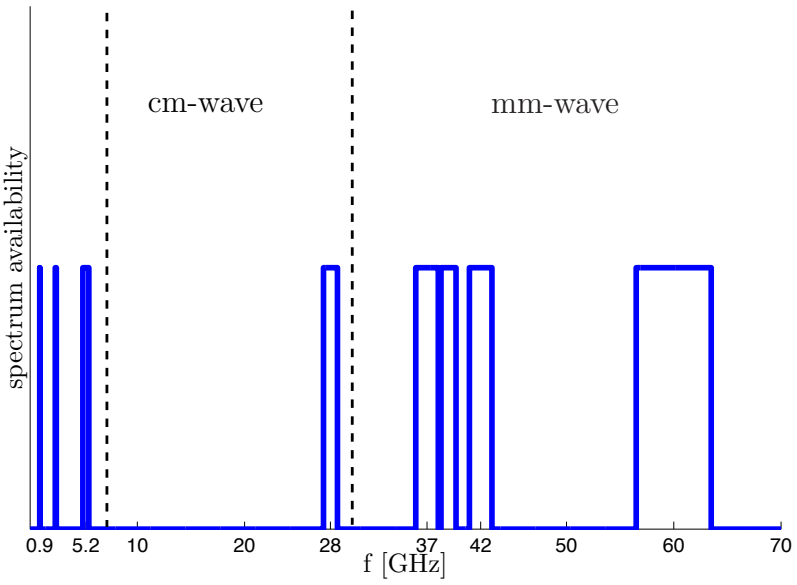

Figure 1.1: Mm-wave spectrum for 5G.

presents some challenges including path-loss and atmospheric attenuation.

However, it has been shown that attenuation due to rain and atmospheric absorption has a negligible impact on the mm-wave at 28 GHz to 38 GHz for small distances (i.e.,less than 1 km) [Zha06]. Due to attenuation at mm-wave frequencies, directional antennas[1] can be used at the transmitters and receivers to overcome the path-loss effects. Using a large number of antennas provides narrow beams towards the user that makes the mm-wave link highly directional. Moreover, the large bandwidth at the mm-wave frequencies provides TOA estimates of high accuracy. Higher directionality and higher TOA estimation accuracy lead to better localisation accuracy.

Furthermore, the location of the user is extremely important for the transmitter in highly directional communication. Knowing the location of the user the transmitter can steer the beam directly or to a reflected path. For the case that the line-of-sight (LOS) is blocked, steering the beam to the reflected path with the strongest signal power can be helpful for user localization. The data transmission is increased based on the statistical channel knowledge for user location. This leads to a synergy between localization and communication. In today's technologies such as global positioning system (GPS), accurate location information cannot be provided for indoors and in urban canyons. Other technologies such as ultra-wide bandwidth (UWB), can provide indoor localization with

[1]Directional antenna is an antenna designed to radiate or receive greater power in specific directions allowing for reduced interference from unwanted sources.

the cost of high hardware complexity [She10a]. Also, WiFi can provide indoor localization at low cost but not so high accuracy as GPS outdoors and UWB indoors [Fol13].

The use of 5G technologies to obtain position and orientation was previously explored in [San02, Den14, Var14b] for mm-wave and in [Hu14, Gue15, Sav15] for massive MIMO. Beam training protocols through direction of arrival[2](DOA) were considered in [San02]. A hypothesis testing user localization approach was presented in [Den14] using the concept of channel sparsity that is due to few and clustered paths. These methods limit virtual angle spacings $1/N_{\mathrm{Tx}}$ and $1/N_{\mathrm{Rx}}$ due to the limited number of antenna elements in the transmitter N_{Tx} and receiver N_{Rx}. Localization based on received signal strength (RSS) was considered in [Var14a]. This approach provides meter-level positioning accuracy. A method to estimate the position of the user devices using an extended Kalman filter combined with travel time of the signal from the transmitter to the receiver (TOA) and DOA estimations in the uplink was proposed in [Wer15a, Koi16]. This method assumes line-of-sight (LOS) propagation thanks to the high density of the access nodes and it estimates the clock offsets between user nodes. A method based on DOA and RSS estimation for non-cooperative transmitter localization was considered in [Wer15b]. This method uses an antenna structure that can selectively receive energy from different sectors (sectorized antennas) to obtain sector-powers as sufficient statistics for DOA and RSS estimation. However, the method assumes that different samples in a sectorized antenna are received sequentially in time, what can slow down the localization. Using massive MIMO systems, the work in [Hu14] considered angle-of-arrival (AOA)/angle-of-departure (AOD)[3] estimation for localization, and [Gue15] considered the localization in an LOS scenario by joint TOA, AOA, and AOD.

In this chapter, it is shown that mm-wave and massive MIMO, both candidates for 5G networks, are also enabling technologies for localization. First, a brief overview of 5G systems and the main challenges including path-loss effects are provided. Different path-loss models are presented and the main differences between the path-loss effects in the mm-wave frequencies and UWB systems are explained. For the sake of comparison, UWB systems are used due to providing higher localization accuracy for indoor applications compared to WiFi. Since the estimation of mm-wave channels is of critical importance for user localization, the physical channel model for mm-wave systems together with the limited scattering property are presented. This property leads to the sparsity of the

[2]DOA or AOA are defined as the angle between the received beam with respect to a reference line in the receive antenna array.

[3]AOD is defined as the angle between the transmitted beam with respect to a reference line in the transmit antenna array.

mm-wave channels, which differs from UWB channels since the later are rich in scattering. It is demonstrated that the TOA, AOA, and AOD can be estimated using the sparsity of the mm-wave channels. Hybrid beamformers are explained as the most promising solution for accurate beam steering in mm-wave; they can be used to generate narrow beams used for the user localization by beam training protocols. Moreover, different localization techniques based on the TOA, AOA, and AOD and their combination are presented as the promising solutions in the mm-wave frequencies. Finally, the problem of joint data and pilot design has been addressed.

This chapter is organized as follows. Section 1.2 represents an overview of 5G systems. Section 1.3 proposes localization with the OFDM signals and their applications in the long term evolution (LTE) systems and 60 GHz indoor. Section 1.4 provides an overview on the mm-wave channels, parameter estimation, sparsity in the estimation of AOA/AOD, and localization. Section 1.5 presents motivations and objectives. Finally, thesis outline and research contributions are presented in Sections 1.5 and 1.6, respectively.

1.2 5G Systems

In this section, we briefly describe 5G systems, their properties and benefits. First, 5G waveforms and their properties are briefly explained. Second, mm-wave systems are explained in terms of their carrier frequencies, bandwidth, and data rate. Third, the benefits and challenges of the massive MIMO systems are described. Fourth, the concept of device-centric architecture in 5G systems is addressed. Finally, the concepts of device to device (D2D) communication, location-aware communications, and ultra dense networks are described.

1.2.1 5G Waveforms

The 5G waveforms are divided into single-carrier waveforms and multi-carrier OFDM-based waveforms. The key design targets for the physical layer waveforms in 5G are: higher spectral efficiency, lower in-band and out-of-band emissions, asynchronous multiple access, lower power consumption, and lower implementation complexity. In this section, the properties of each waveforms are briefly described to justify the use of multi-carrier OFDM-based waveforms in this dissertation.

Single-Carrier Waveforms

Signel-carrier waveforms provide lower peak-to-average power ratio (PAPR) that leads to high power amplifier (PA) efficiency and extended battery life. Moreover, in the presence of multipath the equalizer is needed to achieve high spectral efficiency. Some examples for the single-carrier waveforms are: constant envelope waveforms such as minimum-shift keying (MSK) (adopted by IEEE 802.15.4) and Gaussian minimum-shift keying (GMSK) (adopted by global system for mobile communications (GSM) and Bluetooth), single-carrier quadrature amplitude modulation (SC-QAM) (adopted by EV-DO and UMTS) [Sor06], single-carrier frequency domain equalization (SC-FDE) (adopted by IEEE 802.11ad), single-carrier frequency-division multiplexing (SC-FDM) (adopted by LTE uplink), and zero-tail SC-FDM.

- Constant envelope waveforms such as MSK and GMSK provide higher transmit efficiency by allowing constant transmit carrier power, i.e., 0 dB PAPR. Moreover, they are able to suppress the side lobes and allow asynchronous multiplexing with reasonable receiver complexity. However, the main drawback is the reduced spectral efficiency [Wan08, Mur81].

- To improve the spectral efficiency of the constant envelope waveforms with increasing receiver complexity due to the equalization algorithm, SC-QAM is a good candidate. Moreover, the PAPR is still low and asynchronous multiplexing is allowed.

- The equivalent form of SC-QAM with cyclic prefix (CP) is SC-FDE that enables simple frequency domain equalization (FDE) implementation for single-carrier waveform to improve spectral efficiency under multipath fading. The main drawback of this waveform is the degradation of the spectral efficiency due to the added CP [Fal02].

- To mitigate multipath degradation with FDE, SC-FDM is applied. Moreover, SC-FDM provides dynamic bandwidth allocation due to the flexibility in allocating different bandwidth to multiple users through frequency multiplexing i.e., single-carrier frequency-division multiple access (SC-FDMA) [YJ10].

- Finally, zero-tail SC-FDM provides flexible bandwidth assignment with improved spectral efficiency due to removal of CP. However, configuring the zero-tail leads to extra signaling overhead.

Multi-Carrier Waveforms

Multi-carrier OFDM-based waveforms support orthogonal sub-carriers within a given bandwidth. Moreover, multi-carrier OFDM-based waveforms are easily integrated with MIMO that leads to high spectral efficiency. Some examples for the multi-carrier waveforms are: cyclic prefix OFDM (CP-OFDM) (adopted by LTE), CP-OFDM with[4] weighted overlap and add (WOLA) (existing LTE implementation), universal-filtered multi-carrier (UFMC), filter bank multi-carrier (FBMC), and generalized frequency division multiplexing (GFDM) [Ban14].

- CP-OFDM is efficient due to using inverse fast Fourier transform (IFFT)/fast Fourier transform (FFT) in the transmitter and receiver, respectively. The spectrum allocation to different users is flexible and the application of MIMO technology is flexible. Moreover, the multipath mitigation is possible using simple FDE. An application of CP-OFDM with WOLA is used in LTE downlink.

- UFMC uses band-pass transmit filter for each resource block that only passes the assigned resource block. A guard interval of zeros is added between successive IFFT symbols in the transmitter to prevent intersymbol interference (ISI) due to transmit filter delay. UFMC provides similar out-of-band interference suppression performance to CP-OFDM with WOLA. However, the complexity of the transmitter and receiver is increased and the systems is prone to ISI due to the lack of CP [Wan14].

- FBMC improves spectral property using prototype filter with frequency domain over-sampling. The main advantage of FBMC is superior side-lobe decay than other multi-carrier waveforms but the benefit reduces with PA non-linearity. However, the complexity of the receiver is increased, the systems are susceptible to ISI under non-flat channel, and integration with MIMO is more complex than OFDM [Dor14, FB11, Bel10, Fan13].

- In GFDM, multiple OFDM symbols are grouped into a block, with a CP added to the block. In each block the prototype filter is cyclic-shift in time among different OFDM symbols. The main advantage of GFDM is the better out-of-band interference suppression than CP-OFDM with/without WOLA. However, it requires complicated receiver to handle ISI/intercarrier interference (ICI), the block latency is increased, and multiplexing with CP-OFDM requires large guard band [Mic14].

[4]WOLA is a weighted overlap and add technique for the improvement of out-of-band and in-band asynchronous user interference suppression.

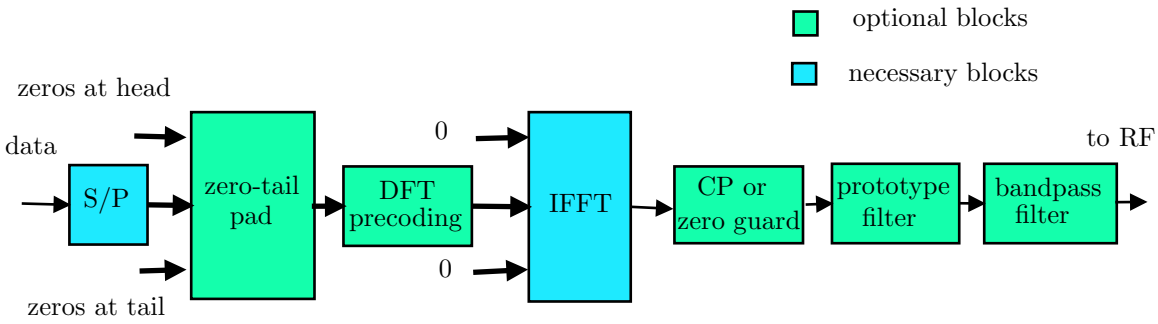

waveforms	zero-tail pad	DFT precoding	IFFT	CP or zero guard	prototype filter	bandpass filter
CP-OFDM/WOLA			used	CP	used	
UFMC			used	zero guard		used
FBMC			used		used	
SC-FDM/WOLA		used	used	CP	used	
zero-tail SC-FDM	used	used	used			

Figure 1.2: Different implementation options for single-carrier and multi-carrier OFDM-based waveforms.

Fig. 1.2 shows different blocks that are used for each single-carrier and multi-carrier OFDM-based waveforms. As it is observed, the common blocks among all the waveforms are IFFT and serial/parallel (S/P) shown by the blue colors, while the blocks shown with the green colors are optional and used to form the specific waveforms. Then, the data is transmitted through necessary and optional blocks to the radio-frequency (RF) using a specific waveform.

In conclusion, multi-carrier OFDM-based waveforms in the form of CP-OFDM offer higher spectral efficiency and low implementation complexity and are good candidates for the downlink with a more relaxed energy efficiency requirement. Moreover, they lead to efficient use of power and bandwidth for cooperative localization as will be explained in more details in Section 1.3.

1.2.2 Mm-Wave

The mm-wave band provides 5G systems with an amount of bandwidth on the order of GHz. Some of the implications of using the mm-wave spectrum include:

- The possibility to use of cognitive radio techniques to share the spectrum with

satellite or radar systems.

- The capability to generate very narrow beams with smaller directional and adaptive antenna arrays thanks to small wavelength.

Mm-wave can provide high peak, average and outage rates on the order of gigabit per second (Gbps), as required in different 5G scenarios e.g., autonomous driving. Moreover, it leads to better localization accuracy due to providing the bandwidth of the order of GHz that leads to higher resolution in the estimation of the TOA for localization purposes. Finally, in mm-wave frequencies the dimension of antenna arrays is sufficiently small and it is possible to jointly apply mm-wave and massive MIMO for indoor localization using AOA/AOD estimation.

1.2.3 Massive MIMO

Massive MIMO systems can operate either at mm-wave frequencies or lower ones [Swi13]. Massive MIMO systems are considered as systems with large number of antenna elements[5] in the transmitter $N_{\mathrm{Tx}} \gg 1$ and with P single-antenna or multi-antenna terminals. To suppress interference and achieve the sum capacity of the multi-user channel, it is required to have P channel vectors mutually orthogonal (favorable propagation). For the case of mutually non-orthogonal channel vectors, advanced signal processing methods (e.g., dirty paper coding [Cai03]) are used. Favorable propagation can be achieved with sufficiently large number of antenna elements N_{Tx} (e.g., $N_{\mathrm{Tx}} = 100$) for a given number of single-antenna terminals P (e.g., $P = 12$) in non-line-of-sight (NLOS) environments with rich scattering or LOS environments with dropping a few worst terminals that cause non-orthogonal channel vectors. Massive MIMO enables simple spatial multiplexing/demultiplexing procedures. However, channel estimation is a challenging step in the massive MIMO systems. The channel coherency is limitted by the propagation environment, user mobility, and the carrier frequency that limits the number of orthogonal pilots. Moreover, reuse of pilots leads to pilot contamination that needs to be mitigated [Che14]. Fig. 1.3 shows a massive MIMO system in the uplink and downlink for LOS propagation with the base station (BS) equipped with N_{Tx} antennas that serves P single-antenna terminals. Finally, massive MIMO systems either at mm-wave frequencies or lower ones can be used for localization by estimating the AOA/AOD with high accuracy due to using large number of antenna arrays in the transmitter and the receiver.

[5]At a typical cellular frequency of 2 GHz; the wavelength is 15 cm and up to 400 dual-polarized antennas can thus be deployed in a 1.5 m × 1.5 m array.

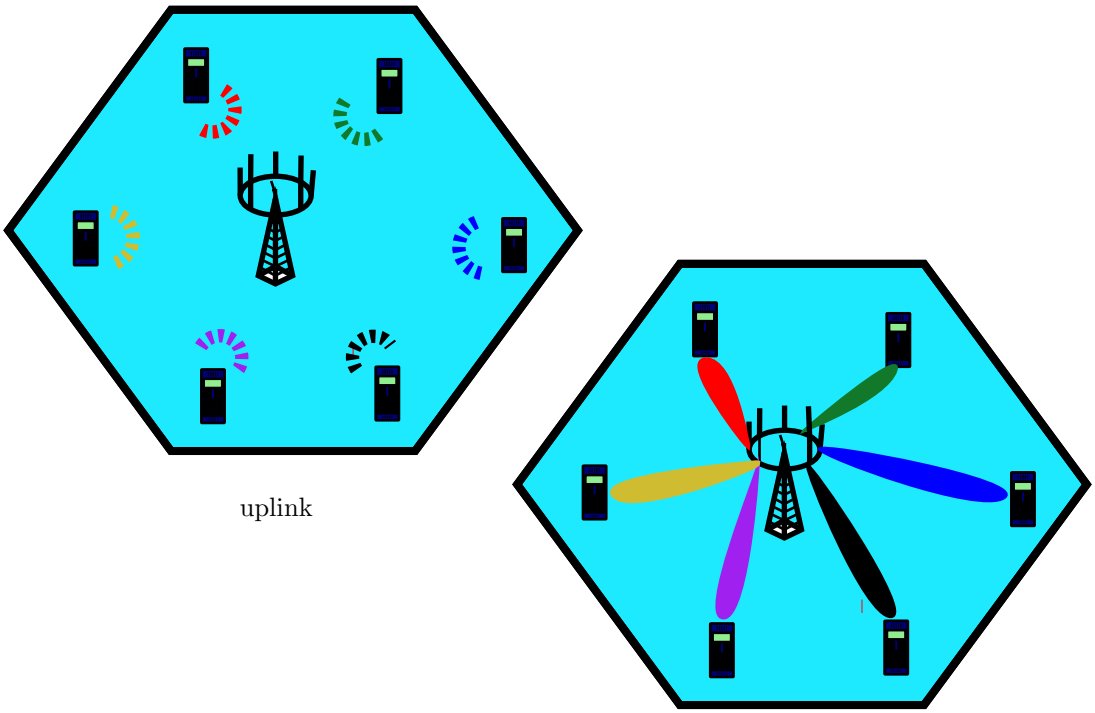

Figure 1.3: Illustration of the massive MIMO system in the uplink and downlink for LOS propagation.

1.2.4 Device-Centric Architecture

Device-centric architectures provide a promising approach to meet the increasing demand for throughput that is required by applications in today's mobile devices, such as video streaming that requires at leat 0.5 Mbps data rate. The uplink and downlink as well as control and data channels need to be reconsidered. In particular, the cell-centric architecture should evolve into a device-centric meaning that a given device should be able to exchange multiple information flows through different sets of heterogeneous nodes [Boc14]. Fig. 1.4 shows the cell-centric and device-centric networks where in the cell-centric network each user is communicating with the BS of the same cell directly while in the device-centric network each user can cooperate with the other users directly or act as a relay to other users for the communication with the BS or other users. More details on the different types of device to device communication are described later in this section. Among the device sentric and massive MIMO for 5G, mm-wave is a good candidate for localization due to higher bandwidth and smaller size of antenna arrays due to smaller wavelength. This enables highly directional links that are the key for the estimation of AOA/AOD for localization purposes. Consequently, the main focus is on the mm-wave

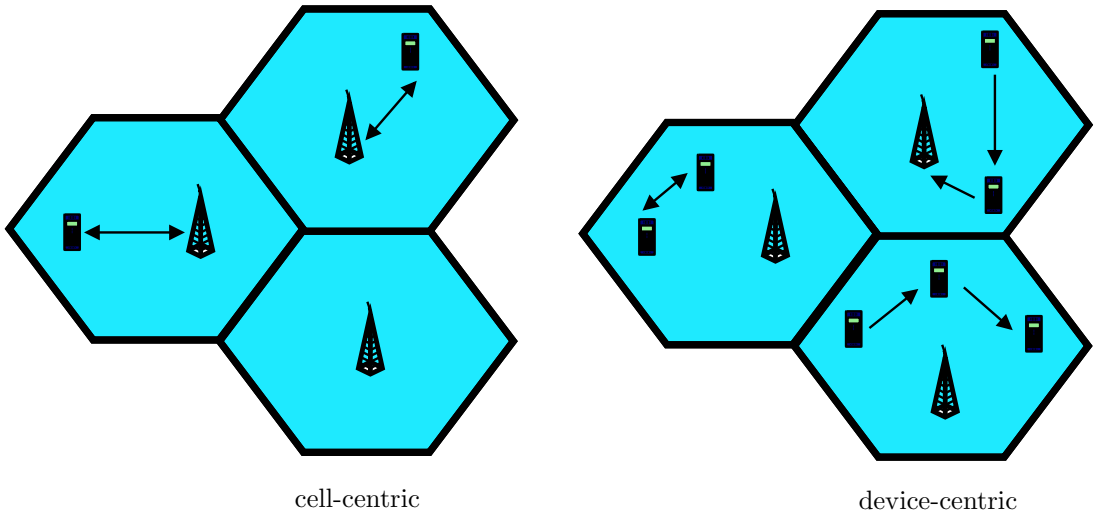

Figure 1.4: Illustration of the cell-centric (left) and the device-centric network (right).

localization for the rest of this chapter.

Device-Centric and Cell-Centric Positioning

In cell-centric localization, each agent communicates with multiple anchors[6]. This requires high density of the anchors and long-range transmissions. In device-centric localization, the agents can obtain the information from both anchors and agents. Consequently, high anchor density or long-range transmissions are no longer required [Wym09]. If an agent cannot obtain its position based on distance estimates with respect to the anchors, device-centric localization is used to cooperatively obtain the position. This increases localization accuracy and coverage [7].

1.2.5 D2D Communication

D2D communication can potentially reduce latency and power consumption and increase peak data rates. In the device level 5G cellular network, each device communicate directly to another device or through the support of other devices. The BS either partially or fully controls resource, destination, and ralaying devices or not have any control. Four types of device-level communications are briefly described [Teh14].

[6] At least 3 anchors are required for 3D localization.
[7] The fraction of nodes with accurate location estimate is called coverage.

Device relaying communication with base station controlled link

For a device located at the edge of a cell, the signal strength is poor and it is required to communicate with the BS by relaying the information through the other devices.

Direct device to device communication with base station controlled link

In this architecture, the two devices are directly communicating with the links information provided by the BS.

Device relaying communication with device controlled link

Both communication and links information are provided by the other devices and the BS is not involved in communication and link information.

Direct device to device communication with device controlled link

Two devices are directly communicating and the link information is controled by the devices.

Two of the most important challenges in D2D communication are security and interference management [Cha09]. Security is important due to the fact that the routing of information is through the other users. Interference becomes important especially for the case of device relaying communication with device controller and direct device to device communication where the centralized methods cannot be employed.

1.2.6 Location-Aware Communications

5G networks can benefit from location information. In particular for the case of D2D resource allocation, D2D links share the same cellular resources that potentially interfere with each other. For instance for the case of reusing the uplink resources, D2D transmissions interfere with cellular transmissions at the base station. To limit the the interference, either maximum transmission power should be limitted or D2D should not be allowed in the regions close to the base station. Consequently, position information of the user is of critical importance for resource allocation to ensure sufficiently large physical separation between the D2D and base station. To this end, distance and virtual sectoring based resource allocation techniques are proposed in [Kur15]. Distance based resource allocation uses a pre-selected distance constraint to control interference between D2D and cellular

nodes. Virtual sectoring based resource allocation relies on AOA measurements. In this approach, a D2D pair will reuse the radio resource that belongs to the vertically opposite sector based on the specified number of virtual sectors in the cell.

Another method to minimize the interference to the primary users in cognitive radio is the spatial spectrum sensing that can be adapted in 5G. In this approach, Gaussian processes (GPs) are used for predicting location-dependent channel qualities and provide statistical description of channel quality measurement in any location and any time. More specifically, the power from primary users can be estimated through secondary users resulting power density maps that allows resource allocation in the frequency bands that are not crowded [Tar14, Nev12, Dam13, San09].

For vehicle-to-vehicle (V2V) networks, large-scale characteristics of the wireless channel (i.e. path loss) may be captured using channel or position/motion measurements [Dan12]. It has been shown that the feedback of position information to accomplish link adaptation is favorable compared to the overhead for the feedback of path-loss information. Particularly, for the case that path-loss changes rapidly.

1.2.7 Ultra Dense Networks

The throughput of a user in 5G networks is increased by the network densification. Densification in 5G networks is achieved in the spatial and frequency domain through the deployment of small cells and using additional spectrum (e.g., millimeter wave bands spanning from 30 to 300 GHz) [Bhu14]. Due to the use of small cells or cell splitting for spatial densification, path-loss is reduced while both desired and interfering signals are increased. Consequently, to translate densification into enhanced user experience backhaul densification is required together with space and frequency densification. Cloud radio access network (Cloud-RAN) architecture with coordinated multipoint processing (CoMP) where transmit/receive processing is centralized at a single processor transmofrms the systems into a near interference free system. Massive MIMO and mm-wave communication serve as the other candidates to improve capacity for wireless backhaul.

Mobility Management in Ultra Dense Networks

A moving node in a network or a group of such nodes form a moving network that can communicate with the other fixed or mobile nodes. This enhance the coverage for potentially large populations of jointly moving communication devices [Gup15]. Tracking and predicting the device locations in the radio network is beneficial from various points of

views. Location aware communications may be considered as one of the advantages of prediciting the user locations in the wireless network. The combination of radio environment maps and predicted user node locations are used within the network for proactive radio resource management (RRM). This leads to power consumption and load balancing at the moment and near future together with proactively allocating orthogonal radio resources in time and frequency [Hak15]. Predicted user locations can be used for different applications including location data for self-driving cars, autonomous vehicles and robots.

1.3 OFDM Localization

Based on the discussion in Section 1.2.1, OFDM signals are good candidates for 5G systems due to providing high data rate, less implementation complexity, and can be easily integrated with MIMO. In this section, localization using the estimation of arrival time with OFDM signals, applications in LTE and 60 GHz indoor, and combination with communication are briefly explained.

1.3.1 Localization Based on Timing Estimation

OFDM systems require high timing synchronization accuracy to accuratly receive the signal, thus the estimation of symbol timing of the received signal is of critical importance. Once the timing estimation is achieved, the distance between BS and mobile station (MS) can be obtained. Consequently, the location of the MS is obtained by measuring the distance from the BSs. So, here we present the algorithms for the timing estimation that help localization of the MS.

Correlation-Based

In correlation based timing estimation, the cross correlation between the received signal and a known reference replica is obtained at the receiver. Then, the arrival time is estimated by finding the sample where the correlation has a maximum.

Preamble-Based

In the preamble-based methods, the autocorrelation between the received signal and conjugation of delayed received signal is obtained. The algorithm ensures better performance compared to the previous method because phase information suffers from high variations

under bad channel conditions, so two adjacent symbols are affected almost equally and they still have high correlation [Yua08]. Different preamble structures can be used for this method including: Schmidl preamble, Park preamble, Kim preamble, Ren preamble, and Kang preamble [Sch97, GR05, Par02, Kim05].

Cooperative OFDM Localization

One common approach in either source localization or navigation problem relies on time difference of arrival (TDOA) measurements to multiple sensors. In TDOA-based methods, there are either two BSs transmitting the same signal or two spatially separated MSs measuring the same transmission. In most of the cases only one BS is available, hence multiple MSs must cooperate by sharing data. As opposed to received signal strength (RSS) and AOA based methods for localization, sharing data for TDOA-based localization methods require significant bandwidth. This is due to the fact that TDOA-based localization applies generalized cross correlation of the two received signals that requires retransmission of a long portion of the signal. The retransmission of a long portion of the signal may require a large amount of bandwidth and power, which are limited resources for mobile. Exploiting the structure of OFDM signal reduce the amount of information that needs to be shared among the MSs and leads to efficient use of power and bandwidth. This is due to the fact that the beginning and the end of each block in CP-OFDM are identical due to the presence of CP. Consequently, each MS can estimate some statistical feature of each block (e.g., the sample mean or variance) and transmits the sequence of block reception times and the associated feature values to another MS, rather than retransmitting the entire signal [Mar09].

1.3.2 Applications

Some of the applications of the OFDM signals in the LTE systems and 60 GHz indoor for localization are explained in this section.

LTE

LTE systems use OFDM signals in the downlink due to robustness to radio channel dispersion with reduced receiver complexity [Ses11]. In the LTE systems, physical channels are carrying information at higher levels and are defined as: physical downlink shared channel (PDSCH), physical broadcast channel (PBCH), physical multicast channel (PMCH),

physical control format indicator channel (PCFICH), physical downlink control channel (PDCCH), and physical hybrid ARQ indicator channel (PHICH). There are four types of downlink reference signals in the LTE systems each transmitted using a single antenna port and are defined as:

- multimedia broadcast over single frequency network (MBSFN) reference signals. signals.
- cell-specific reference signal (CRS).
- user equipment (UE) specific reference signals.
- positioning reference signal (PRS).

For timing estimation, LTE systems use PRS signals in the downlink to improve the timing measurements by decreasing the inter-cell interference. PRS signals help estimating the channel impulse response to equalize the signal correctly. Moreover, it solves the interfernce between data and pilot by avoiding the data transmission in the resource blocks dedicated for positioning, e.g., PDSCH is not transmitted in the positioning subframe. Fig. 1.5 shows the allocation of data (blue lines) and pilots (red lines) for one OFDM symbol and a given channel magnitude shown by the green dashed curve where each subcarrier is used as either data or pilot.

PRS signals are sent in one to six consecutive subframes with a specific offsetΔ_{PRS} with the configuration index I_{PRS} and the period T_{PRS} [Ses11]. Fig. 1.6 shows the configuration of the complex-valued symbols of the PRS in time and frequency. The main parameters of PRS signals are given in Table 1.1.

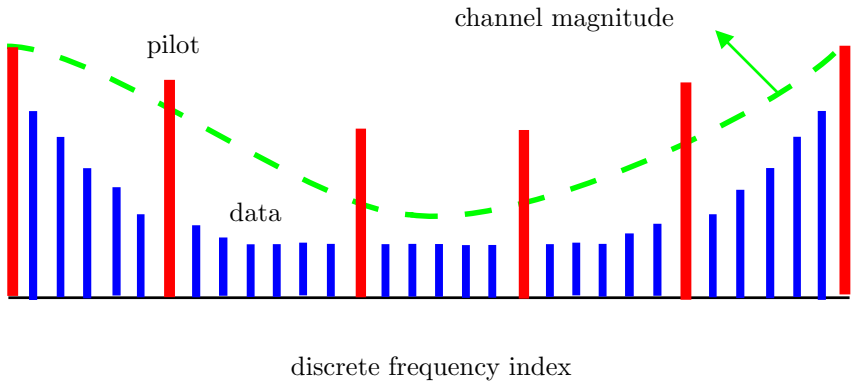

Figure 1.5: Data and pilots subcarrier power allocation for a given channel frequency response.

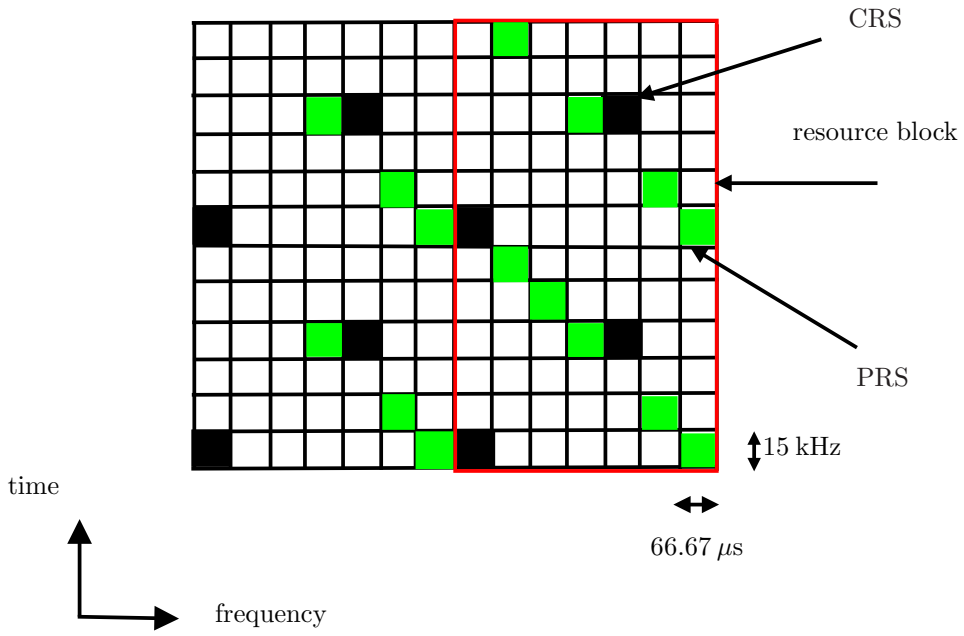

Figure 1.6: Time and frequency distribution of the LTE CRS and PRS pilot signals.

Table 1.1: Main parameters of the PRS.

PRS bandwidth	1.4, 3, 5, 10, 15, and 20 MHz
PRS periodicity	160, 320, 640, or 1280 ms
consecutive subframes	1, 2, 4, or 6
PRS muting information	2, 4, 8, 16 bits
PRS pattern	6-reuse in frequency
PRS sequence	length-31 Gold sequence

60 GHz Indoor

For 60 GHz indoor localization, OFDM signals can be used to measure the differential time difference of arrival (DTDOA). The localization is based on distance measurements of a node with unknown position, e.g., MS, and the nodes with the known positions, e.g., BSs. In the DTDOA for 60 GHz indoor localization with OFDM signals the BSs do not need to be synchronized and just exchange data with the host PC. There is a link between each BS and the host PC to collect time stamps and to perform calculations for the localization of the MS. The master BS initialize the localization process by transmitting a pseudo noise (PN) sequence received by slave BSs. The receiving time is precisely recorded by the slave BSs with their local clocks. Then, the MS transmits the PN sequence to all the BSs with the receiving time again recorded by all the BSs. The difference between the request and the response signals are calculated and sent to the host PC. Then, the pair wise propagation time differences between different BSs are used to eliminate the processing

time in the MS that is called DTDOA. In contrast to TDOA no time synchronization is required. More details on the 60 GHz indoor localization with OFDM signals can be found in [Win06].

1.4 Mm-Wave Localization

Mm-wave RF signals are the best solutions to be utilized for high speed data transmission. Moreover, multi-carrier OFDM-based signals can be used in mm-wave frequencies for the bandwidth of the order of GHz to provide better localization capabilities that also helps high speed data transmission in 5G systems. Some examples for OFDM-based signals in mm-wave frequencies are personal area network (PAN) and wireless local area network (WLAN) standards that use about 2 GHz of bandwidth and support OFDM or SC-FDE type modulations to provide data rates up to 6 Gbps. Consequently, in this section we briefly describe mm-wave channels, the methods to estimate the channel parameters including AOA/AOD and TOA using the sparsity of the mm-wave channels, and mm-wave localization techniques in LOS, in the presence of clusters, and the case of blocked LOS. First, different path-loss models for mm-wave channels are described. Second, a double directional channel model is presented. Third, some estimation techniques are proposed and the concept of channel sparsity in mm-wave is explained. Fourth, multi-beam transmission, hybrid beamformers, and beam training protocols are described as the key elements for AOA/AOD estimation. Finally, some of the mm-wave localization techniques in terms of position and rotation angle estimation are described.

1.4.1 Mm-Wave MIMO Channel Model

In a mm-wave MIMO system, channel parameters including AOA/AOD, channel gains, and TOA (i.e., the parameters that describe multipath components (MPCs)) are used for the localization purposes. A common approach for modeling the mm-wave MIMO channels is to group a set of rays with some close parameters in a cluster. Consequently, the channel response between the receiver and the transmitter can be written as the sum of K specular MPCs and the LOS as [Ric05, Gus14, Alm07]

$$\mathbf{H}(t,f)=\sum_{k=0}^{K}\rho_k\mathbf{B}_{\mathrm{Rx}}(f,\theta_{\mathrm{Rx},k})\mathbf{X}_k\mathbf{B}_{\mathrm{Tx}}^{\mathrm{T}}(f,\theta_{\mathrm{Tx},k})e^{-j2\pi f\tau_k}e^{j2\pi t\nu_k}, \tag{1.4.1}$$

where ρ_k denotes the path-loss of the n-th cluster that can be obtained using the geometry based statistical models [Li15, Li14], $\mathbf{B}_{\mathrm{Tx}}(f,\theta_{\mathrm{Tx},k}) \in \mathbb{C}^{N_{\mathrm{Tx}}\times 2}$ and $\mathbf{B}_{\mathrm{Rx}}(f,\theta_{\mathrm{Rx},k}) \in \mathbb{C}^{N_{\mathrm{Rx}}\times 2}$ denote the complex beam pattern of the transmit array and the receive array with horizontal and vertical polarisation, respectively, $\mathbf{X}_k \in \mathbb{C}^{2\times 2}$ contains the four polarimetric transmission coefficients for the k-th MPC, τ_k is the k-th TOA, and ν_k denotes the Doppler frequency for the k-th MPC.

1.4.2 Parameter Estimation

Some of the typical algorithms used in channel estimation in 5G are:

1. Space-alternating generalized expectation maximization (SAGE).
2. Joint and iterative maximum likelihood estimation in [Ric06], named RIMAX.

In the parameter estimation of the MPC, it is usually assumed the impulse response in (1.4.1) to consist of specular scattering.

SAGE

Particularly, SAGE algorithm (that is an algorithm based on expectation maximization and successively cancels interference) uses this assumption [Fle99]. The SAGE algorithm jointly estimates MPC parameters, i.e., AOA/AOD, channel gains, Doppler shifts, and TOAs.

The SAGE method can be considered as the preferred algorithm to estimate the MPC parameters due to the fact that in the mm-wave frequencies most of the power can be attributed to specular components. In the SAGE algorithm, the channel response in (1.4.1) consists of the superposition of $K + 1$ plane waves where K is the number of MPCs with specular scattering property, and the index 0 denotes the LOS path, which is omitted for the obstructed-line-of-sight (OLOS) scenario.

RIMAX

In addition to specular scattering, considering diffuse scattering improves the parameter estimation. RIMAX is an estimation method that considers the diffuse scattering in addition to specular scattering to improve the estimation of parameters. Moreover, an extended Kalman filter can be used for tracking the parameters in a sequential way for the case of time-varying channels.

1.4.3 Multi-Beam Transmission

To overcome the severe effect of path-loss [8] in mm-wave frequencies, one can increase the number of antenna elements to achieve beamforming gain. There exist some challenges in using a large number of antennas (from a few tens to hundreds of antennas) in the transmitter and receiver. One of the main challenges in using large number of antenna elements is to design beamformers that can generate narrow beams. In practice, analog beamformers using phase shifters suffer from the quantization error and fail to point the beam with sufficient accuracy [Han15, Poo12]. Moreover, digital beamformers in their conventional form require digital-to-analog-converter (DAC) for each antenna element in the transmitter and analog-to-digital-converter (ADC) for each antenna element in the receiver. Considering the large number of antenna elements in the transmitter and receiver, and the fact that DACs and ADCs consume a lot of power at mm-wave, one needs to use a more efficient way for beamforming. Moreover, multi-stream transmission using hybrid beamformers is required for both communication and localization purposes [Alk14, Pis14, Zhu16]. Particularly, it is critical to have more than one beam towards each user in order to make localization possible, as it will be explained in more detail later on.

In this section, first we review the hybrid beamformers as an important way for multi-beam transmission to obtain AOA/AOD that are used for localization purposes using the sparsity of the mm-wave MIMO channel in the beamspace. Second, a beam training protocol to find the strongest link between transmitter and receiver and consequently estimation of AOA/AOD as a key step for the localization is investigated.

Hybrid beamformers

Hybrid beamformers are used to avoid the complexity in the implementation of the typical digital beamformers that require DAC for each antenna of the transmitter and ADC for each antenna of the receiver, i.e., N_{Tx} DACs in the transmitter and N_{Rx} ADCs in the receiver. Instead, hybrid beamformers use $M_t < N_{\mathrm{Tx}}$ and $M_r < N_{\mathrm{Rx}}$ DACs and ADCs in the transmitter and receiver, respectively, where M_t and M_r denote the number of transmit and received beams that are much smaller than the number of antenna elements. Moreover, they provide multi-beam transmission like digital beamformers but with less complexity. Especially, in the estimation of AOD and AOA in LOS conditions one needs to send more than one beam at each transmission as will be explained in the next section.

[8] For a given distance, the FSPL at 60 GHz is 28 dB larger than 2.4 GHz.

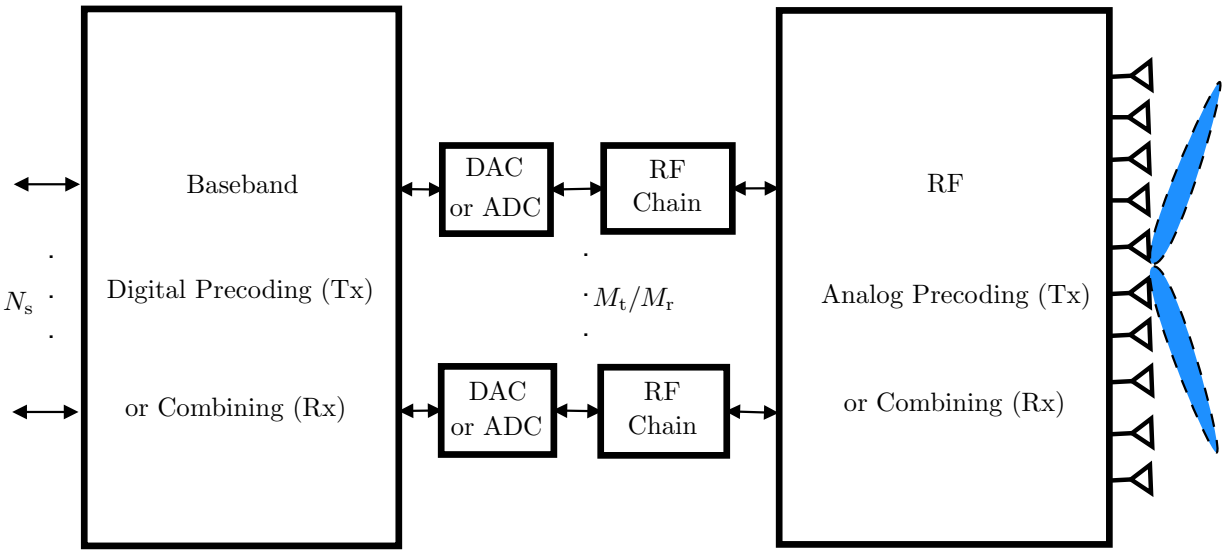

Figure 1.7: MIMO architecture at mm-wave based on hybrid analog-digital precoding and combining.

Hybrid beamformers are comprised of a baseband digital pre-coder, DACs, radio frequency (RF) chains, and a RF analog pre-coder in the transmitter; and analog RF combiner, RF chains, ADCs, and a baseband digital combiner in the receiver. More details about hybrid beamformers in the lower frequencies can be found in [Zha05, Sud06].

Fig. 1.7 shows the MIMO architecture at mm-wave using a hybrid beamformer in which N_s data streams are fed to the baseband digital pre-coder, $M_t > N_s$ outputs of the baseband precoder are converted to analog and used to generate M_t beams through RF chains that are connected to the antenna arrays by the RF analog pre-coder. On the receiver side, the received signals are fed to the RF analog combiner to capture the M_r beams, then the resulting signals are converted to digital and fed to the baseband digital combiner to reconstruct the N_s transmitted data streams.

Hybrid analog precoder/combiner can be implemented in two different ways using phase shifters and switches [Haj05, Piv13, MR15]. Although the lack of precision of analog shifter can be compensated in the digital precoder/combiner, using switches instead of analog phase shifters exploits the sparse nature of the mm-wave channel by implementing a compressed spatial sampling on the received signal and further reduces the complexity of the hybrid architecture using phase shifters.

Beam training protocols

The beam training protocol is a very important step in the AOA/AOD estimation and will be briefly explained in this section. The beam training protocol included in IEEE 802.11ad includes three major steps [ISO14]:

- Sector Level Sweep (SLS): This stage is based on a coarse combination between the sector (at the transmitter side) and antenna (at the receiver side). The transmitter sends signals for each of its sectors, with a number of sectors up to 64 per antenna. After completing the sweep by the transmitter, the MS selects the best sector and sends feedback to the transmitter. At the end of this stage a coarse estimation of the AOD is obtained.

- Beam Refinement Protocol (BRP): In this stage, the coarse estimation of the AOD will be refined by sending the orthogonal beams within the optimal sector found from the previous stage. The receiver sends feedback to the transmitter regarding the success of the new beam. At the end of this stage a refined estimation of the AOD is obtained.

- Beam tracking: This stage includes a periodic refinement over a small number of antenna configurations.

Beam training protocols can be generalized for hybrid precoding rather than only for analog beamformers. The main advantage is the capability to steer the beam with more accuracy than using only phase shifters thanks to the compensation of the error in analog part using the digital pre-coder. This approach starts with the coarse search for the best AOA/AOD and channel gains (SLS step) and refines the estimated values (BRP step) in the final stages using a novel multi-resolution beamforming codebook.

Fig. 1.8 illustrates the beam training protocol as an important strategy to find the best link between the BS and the MS. Particularly, when one link is not strong enough or is blocked and cannot be used to estimate the channel parameters (i.e., AOA/AOD, delay, and channel gain), using first the beam training protocol, we can obtain the sector that provides the LOS conditions, and then we use the LOS link[9] to localize the MS using the AOA/AOD and delay estimates, as will be discussed below. In what follows, we provide an overview on the localization of the MS using AOA/AOD, and TOA in a mm-wave MIMO system.

[9] Although, it is possible to use the information from the NLOS link for localization as will be discussed in the next section.

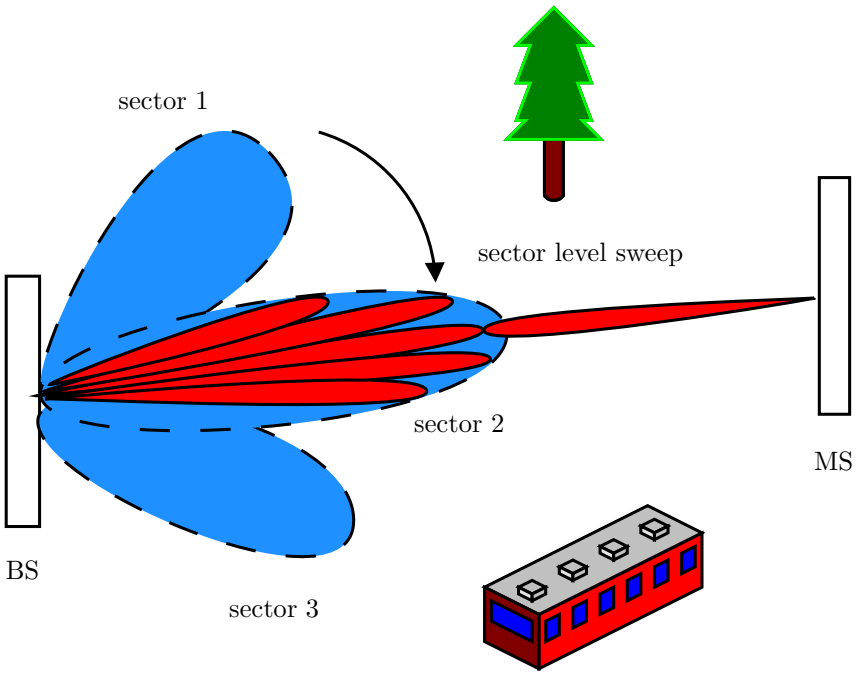

Figure 1.8: Finding the optimal sector and beam for the localization of the MS by the SLS and BRP.

1.4.4 Mm-Wave localization Techniques

From the above discussion, we interpret that all the aforementioned methods either use the information from angles, delays, or RSS. However, one may envision that both angles and delays can be used for the localization at the same time. Particularly, large number of antenna elements in the transmitter and receiver in the 5G systems provides steerable narrow beams that can be used for localization with AOA/AOD and TOA.

Fig. 1.9 shows the LOS link for the localization of the MS using joint angle and delay measurements. The TOA provides a circle with the radius of d_0 from the MS centered in $\mathbf{q}$, AOD and AOA provide lines that eventually leads to the localization of the MS as shown in Fig. 1.10. This can be simply expressed as

$$(q_x - p_x)^2 + (q_y - p_y)^2 = d_0^2, \tag{1.4.2}$$

and

$$\tan(\theta_{\mathrm{Tx},0}) = \frac{p_y - q_y}{p_x - q_x}. \tag{1.4.3}$$

Solving (1.4.2) and (1.4.3) leads to

$$\mathbf{p} = \mathbf{q} + d_0 \mathbf{u}(\theta_{\mathrm{Tx},0}),$$

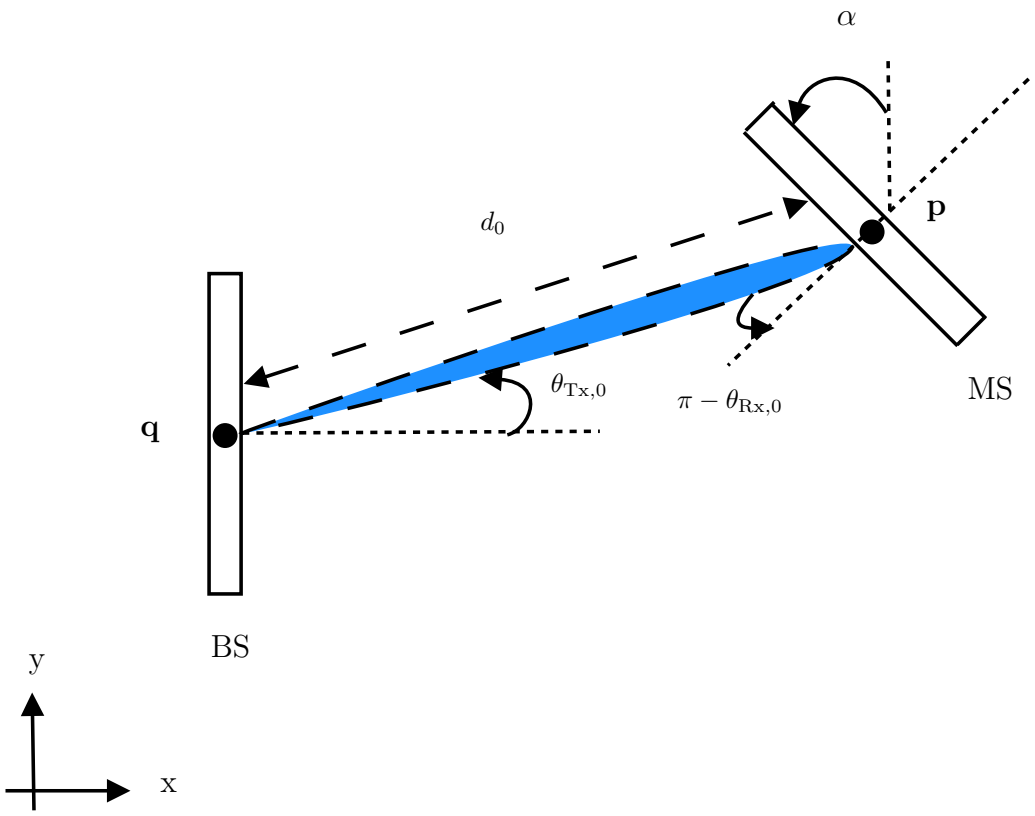

Figure 1.9: LOS link for the localization based on joint AOA/AOD and TOA estimation.

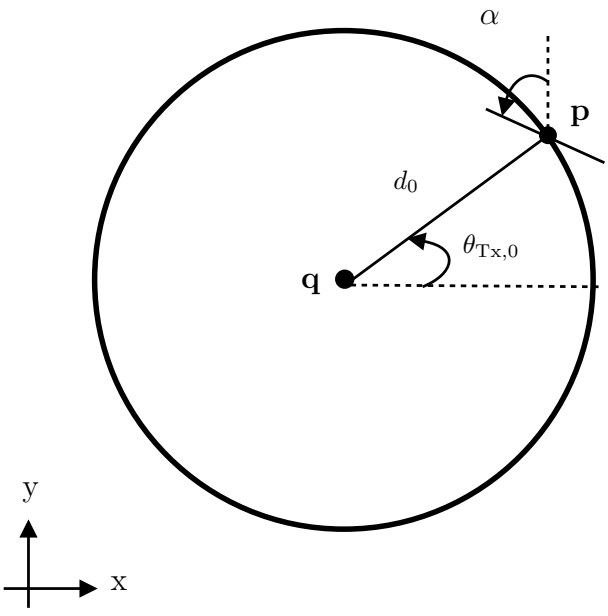

Figure 1.10: Demonstration of the localization in the LOS with TOA and AOA/AOD.

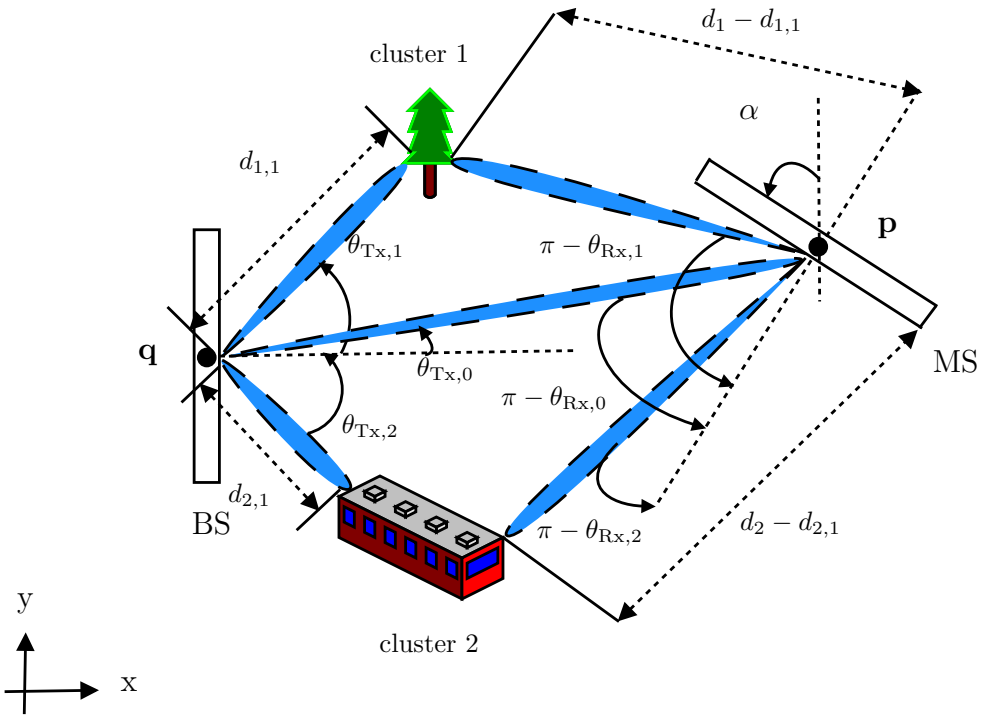

Figure 1.11: LOS in the presence of clusters for the localization based on joint AOA/AOD and TOA estimation.

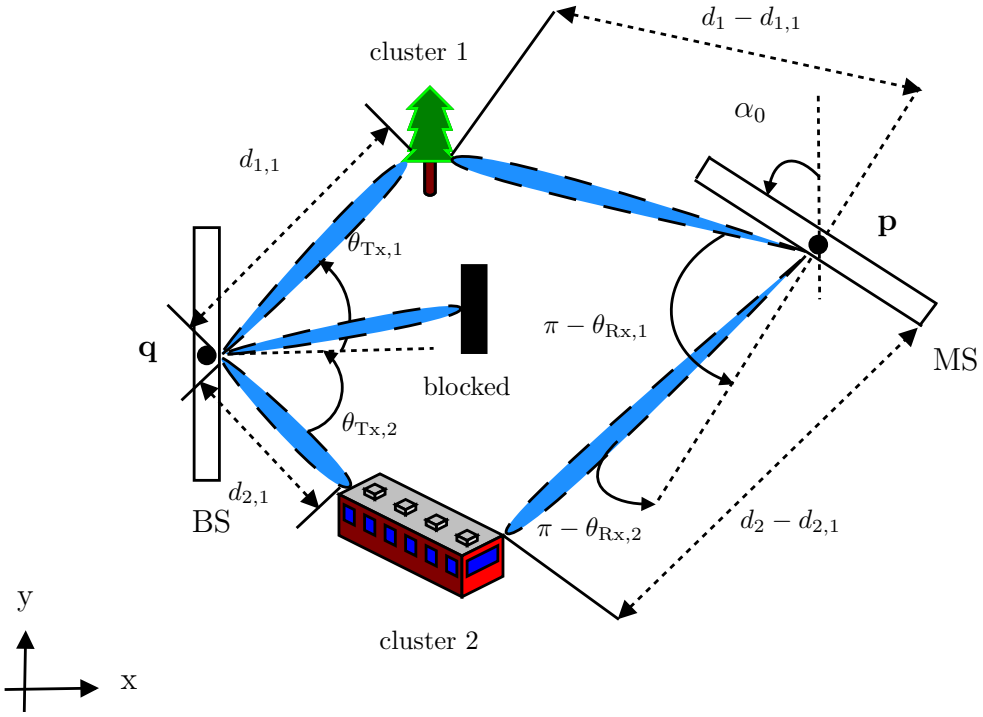

Figure 1.12: NLOS link for the localization based on joint AOA/AOD and TOA estimation.

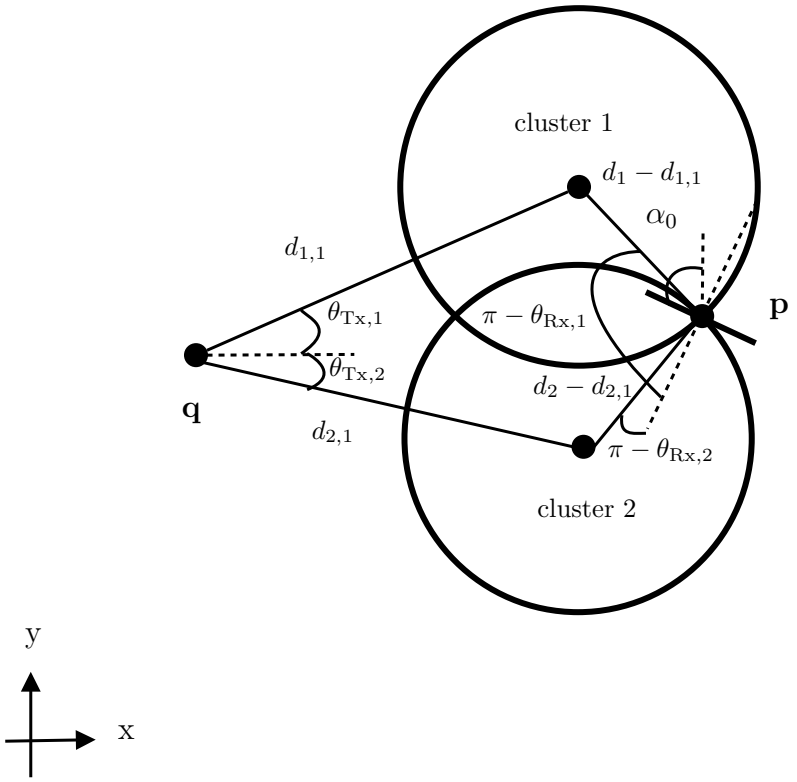

Figure 1.13: Demonstration of the localization in the NLOS with TOA and AOA/AOD.

where $\mathbf{u}(\theta_{\mathrm{Tx},0}) = [\cos(\theta_{\mathrm{Tx},0}), \sin(\theta_{\mathrm{Tx},0})]^{\mathrm{T}}$. Moreover, the orientation is obtained as $\alpha = \pi + \theta_{\mathrm{Tx},0} - \theta_{\mathrm{Rx},0}$. Fig. 1.11 shows the LOS link in the presence of clusters. In this case, the presence of clusters reduces the localization accuracy depending on the location of the clusters towards the LOS link as will be shown in the simulation results. Moreover, the orientation is *only* estimated through the LOS link and the clusters do not provide any information on the orientation of the MS.

Fig. 1.12 demonstrates the use of NLOS links [10] for the localization of the MS using joint angle and delay measurements and a given orientation α_0. In this case the location of the MS can be obtained using the following equations

$$\|\mathbf{p} - \mathbf{s}_1\| + \|\mathbf{q} - \mathbf{s}_1\| = d_1, \tag{1.4.4}$$

$$\|\mathbf{p} - \mathbf{s}_2\| + \|\mathbf{q} - \mathbf{s}_2\| = d_2, \tag{1.4.5}$$

$$\mathbf{s}_1 = \mathbf{q} + d_{1,1}\mathbf{u}(\theta_{\mathrm{Tx},1}), \tag{1.4.6}$$

$$\mathbf{s}_2 = \mathbf{q} + d_{2,1}\mathbf{u}(\theta_{\mathrm{Tx},2}), \tag{1.4.7}$$

[10] This can be also considered as the blocked LOS as in the mm-wave frequencies blockage happens quite often especially for indoor localization.

$$\tan(\pi - (\theta_{\mathrm{Rx},1} + \alpha_0)) = \frac{s_{1,y} - p_y}{p_x - s_{1,x}}, \tag{1.4.8}$$

$$\tan(\pi - (\theta_{\mathrm{Rx},2} + \alpha_0)) = \frac{-s_{2,y} + p_y}{p_x - s_{2,x}}, \tag{1.4.9}$$

where $\mathbf{q}$ is known, $\{\theta_{\mathrm{Tx},k}, \theta_{\mathrm{Rx},k}, d_k\}$ denotes the set of estimated parameters that are assumed to be known, $\mathbf{p}$ is the unknown location of the MS, and $\{\mathbf{s}_k, d_{k,1}\}$ denotes the set of unknown parameters including the location of the k-th cluster $\mathbf{s}_k$ and the distance between the k-th cluster and the BS $d_{k,1}$. Considering 2-D localization, there are 8 unknown parameters that can be obtained by the above set of equations. The TOA from two clusters provide the intersection from two circles as shown in Fig. 1.13, while the AOAs provide the lines for the localization of the MS.

1.5 Motivation and Objectives

High data rate with good localization accuracy is a challenging problem in 5G systems. Signals that are designed for one application, e.g., high data rate communication, perform poorly for the other application, e.g., localization. Moreover, in the WNL the performance of the signals designed for localization of the MS is susceptible to the network uncertainties such as position and channel uncertainties. Fig. 1.14 shows the effect of the agent movement in the uncertainty disk that leads to the wrong estimation of the location of the MS. Thus, novel design algorithms using OFDM signals are proposed to counteract the effect of poor performance in terms of localization or communication and network uncertainties. Using the OFDM signals is of interest due to the allocation of some of the subcarriers for data transmission and the rest of subcarriers for localization and channel estimation. Moreover, due to frequency diversity OFDM signals enable saving the total required power for WNL in the presence of network uncertainties.

In mm-wave localization, the main challenge is the severe effect of path-loss. It is important to find a solution for the the severe effect of path-loss due to good capabilities of the mm-wave frequencies for indoor localization including large bandwidth. To this end, large number of antenna arrays can be used in the transmitter and receiver. However, using the large number of antenna arrays requires designing the beamformers to form the beams towards the nodes with unknown positions. Thus, a novel estimation approach using the sparsity of mm-wave channels can be applied to estimate the AOA/AOD and consequently TOA that are required for localization of the MS. Particularly, a hybrid precoding system with OFDM signals for the goal of position and orientation estimation

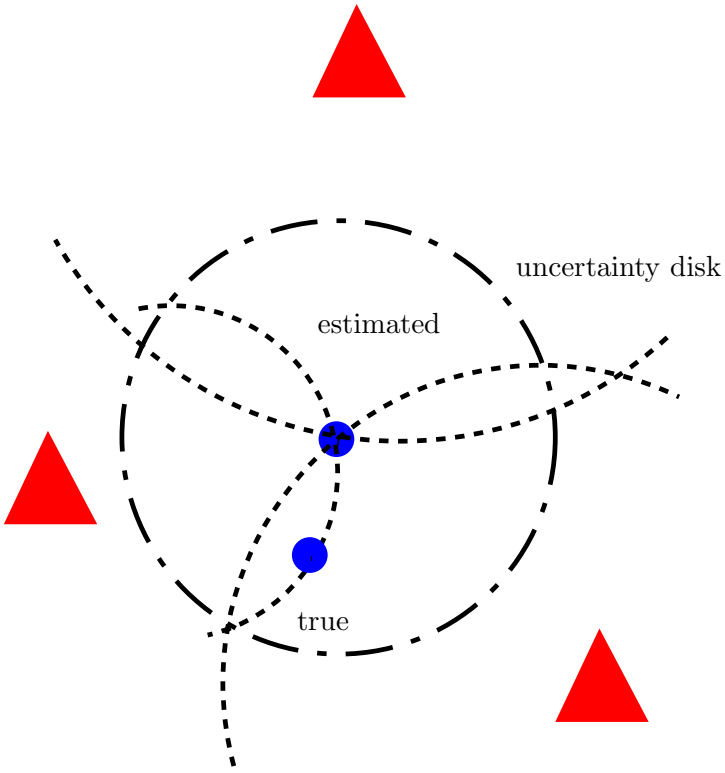

Figure 1.14: Illustration of the effect of position uncertainty on WNL.

of the MS that helps increasing the spectral efficiency is critical for 5G systems.

The aim of this thesis is to explore the capabilities of OFDM signals for joint localization and communication, WNL, and sparse estimation of channel parameters for 5G localization.

1.6 Thesis Outline

Chapter 2 provides background on joint data and pilot design for the joint localization and communication purposes using OFDM signals. In particular, the problem is extended for the case of time varying channels as the extension to the previously proposed results for static channels [Mon13].

Chapter 3 provides an extensive research on ergodic and robust power allocations for OFDM WNL. Different power allocation methods are proposed for minimizing the total power with respect to constraints on the localization accuracy. Ergodic power allocation is proposed based on the sample average representation of the expected squared position error bound (SPEB) and the solution is obtained using the semidefinite optimization.

Robust allocations using different uncertainties on the channel coefficients are proposed.

Chapter 4 provides an extensive research on the 5G position and orientation estimation. The fundamental bounds on the position and orientation together with channel parameters in the presence of clusters are proposed. The sparse estimation algorithms are proposed to achieve the proposed bounds.

1.7 Research Contributions

The work of this dissertation has been presented in several publications such as journals, book chapters, and international conferences. These research contributions are listed for every chapter.

Chapter 2

The main result of this chapter is the OFDM signal design for joint localization and communication for the case of time-varying frequency selective channels. The results in this chapter have been published either directly or indirectly in the following international conferences or are supposed to be submitted as journal papers:

[1] A. Shahmansoori, R. Montalban, J. A. Lopez-Salcedo,G. Seco-Granados, "Design of OFDM Sequences for Joint Communications and Positioning Based on the Asymptotic Expected CRB," in International Conference on Localization and GNSS (ICL-GNSS), 2014.

[2] A. Shahmansoori, R. Montalban, G. Seco-Granados, "Effect of Channel Variability on Pilot Design for Joint Communications and Positioning in OFDM," Proc. IEEE Intl. Symposium on Wireless Communication Systems (ISWCS), Aug 26 2014.

[3] A. Shahmansoori, R. Montalban, G. Seco-Granados, "Optimal OFDM Pilot Sequences for Time-Delay and Channel Estimation Based on the Expected CRB for a Large Number of Subcarriers," in The 15th IEEE International Workshop on Signal Processing Advances in Wireless Communications (SPAWC), 2014.

Chapter 3

The main result of this chapter is the design of ergodic and robust power allocations for OFDM WNL. Different channel uncertainties are considered for the aforementioned

allocations and the results are compared with their single-carrier counterparts. The result of this chapter is submitted to the following journal and conference papers:

[4] Arash Shahmansoori, Gonzalo Seco-Granados, and Henk Wymeersch, "Robust and Ergodic Power Allocation for OFDM Wireless Network Localization," submitted to IEEE Transactions on Wireless Communications, May 2016.

[5] Arash Shahmansoori, Gonzalo Seco-Granados, Henk Wymeersch, "Robust Power Allocation for OFDM Wireless Network Localization," IEEE International Conference on Communications (ICC) 2015.

Chapter 4

The main result of this chapter is the fundamental bounds on the position and orientation estimation for 5G localization in the presence of clusters. The sparse estimation methods are developed that approach the aforementioned bounds. The results in this paper have been/supposed to be submitted to the following journal, conference papers, and book chapter:

[6] Arash Shahmansoori, Gabriel E. Garcia, Giuseppe Destino, Gonzalo Seco-Granados, Henk Wymeersch, "5G Position and Orientation Estimation through Millimeter Wave MIMO," IEEE Global Telecomm. Conf. (GLOBECOM) 2015.

[7] Arash Shahmansoori, Gonzalo Seco-Granados, Henk Wymeersch, "Survey on 5G Positioning," Multi-Technology Positioning, to appear as a book chapter published by Springer.

[8] Arash Shahmansoori, Gabriel E. Garcia, Giuseppe Destino, Gonzalo Seco-Granados, Henk Wymeersch, "Position and Orientation Estimation through Millimeter Wave MIMO in 5G Systems," to be submitted to IEEE Transactions on Signal Processing.

Chapter 2

OFDM Allocation under Timing Accuracy Constraints

2.1 Introduction

The design of combined positioning and communication systems that can perform well in terms of high-data-rate transmission and delay estimation accuracy is a challenging problem. In general, the signals used for one purpose perform poorly in the other case.

To date different approaches are proposed for the signal design for channel estimation that leads to equi-power and equi-space pilots [Neg98, Bar03, Min06]. Pilot design for carrier frequency offset (CFO) estimation and joint estimation of channel and CFO are proposed in [Min05] and [Sto03], respectively. However, joint data and pilot design based on channel and time-delay estimation is received a little attention.

Recently, joint data and pilot designs based on Cramér-Rao bound (CRB) and expected CRB (ECRB) of time-delay and channel coefficients are investigated by solving the relaxed optimization and masking the relaxed solution to allow subcarriers to be used either for estimation or data transmission [Lar11, Mon13]. However, the methods are not taking into account the effect of channel variations with time that usually happens in reality, and only consider the designs for static channels. In other words, they assume that channel coefficients are the same for different OFDM symbols. Specially, in the long-term evolution (LTE) systems one needs to design an optimal positioning reference signal that can be applied for high data rate communications and achieve desired time-delay estimation accuracy.

The design of data and pilots in time and frequency for high-data rate communications

with a given time-delay estimation accuracy that is used for localization is of critical importance in the 5G systems. As an application, for mobility management in ultra dense networks power consumption and load balancing is necessary with allocating orthogonal radio resources in time and frequency. In this chapter, we consider time-varying frequency selective channels for the joint design of data and pilots based on the expected CRB (ECRB) of time-delay and channel coefficients. The proposed model is more general than [Lar11, Mon13] by considering time variations and not assuming time-delays to be resolvable, i.e., it is not assumed that $\tau_l = \tau_1 + (l-1)T_s$ where τ_1 is the delay from the first path and T_s denotes the sampling period. The ECRB of time-delay and channel coefficients are used to obtain the approximate lower bound of channel capacity that is used for combined data and pilot optimization to maximize the capacity for a certain time-delay accuracy. The optimization problem is not convex, so we obtain the relaxed solution and consider data and pilot accordingly by applying a two-dimensional mask. The results show that the close-to-optimal solution requires the semi stair-wise pattern of the pilots.

2.2 System Model and Preliminaries

Using the assumption that channel variations in delay subspace is much slower than channel variations in the amplitude subspace [Sim04], see Appendix 2.A, we obtain[1]

$$\mathbf{r} = \mathbf{B}(\mathbf{I}_K \otimes \left[\mathbf{\Gamma}(\tau_1)\widetilde{\mathbf{g}}_f \ \ldots \ \mathbf{\Gamma}(\tau_L)\widetilde{\mathbf{g}}_f\right])\mathbf{h} + \mathbf{w}, \tag{2.2.2}$$

wherein $\mathbf{B}$ is an $KN \times KN$ diagonal matrix with $N \times N$ diagonal matrix at the ith OFDM symbol as $\mathbf{B}_i$ and N and K being the number of subcarriers and OFDM symbols, respectively, $\mathbf{I}_K$ is $K \times K$ identity matrix, $\mathbf{\Gamma}(\tau_i)$ is an $N \times N$ diagonal matrix with the kth diagonal element of $\exp(-j\frac{2\pi}{N}k\tau_i)$ for $k = 0, \ldots, N-1$ with τ_i denoting the ith delay, $\widetilde{\mathbf{g}}_f$ is an $N \times 1$ vector defined as $\widetilde{\mathbf{g}}_f^{\mathrm{T}} = [\widetilde{g}_f(0), \ldots, \widetilde{g}_f(N-1)]$ with $\widetilde{g}_f(k)$ defined as multiplication of kth row of DFT matrix $\mathbf{F}$ with $N-W$ zero-padded sampled response vector of transmit, channel, and receiver filter $\widetilde{\mathbf{g}}^{\mathrm{T}} = [g(0T), \ldots, g((W-1)T), 0, \ldots, 0]$ where W denotes the maximum number of the non-zero samples, $\mathbf{h}^{\mathrm{T}} = [\mathbf{h}_1^{\mathrm{T}}, \ldots, \mathbf{h}_K^{\mathrm{T}}]$ in

[1] Also, if we assume that the delay from the lth path can be written as a function of the delay from the first path as $\tau_l = (l-1)+\tau_1$ and $g(lT) = \delta(lT)$ where $\delta(.)$ denotes the Dirac delta function [Lar11, Mon13], then (2.2.2) can be further simplified as

$$\mathbf{y} = \mathbf{B}(\mathbf{I}_K \otimes \mathbf{\Gamma}(\tau_1)\mathbf{F}_L)\mathbf{h} + \mathbf{w}, \tag{2.2.1}$$

which is the extended version of the model proposed in [Lar11, Mon13] for K OFDM symbols.

which $\mathbf{h}_i$ is an $L \times 1$ complex amplitude of different paths for the ith OFDM symbol, $\mathbf{w}^{\mathrm{T}} = [\mathbf{w}_1^{\mathrm{T}}, \ldots, \mathbf{w}_K^{\mathrm{T}}]$ where $\mathbf{w}_i$ is an $N \times 1$ zero-mean complex Gaussian noise vector with the variance of σ_w^2, and $\mathbf{r}$ denotes the $KN \times 1$ received signal.

2.3 Fundamental Bounds

In this section, first we compute the Cramér-Rao bound (CRB) of joint time-delay of the first path τ_1 and complex fading coefficients $\mathbf{h}$. Then, an approximate expression for the joint ECRB of τ_1 and $\mathbf{h}$ is investigated using the Laplace approximation. Then, we obtain the bounds for the special case of $\widetilde{\mathbf{g}}_f = \mathbf{1}$ and $\tau_l = \tau_1 + (l-1)T_s$.

2.3.1 FIM

Let $\boldsymbol{\xi} = [\boldsymbol{\tau}^{\mathrm{T}}, \Re[\mathbf{h}^{\mathrm{T}}], \Im[\mathbf{h}^{\mathrm{T}}]]^{\mathrm{T}}$ denote the parameter vector of interest, where $\Re[.]$ and $\Im[.]$ stand for real and imaginary parts of $\mathbf{h}$ respectively. The received signal vector $\mathbf{r}$ is a circularly symmetric Gaussian vector with mean defined as $\boldsymbol{\mu} = \mathbf{B}(\mathbf{I}_K \otimes \left[\boldsymbol{\Gamma}(\tau_1)\widetilde{\mathbf{g}}_f \ \ldots \ \boldsymbol{\Gamma}(\tau_L)\widetilde{\mathbf{g}}_f\right])\mathbf{h}$ and covariance $\mathbf{C} = \sigma_w^2\mathbf{I}$. It is known that the FIM for estimation of $[\,\boldsymbol{\xi}^{\mathrm{T}} \ \sigma_w^2\,]^{\mathrm{T}}$ is block diagonal i.e., the estimation of $\boldsymbol{\xi}$ is decoupled from that of σ_w^2 [Sto03]. Therefore, we only consider the FIM of $\boldsymbol{\xi}$, $\mathbf{I}(\boldsymbol{\xi})$ defined as

$$\mathbf{I}(\boldsymbol{\xi}) = \frac{2}{\sigma_w^2}\Re\left[\frac{\partial\widetilde{\boldsymbol{\mu}}^{\mathrm{H}}}{\partial\boldsymbol{\xi}}\mathbf{P}\frac{\partial\widetilde{\boldsymbol{\mu}}}{\boldsymbol{\xi}^{\mathrm{T}}}\right], \tag{2.3.1}$$

where $\widetilde{\boldsymbol{\mu}} = (\mathbf{I}_K \otimes \left[\boldsymbol{\Gamma}(\tau_1)\widetilde{\mathbf{g}}_f \ \ldots \ \boldsymbol{\Gamma}(\tau_L)\widetilde{\mathbf{g}}_f\right])\mathbf{h}$, and $\mathbf{P} = \mathbf{B}^{\mathrm{H}}\mathbf{B}$. The FIM can be written as (see the Appendix 2.B)

$$\mathbf{I}(\boldsymbol{\xi}) = \frac{2}{\sigma_w^2}\begin{bmatrix} \widetilde{\mathbf{Q}} & \Im[\mathbf{Z}] & \Re[\mathbf{Z}] \\ -\Im[\mathbf{Z}^{\mathrm{H}}] & \Re[\mathbf{Y}^{\mathrm{H}}\mathbf{P}\mathbf{Y}] & -\Im[\mathbf{Y}^{\mathrm{H}}\mathbf{P}\mathbf{Y}] \\ \Re[\mathbf{Z}^{\mathrm{H}}] & \Im[\mathbf{Y}^{\mathrm{H}}\mathbf{P}\mathbf{Y}] & \Re[\mathbf{Y}^{\mathrm{H}}\mathbf{P}\mathbf{Y}] \end{bmatrix}, \tag{2.3.2}$$

where

$$\widetilde{\mathbf{Q}} = \sum_{i=1}^{K}\Re\begin{bmatrix} \mathbf{Q}_i^{11} & \ldots & \mathbf{Q}_i^{1L} \\ \vdots & \ddots & \vdots \\ \mathbf{Q}_i^{L1} & \ldots & \mathbf{Q}_i^{LL} \end{bmatrix}, \tag{2.3.3}$$

and

$$\mathbf{Z}^{\mathrm{H}} = \left[\mathbf{X}_1^{\mathrm{H}}\mathbf{h} \ \ldots \ \mathbf{X}_d^{\mathrm{H}}\mathbf{h}\right], \tag{2.3.4}$$

with $\mathbf{Q}_i^{lm}$ is defined for $l = m = 1, \ldots, d$ as $\mathbf{Q}_i^{lm} = h_{l,i}^* h_{m,i} \widetilde{\mathbf{g}}_f^{\mathrm{H}} \mathbf{\Gamma}(\tau_l - \tau_m) \mathbf{D}^{\mathrm{H}} \mathbf{P}_i \mathbf{D} \widetilde{\mathbf{g}}_f$, $\mathbf{P}_i$ is an $N \times N$ diagonal matrix of input power at the ith OFDM symbol, and $\mathbf{D}$ is the derivative matrix of $\mathbf{\Gamma}(\tau_i)$ with respect to τ_i that results an $N \times N$ diagonal matrix with the kth entry equal to $\frac{2\pi}{N} k$ for $k = 0, \ldots, N-1$. Also, $\mathbf{X}_l$ is defined as $\mathbf{X}_l = \mathbf{Y}_l^{\mathrm{H}} \mathbf{P} \mathbf{Y}$ with $\mathbf{Y}$ and $\mathbf{Y}_l$ defined as

$$\mathbf{Y} = (\mathbf{I}_K \otimes \left[\mathbf{\Gamma}(\tau_1) \widetilde{\mathbf{g}}_f \ \ldots \ \mathbf{\Gamma}(\tau_L) \widetilde{\mathbf{g}}_f \right]),$$

and

$$\mathbf{Y}_i = (\mathbf{I}_K \otimes \left[\mathbf{0} \ \ldots \ \mathbf{0} \ \mathbf{D} \ \mathbf{\Gamma}(\tau_i) \widetilde{\mathbf{g}}_f \ \mathbf{0} \ \ldots \ \mathbf{0} \right]),$$

respectively. Using the formula for the inverse of block matrices [Kay10], we obtain $\mathrm{CRB}(\boldsymbol{\tau})$ and $\mathrm{CRB}([\Re[\mathbf{h}^{\mathrm{T}}], \Im[\mathbf{h}^{\mathrm{T}}]]^{\mathrm{T}})$ as

$$\mathrm{CRB}(\boldsymbol{\tau}) = \frac{\sigma_w^2}{2} \mathbf{\Phi}^{-1}, \tag{2.3.5}$$

and

$$\mathrm{CRB}([\Re[\mathbf{h}^{\mathrm{T}}], \Im[\mathbf{h}^{\mathrm{T}}]]^{\mathrm{T}}) = \frac{\sigma_w^2}{2} \mathbf{\Psi}^{-1}, \tag{2.3.6}$$

where $\mathbf{\Phi} = \widetilde{\mathbf{Q}} - \mathbf{F}_b^{\mathrm{H}} \mathbf{F}_a^{-1} \mathbf{F}_b$, and $\mathbf{\Psi} = \mathbf{F}_a - \mathbf{F}_b \widetilde{\mathbf{Q}}^{-1} \mathbf{F}_b^{\mathrm{H}}$ with

$$\mathbf{F}_a = \begin{bmatrix} \Re[\mathbf{Y}^{\mathrm{H}} \mathbf{P} \mathbf{Y}] & -\Im[\mathbf{Y}^{\mathrm{H}} \mathbf{P} \mathbf{Y}] \\ \Im[\mathbf{Y}^{\mathrm{H}} \mathbf{P} \mathbf{Y}] & \Re[\mathbf{Y}^{\mathrm{H}} \mathbf{P} \mathbf{Y}] \end{bmatrix},$$

$$\mathbf{F}_b = \begin{bmatrix} -\Im[\mathbf{Z}^{\mathrm{H}}] \\ \Re[\mathbf{Z}^{\mathrm{H}}] \end{bmatrix},$$

$$\widetilde{\mathbf{Q}} = \sum_{i=1}^{K} \Re \begin{bmatrix} Q_i^{11} & \ldots & Q_i^{1L} \\ \vdots & \ddots & \vdots \\ Q_i^{L1} & \ldots & Q_i^{LL} \end{bmatrix},$$

$$\mathbf{Z}^{\mathrm{H}} = \left[\mathbf{X}_1^{\mathrm{H}} \mathbf{h} \ \ldots \ \mathbf{X}_d^{\mathrm{H}} \mathbf{h} \right],$$

$$\mathbf{Y} = (\mathbf{I}_K \otimes \left[\mathbf{\Gamma}(\tau_1) \widetilde{\mathbf{g}}_f \ \ldots \ \mathbf{\Gamma}(\tau_L) \widetilde{\mathbf{g}}_f \right]),$$

with $Q_i^{lm} = h_{l,i}^* h_{m,i} \widetilde{\mathbf{g}}_f^{\mathrm{H}} \mathbf{\Gamma}(\tau_l - \tau_m) \mathbf{D}^{\mathrm{H}} \mathbf{P}_i \mathbf{D} \widetilde{\mathbf{g}}_f$ for $l = m = 1, \ldots, d$. Finally, we obtain the CRB of time-delay and complex coefficients $\Re[\mathbf{h}] + j\Im[\mathbf{h}]$ from the real and imaginary parts of $\mathbf{h}$ as

$$\mathrm{CRB}(\boldsymbol{\tau}) = \frac{\sigma_w^2}{2} (\underbrace{\widetilde{\mathbf{Q}} - \Re[\mathbf{Z}(\mathbf{Y}^{\mathrm{H}} \mathbf{P} \mathbf{Y})^{-1} \mathbf{Z}^{\mathrm{H}}]}_{\mathbf{\Phi}})^{-1}, \tag{2.3.7}$$

and

$$\mathrm{CRB}(\mathbf{h}) = \frac{\sigma_w^2}{2}(2(\mathbf{Y}^{\mathrm{H}}\mathbf{P}\mathbf{Y})^{-1} + \boldsymbol{\Upsilon}\boldsymbol{\Phi}^{-1}\boldsymbol{\Upsilon}^{\mathrm{H}}). \tag{2.3.8}$$

Taking the expectation with respect to channel coefficients $\mathbf{h}$, using Laplace approximation $\mathbb{E}[\frac{X}{Y}] \approx \frac{\mathbb{E}[X]}{\mathbb{E}[Y]}$, and assuming the real and imaginary parts of channel coefficients $\Re[\mathbf{h}]$ and $\Im[\mathbf{h}]$ are independent or $\mathbb{E}[\Re[\mathbf{h}]\Im[\mathbf{h}^{\mathrm{H}}]] = \mathbf{0}$, we obtain the ECRB of time-delay and channel coefficients as

$$\mathrm{ECRB}(\boldsymbol{\tau}) \approx \frac{\sigma_w^2}{2}(\underbrace{\widetilde{\mathbf{Q}}_D - \boldsymbol{\Phi}_R}_{\widetilde{\boldsymbol{\Phi}}})^{-1}, \tag{2.3.9}$$

and

$$\mathrm{ECRB}(\mathbf{h}) \approx \frac{\sigma_w^2}{2}(2(\mathbf{Y}^{\mathrm{H}}\mathbf{P}\mathbf{Y})^{-1} + (\mathbf{Y}^{\mathrm{H}}\mathbf{P}\mathbf{Y})^{-1}\mathbf{X}^{\mathrm{H}}(\widetilde{\boldsymbol{\Phi}}^{-1} \otimes \mathbf{C}_h)\mathbf{X}(\mathbf{Y}^{\mathrm{H}}\mathbf{P}\mathbf{Y})^{-1}), \tag{2.3.10}$$

where

$$\boldsymbol{\Phi}_R = \Re\begin{bmatrix} \mathrm{tr}\{\boldsymbol{\Xi}_{11}\mathbf{C}_h\} & \dots & \mathrm{tr}\{\boldsymbol{\Xi}_{1L}\mathbf{C}_h\} \\ \vdots & \ddots & \vdots \\ \mathrm{tr}\{\boldsymbol{\Xi}_{L1}\mathbf{C}_h\} & \dots & \mathrm{tr}\{\boldsymbol{\Xi}_{LL}\mathbf{C}_h\} \end{bmatrix},$$

and $\boldsymbol{\Xi}_{ij} = \mathbf{X}_i(\mathbf{Y}^{\mathrm{H}}\mathbf{P}\mathbf{Y})^{-1}\mathbf{X}_j^{\mathrm{H}}$, $\mathbf{X}^{\mathrm{H}} = [\mathbf{X}_1^{\mathrm{H}}, \dots, \mathbf{X}_L^{\mathrm{H}}]$, $\widetilde{\mathbf{Q}}_D$ is defined as

$$\widetilde{\mathbf{Q}}_D = \sum_{i=1}^{K}\begin{bmatrix} \overline{|h_{1,i}|^2}\widetilde{Q} & \dots & \mathbf{0} \\ \vdots & \ddots & \vdots \\ \mathbf{0} & \dots & \overline{|h_{L,i}|^2}\widetilde{Q} \end{bmatrix},$$

with $\widetilde{Q} = \widetilde{\mathbf{g}}_f^{\mathrm{H}}\mathbf{D}^{\mathrm{H}}\mathbf{P}_i\mathbf{D}\widetilde{\mathbf{g}}_f$, and $\overline{|h_{l,i}|^2} = \mathbb{E}[|h_{l,i}|^2]$.

2.3.2 Special Case

We compute the Fisher information matrix (FIM), CRB, and ECRB of time-delay and channel coefficients for the special case when $\widetilde{\mathbf{g}}_f = \mathbf{1}$ and $\tau_l = \tau_1 + (l-1)T_s$. Choosing the time-delay as $\tau_l = \tau_1 + (l-1)T_s$ converts the FIM to the following form (see the Appendix 2.C)

$$\mathbf{J}(\boldsymbol{\zeta}) = \frac{2}{\sigma_w^2}\begin{bmatrix} \mathbf{1}^{\mathrm{T}}\widetilde{\mathbf{Q}}\mathbf{1} & \Im[\mathbf{1}^{\mathrm{T}}\widetilde{\mathbf{Z}}] & \Re[\mathbf{1}^{\mathrm{T}}\widetilde{\mathbf{Z}}] \\ -\Im[\widetilde{\mathbf{Z}}^{\mathrm{H}}\mathbf{1}] & \Re[\widetilde{\mathbf{Y}}^{\mathrm{H}}\mathbf{P}\widetilde{\mathbf{Y}}] & -\Im[\widetilde{\mathbf{Y}}^{\mathrm{H}}\mathbf{P}\widetilde{\mathbf{Y}}] \\ \Re[\widetilde{\mathbf{Z}}^{\mathrm{H}}\mathbf{1}] & \Im[\widetilde{\mathbf{Y}}^{\mathrm{H}}\mathbf{P}\widetilde{\mathbf{Y}}] & \Re[\widetilde{\mathbf{Y}}^{\mathrm{H}}\mathbf{P}\widetilde{\mathbf{Y}}] \end{bmatrix}, \tag{2.3.11}$$

where $\boldsymbol{\zeta} = [\tau_1, \Re[\mathbf{h}^{\mathrm{T}}], \Im[\mathbf{h}^{\mathrm{T}}]]^{\mathrm{T}}$ denotes the parameter vector of interest, $\mathbf{1}$ is $L \times 1$ vector with all-one elements, $\widetilde{\mathbf{Z}}$ is defined as $\widetilde{\mathbf{Z}}^{\mathrm{H}} = \left[\widetilde{\mathbf{X}}_1^{\mathrm{H}}\mathbf{h} \ \ldots \ \widetilde{\mathbf{X}}_L^{\mathrm{H}}\mathbf{h}\right]$, with $\widetilde{\mathbf{X}}_l = \widetilde{\mathbf{Y}}_l^{\mathrm{H}}\mathbf{P}\widetilde{\mathbf{Y}}$ where

$$\widetilde{\mathbf{Y}} = \mathbf{I}_K \otimes \left[\mathbf{f}_1 \ \ldots \ \mathbf{f}_L\right],$$

$$\widetilde{\mathbf{Y}}_l = \mathbf{I}_K \otimes \left[0 \ \ldots \ 0 \ \mathbf{D}\mathbf{f}_l \ 0 \ \ldots \ 0\right],$$

and $\mathbf{f}_l$ is an $N \times 1$ vector with the kth entry equal to $e^{-j\frac{2\pi}{N}k(l-1)}$ for $l = 1, \ldots, L$ and $k = 0, \ldots, N-1$. Consequently, we obtain the CRB of time-delay from the first path $\mathrm{CRB}(\tau_1)$ and the CRB of channel coefficients $\mathrm{CRB}(\mathbf{h})$ as

$$\mathrm{CRB}(\tau_1) = \frac{\sigma_w^2}{2}(\underbrace{\mathbf{1}^{\mathrm{T}}\widetilde{\mathbf{Q}}\mathbf{1} - \mathbf{1}^{\mathrm{T}}\widetilde{\mathbf{Z}}(\widetilde{\mathbf{Y}}^{\mathrm{H}}\mathbf{P}\widetilde{\mathbf{Y}})^{-1}\widetilde{\mathbf{Z}}^{\mathrm{H}}\mathbf{1}}_{\gamma})^{-1}, \tag{2.3.12}$$

and

$$\mathrm{CRB}(\mathbf{h}) = \frac{\sigma_w^2}{2}(2(\widetilde{\mathbf{Y}}^{\mathrm{H}}\mathbf{P}\widetilde{\mathbf{Y}})^{-1} + \gamma^{-1}(\widetilde{\mathbf{Y}}^{\mathrm{H}}\mathbf{P}\widetilde{\mathbf{Y}})^{-1}\widetilde{\mathbf{Z}}^{\mathrm{H}}\mathbf{1}\mathbf{1}^{\mathrm{T}}\widetilde{\mathbf{Z}}(\widetilde{\mathbf{Y}}^{\mathrm{H}}\mathbf{P}\widetilde{\mathbf{Y}})^{-1}). \tag{2.3.13}$$

Taking the expectation with respect to channel coefficients and using the Laplace approximation, we obtain

$$\mathrm{ECRB}(\tau_1) \approx \frac{\sigma_w^2}{2}(\mathbf{1}^{\mathrm{T}}\widetilde{\mathbf{Q}}_D\mathbf{1} - \mathrm{tr}\{[\widetilde{\mathbf{X}}(\widetilde{\mathbf{Y}}^{\mathrm{H}}\mathbf{P}\widetilde{\mathbf{Y}})^{-1}\widetilde{\mathbf{X}}^{\mathrm{H}}][\mathbf{1}\mathbf{1}^{\mathrm{T}} \otimes \mathbf{C}_h]\})^{-1}, \tag{2.3.14}$$

and

$$\mathrm{ECRB}(\mathbf{h}) \approx \frac{\sigma_w^2}{2}(2(\widetilde{\mathbf{Y}}^{\mathrm{H}}\mathbf{P}\widetilde{\mathbf{Y}})^{-1} + \widetilde{\gamma}^{-1}(\widetilde{\mathbf{Y}}^{\mathrm{H}}\mathbf{P}\widetilde{\mathbf{Y}})^{-1}\widetilde{\mathbf{X}}^{\mathrm{H}}(\mathbf{1}\mathbf{1}^{\mathrm{T}} \otimes \mathbf{C}_h)\widetilde{\mathbf{X}}(\widetilde{\mathbf{Y}}^{\mathrm{H}}\mathbf{P}\widetilde{\mathbf{Y}})^{-1}), \tag{2.3.15}$$

where

$$\widetilde{\gamma} = \mathbf{1}^{\mathrm{T}}\widetilde{\mathbf{Q}}_D\mathbf{1} - \mathrm{tr}\{[\widetilde{\mathbf{X}}(\widetilde{\mathbf{Y}}^{\mathrm{H}}\mathbf{P}\widetilde{\mathbf{Y}})^{-1}\widetilde{\mathbf{X}}^{\mathrm{H}}][\mathbf{1}\mathbf{1}^{\mathrm{T}} \otimes \mathbf{C}_h]\},$$

and $\widetilde{\mathbf{X}}^{\mathrm{H}} = \left[\widetilde{\mathbf{X}}_1^{\mathrm{H}} \ \ldots \ \widetilde{\mathbf{X}}_L^{\mathrm{H}}\right]$.

2.3.3 The Choice for Channel Covariance Matrix

Allowing the correlation between channel coefficients in each burst and from burst to burst using the zero-order bessel function pattern or uniform Doppler spectrum one can

obtain the channel covariance matrix $\mathbf{C}_h$. By definition, we obtain

$$\mathbf{C}_h = \begin{bmatrix} \mathbf{C}_h^{11} & \dots & \mathbf{C}_h^{1K} \\ \vdots & \ddots & \vdots \\ \mathbf{C}_h^{K1} & \dots & \mathbf{C}_h^{KK} \end{bmatrix}, \tag{2.3.16}$$

where $\mathbf{C}_h^{ij}$ is defined as $\mathbf{C}_h^{ij} = \mathbb{E}[\mathbf{h}_i \mathbf{h}_j^{\mathrm{H}}]$. If we assume that different channel coefficients in each burst are correlated but uncorrelated from burst to burst, then the off-diagonal block matrices $\mathbf{C}_h^{ij}$ for $i \neq j$ are diagonal with diagonal entries proportional to Doppler spectrum of the form of zero-order bessel function $J_0(2\pi f_D(i-j)T)$ or flat Doppler spectrum $1/f_D$ where f_D represents the maximum Doppler frequency.

2.4 Channel Capacity with Partially Known CSI

In this section, we obtain channel capacity as a function of power vector $\mathbf{p}$ and ECRB of time-delay and channel coefficients. It is assumed that $\tau_l = (l-1) + \tau_1$ and $g(lT) = \delta(lT)$ and the model in (2.2.1) is used. Defining $\boldsymbol{\iota}(\tau_1, \mathbf{h})$ as $\boldsymbol{\iota}(\tau_1, \mathbf{h}) = (\mathbf{I}_K \otimes \boldsymbol{\Gamma}(\tau_1)\mathbf{F}_L)\mathbf{h}$, and replacing it by its estimated version plus the error term in the estimation as $\boldsymbol{\iota}(\tau_1, \mathbf{h}) = \widehat{\boldsymbol{\iota}}(\tau_1, \mathbf{a}) + \widetilde{\boldsymbol{\iota}}(\tau_1, \mathbf{a})$, (2.2.2) can be written as

$$\mathbf{r} = \mathbf{B}(\widehat{\boldsymbol{\iota}}(\tau_1, \mathbf{h}) + \widetilde{\boldsymbol{\iota}}(\tau_1, \mathbf{h})) + \mathbf{w}. \tag{2.4.1}$$

We can rewrite (2.4.1) as

$$\mathbf{r} = (\widehat{\mathbf{H}}(\tau_1, \mathbf{h}) + \widetilde{\mathbf{H}}(\tau_1, \mathbf{h}))\mathbf{b} + \mathbf{w}, \tag{2.4.2}$$

where $\mathbf{H}(\tau_1, \mathbf{h})$ is the diagonal form of vector $\boldsymbol{\iota}(\tau_1, \mathbf{h})$ with $\boldsymbol{\iota}(\tau_1, \mathbf{a})$ as the main diagonal, $\widehat{\mathbf{H}}(\tau_1, \mathbf{h})$ and $\widetilde{\mathbf{H}}(\tau_1, \mathbf{h})$ are diagonal forms of $\widehat{\boldsymbol{\iota}}(\tau_1, \mathbf{h})$ and $\widetilde{\boldsymbol{\iota}}(\tau_1, \mathbf{a})$ with $\widehat{\boldsymbol{\iota}}(\tau_1, \mathbf{h})$ and $\widetilde{\boldsymbol{\iota}}(\tau_1, \mathbf{h})$ as the main diagonal elements, respectively, and $\mathbf{b}$ is the vector form of the diagonal input $\mathbf{B}$ that is formed by the diagonal elements of $\mathbf{B}$ as $\mathbf{b}^{\mathrm{T}} = \Big[B[0] \dots B[KN-1]\Big]$. It can be shown that the lower bound of the ergodic capacity $\overline{C}_{lb}$ is of the form of [Has03]

$$\overline{C}_{lb} = \frac{1}{NK}\mathbb{E}[\log_2 \det(\mathbf{I} + \mathbf{P}\mathbf{R}_e^{-1}\widehat{\mathbf{H}}\widehat{\mathbf{H}}^{\mathrm{H}})], \tag{2.4.3}$$

where

$$\widehat{\mathbf{H}}\widehat{\mathbf{H}}^{\mathrm{H}} = \mathrm{diag}\{(\mathbf{I}_K \otimes \mathbf{F}_L)\mathbf{h}\mathbf{h}^{\mathrm{H}}(\mathbf{I}_K \otimes \mathbf{F}_L^H)\}, \tag{2.4.4}$$

and

$$\mathbf{R}_e = \mathbf{P}\mathbf{C}_{\widetilde{\mathbf{H}}} + \sigma_w^2\mathbf{I}, \tag{2.4.5}$$

with $\mathbf{C}_{\widetilde{\mathbf{H}}}$ defined as $\mathbf{C}_{\widetilde{\mathbf{H}}} = \widetilde{\mathbf{H}}\widetilde{\mathbf{H}}^{\mathrm{H}}$. We obtain the approximate value for the lower bound of ergodic capacity $\mathbf{C}_{\widetilde{\mathbf{H}}}$ by moving the expectation inside the $\log_2\det(.)$ function using Jensens inequality and applying $\mathbb{E}[\frac{\mathbf{X}}{\mathbf{Y}}] \approx \frac{\mathbb{E}[\mathbf{X}]}{\mathbb{E}[\mathbf{Y}]}$. The result is

$$\overline{C}_{lb} \approx \frac{1}{NK}\log_2\det(\mathbf{I} + \mathbf{P}\widetilde{\mathbf{R}}_e^{-1}\mathbb{E}[\widehat{\mathbf{H}}\widehat{\mathbf{H}}^{\mathrm{H}}]), \tag{2.4.6}$$

where

$$\mathbb{E}[\widehat{\mathbf{H}}\widehat{\mathbf{H}}^{\mathrm{H}}] = \mathrm{diag}\{(\mathbf{I}_K \otimes \mathbf{F}_L)\mathbf{C}_h(\mathbf{I}_K \otimes \mathbf{F}_L^{\mathrm{H}})\}, \tag{2.4.7}$$

and

$$\widetilde{\mathbf{R}}_e = \mathbf{P}\overline{\mathbf{C}}_{\widetilde{\mathbf{H}}} + \sigma_w^2\mathbf{I}, \tag{2.4.8}$$

with $\overline{\mathbf{C}}_{\widetilde{\mathbf{H}}}$ defined as $\overline{\mathbf{C}}_{\widetilde{\mathbf{H}}} = \mathbb{E}[\widetilde{\mathbf{H}}\widetilde{\mathbf{H}}^{\mathrm{H}}]$. This represents the expected value of the estimation error that can be lower bounded using the ECRB of time-delay and channel coefficients that can be further converted to $\boldsymbol{\iota}(\tau_1, \mathbf{h})$ as a function of time-delay τ_1 and channel coefficients $\mathbf{h}$ as

$$\overline{\mathbf{C}}_{\widetilde{\mathbf{H}}} \succeq \mathrm{diag}\{\mathbb{E}[\widetilde{\mathbf{h}}'(\boldsymbol{\zeta})\widetilde{\mathbf{J}}^{-1}(\boldsymbol{\zeta})(\widetilde{\mathbf{h}}'(\boldsymbol{\zeta}))^{\mathrm{H}}]\}, \tag{2.4.9}$$

where

$$\widetilde{\mathbf{h}}'(\boldsymbol{\zeta}) = [\boldsymbol{\alpha} \quad \boldsymbol{\Delta}],$$

$$\widetilde{\mathbf{J}}^{-1}(\boldsymbol{\zeta}) = \mathbf{T}_t\mathbf{J}^{-1}(\boldsymbol{\zeta})\mathbf{T}_t^{\mathrm{H}},$$

and we define $\boldsymbol{\alpha} = (\mathbf{I}_K \otimes \mathbf{D}\boldsymbol{\Gamma}(\tau_1)\mathbf{F}_L)\mathbf{h}$ and $\boldsymbol{\Delta} = (\mathbf{I}_K \otimes \boldsymbol{\Gamma}(\tau_1)\mathbf{F}_L)$, and $\mathbf{T}_t$ is the conversion matrix to convert real and imaginary parts $\Re[\mathbf{h}]$ and $\Im[\mathbf{h}]$ of channel coefficients to the complex coefficients $\mathbf{h}$, and it is defined as

$$\mathbf{T}_t = \begin{bmatrix} 1 & \mathbf{0}^{\mathrm{T}} & \mathbf{0}^{\mathrm{T}} \\ \mathbf{0} & \mathbf{I} & j\mathbf{I} \end{bmatrix}.$$

Finally, replacing the inverse of the converted FIM $\widetilde{\mathbf{J}}^{-1}$ in (2.4.9) and simplifications, see the Appendix 2.D, we obtain

$$\mathrm{diag}\{\mathbb{E}[\widetilde{\mathbf{h}}'(\boldsymbol{\zeta})\widetilde{\mathbf{J}}^{-1}(\boldsymbol{\zeta})(\widetilde{\mathbf{h}}'(\boldsymbol{\zeta}))^{\mathrm{H}}]\} = \mathrm{diag}\{\boldsymbol{\Delta}\mathrm{ECRB}(\mathbf{h})\boldsymbol{\Delta}^{\mathrm{H}}\} + \mathrm{ECRB}(\tau_1)\mathrm{diag}\{\mathbb{E}[\boldsymbol{\alpha}\boldsymbol{\alpha}^{\mathrm{H}}]\}, \tag{2.4.10}$$

where

$$\mathrm{diag}\{\boldsymbol{\Delta}\mathrm{ECRB}(\mathbf{h})\boldsymbol{\Delta}^{\mathrm{H}}\} = \mathrm{diag}\{(\mathbf{I}_K \otimes \mathbf{F}_L)\mathrm{ECRB}(\mathbf{h})(\mathbf{I}_K \otimes \mathbf{F}_L^{\mathrm{H}})\}, \tag{2.4.11}$$

and

$$\mathrm{diag}\{\mathbb{E}[\boldsymbol{\alpha}\boldsymbol{\alpha}^{\mathrm{H}}]\} = \mathrm{diag}\{(\mathbf{I}_K \otimes \mathbf{D}\mathbf{F}_L)\mathbf{C}_h(\mathbf{I}_K \otimes \mathbf{F}_L^{H}\mathbf{D}^{\mathrm{H}})\}. \tag{2.4.12}$$

Using (2.4.6)-(2.4.10), we conclude that the approximate value for the lower bound of ergodic capacity is a function of ECRB of time-delay ECRB(τ_1), ECRB of channel coefficients ECRB($\mathbf{h}$), input power for different OFDM symbols $\mathbf{P}$, and interpolated frequency response of channel covariance matrix $\mathbf{C}_h$ in time and frequency or $(\mathbf{I}_K \otimes \mathbf{F}_L)\mathbf{C}_h(\mathbf{I}_K \otimes \mathbf{F}_L^{\mathrm{H}})$.

2.5 Combined Data and Pilot Design

In this section, we formulate the optimization problem used for the pilot design for joint communication and time-delay estimation. To maximize the cost function that is the lower bound of an approximation of the ergodic capacity (2.4.6), one needs to solve the following optimization problem

$$(P1)\begin{cases} \max\limits_{\mathbf{p}} & \overline{C}_{lb} \\ \text{s.t.} & \mathrm{ECRB}(\tau_1) \leq \epsilon \\ & \mathbf{1}^{\mathrm{T}}\mathbf{p} \leq P_T \\ & \mathbf{p}_p^{\mathrm{T}}\mathbf{p}_d = 0 \\ & \mathbf{p}_p \succeq \mathbf{0}; \mathbf{p}_d \succeq \mathbf{0}, \end{cases} \tag{2.5.1}$$

where $\mathbf{p}_p$ and $\mathbf{p}_d$ are the pilot and data power vectors. The first constraint limits the time-delay estimation accuracy by introducing a small value ϵ as the upper bound, the second constraint limits the total power for the design to P_T while the power vector $\mathbf{p}$ stands for the sum of data and pilot vectors $\mathbf{p} = \boldsymbol{p}_p + \boldsymbol{p}_d$, the third constraint makes the problem to be combinatorial and non-convex, and finally the last constraint assure the data and pilot vectors to be non-negative. We propose the relaxed form of the problem

by removing the third constraint as

$$(P2)\begin{cases}\max\limits_{\mathbf{p}} & \overline{C}_{lb} \\ \text{s.t.} & \text{ECRB}(\tau_1) \leq \epsilon \\ & \mathbf{1}^{\mathrm{T}}\mathbf{p} \leq P_T \\ & \mathbf{p}_p \succeq \mathbf{0}; \mathbf{p}_d \succeq \mathbf{0}. \end{cases} \tag{2.5.2}$$

Problem $(P2)$ can be solved using the interior point method. After solving the relaxed optimization problem $(P2)$ we choose the subcarriers that are used as both data and pilot as pilot if the pilot power is much stronger than data, as data if the data power is much stronger than the pilot, and if they are of similar value data and pilots are allocated such that the time-delay estimation accuracy constraint is fulfilled with sufficiently high data rate. This way, we obtain a close-to-optimal solution for the joint time-delay estimation and communication design problem.

2.6 Simulation Results

2.6.1 Simulation Setup

Static Channels

For static channels, we use IEEE 802.11 channel model with the maximum number of paths $L = \lceil 10 \times \sigma_\tau / T_s \rceil$ where σ_τ is the RMS delay spread and T_s represents the sampling period.

Time-Varying Channels

In the following, we present numerical evaluations of the two dimensional combined data and pilot design for time-varying frequency selective channels. The simulation settings are $N = 32$, $K = 30$, $L = 5$, and $\tau_1^{'} = (\tau_1/T_s) = 0.1$. Further, we consider 32 subcarriers with$\Delta\ f = 15\,\text{KHz}$ resulting the bandwidth of 480 KHz. The signal-to-noise ratio (SNR) is defined as SNR $\triangleq P_T/\sigma_w^2$ and is set to 27 dB. We use the channel covariance matrix in (2.3.16) with allowing correlation between different channel taps within each OFDM symbol C_h^{ii} and diagonal pattern for correlation between symbol to symbol C_h^{ij} using the zero-order bessel function $J_0(2\pi f_D(i-j)T)$ with notmalized Doppler frequency of

$f_D = 0.3$. To compare the result with [Mon13], we consider transmit, channel, and received filter response as a simple delta function $g(lT) = \delta(lT)$ and assume $\tau_l = (l-1)+\tau_1$.

2.6.2 Results and Discussion

Joint Design

Fig. 2.1(a)-2.1(c) show the joint design of pilots and data power allocations based on the proposed channel model with maximum number of paths $L = 4$, $L = 6$, and $L = 8$, with diagonal channel covariance matrices, i.e. independent channel coefficients, defined in the simulation parameters, and number of subcarriers $N = 48$. The results show that using the channel of length L, joint design of pilots and data power allocations requires at least $L + 2$ pilots for estimation with the rest of subcarriers saved for data transmission. Obviously, increasing the number of taps from $L = 4$ to $L = 8$ reduces the capacity by around 2.3% since the number of subcarriers for data transmission is reduced.

Fig 2.2 shows the joint design of data and pilots. Channel capacity for the combined design optimization problem ($P1$) is 1.12 for the upper bound of time-delay estimation accuracy of ϵ =1e-5 and the SNR of 27 dB. The position of pilots follows a semi stair-wise pattern that is what we more or less see as in the PRS sequences of LTE.

Comparison Study

In this part, we compare the behavior of optimization problems (P1) and (P2) then the behavior of the optimization with and without considering the time-delay estimation constraint is investigated. Fig. 2.3 compares the lower bound of channel capacity for the different values of the upper bound of time delay estimation accuracy parameter ϵ of the problems (P1) and (P2). The relaxed solution allowing each subcarrier to be used as data and pilot provides 31% higher capacity in the flat part of the curves comparing to the solution after masking and limiting each subcarriers to be considered as either data or pilot. Fig. 2.3 shows that by reducing ϵ, that is, increasing the accuracy in the estimation of time-delay, the capacity is reduced since more subcarriers are needed to be allocated as pilots. Fig. 2.4 and Fig. 2.5 compares the designs with and without considering time delay constraint in terms of ECRB(τ_1) and C_{lb} for different SNR and with the upper bound on the time delay estimation accuracy of $\epsilon = 1e-5$ respectively. Interestingly, based on Fig. 2.4 after SNR = 29 dB the delay constraint is fulfilled without considering it in the optimization problem as a constraint. This means that by increasing the SNR the

time delay constraint in the optimization problem can be fulfilled even without directly applying it in the optimization problem. Fig. 2.5 shows that after SNR = 27 dB the values for the channel capacity with and without considering the delay constraint converge since the delay constraint is fulfilled by increasing the SNR even for the case that is not applied directly as a constraint in the optimization problem.

2.7 Conclusion

Combined design of data and pilots considering the effect of channel variations for different OFDM symbols improves the channel capacity comparing to the designs without considering the effect of time variations for a given time-delay estimation accuracy. Results show that joint design of data and pilots leads to a better performance in terms of capacity for a desired value of the time-delay estimation accuracy.

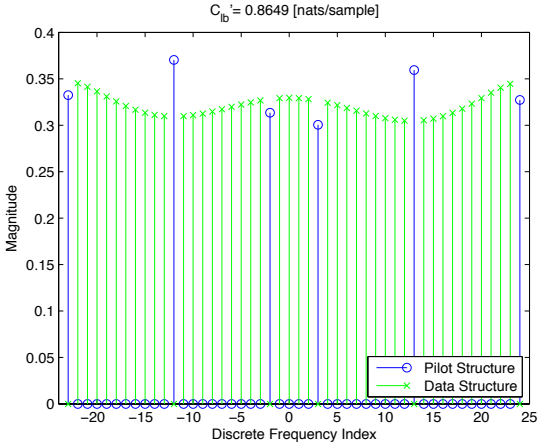

(a) $L = 4$

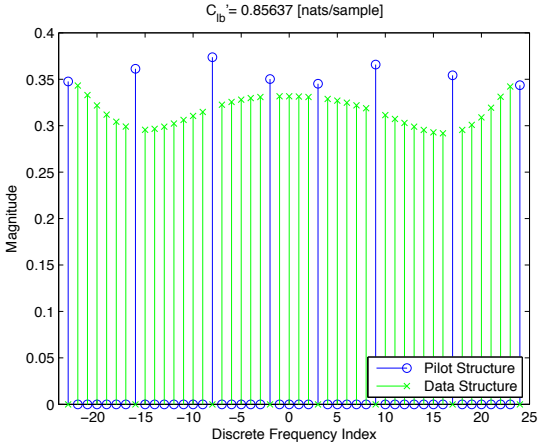

(b) $L = 6$

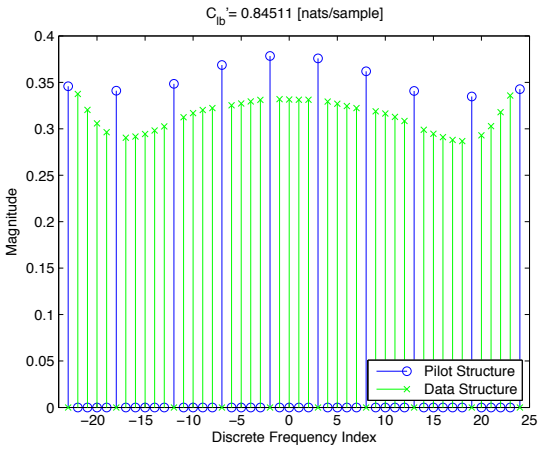

(c) $L = 8$

Figure 2.1: Joint design of pilot and data power allocations for the channels of different length.

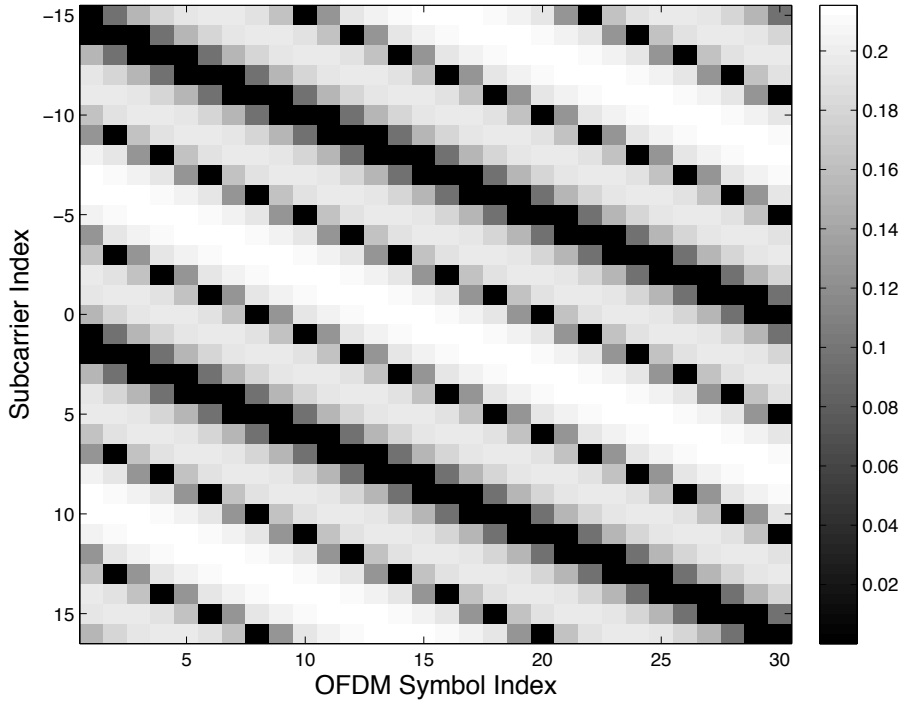

Figure 2.2: Joint Data and pilot allocations in a block-fading time-varying OFDM system.

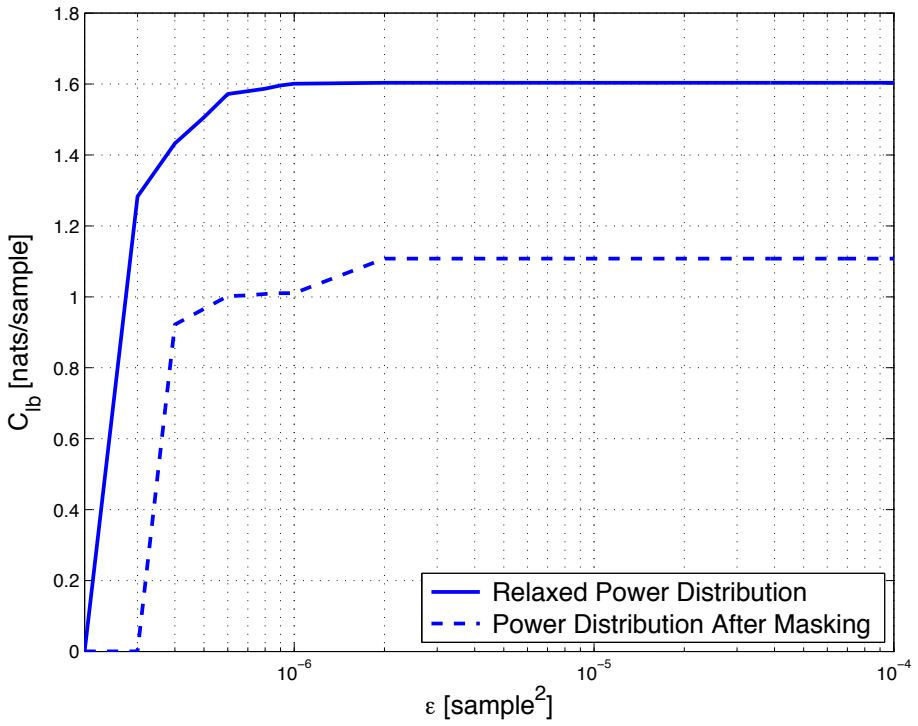

Figure 2.3: Channel capacity versus the upper bound of time-delay estimation accuracy.

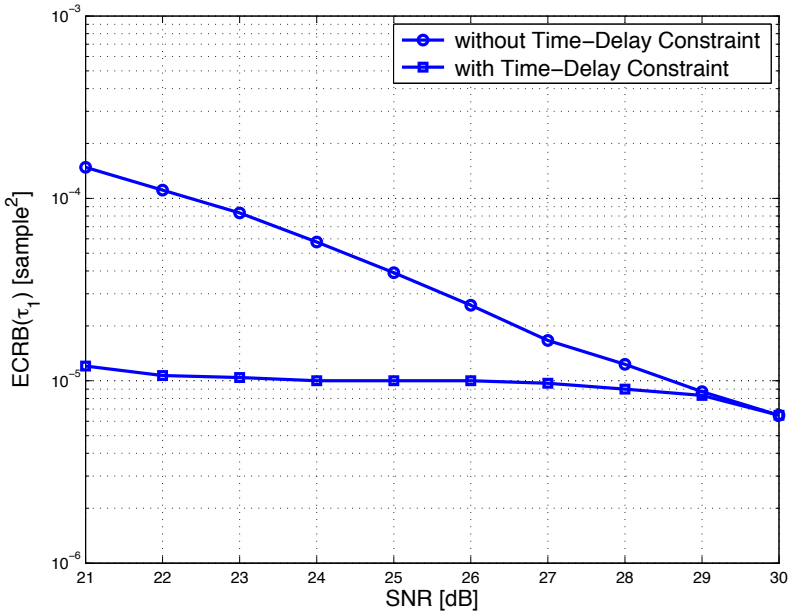

Figure 2.4: ECRB of time-delay versus SNR with and without applying time-delay constraint in the optimization.

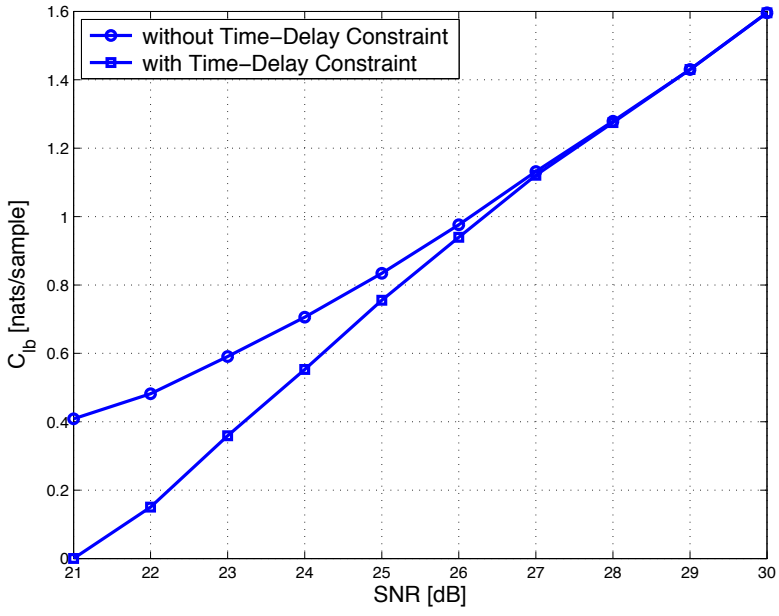

Figure 2.5: Channel capacity versus the SNR with and without time-delay constraint.

Appendix 2.A

Proof for (2.2.2)

The sampled received signal at $t = nT_s$ from a standard OFDM block passed through a frequency selective and time-varying channel at the ith OFDM symbol after removing the guard interval is

$$\tilde{r}_i[n] = \sum_{m\in\mathbb{Z}} s_i[n-m]\kappa_i[m] + w_i[n], \tag{2.A.1}$$

where $\tilde{r}_i[n] = \tilde{r}_i(nT_s)$, $\kappa_i[m] = \kappa_i(mT_s)$, $s_i[n]$ is the inverse DFT of the input at the n'th subcarrier defined as $s_i[n] = 1/\sqrt{N}\sum_{n'=0}^{N-1} B_i[n']e^{j\frac{2\pi}{N}n'n}$, and $w_i[n] = w_i(nT_s)$. We assume that $\kappa_i[m]$ has a limited time support of W such that $\kappa_i[m] = 0$ for $m \notin [0, W-1]$. By Poisson summation formula, it turns out that

$$\begin{aligned}\sum_m \kappa_i[m]e^{-j\frac{2\pi}{N}mk} &= \frac{1}{T_s}\sum_l K_i(\frac{l}{T_s} + \frac{k}{NT_s}) \\ &\overset{(a)}{=} \frac{1}{T_s}K_i(\frac{k}{NT_s}) \\ &\overset{(b)}{=} \sum_{l=0}^{W-1} \kappa_{i,l}e^{-j\frac{2\pi}{N}lk},\end{aligned} \tag{2.A.2}$$

where (a) is obtained based on the fact that only the first term of the summation is supported, and (b) is the direct result of the DFT of the channel response $\kappa_{i,l}$ with the time support of W. Replacing $s_i[n]$ by $s_i[n] = 1/\sqrt{N}\sum_{n'=0}^{N-1} B_i[n']e^{j\frac{2\pi}{N}n'n}$ and using (2.A.1), we obtain

$$\tilde{r}_i[n] = \frac{1}{\sqrt{N}}\sum_{n'=0}^{N-1} B_i[n']\sum_{l=0}^{W-1}\kappa_{i,l}e^{j\frac{2\pi}{N}n'(n-l)} + w_i[n]. \tag{2.A.3}$$

Taking the DFT of $\tilde{r}_i[n]$ shown as $r_i[n']$ and writing the result in a matrix-vector form results

$$\mathbf{r}_i = \mathbf{B}_i \mathbf{F}_W \boldsymbol{\kappa}_i + \mathbf{w}_i, \tag{2.A.4}$$

where $\mathbf{B}_i$ represents an $N \times N$ diagonal matrix of the input at ith OFDM symbol, $\mathbf{F}_W$ is the first W columns of the discrete Fourier transform (DFT) matrix $\mathbf{F}$, and κ_i is an $W \times 1$ sampled channel response at the ith OFDM symbol.

The channel vector κ_i can be decomposed as the multiplication of a slow-varying matrix $\mathbf{G}(\boldsymbol{\tau})$ and fast-varying fading coefficients $\mathbf{h}_i$ as $\boldsymbol{\kappa}_i = \mathbf{G}(\boldsymbol{\tau})\mathbf{h}_i$ where $\mathbf{G}(\boldsymbol{\tau})$ is an $W \times L$ matrix as a result of sampling the transmit, channel, and received filter responses for L different paths and W samples, $\mathbf{h}_i$ is an $L \times 1$ complex amplitude of different path for the ith OFDM symbol, and $\boldsymbol{\tau}$ is the delay vector for L paths defined as $\boldsymbol{\tau}^{\mathrm{T}} = [\tau_1, ..., \tau_L]$. Replacing $\kappa_i = \mathbf{G}(\boldsymbol{\tau})\mathbf{h}_i$ in (2.A.4), vectorizing for K OFDM symbols, zero-padding the ith column of $\mathbf{G}(\boldsymbol{\tau})$ by $N - W$ as $\widetilde{\mathbf{g}}^{\mathrm{T}}(\tau_i) = [g(0T - \tau_i), ..., g((W-1)T - \tau_i), 0, ..., 0]$, and applying the DFT matrix $\mathbf{F}$ we obtain (2.2.2).

Appendix 2.B

Proof for (2.3.2)

To obtain each block of FIM, we use the fact that

$$\begin{aligned}
\frac{\partial \widetilde{\boldsymbol{\mu}}^{\mathrm{H}}}{\partial \tau_i} &= j\mathbf{h}^{\mathrm{H}} \mathbf{Y}_i^{\mathrm{H}}, \\
\frac{\partial \widetilde{\boldsymbol{\mu}}^{\mathrm{H}}}{\partial \Re[\mathbf{h}]} &= \mathbf{Y}^{\mathrm{H}}, \\
\frac{\partial \widetilde{\boldsymbol{\mu}}^{\mathrm{H}}}{\partial \Im[\mathbf{h}]} &= -j\mathbf{Y}^{\mathrm{H}}.
\end{aligned} \tag{2.B.1}$$

Therefore, we obtain each block of the FIM as

$$\frac{2}{\sigma_w^2} \Re[\frac{\partial \widetilde{\boldsymbol{\mu}}^{\mathrm{H}}}{\partial \boldsymbol{\tau}} \mathbf{P} \frac{\partial \widetilde{\boldsymbol{\mu}}}{\partial \boldsymbol{\tau}^{\mathrm{T}}}] = \sum_{i=1}^{K} \frac{2}{\sigma_w^2} \Re \begin{bmatrix} \mathbf{Q}_i^{11} & \dots & \mathbf{Q}_i^{1L} \\ \vdots & \ddots & \vdots \\ \mathbf{Q}_i^{L1} & \dots & \mathbf{Q}_i^{LL} \end{bmatrix}, \tag{2.B.2}$$

$$\frac{2}{\sigma_w^2}\Re[\frac{\partial\widetilde{\boldsymbol{\mu}}^{\mathrm{H}}}{\partial\boldsymbol{\tau}}\mathbf{P}\frac{\partial\widetilde{\boldsymbol{\mu}}}{\partial\Re[\mathbf{h}^{\mathrm{T}}]}] = \frac{2}{\sigma_w^2}\begin{bmatrix}\Im[\mathbf{h}^{\mathrm{H}}\mathbf{X}_1]\\ \vdots \\ \Im[\mathbf{h}^{\mathrm{H}}\mathbf{X}_L]\end{bmatrix}, \tag{2.B.3}$$

$$\frac{2}{\sigma_w^2}\Re[\frac{\partial\widetilde{\boldsymbol{\mu}}^{\mathrm{H}}}{\partial\boldsymbol{\tau}}\mathbf{P}\frac{\partial\widetilde{\boldsymbol{\mu}}}{\partial\Im[\mathbf{h}^{\mathrm{T}}]}] = \frac{2}{\sigma_w^2}\begin{bmatrix}\Re[\mathbf{h}^{\mathrm{H}}\mathbf{X}_1]\\ \vdots \\ \Re[\mathbf{h}^{\mathrm{H}}\mathbf{X}_L]\end{bmatrix}, \tag{2.B.4}$$

$$\frac{2}{\sigma_w^2}\Re[\frac{\partial\widetilde{\boldsymbol{\mu}}^{\mathrm{H}}}{\partial\Re[\mathbf{h}]}\mathbf{P}\frac{\partial\widetilde{\boldsymbol{\mu}}}{\partial\Re[\mathbf{h}^{\mathrm{T}}]}] = \frac{2}{\sigma_w^2}\Re[\mathbf{Y}^{\mathrm{H}}\mathbf{P}\mathbf{Y}], \tag{2.B.5}$$

$$\frac{2}{\sigma_w^2}\Re[\frac{\partial\widetilde{\boldsymbol{\mu}}^{\mathrm{H}}}{\partial\Im[\mathbf{h}]}\mathbf{P}\frac{\partial\widetilde{\boldsymbol{\mu}}}{\partial\Im[\mathbf{h}^{\mathrm{T}}]}] = \frac{2}{\sigma_w^2}\Re[\mathbf{Y}^{\mathrm{H}}\mathbf{P}\mathbf{Y}], \tag{2.B.6}$$

$$\frac{2}{\sigma_w^2}\Re[\frac{\partial\widetilde{\boldsymbol{\mu}}^{\mathrm{H}}}{\partial\Re[\mathbf{h}]}\mathbf{P}\frac{\partial\widetilde{\boldsymbol{\mu}}}{\partial\Im[\mathbf{h}^{\mathrm{T}}]}] = -\frac{2}{\sigma_w^2}\Im[\mathbf{Y}^{\mathrm{H}}\mathbf{P}\mathbf{Y}]. \tag{2.B.7}$$

That can be formed as (2.3.2).

Appendix 2.C

Proof for the FIM of the Special Case

Considering the fact that $\widetilde{\boldsymbol{\mu}}$ is a function of $\psi_l = \tau_l = \tau_1 + (l-1)T_s$, real and imaginary parts of channel coefficients, and using the chain rule for the derivative of a function, we obtain

$$\frac{\partial\widetilde{\boldsymbol{\nu}}}{\partial\tau_1} = \sum_{i=1}^{L}\frac{\partial\widetilde{\boldsymbol{\mu}}}{\partial\psi_i}\overbrace{\frac{\partial\psi_i}{\partial\tau_1}}^{1}|_{\psi_i=\tau_i} = \sum_{i=1}^{L}\frac{\partial\widetilde{\boldsymbol{\mu}}}{\partial\tau_i}, \tag{2.C.1}$$

where $\widetilde{\boldsymbol{\nu}}$ is a function of τ_1 and real and imaginary parts of channel coefficients. Using (2.C.1), we obtain each block of the FIM for the special case as

$$\frac{\partial\widetilde{\boldsymbol{\nu}}^{H}}{\partial\tau_1}\mathbf{P}\frac{\partial\widetilde{\boldsymbol{\nu}}}{\partial\tau_1} = \sum_{i'=1}^{L}\sum_{i=1}^{L}\frac{\partial\widetilde{\boldsymbol{\mu}}^{\mathrm{H}}}{\partial\tau_i}\mathbf{P}\frac{\partial\widetilde{\boldsymbol{\mu}}}{\partial\tau_{i'}}. \tag{2.C.2}$$

The above expression is equal to $\mathbf{1}^{\mathrm{T}}\widetilde{\mathbf{Q}}\mathbf{1}$.

$$\Re[\frac{\partial\widetilde{\boldsymbol{\nu}}^{\mathrm{H}}}{\partial\tau_1}\mathbf{P}\frac{\partial\widetilde{\boldsymbol{\nu}}}{\Re[\mathbf{h}^{\mathrm{T}}]}] = \sum_{i=1}^{L}\Im[\frac{\partial\widetilde{\boldsymbol{\mu}}^{\mathrm{H}}}{\partial\tau_i}\mathbf{P}\frac{\partial\widetilde{\boldsymbol{\mu}}}{\Re[\mathbf{h}^{\mathrm{T}}]}]. \tag{2.C.3}$$

The above expression is equal to $\Im[\mathbf{1}^{\mathrm{T}}\widetilde{\mathbf{Z}}]$, the same way we can prove the expression for $\Re[\mathbf{1}^{\mathrm{T}}\widetilde{\mathbf{Z}}]$. Note that the expression for $\widetilde{\mathbf{Y}}^{\mathrm{H}}\mathbf{P}\widetilde{\mathbf{Y}}$ easily follows by replacing $\tau_l = \tau_1 + (l-1)T_s$ and $\widetilde{\mathbf{g}}_f = \mathbf{1}$ in the definition of $\mathbf{Y}$.

Appendix 2.D

Proof for (2.4.10)

We obtain the inverse of converted FIM as

$$\frac{2}{\sigma_w^2}\mathbf{J}^{-1}(\boldsymbol{\zeta}) = \gamma^{-1}\begin{bmatrix} 1 & \Im[\boldsymbol{\beta}^{\mathrm{T}}] & -\Re[\boldsymbol{\beta}^{\mathrm{T}}]\Im[\boldsymbol{\beta}] & \gamma\boldsymbol{\Omega}_{11} & \gamma\boldsymbol{\Omega}_{12} \\ -\Re[\boldsymbol{\beta}] & \gamma\boldsymbol{\Omega}_{21}^{\mathrm{T}} & & \gamma\boldsymbol{\Omega}_{22} & \end{bmatrix}. \tag{2.D.1}$$

Also, the elements of the inverse of the FIM are found as

$$\boldsymbol{\beta} = (\widetilde{\mathbf{Y}}^{\mathrm{H}}\mathbf{P}\widetilde{\mathbf{Y}})^{-1}\mathbf{z}, \tag{2.D.1a}$$
$$\boldsymbol{\Omega}_{11} = \Re[(\widetilde{\mathbf{Y}}^{\mathrm{H}}\mathbf{P}\widetilde{\mathbf{Y}})^{-1}] + \gamma^{-1}\Im[\boldsymbol{\beta}]\Im[\boldsymbol{\beta}^{\mathrm{T}}], \tag{2.D.1b}$$
$$\boldsymbol{\Omega}_{12} = -\Im[(\widetilde{\mathbf{Y}}^{\mathrm{H}}\mathbf{P}\widetilde{\mathbf{Y}})^{-1}] - \gamma^{-1}\Im[\boldsymbol{\beta}]\Re[\boldsymbol{\beta}^{\mathrm{T}}], \tag{2.D.1c}$$
$$\boldsymbol{\Omega}_{21} = \Im[(\widetilde{\mathbf{Y}}^{\mathrm{H}}\mathbf{P}\widetilde{\mathbf{Y}})^{-1}] - \gamma^{-1}\Re[\boldsymbol{\beta}]\Im[\boldsymbol{\beta}^{\mathrm{T}}], \tag{2.D.1d}$$
$$\boldsymbol{\Omega}_{22} = \Re[(\widetilde{\mathbf{Y}}^{\mathrm{H}}\mathbf{P}\widetilde{\mathbf{Y}})^{-1}] + \gamma^{-1}\Re[\boldsymbol{\beta}]\Re[\boldsymbol{\beta}^{\mathrm{T}}]. \tag{2.D.1e}$$

Using the conversion matrix $\mathbf{T}_t$ we obtain

$$\frac{2}{\sigma_w^2}\widetilde{\mathbf{J}}^{-1}(\boldsymbol{\zeta}) = \left[\gamma^{-1}\ j\gamma^{-1}\boldsymbol{\beta}^{\mathrm{H}} - j\gamma^{-1}\boldsymbol{\beta}\ 2(\widetilde{\mathbf{Y}}^{\mathrm{H}}\mathbf{P}\widetilde{\mathbf{Y}})^{-1} + \gamma^{-1}\boldsymbol{\beta}\boldsymbol{\beta}^{\mathrm{H}}\right], \tag{2.D.2}$$

$$\begin{aligned}\mathrm{diag}\{\mathbb{E}[\widetilde{\mathbf{h}}'(\boldsymbol{\zeta})\widetilde{\mathbf{J}}^{-1}(\boldsymbol{\zeta})(\widetilde{\mathbf{h}}'(\boldsymbol{\zeta}))^{\mathrm{H}}]\} = \\ \mathrm{diag}\{\mathbb{E}[\boldsymbol{\Delta}\mathrm{CRB}(\mathbf{a})\boldsymbol{\Delta}^{\mathrm{H}}] \\ + \mathbb{E}[\boldsymbol{\alpha}\mathrm{CRB}(\tau_1)\boldsymbol{\alpha}^{\mathrm{H}}] + \frac{\sigma_w^2}{2}\mathbb{E}[\mathbf{X}+\mathbf{X}^{\mathrm{H}}]\},\end{aligned} \tag{2.D.3}$$

$$\mathbf{X} = j\gamma^{-1}\boldsymbol{\alpha}\boldsymbol{\beta}^{\mathrm{H}}\boldsymbol{\Delta}^{\mathrm{H}}. \tag{2.D.4}$$

Using the property $\mathrm{diag}\{\mathbf{u}\}\mathrm{diag}\{\mathbf{v}^{\mathrm{H}}\} = \mathrm{diag}\{\mathbf{u}\mathbf{v}^{\mathrm{H}}\}$ where $\mathbf{u}$ and $\mathbf{v}$ are arbitrary column vectors, one can easily prove that $\mathrm{diag}\{\mathbb{E}[\mathbf{X}+\mathbf{X}^{\mathrm{H}}]\} = \mathbf{0}$. Therefore, we obtain (2.4.10).

Chapter 3

OFDM Wireless Network Localization

3.1 Introduction

High-accuracy localization is of critical importance in many location-based applications and services, e.g., cellular positioning, search-and-rescue tasks, blue-force tracking, communication, and military systems [Say05, God05]. WNL refers to the process of finding the positions of users (agents) using measurements to nodes with known positions (anchors). The transmission power of the nodes plays an important role in WNL, not only in terms of lifetime and throughput, but also in positioning accuracy [Mes07]. Therefore, an optimal power allocation among both anchors and subcarriers is important for reducing power consumption and increasing positioning accuracy.

Several power allocation methods have been presented for single-carrier transmission in synchronous networks [She14, Dai14]. These methods include the positioning accuracy as either an objective or a constraint, using fundamental performance limits. In [She10b, She10c], the fundamental limits of wideband localization have been derived in terms of SPEB and directional position error bound (DPEB) for the case of single-carrier signals. To overcome the uncertainties on the network parameters, a robust power allocation has been proposed in [Li13] by converting the minimization of the SPEB and of the maximum DPEB (mDPEB) subject to a total power constraint into semidefinite programming (SDP) and second-order cone programming (SOCP) forms. The authors in [She14, Dai14, Li13] assumed a unicast transmission scheme, that is to say, when an anchor transmits a signal, it is only listened by one agent. However, for a synchronous net-

work, this leads to suboptimal solutions in terms of total required power by the anchors. Moreover, current and emerging communications standards generally employ multi-carrier signals, in particular orthogonal frequency division multiplexing (OFDM). Multicarrier transmissions are beneficial when the data rates increase and hence wider bandwidths are needed. Current research for localization using OFDM signals is mainly focused on time delay estimation [DPR12]. In [Sha15], a power allocation for OFDM WNL is developed by converting the optimization into SDP form and numerical averaging over the position error bound.

In this chapter, we extend [Sha15] and formulate the ergodic and robust power allocations in an OFDM WNL with uncertainties on the network parameters (which include the channel coefficients and the positions of the agents) based on the fundamental statistical limits, rather than focusing on a specific localization technique. Our main contributions are summarized as follows.

- We develop an ergodic power allocation that minimizes the total power subject to a maximum acceptable value for the expected SPEB, averaged over a set of channel coefficients and agents' positions.
- We develop a robust power allocation to minimize the total power subject to a maximum acceptable value for the worst-case SPEB, maximized over a set of channel coefficients and agents' positions.

The remainder of this chapter is organized as follows. The system model, including the different types of uncertainty, are presented in Section 3.2. A standard non-robust power allocation, ignoring uncertainty, is summarized in Section 3.3. The proposed ergodic and robust power allocations are derived in Sections 3.4 and 3.5, respectively. The different approaches are compared numerically in Section 3.6, before we draw conclusions in Section 3.7.

Notation: $\text{diag}\{\mathbf{X}_m\}_{m\in\mathcal{M}}$ denotes the block-diagonal matrix with the mth block equal to $\mathbf{X}_m$ and m in the set of indices $\mathcal{M}$; $\text{diag}\{x_m\}_{m=0}^{M-1}$ denotes an $M\times M$ diagonal matrix formed with the values x_m; $\{\mathbf{x}_i\}$ represents the set of all vectors $\mathbf{x}_i$ for all possible values of the subindex i; $\mathbf{I}_N$ is the $N\times N$ identity matrix; $\mathbf{1}_N$ is the $N\times 1$ all-one vector; $\|.\|$ denotes the l_2-norm; $\otimes$ denotes the Kronecker product; $\text{tr}\{\mathbf{X}\}$ denotes the trace of the matrix $\mathbf{X}$; $\mathbf{X}\succeq\mathbf{Y}$ means that the matrix $\mathbf{X}-\mathbf{Y}$ is positive semi-definite (PSD); $\mathbf{X}\succ\mathbf{Y}$ means that the matrix $\mathbf{X}-\mathbf{Y}$ is positive definite; $\mathbf{x}\succeq\mathbf{y}$ and $\mathbf{x}\succ\mathbf{y}$ mean that all the elements of $\mathbf{x}-\mathbf{y}$ are nonnegative and positive, respectively; and $\Re\{.\}$ and $\Im\{.\}$ denote the real and imaginary parts, respectively.

3.2 System Model

In this section, we present the signal model for multi-carrier network localization. Then, uncertainty models for network parameters are defined.

3.2.1 Observation Model

Consider a wireless network with N_b anchors with known positions and N_a agents with unknown positions. The sets of agents and anchors are denoted by $\mathcal{N}_a = \{1, \ldots, N_a\}$ and $\mathcal{N}_b = \{N_a + 1, \ldots, N_a + N_b\}$, respectively. The two-dimensional positions of kth agent and jth anchor are denoted by $\mathbf{q}_k = [x_k \ y_k]^{\mathrm{T}}$ for $k \in \mathcal{N}_a$ and $\mathbf{q}_j = [x_j \ y_j]^{\mathrm{T}}$ for $j \in \mathcal{N}_b$. Anchors may be elements of the fixed infrastructure, whereas agents may be mobile users. We assume that all nodes are perfectly synchronized [Li13] and use OFDM transmissions from anchors to agents to localize the agents. We will focus on the case where each anchor j sends an OFDM signal, which is received by *all* agents (multicast transmission). However, all methods are easily modified for the case where each anchor j sends an OFDM signal that is received by *one* agent at a time (unicast transmission).

We denote as $\mathbf{r}_{k,j}$ the $N \times 1$ vector representing the received signal by agent k produced by the transmission of anchor j with N subcarriers, after cyclic prefix removal and transformation to the frequency domain. The vector $\mathbf{r}_{k,j}$ can be expressed as [Lar11, San12, Mor09]

$$\mathbf{r}_{k,j} = \mathbf{\Gamma}(t_{k,j})\mathbf{B}_j\mathbf{F}_L\mathbf{h}_{k,j} + \mathbf{w}_{k,j}, \tag{3.2.1}$$

where $\mathbf{B}_j = \mathrm{diag}\{B_j[n]\}_{n=-N/2}^{N/2}$ is an $N \times N$ diagonal matrix representing the N symbols sent by anchor j on each of the subcarriers, $\mathbf{F}_L$ represents the first L columns of the $N \times N$ discrete Fourier transform (DFT) matrix with L being the number of channel taps between nodes j and k (without loss of generality, we assume the same number of taps for all channels), $\mathbf{h}_{k,j} = [h_{k,j}^{(1)} \ldots h_{k,j}^{(L)}]^{\mathrm{T}}$ with the real and imaginary parts defined as $\mathbf{h}_{R,k,j}$ and $\mathbf{h}_{I,k,j}$ is the channel response between the corresponding anchor and agent, respectively, $\mathbf{\Gamma}(t_{k,j}) = \mathrm{diag}\{\exp(-j2\pi n t_{k,j}/T)\}_{n=-N/2}^{N/2}$ where $t_{k,j}$ is the arrival time of the first path and is given by $t_{k,j} = \|\mathbf{q}_k - \mathbf{q}_j\|/c$ with c representing the speed of light. The symbol time duration is denoted as T, and $\mathbf{w}_{k,j}$ is an $N \times 1$ noise vector distibuted as $\mathcal{CN}(\mathbf{0}, \sigma_w^2\mathbf{I}_N)$. We introduce $\mathbf{r}$ as the vector representation of the received waveforms by all agents from all anchors, given by $\mathbf{r} = [\mathbf{r}_1^{\mathrm{T}} \ \ldots \ \mathbf{r}_{N_a}^{\mathrm{T}}]^{\mathrm{T}}$ with $\mathbf{r}_k = [\mathbf{r}_{k,N_a+1}^{\mathrm{T}} \ \ldots \ \mathbf{r}_{k,N_a+N_b}^{\mathrm{T}}]^{\mathrm{T}}$.

Note that for unicast operation, each anchor j will send different OFDM signals to each agent. In terms of the model, the only difference is that we have to replace $\mathbf{B}_j$ by $\mathbf{B}_{k,j}$ in (3.2.1).

Our goal is to minimize the total transmission power ($P_{\mathrm{T,multi}} = \sum_{j\in\mathcal{N}_b} \mathrm{tr}\{\mathbf{P}_j\}$ where $\mathbf{P}_j = \mathbf{B}_j^{\mathrm{H}}\mathbf{B}_j$ for multicast and $P_{\mathrm{T,uni}} = \sum_{k\in\mathcal{N}_a}\sum_{j\in\mathcal{N}_b} \mathrm{tr}\{\mathbf{P}_{k,j}\}$ where $\mathbf{P}_{k,j} = \mathbf{B}_{k,j}^{\mathrm{H}}\mathbf{B}_{k,j}$ for unicast) required to obtain a certain positioning accuracy in terms of the fundamental statistical limits in the presence of uncertainties in the channel and the agent positions. We note that we do not consider different subcarriers for different users, so that each user can make use of the full system bandwidth.

3.2.2 Uncertainty Model

We consider a scenario in which we have some a priori information regarding the channel coefficients and the locations of the agents.

For the channel, we consider that $\mathbf{h}_{k,j} = \hat{\mathbf{h}}_{k,j} + \boldsymbol{\Delta}\mathbf{h}_{k,j}$, where $\hat{\mathbf{h}}_{k,j}$ is an a priori estimate of the channel and $\boldsymbol{\Delta}\mathbf{h}_{k,j}$ is the uncertainty on the channel, belonging to either the sets $\mathcal{H}_{k,j}^{(1)}$ or $\mathcal{H}_{k,j}^{(2)}$, with

$$\mathcal{H}_{k,j}^{(1)} \triangleq \{\boldsymbol{\Delta}\mathbf{h}_{k,j} : \|\boldsymbol{\Delta}\mathbf{h}_{k,j}\| \leq \epsilon\}, \tag{3.2.2}$$

$$\mathcal{H}_{k,j}^{(2)} \triangleq \{\boldsymbol{\Delta}\mathbf{h}_{k,j} : |\Delta h_{k,j,l}| \leq \epsilon_l, l = 1, ..., L\}. \tag{3.2.3}$$

Here,$\Delta\ h_{k,j,l}$ is the uncertainty of the lth channel tap, while ϵ_l and ϵ represent bounds on the uncertainty. Denoting by $\phi_{k,j} = \pm\arctan(y_k - y_j)/(x_k - x_j)$ the angle between the jth anchor and kth agent with respect to the positive x axis (with positive sign for $x_k > x_j$ and $y_k > y_j$ or $x_k < x_j$ and $y_k < y_j$ and negative sign otherwise), we can write $\phi_{k,j} = \hat{\phi}_{k,j} + \Delta\phi_{k,j}$, where $\hat{\phi}_{k,j}$ is an a priori estimate and$\Delta\ \phi_{k,j}$ is the uncertainty of the angle, limited to $|\Delta\phi_{k,j}| \leq \delta_{k,j}$, with $0 \leq \delta_{k,j} < \pi\ /2$. Fig. 3.1 shows the network scheme with four anchors and the k-th agent with the agent's actual position to lie within a circle of radius ϵ_d, and the relative angle between the k-th agent and the j-th anchor is shown by $\phi_{k,j}$.

3.3 Non-Robust Power Allocation

In this section, we provide the SPEB for OFDM signals and the formulation of the non-robust power allocation, without considering any uncertainties.

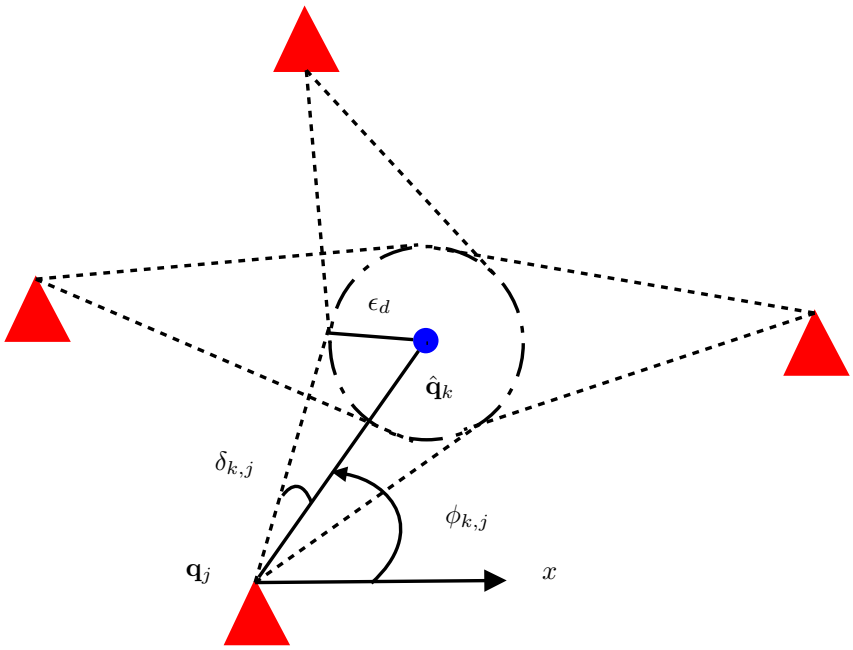

Figure 3.1: Illustration of the uncertainty model for WNL for agent k with the angular uncertainty $\delta_{k,j}$ and the relative angle $\phi_{k,j}$.

3.3.1 Squared Position Error Bound

We consider the agents' positions and channel coefficients as deterministic unknown parameters and we determine the corresponding Fisher information matrix (FIM). From this FIM, we can derive the SPEB. Let us define $\boldsymbol{\eta} = [\mathbf{q}_1^{\mathrm{T}} \dots \mathbf{q}_{N_a}^{\mathrm{T}} \ \boldsymbol{\theta}_1^{\mathrm{T}} \dots \boldsymbol{\theta}_{N_a}^{\mathrm{T}}]^{\mathrm{T}}$ where the whole set of channel coefficients is $\boldsymbol{\theta}_k = [\mathbf{k}_{k,N_a+1}^{\mathrm{T}} \dots \mathbf{k}_{k,N_a+N_b}^{\mathrm{T}}]^{\mathrm{T}}$, in which $\mathbf{k}_{k,j} = [\mathbf{h}_{R,k,j}^{\mathrm{T}} \ \mathbf{h}_{I,k,j}^{\mathrm{T}}]^{\mathrm{T}}$. The FIM of the parameters in $\boldsymbol{\eta}$ is

$$\mathbf{J}_{\boldsymbol{\eta}} = \mathbb{E}_{\mathbf{r}|\boldsymbol{\eta}}[-\frac{\partial^2 \ln f(\mathbf{r};\boldsymbol{\eta})}{\partial \boldsymbol{\eta} \partial \boldsymbol{\eta}^{\mathrm{T}}}]. \tag{3.3.1}$$

This FIM is a $2(N_a N_b L + N_a) \times 2(N_a N_b L + N_a)$ real PSD matrix, with the property that for any unbiased estimate $\hat{\boldsymbol{\eta}}$ of $\boldsymbol{\eta}$, it holds that [Kay10]

$$\mathbb{E}_{\mathbf{r}|\boldsymbol{\eta}}[(\hat{\boldsymbol{\eta}} - \boldsymbol{\eta})(\hat{\boldsymbol{\eta}} - \boldsymbol{\eta})^{\mathrm{T}}] \succeq \mathbf{J}_{\boldsymbol{\eta}}^{-1}. \tag{3.3.2}$$

The FIM $\mathbf{J}_{\boldsymbol{\eta}}$ has the following form

$$\mathbf{J}_{\boldsymbol{\eta}} = \begin{bmatrix} \boldsymbol{\Phi}(\mathbf{q},\mathbf{q}) & \boldsymbol{\Phi}(\mathbf{q},\boldsymbol{\theta}_1) & \dots & \boldsymbol{\Phi}(\mathbf{q},\boldsymbol{\theta}_{N_a}) \\ \boldsymbol{\Phi}(\boldsymbol{\theta}_1,\mathbf{q}) & \boldsymbol{\Phi}(\boldsymbol{\theta}_1,\boldsymbol{\theta}_1) & \dots & \boldsymbol{\Phi}(\boldsymbol{\theta}_1,\boldsymbol{\theta}_{N_a}) \\ \vdots & & \ddots & \vdots \\ \boldsymbol{\Phi}(\boldsymbol{\theta}_{N_a},\mathbf{q}) & \boldsymbol{\Phi}(\boldsymbol{\theta}_{N_a},\boldsymbol{\theta}_1) & \dots & \boldsymbol{\Phi}(\boldsymbol{\theta}_{N_a},\boldsymbol{\theta}_{N_a}) \end{bmatrix}, \tag{3.3.3}$$

where we have used the following definitions $\mathbf{q} = [\mathbf{q}_1^{\mathrm{T}} \dots \mathbf{q}_{N_a}^{\mathrm{T}}]^{\mathrm{T}}$,

$$\boldsymbol{\Phi}(\mathbf{x},\mathbf{y}) \triangleq \frac{2}{\sigma_w^2} \Re\left\{ \frac{\partial \boldsymbol{\mu}^{\mathrm{H}}}{\partial \mathbf{x}} \frac{\partial \boldsymbol{\mu}}{\partial \mathbf{y}^{\mathrm{T}}} \right\}, \tag{3.3.4}$$

and $\boldsymbol{\mu} \triangleq \bar{\boldsymbol{\Gamma}}(\mathbf{t})(\mathbf{I}_{N_a} \otimes \mathbf{B})\bar{\mathbf{F}}_L\mathbf{h}$ with $\bar{\boldsymbol{\Gamma}}(\mathbf{t}) = \mathrm{diag}\{\bar{\boldsymbol{\Gamma}}(\mathbf{t}_k)\}_{k\in\mathcal{N}_a}$, $\mathbf{B} = \mathrm{diag}\{\mathbf{B}_j\}_{j\in\mathcal{N}_b}$, $\bar{\mathbf{F}}_L = \mathbf{I}_{N_aN_b} \otimes \mathbf{F}_L$, $\mathbf{h} = [\mathbf{h}_1^{\mathrm{T}} \dots \mathbf{h}_{N_a}^{\mathrm{T}}]^{\mathrm{T}}$, in which $\bar{\boldsymbol{\Gamma}}(\mathbf{t}_k)$ and $\mathbf{h}_k$ are defined as

$$\bar{\boldsymbol{\Gamma}}(\mathbf{t}_k) = \mathrm{diag}\{\boldsymbol{\Gamma}(t_{k,j})\}_{j\in\mathcal{N}_b},$$

and $\mathbf{h}_k = [\mathbf{h}_{k,N_a+1}^{\mathrm{T}} \ \dots \ \mathbf{h}_{k,N_a+N_b}^{\mathrm{T}}]^{\mathrm{T}}$. The terms $\boldsymbol{\Phi}(\boldsymbol{\theta}_k,\boldsymbol{\theta}_m)$, $\boldsymbol{\Phi}(\mathbf{q}_k,\mathbf{q}_m)$, $\boldsymbol{\Phi}(\boldsymbol{\theta}_m,\mathbf{q}_k)$, and $\boldsymbol{\Phi}(\mathbf{q}_k,\boldsymbol{\theta}_m)$ are zero for $k \neq m$ (see Appendix 3.A), so that the equivalent FIM (EFIM) of the agents' positions is given by

$$\mathbf{J}_e(\mathbf{q}) = \zeta \sum_{j\in\mathcal{N}_b} \mathrm{diag}\{\lambda_{1,j}\mathbf{J}_r(\phi_{1,j}), \dots, \lambda_{N_a,j}\mathbf{J}_r(\phi_{N_a,j})\}, \tag{3.3.5}$$

where $\zeta = 2/(c^2\sigma_w^2)$, $\mathbf{J}_r(\phi_{k,j}) = \mathbf{u}_r(\phi_{k,j})\mathbf{u}_r^{\mathrm{T}}(\phi_{k,j})$ with $\mathbf{u}_r(\phi_{k,j}) = [\cos\phi_{k,j} \ \sin\phi_{k,j}]^{\mathrm{T}}$ is the so-called ranging direction matrix (RDM) and $\lambda_{k,j}$ is the ranging information intensity (RII), given by [Sha15]

$$\lambda_{k,j} = \mathbf{h}_{k,j}^{\mathrm{H}}\mathbf{M}_j^{(1)}(\mathbf{p}_j)\mathbf{h}_{k,j} - \mathbf{h}_{k,j}^{\mathrm{H}}\mathbf{M}_j^{(2)}(\mathbf{p}_j)\mathbf{h}_{k,j}, \tag{3.3.6}$$

where

$$\mathbf{M}_j^{(1)}(\mathbf{p}_j) = \mathbf{F}_L^{\mathrm{H}}\mathbf{D}^{\mathrm{H}}\mathbf{P}_j\mathbf{D}\mathbf{F}_L, \tag{3.3.7}$$

$$\mathbf{M}_j^{(2)}(\mathbf{p}_j) = \boldsymbol{\Xi}^{\mathrm{H}}(\mathbf{p}_j)\boldsymbol{\Sigma}^{-1}(\mathbf{p}_j)\boldsymbol{\Xi}(\mathbf{p}_j), \tag{3.3.8}$$

in which $\mathbf{D} = \mathrm{diag}\{j2\pi n/T\}_{n=-N/2}^{N/2}$, $\boldsymbol{\Xi}(\mathbf{p}_j) = \mathbf{F}_L^{\mathrm{H}}\mathbf{P}_j\mathbf{D}\mathbf{F}_L$, and $\boldsymbol{\Sigma}(\mathbf{p}_j) = \mathbf{F}_L^{\mathrm{H}}\mathbf{P}_j\mathbf{F}_L$. Finally, the SPEB for kth agent is given by

$$\mathcal{P}_k(\{\mathbf{p}_j\}) \triangleq \mathrm{tr}\{\mathbf{J}_e^{-1}(\mathbf{q}_k)\}, \tag{3.3.9}$$

where $\mathbf{p}_j$ is the $N \times 1$ vector of transmitted power taken from the main diagonal of $\mathbf{P}_j$, and

$$\mathbf{J}_e(\mathbf{q}_k) = \zeta \sum_{j \in \mathcal{N}_b} \lambda_{k,j} \mathbf{J}_r(\phi_{k,j}). \tag{3.3.10}$$

3.3.2 Formulation of the Non-Robust Power Allocation Problem

The non-robust power allocation consists in obtaining the values of $\{\mathbf{p}_j\}$ that are optimum for the estimated values of the channel and angles, $\hat{\mathbf{h}}_{k,j}$ and $\hat{\phi}_{k,j}$, which are therefore used in the formulation of the problem. For multicast[1] transmission, it has the following form

$$\begin{aligned}
\mathcal{A}_{\text{NR}}: \underset{\{\mathbf{p}_j\}}{\text{minimize}} \quad & \sum_{j \in \mathcal{N}_b} \mathbf{1}^{\text{T}} \mathbf{p}_j && \text{(3.3.10a)} \\
\text{subject to} \quad & \mathcal{P}_k(\{\mathbf{p}_j\}) \leq \beta, \ \forall k \in \mathcal{N}_a && \text{(3.3.10b)} \\
& \mathbf{p}_j \succeq \mathbf{0}, \ \forall j \in \mathcal{N}_b && \text{(3.3.10c)}
\end{aligned}$$

where β is maximum acceptable SPEB of the agents. We note that: (3.3.10a) aims at minimizing the total power of the anchors required to localize the agents; (3.3.10b) sets an upper bound β to the SPEB of the agents; (3.3.10c) restricts the anchor power vectors $\mathbf{p}_j$ to be non-negative. Problem $\mathcal{A}_{\text{NR}}$ is the extension to multicarrier signals of minimum energy cost problem in [Li13] for multicast transmission. Finally, we note that $\mathcal{A}_{\text{NR}}$ is a convex optimization problem.

The problem $\mathcal{A}_{\text{NR}}$ can be written in the SDP form [Boy04] by replacing each constraint in (3.3.10b) by

$$\mathbf{J}_e(\mathbf{q}_k) \succeq \widetilde{\mathbf{G}}_k, \tag{3.3.11}$$

$$\widetilde{\mathbf{\Theta}}(\widetilde{\mathbf{G}}_k; \beta) \succeq \mathbf{0}, \tag{3.3.12}$$

where $\widetilde{\mathbf{G}}_k$ is a 2×2 auxiliary matrix and

$$\widetilde{\mathbf{\Theta}}(\widetilde{\mathbf{G}}_k; \beta) = \begin{bmatrix} \beta & \widetilde{\mathbf{v}}_1^{\text{T}} & \widetilde{\mathbf{v}}_2^{\text{T}} \\ \widetilde{\mathbf{v}}_1 & \widetilde{\mathbf{G}}_k & \mathbf{0} \\ \widetilde{\mathbf{v}}_2 & \mathbf{0} & \widetilde{\mathbf{G}}_k \end{bmatrix}, \tag{3.3.13}$$

where $\widetilde{\mathbf{v}}_1 = [1, 0]^{\text{T}}$ and $\widetilde{\mathbf{v}}_2 = [0, 1]^{\text{T}}$. Moreover, the matrix inequality $\mathbf{J}_e(\mathbf{q}_k) \succeq \widetilde{\mathbf{G}}_k$ can be

[1] All of the optimization problems within this paper can be easily reformulated for unicast transmission by replacing $\mathbf{p}_j$ with $\mathbf{p}_{k,j}$ and $\sum_{j \in \mathcal{N}_b} \mathbf{1}^{\text{T}} \mathbf{p}_j$ with $\sum_{k \in \mathcal{N}_a} \sum_{j \in \mathcal{N}_b} \mathbf{1}^{\text{T}} \mathbf{p}_{k,j}$ with $\mathbf{p}_{k,j}$ defined as an $N \times 1$ power vector for transmission from the jth anchor to the kth agent.

written as a linear matrix inequality on the power vector $\mathbf{p}_j$. In particular, we can replace $\mathbf{J}_e(\mathbf{q}_k) \succeq \widetilde{\mathbf{G}}_k$ by $\mathbf{\Pi}_k(\{\mathbf{p}_j\}, \widetilde{\mathbf{G}}_k) \succeq \mathbf{0}$, where

$$\mathbf{\Pi}_k(\{\mathbf{p}_j\}, \widetilde{\mathbf{G}}_k) = \begin{bmatrix} \sum_{j\in\mathcal{N}_b} \nu_{k,j}(\mathbf{p}_j)\mathbf{J}_r(\hat{\phi}_{k,j}) - \widetilde{\mathbf{G}}_k & \mathbf{\Psi}_k^{\mathrm{H}}(\{\mathbf{p}_j\}) \\ \mathbf{\Psi}_k(\{\mathbf{p}_j\}) & \mathbf{\Sigma}(\{\mathbf{p}_j\}) \end{bmatrix}, \tag{3.3.14}$$

in which $\nu_{k,j}(\mathbf{p}_j) = \zeta \hat{\mathbf{h}}_{k,j}^{\mathrm{H}} \mathbf{M}_j^{(1)}(\mathbf{p}_j)\hat{\mathbf{h}}_{k,j}$, $\mathbf{\Psi}_k^{\mathrm{H}}(\{\mathbf{p}_j\}) = [\mathbf{\Psi}_{k,1}^{\mathrm{H}}(\mathbf{p}_1) \dots \mathbf{\Psi}_{k,N_b}^{\mathrm{H}}(\mathbf{p}_{N_b})]$ and

$$\mathbf{\Psi}_{k,j}^{\mathrm{H}}(\mathbf{p}_j) = \sqrt{\zeta}\mathbf{u}_r(\hat{\phi}_{k,j})\hat{\mathbf{h}}_{k,j}^{\mathrm{H}}\mathbf{\Xi}^{\mathrm{H}}(\mathbf{p}_j),$$

$\mathbf{\Sigma}(\{\mathbf{p}_j\}) = \mathrm{diag}\{\mathbf{\Sigma}(\mathbf{p}_1), \dots, \mathbf{\Sigma}(\mathbf{p}_{N_b})\}$.

The non-robust design uses only the estimated channel coefficients and agent locations for the power allocation problem. The main drawback of the proposed non-robust allocation is that the designed power allocation is specific for particular network parameters. This causes the actual SPEB to deviate from the maximum value β when the agent's real positions and channels do not coincide with the ones used in the design. The goal of the ergodic and robust allocations is to control this deviation by taking into account in the design the uncertainty between the real parameters (i.e., channels and positions) and those assumed for the design.

3.4 Ergodic Power Allocation

In this section, we introduce the so-called ergodic power allocation and convert it to an SDP form. The ergodic power allocation problem for the case of multicast design has the following form

$$\mathcal{A}_{\mathrm{E}}: \underset{\{\mathbf{p}_j\}}{\text{minimize}} \quad \sum_{j\in\mathcal{N}_b} \mathbf{1}^{\mathrm{T}}\mathbf{p}_j \tag{3.4.0a}$$

$$\text{subject to} \quad \mathbb{E}_{\boldsymbol{\eta}}[\mathrm{tr}\{\mathbf{J}_e^{-1}(\mathbf{q}_k)\}] \leq \beta,\ \forall k \in \mathcal{N}_a \tag{3.4.0b}$$

$$\mathbf{p}_j \succeq \mathbf{0}.\ \forall j \in \mathcal{N}_b \tag{3.4.0c}$$

We note that (3.4.0b) sets an upper bound β to the *expected* SPEB of the agents, with respect to the channel coefficients $\mathbf{h}_{k,j}$ and agents' positions $\mathbf{q}_k$. Given that the analytical calculation of (3.4.0b) is inaccessible, we resort to a numerical approximation by averaging

over M_q realizations:

$$\frac{1}{M_q}\sum_{m=1}^{M_q}\mathrm{tr}\{[\mathbf{J}_{e,k,m}^{-1}(\{\mathbf{p}_j\})]\}\leq\beta, \tag{3.4.1}$$

where

$$\mathbf{J}_{e,k,m}(\{\mathbf{p}_j\})=\zeta\sum_{j\in\mathcal{N}_b}\lambda_{k,j,m}\mathbf{J}_r(\phi_{k,j,m}), \tag{3.4.2}$$

$$\lambda_{k,j,m}=\mathbf{h}_{k,j,m}^{\mathrm{H}}(\mathbf{M}_j^{(1)}(\mathbf{p}_j)-\mathbf{M}_j^{(2)}(\mathbf{p}_j))\mathbf{h}_{k,j,m}, \tag{3.4.3}$$

with $\mathbf{h}_{k,j,m}$ and $\phi_{k,j,m}$ being generated according to one of the uncertainty models in Section 3.2.2.

Using the same approach as in Section 3.3.2, we can reformulate $\mathcal{A}_{\mathrm{E}}$ in SDP form as

$$\begin{aligned}
\mathcal{A}_{\mathrm{E}}^{\mathrm{SDP}}:\ \underset{\{\mathbf{p}_j\},\{\mathbf{G}_k\}}{\text{minimize}}\quad & \sum_{j\in\mathcal{N}_b}\mathbf{1}^{\mathrm{T}}\mathbf{p}_j && \text{(3.4.3a)}\\
\text{subject to}\quad & \boldsymbol{\Theta}(\mathbf{G}_k;\beta)\succeq\mathbf{0},\ \forall k\in\mathcal{N}_a && \text{(3.4.3b)}\\
& \boldsymbol{\Pi}_{k,m}(\{\mathbf{p}_j\},\mathbf{G}_{k,m})\succeq\mathbf{0},\ \forall k\in\mathcal{N}_a,\forall m\in\mathcal{M}_q && \text{(3.4.3c)}\\
& \mathbf{p}_j\succeq\mathbf{0},\ \forall j\in\mathcal{N}_b && \text{(3.4.3d)}
\end{aligned}$$

where $\mathcal{M}_q=\{1,\ldots,M_q\}$, $\mathbf{G}_k=\mathrm{diag}\{\mathbf{G}_{k,m}\}_{m=1}^{M_q}$ comprises M_q auxiliary 2×2 matrices $\mathbf{G}_{k,m}$,

$$\boldsymbol{\Theta}(\mathbf{G}_k;\beta)=\begin{bmatrix}M_q\beta & \mathbf{v}_1^{\mathrm{T}} & \mathbf{v}_2^{\mathrm{T}}\\ \mathbf{v}_1 & \mathbf{G}_k & \mathbf{0}\\ \mathbf{v}_2 & \mathbf{0} & \mathbf{G}_k\end{bmatrix}, \tag{3.4.4}$$

with $\mathbf{v}_1=\mathbf{1}_{M_q}\otimes\widetilde{\mathbf{v}}_1$ and $\mathbf{v}_2=\mathbf{1}_{M_q}\otimes\widetilde{\mathbf{v}}_2$. The matrix $\boldsymbol{\Pi}_{k,m}(\{\mathbf{p}_j\},\mathbf{G}_{k,m})$ is defined as

$$\begin{aligned}
&\boldsymbol{\Pi}_{k,m}(\{\mathbf{p}_j\},\mathbf{G}_{k,m})= && \text{(3.4.5)}\\
&\begin{bmatrix}\sum_{j\in\mathcal{N}_b}\nu_{k,j,m}(\mathbf{p}_j)\mathbf{J}_r(\phi_{k,j,m})-\mathbf{G}_{k,m} & \boldsymbol{\Psi}_{k,m}^{\mathrm{H}}(\{\mathbf{p}_j\})\\ \boldsymbol{\Psi}_{k,m}(\{\mathbf{p}_j\}) & \boldsymbol{\Sigma}(\{\mathbf{p}_j\})\end{bmatrix},
\end{aligned}$$

in which $\nu_{k,j,m}(\mathbf{p}_j)=\zeta\mathbf{h}_{k,j,m}^{\mathrm{H}}\mathbf{M}_j^{(1)}(\mathbf{p}_j)\mathbf{h}_{k,j,m}$, and $\boldsymbol{\Psi}_{k,m}^{\mathrm{H}}(\{\mathbf{p}_j\})=[\boldsymbol{\Psi}_{k,1,m}^{\mathrm{H}}(\mathbf{p}_1)\ldots\boldsymbol{\Psi}_{k,N_b,m}^{\mathrm{H}}(\mathbf{p}_{N_b})]$, with $\boldsymbol{\Psi}_{k,j,m}^{\mathrm{H}}(\mathbf{p}_j)=\sqrt{\zeta}\mathbf{u}_r(\phi_{k,j,m})\mathbf{h}_{k,j,m}^{\mathrm{H}}\boldsymbol{\Xi}^{\mathrm{H}}(\mathbf{p}_j)$.

3.5 Robust Power Allocation

In this section, we propose a robust power allocation, accounting for the worst-case channel and position uncertainty.

3.5.1 General Formulation

The robust power allocation problem for multicast design is of the following form

$$\begin{aligned} \mathcal{A}_{\mathrm{R}}: \quad \underset{\{\mathbf{p}_j\}}{\text{minimize}} \quad & \sum_{j\in\mathcal{N}_b} \mathbf{1}^{\mathrm{T}}\mathbf{p}_j && \text{(3.5.0a)} \\ \text{subject to} \quad & \mathcal{P}_k^{\max}(\{\mathbf{p}_j\}) \leq \beta,\ \forall k \in \mathcal{N}_a && \text{(3.5.0b)} \\ & \mathbf{p}_j \succeq \mathbf{0},\ \forall j \in \mathcal{N}_b && \text{(3.5.0c)} \end{aligned}$$

where $\mathcal{P}_k^{\max}(\{\mathbf{p}_j\})$ is the worst-case SPEB:

$$\mathcal{P}_k^{\max}(\{\mathbf{p}_j\}) \triangleq \max_{\mathbf{h}_k, \boldsymbol{\phi}_k} \mathcal{P}_k(\{\mathbf{p}_j\}), \tag{3.5.1}$$

in which $\boldsymbol{\phi}_k = [\phi_{k,N_a+1}...\phi_{k,Na+Nb}]^{\mathrm{T}}$. We note that since (3.5.1) is the piecewise maximum over convex functions, the problem $\mathcal{A}_{\mathrm{R}}$ is a convex problem. Therefore, there is a variety of algorithms to solve the robust power allocation with guaranteed convergence (e.g., a cutting plane method), but with high complexity. Our ambition is to propose a potentially suboptimal method but with a reduced complexity. We will achieve this by solving the problem through a minimax game, where one player chooses a best power allocation and the second player the worst possible channel. Such an approach does not necessarily converge, unless the constraints satisfy certain technical conditions [Boy04, Section 10.3.4]. However, simulations show that in practice our algorithm converges.

Due to the structure of the SPEB in (3.3.5), the maximization over $\phi_{k,j}$ for any given value of $\mathbf{h}_{k,j}$ can be determined as in [Li13], by replacing $\mathbf{J}_r(\phi_{k,j})$ with $\mathbf{Q}_r(\hat{\phi}_{k,j}, \delta_{k,j}) = \mathbf{J}_r(\hat{\phi}_{k,j}) - \sin\delta_{k,j}\mathbf{I}_2$. Later, we will rely on the eigen-decomposition of $\mathbf{Q}_r(\hat{\phi}_{k,j}, \delta_{k,j})$. It is readily verified that the two eigen-vectors of $\mathbf{Q}_r(\hat{\phi}_{k,j}, \delta_{k,j})$ are $\mathbf{u}_{r,1}(\hat{\phi}_{k,j}) = [\cos\hat{\phi}_{k,j}, \sin\hat{\phi}_{k,j}]^{\mathrm{T}}$ and $\mathbf{u}_{r,2}(\hat{\phi}_{k,j}) = [-\sin\hat{\phi}_{k,j}, \cos\hat{\phi}_{k,j}]^{\mathrm{T}}$, with eigenvalues $\gamma_{k,j}^{(+)} = 1 - \sin\delta_{k,j} \geq 0$, and $\gamma_{k,j}^{(-)} = -\sin\delta_{k,j} \leq 0$. However, the worst-case channel depends on the power-allocation, and hence we have to resort to an iterative approach, outlined below.

In Algorithm 1, the worst-case channel deviation $\boldsymbol{\Delta}\mathbf{h}_{k,j}^{\mathrm{ws}}$ is determined using a previously determined power allocation, and this power allocation is progressively refined. In

Algorithm 1 Robust Power Allocation

1: Set $m = 1$.
2: Determine an initial guess of $\{\mathbf{p}_j^{(m-1)}\}$.
3: Determine the worst-case channel deviation $\boldsymbol{\Delta}\mathbf{h}_{k,j}^{\text{ws}}$ for the current guess of $\{\mathbf{p}_j^{(m-1)}\}$.
4: Determine a pessimistic power allocation $\{\mathbf{p}_{\text{pess},j}\}$, ignoring $\gamma_{k,j}^{(-)}$. Set $\{\mathbf{p}_j^{(m)} = \mathbf{p}_{\text{pess},j}\}$.
5: Determine $\mathbf{X}_k(\{\mathbf{p}_j\})$ and $\boldsymbol{\Delta}\mathbf{h}_{k,j}^{\text{ws}}$ for the current guess of $\{\mathbf{p}_j^{(m)}\}$.
6: Determine a corrected power allocation $\{\mathbf{p}_j^{(m+1)} = \mathbf{p}_{\text{corr},j}\}$, accounting for $\gamma_{k,j}^{(-)}$.
7: Set $m = m + 1$ and go back to step 5 until $|\Delta P_{T,\text{multi}}^{(m)}| \leq \xi_{\text{th}}$.

what follows, we solve the robust power allocation for two sets of uncertainties on the channel coefficients, $\mathcal{H}_{k,j}^{(1)}$ and $\mathcal{H}_{k,j}^{(2)}$ from Section 3.2.2, according to the above procedure.

3.5.2 Robust Power Allocation for $\boldsymbol{\Delta}\mathbf{h}_{k,j} \in \mathcal{H}_{k,j}^{(1)}$

In this section, first we obtain the worst-case channel deviation $\boldsymbol{\Delta}\mathbf{h}_{k,j}^{\text{ws}}$ (step 2 in Algorithm 1) using an initial guess of $\{\mathbf{p}_j\}$ (step 3 in Algorithm 1). Second, a pessimistic power allocation is obtained based on the worst-case channel deviation (step 4 in Algorithm 1). Third, a corrected power allocation is designed by the inclusion of a PSD matrix in the SDP optimization based on the solution of the pessimistic power allocation and accounting for $\gamma_{k,j}^{(-)}$ (step 6 in Algorithm 1). The algorithm stops when the change in the used power is smaller than a predefined threshold ξ_{th} (step 7 in Algorithm 1).

Worst-Case Channel

The values of the channel coefficients that maximize the SPEB can be obtained by solving the following optimization problem.

$$\underset{\boldsymbol{\Delta}\mathbf{h}_{k,j} \in \mathcal{H}_{k,j}^{(1)}}{\text{minimize}} \quad \lambda_{k,j}. \tag{3.5.2}$$

To solve (3.5.2), we propose the following proposition, requiring introduction of $\boldsymbol{\Omega}_j(\mathbf{p}_j) \triangleq \mathbf{M}_j^{(1)}(\mathbf{p}_j) - \mathbf{M}_j^{(2)}(\mathbf{p}_j)$.

Proposition 1 *Solving (3.5.2) leads to*

$$\boldsymbol{\Delta}\mathbf{h}_{k,j}^{\text{ws}}(\mathbf{p}_j) = -(\boldsymbol{\Omega}_j(\mathbf{p}_j) + \varrho_{k,j}\mathbf{I}_L)^{-1}\boldsymbol{\Omega}_j(\mathbf{p}_j)\hat{\mathbf{h}}_{k,j}, \tag{3.5.3}$$

in which $\varrho_{k,j}$ denotes the Lagrange multiplier associated with the constraint $\boldsymbol{\Delta}\mathbf{h}_{k,j} \in \mathcal{H}_{k,j}^{(1)}$.

Proof: See Appendix 3.B. ■

The value of $\varrho_{k,j}$ can be found numerically relying on the Karush-Kuhn-Tucker (KKT) conditions, as detailed in Appendix 3.C. Substituting (3.5.3) into the definition of $\lambda_{k,j}$ (3.3.6) leads to the worst-case RII

$$\lambda_{k,j}^{\min} = \hat{\mathbf{h}}_{k,j}^{\mathrm{H}} \widetilde{\boldsymbol{\Lambda}}_{k,j}^{\mathrm{H}}(\mathbf{p}_j) \boldsymbol{\Omega}_j(\mathbf{p}_j) \widetilde{\boldsymbol{\Lambda}}_{k,j}(\mathbf{p}_j) \hat{\mathbf{h}}_{k,j}, \tag{3.5.4}$$

in which

$$\widetilde{\boldsymbol{\Lambda}}_{k,j}(\mathbf{p}_j) = \mathbf{I}_L - \mathbf{U}_j(\mathbf{p}_j)(\boldsymbol{\Lambda}_j(\mathbf{p}_j) + \varrho_{k,j}\mathbf{I}_L)^{-1}\boldsymbol{\Lambda}_j(\mathbf{p}_j)\mathbf{U}_j^{\mathrm{H}}(\mathbf{p}_j),$$

with $\mathbf{U}_j(\mathbf{p}_j)$ and $\boldsymbol{\Lambda}_j(\mathbf{p}_j)$ obtained by eigen-decomposition $\boldsymbol{\Omega}_j(\mathbf{p}_j) = \mathbf{U}_j(\mathbf{p}_j)\boldsymbol{\Lambda}_j(\mathbf{p}_j)\mathbf{U}_j^{\mathrm{H}}(\mathbf{p}_j)$. It is clear that $\lambda_{k,j}^{\min}$ depends on $\mathbf{p}_j$ in such a way that $\bar{\mathbf{J}}_{e,k}(\{\mathbf{p}_j\}) \triangleq \sum_{j\in\mathcal{N}_b} \lambda_{k,j}^{\min}\mathbf{Q}_r(\hat{\phi}_{k,j}, \delta_{k,j})$ can no longer be written as a linear function of the power (in contrast to the non-robust and ergodic designs). This is the reason why we have to resort to the procedure in Algorithm 1.

Pessimistic Power Allocation

Given a guess of the power allocation and a corresponding guess of $\boldsymbol{\Delta}\mathbf{h}_{k,j}^{\mathrm{ws}}$, we can express the current guess of the worst-case EFIM as $\bar{\mathbf{J}}_{e,k}(\{\mathbf{p}_j\}) = \hat{\mathbf{J}}_{e,k}(\{\mathbf{p}_j\}) + \mathbf{X}_k(\{\mathbf{p}_j\})$ in which $\hat{\mathbf{J}}_{e,k}(\{\mathbf{p}_j\})$ includes the $\mathbf{M}_j^{(1)}(\mathbf{p}_j)$-related part of the EFIM and the $\mathbf{M}_j^{(2)}(\mathbf{p}_j)$-related part of the EFIM corresponding to the positive eigenvalues $\gamma_{k,j}^{(+)}$, and the PSD matrix $\mathbf{X}_k(\{\mathbf{p}_j\})$ is the $\mathbf{M}_j^{(2)}(\mathbf{p}_j)$-related part of the EFIM corresponding to the negative eigenvalues $\gamma_{k,j}^{(-)}$, that is

$$\mathbf{X}_k(\{\mathbf{p}_j\}) = \zeta \sum_{j\in\mathcal{N}_b} |\gamma_{k,j}^{(-)}| \mathbf{u}_{r,2}(\hat{\phi}_{k,j})(\hat{\mathbf{h}}_{k,j} + \boldsymbol{\Delta}\mathbf{h}_{k,j}^{\mathrm{ws}})^{\mathrm{H}}\mathbf{M}_j^{(2)}(\mathbf{p}_j)(\hat{\mathbf{h}}_{k,j} + \boldsymbol{\Delta}\mathbf{h}_{k,j}^{\mathrm{ws}})\mathbf{u}_{r,2}^{\mathrm{T}}(\hat{\phi}_{k,j}). \tag{3.5.5}$$

Consequently, $\hat{\mathbf{J}}_{e,k}(\{\mathbf{p}_j\})$ can be decomposed as

$$\hat{\mathbf{J}}_{e,k}(\{\mathbf{p}_j\}) = \sum_{j\in\mathcal{N}_b} \widetilde{\nu}_{k,j}(\mathbf{p}_j)\mathbf{Q}_r(\hat{\phi}_{k,j}, \delta_{k,j}) - \widetilde{\boldsymbol{\Psi}}_{k,j}^{\mathrm{H}}(\mathbf{p}_j)\boldsymbol{\Sigma}^{-1}(\mathbf{p}_j)\widetilde{\boldsymbol{\Psi}}_{k,j}(\mathbf{p}_j), \tag{3.5.6}$$

with

$$\widetilde{\nu}_{k,j}(\mathbf{p}_j) = \zeta(\hat{\mathbf{h}}_{k,j} + \boldsymbol{\Delta}\mathbf{h}_{k,j}^{\mathrm{ws}})^{\mathrm{H}}\mathbf{M}_j^{(1)}(\mathbf{p}_j)(\hat{\mathbf{h}}_{k,j} + \boldsymbol{\Delta}\mathbf{h}_{k,j}^{\mathrm{ws}}), \tag{3.5.7}$$

$$\widetilde{\boldsymbol{\Psi}}_{k,j}^{\mathrm{H}}(\mathbf{p}_j) = \sqrt{\zeta\gamma_{k,j}^{(+)}}\mathbf{u}_{r,1}(\hat{\phi}_{k,j})(\hat{\mathbf{h}}_{k,j} + \boldsymbol{\Delta}\mathbf{h}_{k,j}^{\mathrm{ws}})^{\mathrm{H}}\boldsymbol{\Xi}^{\mathrm{H}}(\mathbf{p}_j). \tag{3.5.8}$$

It is now clear that since $\bar{\mathbf{J}}_{e,k}(\{\mathbf{p}_j\}) \succeq \hat{\mathbf{J}}_{e,k}(\{\mathbf{p}_j\})$, a power allocation based on $\hat{\mathbf{J}}_{e,k}(\{\mathbf{p}_j\})$ will lead to an overly robust design (i.e., a pessimistic design). The constraint

$$\mathrm{tr}\{\hat{\mathbf{J}}_{e,k}^{-1}(\{\mathbf{p}_j\})\} \leq \beta$$

can be formulated as an SDP. This SDP (for a given value of $\boldsymbol{\Delta}\mathbf{h}_{k,j}^{\mathrm{ws}}$) is of exactly the same form as the non-robust SDP (3.3.11)–(3.3.14), but in $\widetilde{\boldsymbol{\Pi}}_k(\{\mathbf{p}_j\}, \widetilde{\mathbf{G}}_k)$ from (3.3.14), $\nu_{k,j}(\mathbf{p}_j)$ is replaced by $\widetilde{\nu}_{k,j}(\mathbf{p}_j)$, $\boldsymbol{\Psi}_k^{\mathrm{H}}(\{\mathbf{p}_j\})$ is replaced by $\widetilde{\boldsymbol{\Psi}}_k^{\mathrm{H}}(\{\mathbf{p}_j\})$ and $\mathbf{J}_r(\hat{\phi}_{k,j})$ is replaced by $\mathbf{Q}_r(\hat{\phi}_{k,j}, \delta_{k,j})$. We denote the solution as $\{\mathbf{p}_{\mathrm{pess},j}\}$.

Corrected Power Allocation

For the same guess of $\boldsymbol{\Delta}\mathbf{h}_{k,j}^{\mathrm{ws}}$, we now account for $\mathbf{X}_k(\{\mathbf{p}_{\mathrm{pess},j}\})$ to obtain a less conservative power allocation. This is achieved through the following optimization:

$$\begin{aligned}
\mathcal{A}_{\mathrm{R}}^{\mathrm{SDP}}: \quad \underset{\{\mathbf{p}_j\},\{\widetilde{\mathbf{G}}_k\}}{\text{minimize}} \quad & \sum_{j\in\mathcal{N}_b} \mathbf{1}^{\mathrm{T}}\mathbf{p}_j && \text{(3.5.8a)}\\
\text{subject to} \quad & \widetilde{\boldsymbol{\Theta}}(\widetilde{\mathbf{G}}_k;\beta) \succeq \mathbf{0},\ \forall k \in \mathcal{N}_a && \text{(3.5.8b)}\\
& \widetilde{\boldsymbol{\Pi}}_k(\{\mathbf{p}_j\}, \widetilde{\mathbf{G}}_k; \mathbf{X}_k(\{\mathbf{p}_{\mathrm{pess},j}\})) \succeq \mathbf{0}, && \text{(3.5.8c)}\\
& \mathbf{p}_j \succeq \mathbf{0},\ \forall j \in \mathcal{N}_b && \text{(3.5.8d)}
\end{aligned}$$

in which $\widetilde{\mathbf{G}}_k$ is an auxiliary matrix, $\widetilde{\boldsymbol{\Theta}}(\widetilde{\mathbf{G}}_k;\beta)$ was defined in (3.3.13), and

$$\begin{aligned}
&\widetilde{\boldsymbol{\Pi}}_k(\{\mathbf{p}_j\}, \widetilde{\mathbf{G}}_k; \mathbf{X}_k(\{\mathbf{p}_{\mathrm{pess},j}\})) = && \text{(3.5.9)}\\
&\begin{bmatrix} \sum_{j\in\mathcal{N}_b}\widetilde{\nu}_{k,j}(\mathbf{p}_j)\mathbf{Q}_r(\hat{\phi}_{k,j},\delta_{k,j}) + \mathbf{X}_k(\{\mathbf{p}_{\mathrm{pess},j}\}) - \widetilde{\mathbf{G}}_k & \widetilde{\boldsymbol{\Psi}}_k^{\mathrm{H}}(\{\mathbf{p}_j\}) \\ \widetilde{\boldsymbol{\Psi}}_k(\{\mathbf{p}_j\}) & \boldsymbol{\Sigma}(\{\mathbf{p}_j\}) \end{bmatrix}.
\end{aligned}$$

The solution to $\mathcal{A}_{\mathrm{R}}^{\mathrm{SDP}}$ will be denoted by $\{\mathbf{p}_{\mathrm{corr},j}\}$. Note that the inclusion of the PSD matrix $\mathbf{X}_k(\{\mathbf{p}_{\mathrm{pess},j}\})$ in (3.5.8c) will lead to a reduction in the allocated power, i.e., $\sum_{j\in\mathcal{N}_b}\mathbf{1}^{\mathrm{T}}\mathbf{p}_{\mathrm{corr},j} \leq \sum_{j\in\mathcal{N}_b}\mathbf{1}^{\mathrm{T}}\mathbf{p}_{\mathrm{pess},j}$.

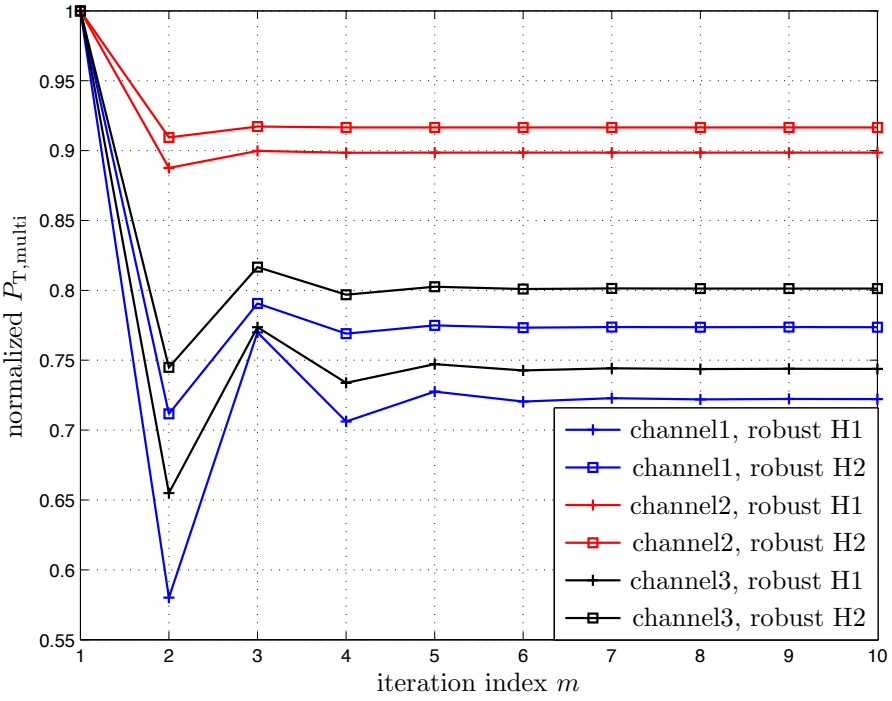

Figure 3.1: Evolution of the normalized total power $P_{\mathrm{T,multi}} = \sum_{j \in \mathcal{N}_b} \mathbf{1}^{\mathrm{T}} \mathbf{p}_{\mathrm{corr},j}$ for $\mathbf{\Delta h}_{k,j} \in \mathcal{H}_{k,j}^{(1)}$ and $\mathbf{\Delta h}_{k,j} \in \mathcal{H}_{k,j}^{(2)}$ and 3 different channels.

Complete Iterative Procedure

The complete procedure proceeds as outlined in Algorithm 1. Starting from an initial guess of the power allocation, the $\mathbf{\Delta h}_{k,j}^{\mathrm{ws}}$ is determined (see Section 3.5.2). Then a conservative power allocation is determined (see Section 3.5.2), followed by a correction (see Section 3.5.2). Then the entire procedure (Section 3.5.2 and Section 3.5.2) is repeated until a measure of convergence is achieved. In our case, we consider the absolute value of the relative change of the total power

$$|\Delta P_{T,\mathrm{multi}}^{(m)}| \triangleq \frac{|P_{T,\mathrm{multi}}^{(m+1)} - P_{T,\mathrm{multi}}^{(m)}|}{P_{T,\mathrm{multi}}^{(m)}},$$

with $P_{\mathrm{T,multi}}^{(m)} = \sum_{j \in \mathcal{N}_b} \mathbf{1}^{\mathrm{T}} \mathbf{p}_j^{(m)}$ to be smaller than a given threshold ξ_{th}, i.e., $|\Delta P_{T,\mathrm{multi}}^{(m)}| \leq \xi_{\mathrm{th}}$.

Table 3.1: Approximate complexity comparison of the non-robust, ergodic and robust power allocations, for N subcarriers, L-path channels, N_a agents, N_b anchors, M_q samples, and $M^{\max}$ iterations in Algorithm 1.

	number of Newton steps	Newton step complexity
non-robust	$\sqrt{(N_aL+N)N_b}$	$N_aN_b^2L^2(N_bL+N)+N^3N_b$
ergodic	$\sqrt{M_qN_bN_aL+NN_b}$	$M_qN_aN_b^2L^2(N_bL+N)+M_q^3N_a+N^3N_b$
robust	$M^{\max}\sqrt{(N_aL+N)N_b}$	$N_aN_b^2L^2(N_bL+N)+N^3N_b$

3.5.3 Robust Power Allocation for $\boldsymbol{\Delta}\mathbf{h}_{k,j} \in \mathcal{H}_{k,j}^{(2)}$

Worst-Case Channel

The worst-case channel for $\boldsymbol{\Delta}\mathbf{h}_{k,j} \in \mathcal{H}_{k,j}^{(2)}$ is found by solving

$$\underset{\boldsymbol{\Delta}\mathbf{h}_{k,j}\in\mathcal{H}_{k,j}^{(2)}}{\text{minimize}} \quad \lambda_{k,j}. \tag{3.5.10}$$

The optimization problem (3.5.10) is formed by a quadratic cost function with linear constraints. This type of problems have no closed-form solution, but it is well-known that it can be solved with the simplex method, interior-point methods (IPMs), or it can be transformed to SDP and solved as an SDP [Boy04].

Pessimistic and Corrected Power Allocations

Similar to Section 3.5.2 and Section 3.5.2, we can follow the same iterative procedure from Algorithm 1. Fig. 3.1 shows the convergence pattern of the proposed algorithm for unicast and multicast transmissions. It turns out that after a few iterations, the algorithm converges.

Remark: Computational Complexity

The complexity of each of the methods can be determined through an analysis based on the extension of the barrier methods with the general inequality constraints [Boy04]. The result, expressed in terms of the number of Newton steps and the complexity per Newton step, is detailed in Table 3.1. We note that with respect to the non-robust allocation, the ergodic allocation has a complexity that is around $M_q^{1.5}$ times higher, while the robust allocation has a complexity around $M^{\max}$ times higher.

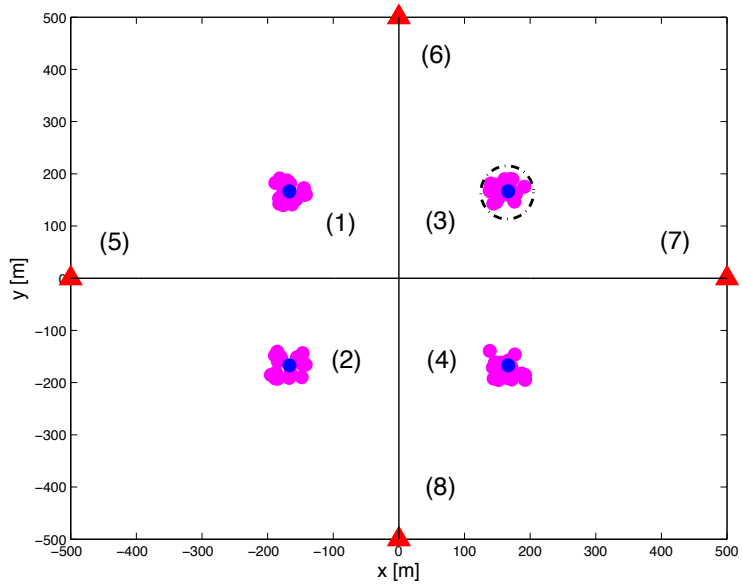

Figure 3.1: Network topology with four anchors (red triangles) and four agents (blue dots) over the 1000 m × 1000 m map. The pink dots represent possible positions due to uncertainty, and the dash-dot circle denotes the uncertainty disk.

3.6 Simulation Results

In this section, we compare the performance of the ergodic, robust, and non-robust designs in terms of the total allocated power, as well as the distribution of the power across subcarriers, and the SPEB performance.

3.6.1 Simulation Setup

We consider a network with $N_b = 4$ anchors and $N_a = 4$ agents. Each agent has a nominal position and nominal channel to each of the anchors. Due to, for instance, movement, the agents' positions and the channels become uncertain. The possible positions after movement are within an uncertainty disk with radius$\Delta\ r = 40\,\text{m}$ around the nominal positions $\mathbf{q}_k$ [m] $\in \{[\pm 166.7 \ \ \pm 166.7]^{\mathrm{T}}\}$ for $k \in \{1, 2, 3, 4\}$, as shown in Fig. 3.1. This position uncertainty then translates to angle uncertainty with$\Delta\ \phi_{k,j} \in [-\delta_{k,j}, +\delta_{k,j}]$, which is obtained using simple trigonometric calculations. For the signals, we set[2] $N/T = 10$ MHz, and $N = 32$ subcarriers. All channels have $L = 5$ taps. Examples of the magnitude of

[2]The most usual working modes of long term evolution (LTE) are based on the 5 MHz and 10 MHz operating bandwidth [3GP14, DPR14]. Thus, we have chosen 10 MHz operating bandwidths in order to represent usual LTE positioning conditions.

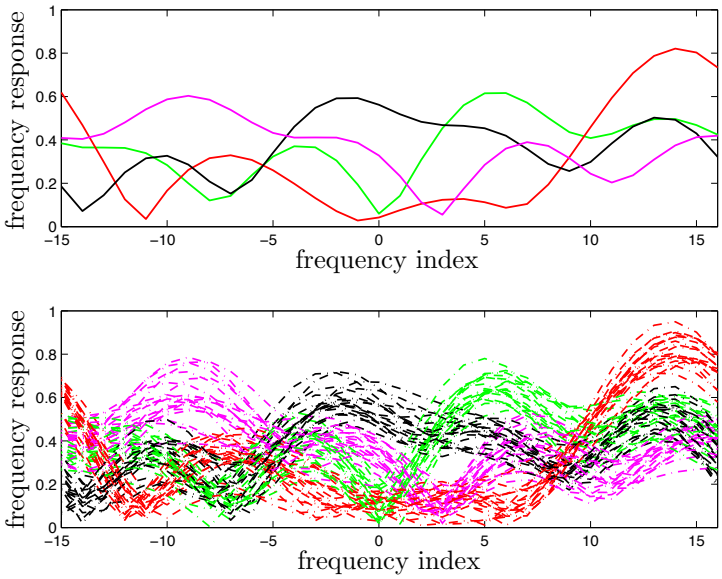

Figure 3.2: Magnitude of the frequency response for channels between anchor $k = 7$ and the agents: nominal response $|\mathbf{F}_L\hat{\mathbf{h}}_{k,j}|$ (top), response with channel uncertainty $|\mathbf{F}_L(\hat{\mathbf{h}}_{k,j} + \boldsymbol{\Delta}\mathbf{h}_{k,j})|$ (bottom).

channel frequency response associated with the nominal channels $\hat{\mathbf{h}}_{k,j}$ generated randomly as $\mathcal{CN}(0, 5\mathbf{I}_L)$ from anchor 7 to all four agents are presented in Fig. 3.2 (top). Channel uncertainties are generated from the uncertainty region based on H1 with $\epsilon = 0.6$ visualized in the frequency domain in Fig. 3.2 (bottom). To evaluate the different power allocations, we consider $N_q = 150$ possible channel and position realizations. Finally, we set the SPEB threshold $\sqrt{\beta} = \sqrt{0.5} = 0.7071$ [m].

We have considered five power allocation approaches:

- *Benchmark:* Power allocation is based on the true positions and channel coefficients after the movement. This is (3.3.10a)–(3.3.10c) using the actual value of the channel and agents' positions. Note that this strategy is not causal, as it relies on the positions after movement.

- *Non-robust:* Power allocation is based on the SDP form of problem $\mathcal{A}_{\text{NR}}$ in (3.3.10a)-(3.3.10c), using the nominal positions and nominal channels. Note that the resulting allocation may violate the SPEB constraint when evaluated in the true positions with the true channels.

- *Ergodic:* Power allocation is based on $\mathcal{A}_{\text{E}}$ in (3.4.0a)–(3.4.0c) with the SDP reformulation of (3.4.4) for M_q realizations of channel coefficients and positions after

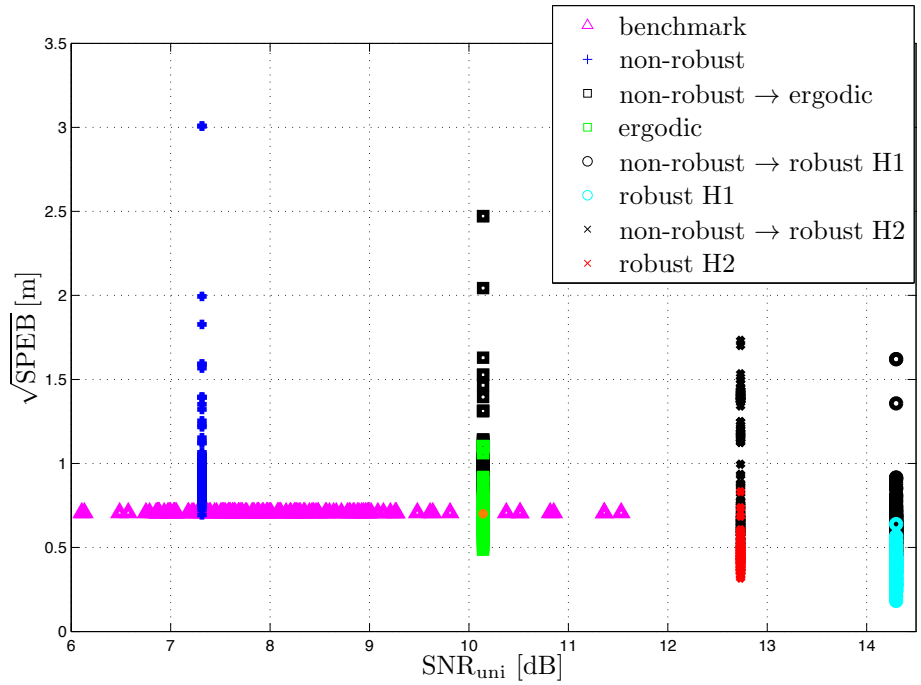

Figure 3.3: Unicast: SPEB after movement vs SNR for 150 channel and position values after movement.

movement. We have found that $M_q = 25$ is sufficient (i.e., power allocations do not change significantly for $M_q > 25$) and we use this value for the remainder of the paper.

- *Robust H1:* Power allocation is based on the solution of the problem $\mathcal{A}_{\text{R}}$ in (3.5.0a)–(3.5.0c) with channel uncertainties modeled to belong to $\mathcal{H}_{k,j}^{(1)}$.
- *Robust H2:* Power allocation is based on the solution of the problem $\mathcal{A}_{\text{R}}$ in (3.5.0a)–(3.5.0c) with channel uncertainties modeled to belong to $\mathcal{H}_{k,j}^{(2)}$. The upper bound on the per-channel tap uncertainty is set to $\epsilon_l = \epsilon/\sqrt{L}$, so that $\mathcal{H}_{k,j}^{(1)} \supset \mathcal{H}_{k,j}^{(2)}$.

For each of these power allocations, we determine the total power as well as the actual SPEB for $N_q = 150$ realizations of the channels and agents' positions after movement. In addition, we also evaluate the SPEB of the non-robust approach when the power is increased to the same level as the ergodic and robust approaches. The SDPs and convex programs are solved using CVX [Gra10].

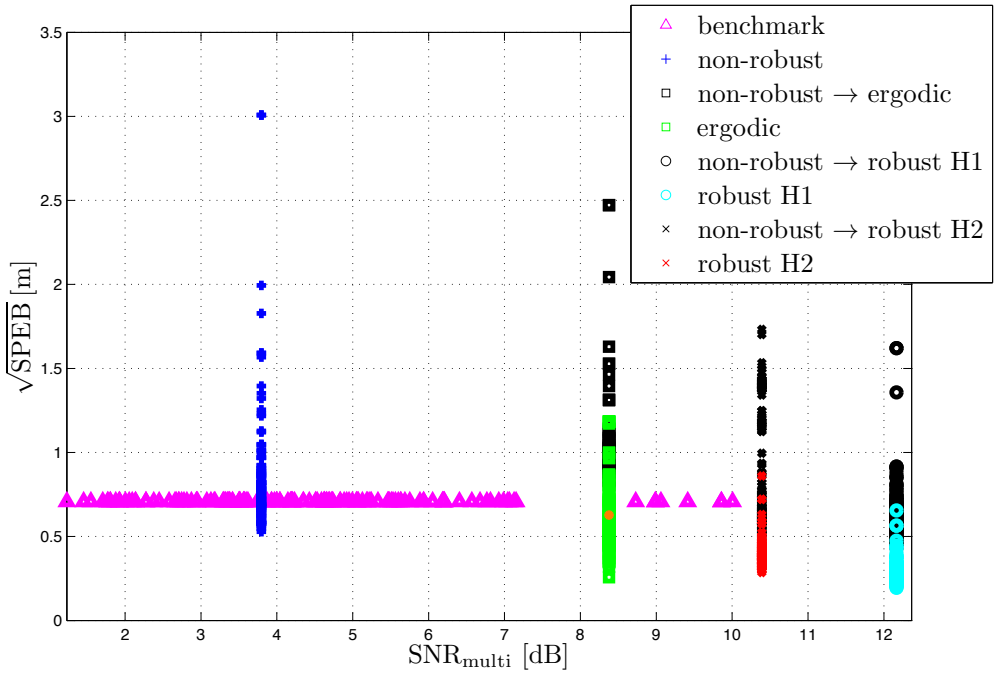

Figure 3.4: Multicast: SPEB after movement vs SNR for 150 channel and position values after movement.

3.6.2 Results and Discussion

Total allocated power

Fig. 3.3–3.4 show the result for unicast and multicast transmissions, respectively. In these plots, we show the SPEB vs $\text{SNR}_{\text{uni}} = P_{\text{T,uni}}/\sigma_w^2$ and $\text{SNR}_{\text{multi}} = P_{\text{T,multi}}/\sigma_w^2$ in which $P_{\text{T,uni}} = \sum_{k\in\mathcal{N}_a}\sum_{j\in\mathcal{N}_b}\mathbf{1}^{\text{T}}\mathbf{p}_{k,j}$ and $P_{\text{T,multi}} = \sum_{j\in\mathcal{N}_b}\mathbf{1}^{\text{T}}\mathbf{p}_j$. For the unicast scenario (Fig. 3.3), the non-causal benchmark method leads to an $\sqrt{\text{SPEB}}$ of exactly 0.7071 m, while the non-robust solution has a fixed power allocation, leading to widely varying SPEB, depending on the positions and channels after movement. We note that for all the 150 channels and positions under evaluation, the SPEB constraint is violated by the non-robust power allocation. The ergodic allocation requires slightly more power than the non-robust design, but leads to a lower SPEB, with an average around the target value of $\sqrt{\beta} = 0.7071$ m. Scaling up the power in the non-robust design to a total level equal to the ergodic design leads to a slight improvement in the SPEB (represented with the black markers in Fig. 3.3), but is still much worse than the ergodic design in terms of the average SPEB. To show the performance of the ergodic design using the sampling average in (3.4.1), the mean value of the SPEB using ergodic design with the sampling

average is shown by the orange '*' on top of the green squares. It can be observed that using the ergodic design with the sampling average in (3.4.1), the resulting allocation very likely fulfills (3.4.0b) with the desired localization accuracy of $\sqrt{\beta} = 0.7071$ m. The approximate performance of the mean value of the sample average close to the desired accuracy of $\sqrt{\beta} = 0.7071$ m can be justified using the sample average approximation for "stochastic programming" problems [Kle01]. The two robust designs require even more power, but are able to meet the SPEB requirement for each realization of the channels and positions after movement based on H1 channel uncertainty. We note that the robust H1 approach requires more power than the robust H2 approach, what is logical given that for the selected ϵ and ϵ_l the H1 uncertainty region is larger than H2. This leads to the fact that the robust H2 for some values after the agent movement slightly violates the benchmark $\sqrt{\beta} = 0.7071$ m due to the fact that the upper bound on the per-channel tap uncertainty is set to $\epsilon_l = \epsilon/\sqrt{L}$, so that $\mathcal{H}_{k,j}^{(1)} \supset \mathcal{H}_{k,j}^{(2)}$. As with the ergodic approach, scaling up the power of the non-robust approach to the level of the robust approaches still violates the SPEB constraint. This means that simply increasing the power is not an efficient way to fulfill the SPEB bound in the presence of channel and position uncertainty, and that the inclusion of the uncertainty in the design itself is fundamental to achieve a given performance without paying an excessive penalty in power. For the multicast scenario (Fig. 3.4), we observe similar trends. Interestingly, for all allocations, the total required power for different power allocation methods in unicast transmission is less than $N_a = 4$ times the total power in multicast transmission. This is due to the fact that while unicast requires more transmissions, each transmission can be optimized (in terms of total power and per-subcarrier allocation) for each individual agent.

Power across subcarriers

We analyze the per-carrier allocation for robust H1 case since the same argument can be made for the other allocations. Fig. 3.5 shows the normalized per-carrier allocations for multicast and unicast transmissions together with non-robust allocations. We observe that subcarriers at the edges are used in all (i.e., robust and non-robust) allocations (as also observed in [Lar11]), while for other subcarriers, robust and non-robust designs allocate power to different subcarriers. This justifies the fact that a scaling of the total power for the non-robust design cannot achieve the same performance as the ergodic and robust designs. Moreover, the unicast transmission allow different power across subcarriers to achieve the desired value of SPEB for each agent. This is the main reason why the total power increase for unicast transmission is less than $N_a = 4$ times the total power for their

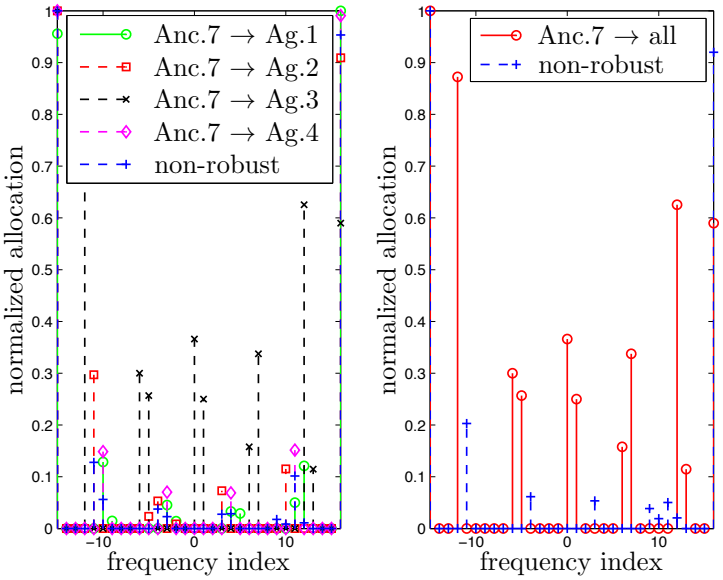

Figure 3.5: Robust H1 power allocation based on (left) unicast transmission and (right) multicast transmission for anchor 7.

multicast counterparts. Finally, it is worth mentioning that the similarity between robust designs increases by reducing the number of channel taps L. Particularly, using $L = 1$ the performance of the robust designs with the assumptions H1 and H2 would be the same, since the channel vector reduces to a scalar.

Performance of the allocations for different uncertainties

In Fig. 3.6–3.8, we investigate the performance of robust and ergodic allocations for $\sqrt{\beta} = 0.7071$ m with different uncertainties on the channel coefficients ϵ, $\epsilon_l = \epsilon/\sqrt{L}$, and$\Delta\ r$ [m] $\in \{0, 10, 20, 30, 40\}$ for multicast and unicast transmissions. In general, the required SNR for ergodic and robust designs increases by increasing the channel and/or location uncertainties. From Fig. 3.6–3.7, we observe that by going from$\Delta\ r = 0$ m to $\Delta r = 40$ m for $\epsilon = \sqrt{L}\epsilon_l = 0.6$, the required increase of the SNR is approximately 2 dB for unicast and 1 dB for multicast with robust H1 and robust H2 allocations. For the ergodic design by going from$\Delta\ r = 0$ m to $\Delta r = 40$ m for $\epsilon = \sqrt{L}\epsilon_l = 0.6$, the required increase of the SNR is approximately 1.1 dB for unicast and 0.9 dB for multicast under H1 uncertainty, and 1.15 dB for unicast and 0.8 dB for multicast under H2 uncertainty. Moreover, the required increase of the SNR for the robust designs based on channel uncertainties for a given location uncertainty is around 6 dB for robust H1, 4 dB for robust H2, and 1dB for ergodic H1 and H2 with multicast and unicast transmissions.

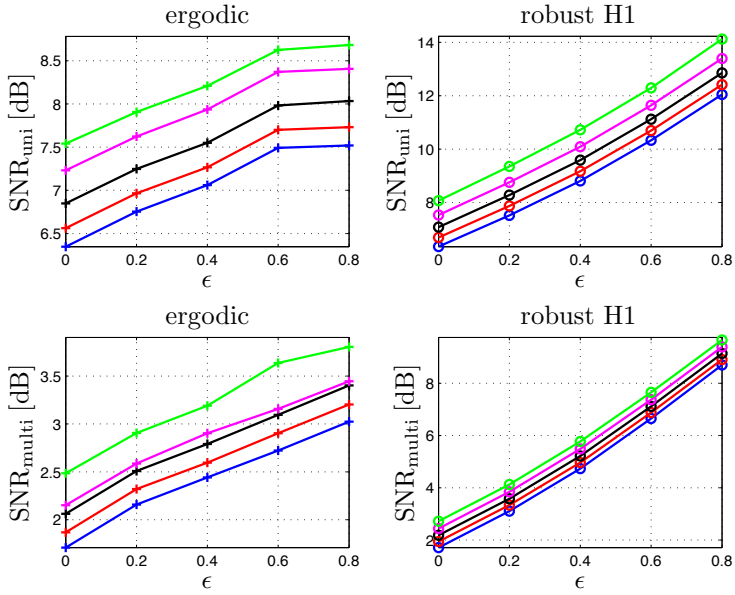

Figure 3.6: Required SNR with respect to channel uncertainty H1 and location uncertainty withΔ r [m] $\in \{0(\text{blue}), 10(\text{red}), 20(\text{black}), 30(\text{pink}), 40(\text{green})\}$ for (top) unicast and (bottom) multicast transmissions and $\sqrt{\beta} = 0.7071$ m.

From Fig. 3.8, it is observed that the maximum increase of the required SNR by only considering the effect of location uncertainty (i.e., $\epsilon = \sqrt{L}\epsilon = 0$) is around 2.3 dB for robust and 1.2 dB for ergodic with unicast transmission, and around 1.4 dB for robust and 0.8 dB for ergodic with multicast transmission. From the above observations, we conclude that the increase of the required SNR based on the location uncertainty for a given channel uncertainty is much smaller than the increase of the required SNR based on channel uncertainty for a given location uncertainty especially for the robust designs.

Comparison with single-carrier allocations

Finally, we compare the non-robust, ergodic, and robust single-carrier transmissions with their multi-carrier counterparts. The EFIM for the position of kth agent with single-carrier allocation is given by [Li13]

$$\mathbf{J}_e(\mathbf{q}_k) = \sum_{j \in \mathcal{N}_b} \xi_{k,j} p_{k,j} \mathbf{J}_r(\phi_{k,j}),$$

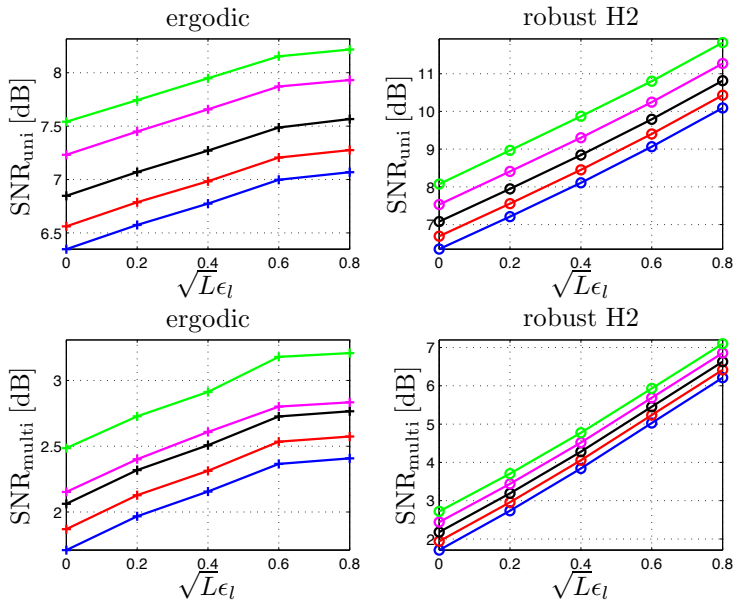

Figure 3.7: Required SNR with respect to channel uncertainty H2 and location uncertainty withΔ r [m] $\in \{0(\text{blue}), 10(\text{red}), 20(\text{black}), 30(\text{pink}), 40(\text{green})\}$ for (top) unicast and (bottom) multicast transmissions and $\sqrt{\beta} = 0.7071$ m.

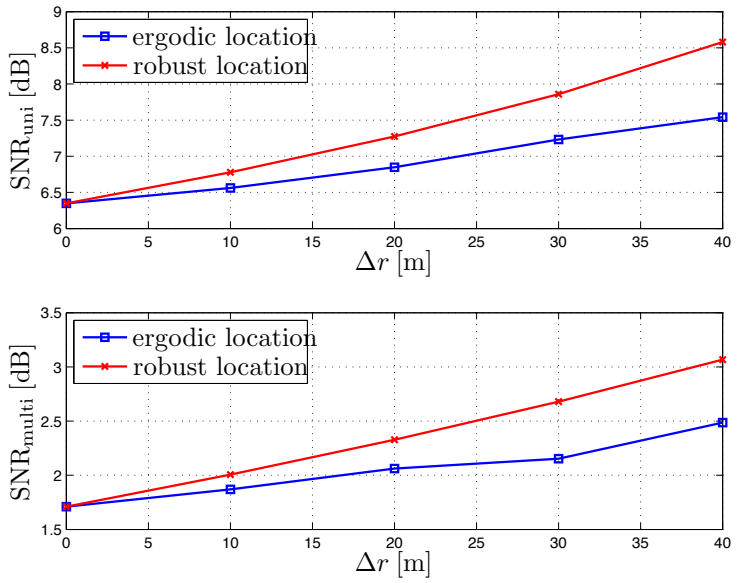

Figure 3.8: Required SNR with respect to location uncertaintyΔ r [m] with $\epsilon = 0$ for (top) unicast and (bottom) multicast transmissions and $\sqrt{\beta} = 0.7071$ m.

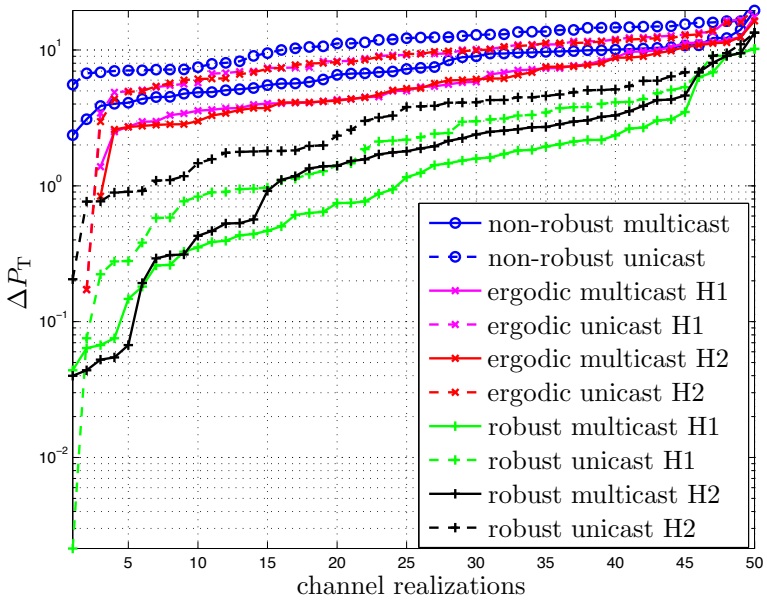

Figure 3.9: Relative change of total power in single-carrier vs multi-carrier designs for different allocations.

where $p_{k,j}$ denotes the transmitted power from anchor j to agent k,

$$\xi_{k,j} = \frac{8\pi^2 W^2}{c^2}(1-\chi_{k,j})\frac{|\alpha_{k,j,1}|^2}{\sigma_w^2},$$

where $W = N/T$ is the effective bandwidth, $\chi_{k,j}$ denotes the path-overlap coefficient, and $\alpha_{k,j,1}$ is the complex channel gain of the first path. To make the comparison with multicarrier transmission possible, we set $|\alpha_{k,j,1}|^2 = \|\mathbf{h}_{k,j}\|^2$ and $\chi_{k,j} = 0$. Although this value of $\chi_{k,j}$ makes the comparison slightly optimistic for single-carrier transmission since the partial overlap of the L paths considered in the multicarrier case could increase the value of $\chi_{k,j}$, this is considered acceptable given that the goal is to show the advantage of multicarrier power allocation for localization. Fig. 3.9 shows the relative total power increase$\Delta\ P_{\mathrm{T}} = (P_{\mathrm{T,sc}} - P_{\mathrm{T,mc}})/P_{\mathrm{T,mc}}$ in single-carrier transmission (with power $P_{\mathrm{T,sc}}$) compared to multi-carrier designs (with power $P_{\mathrm{T,mc}}$) for the different allocations and 50 channel realizations. For visualization purposes, the powers have been sorted. The average relative power increases for multicast are 7.8 (non-robust), 6.1 and 5.9 (ergodic H1 and ergodic H2), and 1.9 and 2.5 (robust H1 and robust H2, respectively). For the unicast scenario, these gains increase with an additional 50% for each approach. In general we observe that multi-carrier transmission requires less power than single-carrier transmission to achieve a given localization accuracy, but this gain diminishes

with increased robustness.

3.7 Conclusion

We have addressed the problem of power allocation for network localization under uncertainty in both channel and user locations. We considered per-channel tap and norm-based uncertainty. We first proposed a non-robust design based on perfect network parameters for OFDM-based positioning via SDP programming. To consider channel and location uncertainties, ergodic and robust power allocations for OFDM-based positioning with multicast and unicast transmission have been developed. We have observed that ergodic and robust designs outperform the non-robust designs even by increasing the total power of the non-robust design uniformly to the level of the ergodic and robust allocations. Moreover, we showed that compared with location uncertainty, channel uncertainty considerably affects the required SNR especially for the robust design. Finally, we observed that the total required power for multi-carrier designs was less than their single-carrier counterparts.

Appendix 3.A

Proof for$\boldsymbol{\Phi}\ (\mathbf{x}_k, \mathbf{x}_m) = \mathbf{0}$ for $k \neq m$

The terms $\boldsymbol{\Phi}(\boldsymbol{\theta}_k, \boldsymbol{\theta}_m)$, $\boldsymbol{\Phi}(\mathbf{q}_k, \mathbf{q}_m)$, $\boldsymbol{\Phi}(\boldsymbol{\theta}_m, \mathbf{q}_k)$, and $\boldsymbol{\Phi}(\mathbf{q}_k, \boldsymbol{\theta}_m)$ are zero for $k \neq m$. We start with $\boldsymbol{\Phi}(\boldsymbol{\theta}_k, \boldsymbol{\theta}_m)$, and continue with $\boldsymbol{\Phi}(\mathbf{q}_k, \mathbf{q}_m)$ and $\boldsymbol{\Phi}(\boldsymbol{\theta}_m, \mathbf{q}_k)$. By definition, we have

$$\boldsymbol{\Phi}(\boldsymbol{\theta}_k, \boldsymbol{\theta}_m) = \frac{2}{\sigma_w^2} \Re \left\{ \frac{\partial \boldsymbol{\mu}^{\mathrm{H}}}{\partial \boldsymbol{\theta}_k} \frac{\partial \boldsymbol{\mu}}{\partial \boldsymbol{\theta}_m} \right\}, \tag{3.A.1}$$

where $\boldsymbol{\mu}$ is defined as

$$\boldsymbol{\mu} = \left[\boldsymbol{\mu}_1^{\mathrm{T}}, \ldots, \boldsymbol{\mu}_{N_a}^{\mathrm{T}} \right]^{\mathrm{T}}, \tag{3.A.2}$$

in which

$$\boldsymbol{\mu}_k = \left[\boldsymbol{\mu}_{k,N_a+1}^{\mathrm{T}}, \ldots, \boldsymbol{\mu}_{k,N_a+N_b}^{\mathrm{T}} \right]^{\mathrm{T}}, \tag{3.A.3}$$

and $\boldsymbol{\mu}_{k,j} = \boldsymbol{\Gamma}(t_{k,j}) \mathbf{B}_j \mathbf{F}_L \mathbf{h}_{k,j}$. Taking the derivative of $\boldsymbol{\mu}^{\mathrm{H}}$ with respect to $\boldsymbol{\theta}_k$ leads to

$$\frac{\partial \boldsymbol{\mu}^{\mathrm{H}}}{\partial \boldsymbol{\theta}_k} = \left[\frac{\partial \boldsymbol{\mu}_1^{\mathrm{H}}}{\partial \boldsymbol{\theta}_k}, \ldots, \frac{\partial \boldsymbol{\mu}_k^{\mathrm{H}}}{\partial \boldsymbol{\theta}_k}, \ldots, \frac{\partial \boldsymbol{\mu}_{N_a}^{\mathrm{H}}}{\partial \boldsymbol{\theta}_k} \right]. \tag{3.A.4}$$

The only non-zero element in (3.A.4) is the term $\partial \boldsymbol{\mu}_k^{\mathrm{H}} / \partial \boldsymbol{\theta}_k$, while the only non-zero element of $\partial \boldsymbol{\mu} / \partial \boldsymbol{\theta}_m$ is the term $\partial \boldsymbol{\mu}_m / \partial \boldsymbol{\theta}_m$. So, the multiplication of these terms is zero for $k \neq m$. A similar argument can be made for the terms $\boldsymbol{\Phi}(\mathbf{q}_k, \mathbf{q}_m)$, $\boldsymbol{\Phi}(\boldsymbol{\theta}_m, \mathbf{q}_k)$, and $\boldsymbol{\Phi}(\mathbf{q}_k, \boldsymbol{\theta}_m)$.

Appendix 3.B

Proof for Proposition 1

The Lagrangian associated with the optimization problem (3.5.2) can be expressed as

$$\mathcal{L}(\boldsymbol{\Delta}\mathbf{h}_{k,j};\varrho_{k,j}) = (\hat{\mathbf{h}}_{k,j}+\boldsymbol{\Delta}\mathbf{h}_{k,j})^{\mathrm{H}}\boldsymbol{\Omega}_j(\mathbf{p}_j)(\hat{\mathbf{h}}_{k,j}+\boldsymbol{\Delta}\mathbf{h}_{k,j})+\varrho_{k,j}(\|\boldsymbol{\Delta}\mathbf{h}_{k,j}\|^2-\epsilon^2), \quad (3.B.1)$$

with the Lagrange multiplier $\varrho_{k,j} \geq 0$. The KKT conditions provide necessary and sufficient conditions for convex optimization problems. From the KKT conditions, the Lagrangian equation is

$$\boldsymbol{\nabla}_{\boldsymbol{\Delta}\mathbf{h}_{k,j}}\mathcal{L}(\boldsymbol{\Delta}\mathbf{h}_{k,j};\varrho^{\mathrm{ws}}_{k,j}) \mid_{\boldsymbol{\Delta}\mathbf{h}^{\mathrm{ws}}_{k,j}} = \mathbf{0}. \quad (3.B.2)$$

Using the Lagrangian equation (3.B.2), we obtain (3.5.3).

Appendix 3.C

Proof for the Lagrange Multiplier $\rho_{k,j}$

To obtain the Lagrange multiplier $\varrho_{k,j}$ for a given value of $\mathbf{p}_j$, we use the Lagrangian equation

$$\frac{\partial}{\partial\varrho_{k,j}}\mathcal{L}(\boldsymbol{\Delta}\mathbf{h}^{\mathrm{ws}}_{k,j};\varrho_{k,j}) \mid_{\varrho^{\mathrm{ws}}_{k,j}} = 0. \quad (3.C.1)$$

This leads to

$$\|\boldsymbol{\Delta}\mathbf{h}^{\mathrm{ws}}_{k,j}\|^2 = \epsilon^2. \quad (3.C.2)$$

Replacing (3.5.3) in (3.C.2) and the eigen-decomposition $\boldsymbol{\Omega}_j(\mathbf{p}_j) = \mathbf{U}_j(\mathbf{p}_j)\boldsymbol{\Lambda}_j(\mathbf{p}_j)\mathbf{U}^{\mathrm{H}}_j(\mathbf{p}_j)$ with $\boldsymbol{\Delta}\mathbf{g}_{k,j} = \mathbf{U}^{\mathrm{H}}_j(\mathbf{p}_j)\boldsymbol{\Delta}\mathbf{h}_{k,j}$ and $\hat{\mathbf{g}}_{k,j} = \mathbf{U}^{\mathrm{H}}_j(\mathbf{p}_j)\hat{\mathbf{h}}_{k,j}$ results:

$$\sum_{l=1}^{L}\frac{\gamma^2_{j,l}}{(\gamma_{j,l}+\varrho^{\mathrm{ws}}_{k,j})^2}|\hat{g}_{k,j,l}|^2 = \epsilon^2, \quad (3.C.3)$$

in which $\gamma_{j,l}$ is the lth entry of the diagonal matrix of the eigenvalues $\boldsymbol{\Lambda}_j(\mathbf{p}_j)$ and $\hat{g}_{k,j,l}$ denotes the lth element of $\hat{\mathbf{g}}_{k,j}$. In principle, (3.C.3) can be efficiently solved using Newton's method. Among the roots of (3.C.3), we choose the one that results the smallest value of the cost function $\lambda_{k,j}$. Note that $\varrho_{k,j}$ cannot be zero as it results $\lambda^{\min}_{k,j} = 0$. Moreover, since the Newton's method requires the initial value for the Lagrange multiplier $\varrho_{k,j}$, we

present the following proposition that provides the necessary condition on the value of $\varrho_{k,j}$ to fulfill (3.C.3) and apply it as the initial value for the Newton's method.

Proposition 2 *A necessary condition on $\varrho_{k,j}$ to fulfill* (3.C.3) *is $\varrho_{k,j} > \varrho_{k,j}^{\max}$ where*

$$\varrho_{k,j}^{\max} = \max_{l} \left(\frac{\gamma_{j,l} |\hat{g}_{k,j,l}|}{\epsilon} - \gamma_{j,l} \right) . \forall l \in \{1, \ldots, L\} \tag{3.C.4}$$

Chapter 4

5G Position and Orientation Estimation

4.1 Introduction

5G communication networks will likely adopt mm-wave and massive MIMO technologies, thanks to a number of favorable properties. In particular, operating at carrier frequencies between 30 and 300 GHz, with large available bandwidths and with highly directional communication, mm-wave can provide extremely high data rates to users through dense spatial multiplexing by using a large number of antennas [Zho11, Rap13]. While these properties are desirable for 5G services, mm-wave communications also face a number of challenges. Among these challenges, the severe path loss at those high carrier frequencies stands out. The resulting loss in SNR must be countered through sophisticated beamforming at the transmitter and/or receiver side, leading to highly directional links [Wan09, Hur13, Tsa11]. However, this in turn requires knowledge of the propagation channel.

Location information can serve as a proxy for channel information to perform beamforming: when the location of the user is known, the base station can steer its transmission to the user, either directly or through a reflected path. This leads to a synergy between localization and communication. However, in order to reap the benefits of location information for highly directional communications, both the devices' positions and orientations should be accurately estimated. Today's technologies cannot always provide this information in an efficient and reliable manner. For instance, the GPS is a well-established technology that can provide location information outdoors. However, in GPS-challenged

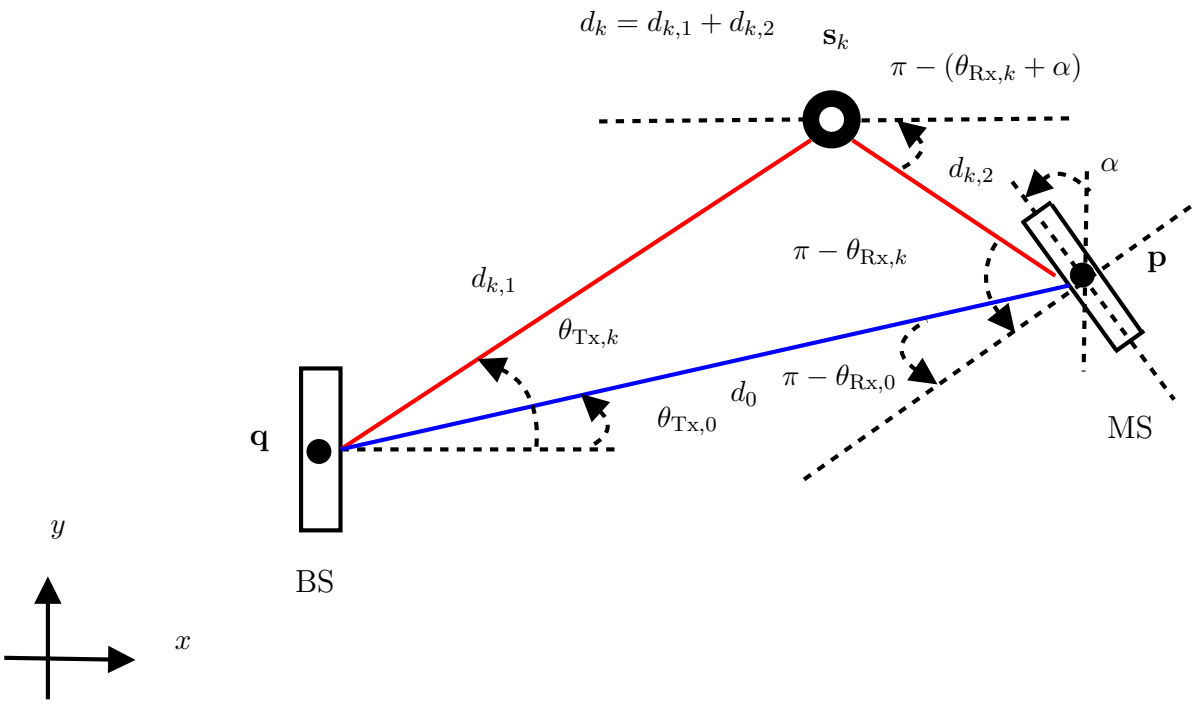

Figure 4.1: Two dimensional illustration of the LOS (blue link) and NLOS (red link) based positioning problem. The BS location $\mathbf{q}$ and BS orientation are known, but arbitrary. The location of the MS $\mathbf{p}$, cluster $\mathbf{s}_k$, rotation angle α, AOAs $\{\theta_{\mathrm{Rx},k}\}$, AODs $\{\theta_{\mathrm{Tx},k}\}$, the channel between BS and MS, and the distance between the antenna centers are unknown.

environments (e.g., indoors and in urban canyons), the accuracy is poor. Other radio technologies, such as UWB can be a solution for indoor positioning, but requires additional infrastructure and suffers from high hardware complexity [She10a].

In this chapter, we show that mm-wave and massive MIMO, which are both candidate features for 5G communication networks, are also enabling technologies for accurate positioning and device orientation estimation. The limited scattering and high-directivity are unique characteristics of mm-wave channel and massive MIMO, respectively. The fundamental bounds on position and orientation are derived in the presence of clusters of a scenario illustrated in Fig. 4.1. In the LOS conditions, angle-of-departure (AOD) is used for the estimation of position while angle-of-arrival (AOA) provides the estimation of orientation. In the non-line-of-sight (NLOS) and OLOS conditions[1], there is no geometrical relation between the AOA/AOD and the rotation angle of the MS. Consequently, the NLOS links do not provide any information on the rotation angle directly. This is addressed in the chapter by obtaining the position error bound (PEB) and analyzing the effect of adding the clusters on the PEB in the presence of the LOS. An algorithm based on the MMV matching pursuit is proposed for the coarse estimation of the AOA/AOD and TOA that are used for the initialization of the EM with a sequential iterative procedure. Finally, the estimated values of AOA/AOD, TOA, and channel coefficients are used for localization using the extended invariance principle (EXIP) in estimation by means of a weighted least squares (WLS) fit [Sto89, Swi02]. The results show that the errors in the estimated values of AOA/AOD and TOA and consequently also in the estimated position and device orientation converge to their corresponding bounds.

Related Work:

The use of 5G technologies to obtain position and orientation was previously explored in [San02, Den14, Var14b] for mm-wave and in [Hu14, Gue15, Sav15] for massive MIMO. The early work [San02] considered estimation and tracking of DOA through beam-switching. User localization was treated in [Den14], formulated as a hypothesis testing problem, limiting the spatial resolution. A different approach was taken in [Var14b], where meter-level positioning accuracy was obtained by measuring received signal strength levels. In the massive MIMO case, [Hu14] considered estimation of angles, while [Gue15] treated joint estimation of delay, AOD, and AOA, in the LOS conditions and evaluated the impact of errors in delays and phase shifters. In [Sav15], positioning was solved using a Gaussian

[1]NLOS is defined as the condition that the LOS path exists and the clusters are not blocking the LOS. OLOS is defined as the condition that the LOS path is blocked by the clusters.

process regressor, operating on a vector of received signal strengths through fingerprinting.

4.2 System Model

We consider a MIMO system with a BS equipped with N_t antennas and a MS equipped by N_r antennas. Locations of the MS and BS are denoted by $\mathbf{p} = [p_x, p_y]^{\mathrm{T}} \in \mathbb{R}^2$ and $\mathbf{q} = [q_x, q_y]^{\mathrm{T}} \in \mathbb{R}^2$ with the $\alpha \in [0, 2\pi)$ denoting the rotation angle of the MS's antenna array.

4.2.1 Transmitter Model

Consider the OFDM based system model in Fig. 4.1 where a BS with hybrid analog/digital precoder communicates with a single MS. At the BS, M_t transmitted symbols $\mathbf{x}[n] = [x_1[n], \ldots, x_{M_t}[n]]^{\mathrm{T}} \in \mathbb{C}^{M_t}$ at each subcarrier $n = 0, \ldots, N-1$ are first precoded using an $M_t \times M_t$ digital precoding matrix $\mathbf{F}_{\mathrm{BB}}[n]$, and transformed to the time-domain using N-point inverse fast Fourier transform (IFFT). A cyclic prefix (CP) of length $T_{\mathrm{CP}} = DT_s$ is added before applying the $N_t \times M_t$ RF precoding $\mathbf{F}_{\mathrm{RF}}$ where T_s is the sampling period. It is assumed that all the arriving paths fall into the interval T_{CP} to avoid ISI. The RF precoding matrix $\mathbf{F}_{\mathrm{RF}}$ is the same for all the subcarriers [Alk15]. For simplicity of notation, we consider the $N_t \times M_t$ transmit beamformer matrix[2] $\mathbf{F}[n] = \mathbf{F}_{\mathrm{RF}}\mathbf{F}_{\mathrm{BB}}[n]$ where $\mathbf{F}[n] = [\mathbf{f}_1[n], \mathbf{f}_2[n], \ldots, \mathbf{f}_{M_t}[n]] \in \mathbb{C}^{N_t \times M_t}$.

4.2.2 Channel Model

We define the channel model with considering the effect of frequency dependent array responses (beam squint) [Bra15]. Assuming steering vectors to be frequency dependent, which is the case for wideband communication (with fractional bandwidth FB $\triangleq B/f_c$ up to 50% where B is the bandwidth and f_c denotes the carrier frequency [Gha02]) and the large number of antenna arrays, the channel model can be expressed as

$$\mathbf{H}[n] = \mathbf{A}_{\mathrm{Rx}}[n]\mathbf{\Gamma}[n]\mathbf{A}_{\mathrm{Tx}}^{\mathrm{H}}[n], \tag{4.2.1}$$

[2]Each column of the wideband transmit beamformer matrix $\mathbf{F}[n]$ can be applied using M antennas in the other dimension (sensor delay line (SDL) [Gha02, Liu09]) or tapped delay line (TDL) [Haw14] of length M for each antenna to obtain a wideband beamforming matrix $\widetilde{\mathbf{F}}$ of size $N_t M \times M_t$ in a frequency independent form.

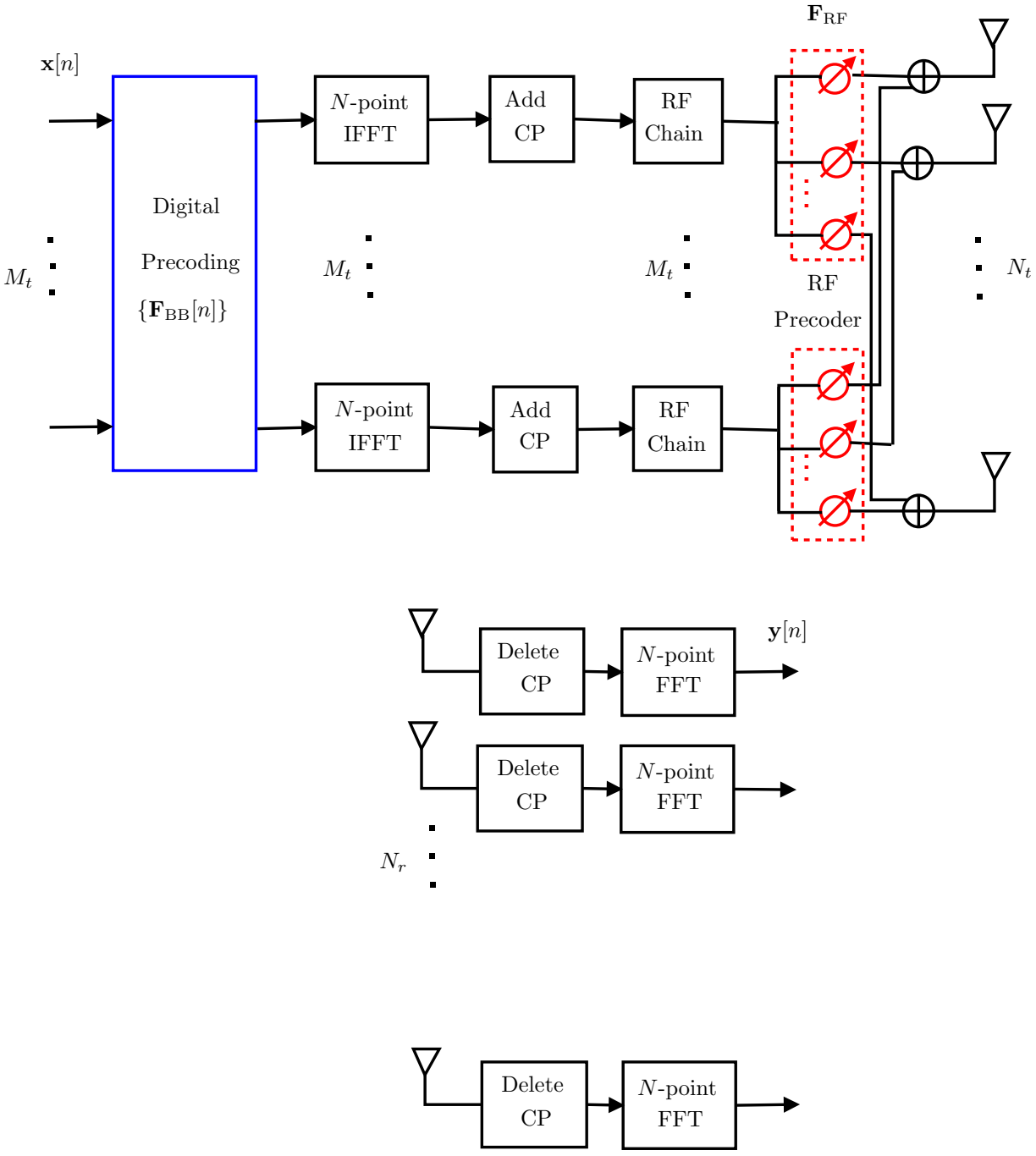

Figure 4.1: A block diagram of the multicarrier based BS that employs hybrid analog/digital precoding. At the MS, the CP is removed and the time domain signal is transformed to frequency domain by employing FFT.

where

$$\mathbf{\Gamma}[n] = \text{diag}\{\gamma_n(h_0, \tau_0), \ldots, \gamma_n(h_K, \tau_K)\},$$
$$\mathbf{A}_{\text{Tx}}[n] = \left[\mathbf{a}_{\text{Tx},n}(\theta_{\text{Tx},0}), \ldots, \mathbf{a}_{\text{Tx},n}(\theta_{\text{Tx},K})\right],$$

and $\mathbf{A}_{\text{Rx}}[n]$ is defined similarly by replacing the subscript Tx by Rx, K is the number of NLOS paths, $\gamma_n(h_k, \tau_k) = \tilde{h}_k e^{-j2\pi n\tau_k/(NT_s)}$ where $\tilde{h}_k = \alpha_k h_k$, $\alpha_k = \sqrt{(N_t N_r)/\rho_k}$ in which ρ_k denotes the path loss between BS and MS for the k-th path, h_k is the complex channel gain for the k-th path, τ_k denotes the time-delay of the k-th path, $\mathbf{a}_{\text{Tx},n}(\theta_{\text{Tx},k}) \in \mathbb{C}^{N_t}$ and $\mathbf{a}_{\text{Rx},n}(\theta_{\text{Rx},k}) \in \mathbb{C}^{N_r}$ are the frequency dependent antenna steering and response vectors, $\theta_{\text{Tx},k}$ and $\theta_{\text{Rx},k}$ are the AOD and AOA of the k-th path, respectively. The wideband antenna steering vector at the transmitter for the uniform linear array (ULA) would be

$$\mathbf{a}_{\text{Tx},n}(\theta_{\text{Tx},k}) = \frac{1}{\sqrt{N_t}}[1, e^{j\frac{2\pi}{\lambda_n}d\sin(\theta_{\text{Tx},k})}, \ldots, e^{j(N_t-1)\frac{2\pi}{\lambda_n}d\sin(\theta_{\text{Tx},k})}]^{\text{T}}, \tag{4.2.2}$$

where[3] $\lambda_n = c/(f_n + f_c)$ is the signal wavelength at the n-th sub-band $f_n = n/T$ where $T = NT_s$ denotes the OFDM symbol duration with T_s being the sampling period, $n = 0, \ldots, N-1$ subcarriers are used so that the bandwidth is $B = N/T$ and c is the speed of light, and d denotes the distance between the antenna elements defined as $d = \lambda_c/2$. Thus, $\mathbf{a}_{\text{Rx},n}(\theta_{\text{Rx},k})$ is defined similarly by replacing the subscript Tx by Rx and N_t by N_r in (4.2.2). The narrowband counterpart of the above channel model is obtained by defining frequency independent array steering vector

$$\mathbf{a}_{\text{Tx}}(\theta_{\text{Tx},k}) = \frac{1}{\sqrt{N_t}}[1, e^{j\frac{2\pi}{\lambda_c}d\sin(\theta_{\text{Tx},k})}, \ldots, e^{j(N_t-1)\frac{2\pi}{\lambda_c}d\sin(\theta_{\text{Tx},k})}]^{\text{T}}, \tag{4.2.3}$$

where $d = \lambda_c/2$ and $\lambda_c = c/f_c$, and $\mathbf{a}_{\text{Rx}}(\theta_{\text{Tx},k})$ is defined similarly by replacing the subscript Tx by Rx and N_t by N_r.

4.2.3 Receiver Model

We define receiver model for the aforementioned channel model. After the CP removal and fast Fourier transform (FFT), the received signal at subcarrier n before processing

[3]The variation of λ_n with respect to $\lambda_c = c/f_c$ for $f_c = 60$ GHz and the bandwidth B ranging from 10 MHz to 500 MHz is sufficiently small, i.e., $\lambda_n/\lambda_c \approx 0.99$.

can be then expressed as

$$\mathbf{y}[n] = \mathbf{H}[n]\mathbf{F}[n]\mathbf{x}[n] + \mathbf{n}[n], \tag{4.2.4}$$

where $\mathbf{H}[n]$ is defined in (4.2.1), and $\mathbf{n}[n] \in \mathbb{C}^{N_r}$ is a Gaussian noise vector with zero mean and two-side power spectral density $N_0/2$. The narrowband receiver model can be obtained similar to (4.2.4) by replacing narrowband channel model as explained in the previous section and wideband beamformer $\mathbf{F}[n]$ with the narrowband counterpart $\mathbf{F}$.

The goal is to obtain position $\mathbf{p}$ and orientation α of the MS from $\mathbf{y}[n]$ for the frequency band $[-B/2, B/2]$. We do not assume any specific receiver-side processing or beamforming to derive a *fundamental* lower bound, i.e., (4.2.4) is used to derive the *fundamental* lower bound.

4.3 Derivation of the Fundamental Bounds

In this section, we derive the FIM and the Cramér-Rao bound (CRB) for the estimation problem of position and orientation of the MS for the LOS without and with NLOS links. Also, we consider the estimation of position of the MS for the case when the LOS is blocked and only the NLOS links exist, i.e., OLOS. We name the case when *only* the LOS exists as LOS, the case when both LOS and NLOS links exist as NLOS, and the case when the LOS is blocked as OLOS.

4.3.1 Channel Parameters

Let $\boldsymbol{\eta} \in \mathbb{R}^{5(K+1)}$ be the vector consisting of the unknown channel parameters

$$\boldsymbol{\eta} = \left[\boldsymbol{\eta}_0^{\mathrm{T}}, \ldots, \boldsymbol{\eta}_K^{\mathrm{T}}\right]^{\mathrm{T}}, \tag{4.3.1}$$

in which $\boldsymbol{\eta}_k$ consists of the unknown channel parameters (delay, AOD, AOA, and channel coefficients) for the k-th path

$$\boldsymbol{\eta}_k = \left[\tau_k, \boldsymbol{\theta}_k^{\mathrm{T}}, \tilde{\mathbf{h}}_k^{\mathrm{T}}\right]^{\mathrm{T}}, \tag{4.3.2}$$

where $\tilde{\mathbf{h}}_k = \left[\tilde{h}_{\mathrm{R},k}, \tilde{h}_{\mathrm{I},k}\right]^{\mathrm{T}}$ is the complex channel gain for the k-th path with $\tilde{h}_{\mathrm{R},k}$ and $\tilde{h}_{\mathrm{I},k}$ being the real and imaginary parts of $\tilde{h}_k$, and $\boldsymbol{\theta}_k = \left[\theta_{\mathrm{Tx},k}, \theta_{\mathrm{Rx},k}\right]^{\mathrm{T}}$.

Defining $\hat{\boldsymbol{\eta}}$ as the unbiased estimator of $\boldsymbol{\eta}$, the mean squared error (MSE) is bounded

as [Kay10]

$$\mathbb{E}_{\mathbf{y}|\boldsymbol{\eta}}\left[(\hat{\boldsymbol{\eta}}-\boldsymbol{\eta})(\hat{\boldsymbol{\eta}}-\boldsymbol{\eta})^{\mathrm{T}}\right] \succeq \mathbf{J}_{\boldsymbol{\eta}}^{-1}, \tag{4.3.3}$$

in which $\mathbb{E}_{\mathbf{y}|\boldsymbol{\eta}}[.]$ denotes the expectation parameterized by the unknown parameters $\boldsymbol{\eta}$, and $\mathbf{J}_{\boldsymbol{\eta}}$ is the $5(K+1)\times 5(K+1)$ FIM defined as

$$\mathbf{J}_{\boldsymbol{\eta}} \triangleq \mathbb{E}_{\mathbf{y}|\boldsymbol{\eta}}\left[-\frac{\partial^2 \ln f(\mathbf{y}|\boldsymbol{\eta})}{\partial\boldsymbol{\eta}\partial\boldsymbol{\eta}^T}\right], \tag{4.3.4}$$

where $f(\mathbf{y}|\boldsymbol{\eta})$ is the likelihood ratio of the random vector $\mathbf{y}$ obtained from the Karhunen-Loeve expansion of $\mathbf{y}[n]$ conditioned on $\boldsymbol{\eta}$. More specifically, $f(\mathbf{y}|\boldsymbol{\eta})$ can be written as [Poo94]

$$f(\mathbf{y}|\boldsymbol{\eta}) \propto \exp\left\{\frac{2}{N_0}\sum_{n=0}^{N-1}\Re\{\boldsymbol{\mu}^{\mathrm{H}}[n]\mathbf{y}[n]\} - \frac{1}{N_0}\sum_{n=0}^{N-1}\|\boldsymbol{\mu}[n]\|^2\right\}, \tag{4.3.5}$$

and $\boldsymbol{\mu}[n] \triangleq \mathbf{H}[n]\mathbf{F}[n]\mathbf{x}[n]$.

4.3.2 FIM

The FIM in (4.3.4) can be structured as

$$\mathbf{J}_{\boldsymbol{\eta}} = \begin{bmatrix} \boldsymbol{\Psi}(\boldsymbol{\eta}_0,\boldsymbol{\eta}_0) & \dots & \boldsymbol{\Psi}(\boldsymbol{\eta}_0,\boldsymbol{\eta}_K) \\ \vdots & \ddots & \vdots \\ \boldsymbol{\Psi}(\boldsymbol{\eta}_K,\boldsymbol{\eta}_0) & \dots & \boldsymbol{\Psi}(\boldsymbol{\eta}_K,\boldsymbol{\eta}_K) \end{bmatrix}, \tag{4.3.6}$$

in which the operator $\boldsymbol{\Psi}(\mathbf{x}_r,\mathbf{x}_s)$ is defined as

$$\boldsymbol{\Psi}(\mathbf{x}_r,\mathbf{x}_s) \triangleq \mathbb{E}_{\mathbf{y}|\boldsymbol{\eta}}\left[-\frac{\partial^2 \ln f(\mathbf{y}|\boldsymbol{\eta})}{\partial\mathbf{x}_r\partial\mathbf{x}_s^{\mathrm{T}}}\right], \tag{4.3.7}$$

with $f(\mathbf{y}|\boldsymbol{\eta})$ replaced from (4.3.5). The sub-matrix $\boldsymbol{\Psi}(\boldsymbol{\eta}_r,\boldsymbol{\eta}_s)$ in (4.3.6) can be written as

$$\boldsymbol{\Psi}(\boldsymbol{\eta}_r,\boldsymbol{\eta}_s) = \sum_{n=0}^{N-1}\boldsymbol{\Psi}_n(\boldsymbol{\eta}_r,\boldsymbol{\eta}_s), \tag{4.3.8}$$

in which the integral is applied element-wise, and

$$\boldsymbol{\Psi}_n(\boldsymbol{\eta}_r,\boldsymbol{\eta}_s) = \begin{bmatrix} \Psi_n(\tau_r,\tau_s) & \boldsymbol{\Psi}_n(\tau_r,\boldsymbol{\theta}_s) & \boldsymbol{\Psi}_n(\tau_r,\mathbf{h}_s) \\ \boldsymbol{\Psi}_n(\boldsymbol{\theta}_r,\tau_s) & \boldsymbol{\Psi}_n(\boldsymbol{\theta}_r,\boldsymbol{\theta}_s) & \boldsymbol{\Psi}_n(\boldsymbol{\theta}_r,\mathbf{h}_s) \\ \boldsymbol{\Psi}_n(\mathbf{h}_r,\tau_s) & \boldsymbol{\Psi}_n(\mathbf{h}_r,\boldsymbol{\theta}_s) & \boldsymbol{\Psi}_n(\mathbf{h}_r,\mathbf{h}_s) \end{bmatrix}. \tag{4.3.9}$$

The entries of $\mathbf{\Psi}_n(\boldsymbol{\eta}_r, \boldsymbol{\eta}_s)$ are derived in Appendix 4.A. The narrowband counterparts for the entries of the FIM for the LOS and without considering the effect of clusters are obtained in [Sha15] by replacing frequency dependent array steering vectors $\mathbf{a}_{\mathrm{Tx},n}(\theta_{\mathrm{Tx},k})$ and $\mathbf{a}_{\mathrm{Rx},n}(\theta_{\mathrm{Rx},k})$ with their frequency independent counterparts $\mathbf{a}_{\mathrm{Tx}}(\theta_{\mathrm{Tx},k})$ and $\mathbf{a}_{\mathrm{Rx}}(\theta_{\mathrm{Tx},k})$, respectively. For the narrowband systems, the summation over subcarriers is applied only to the terms $\mathbf{A}_{k,n}(\tau_r, \tau_s)$ that are defined in the Appendix 4.A.

4.3.3 CRB for Position and Orientation

In this section, we find the Jacobian matrix for the transformation from $\boldsymbol{\eta}$ to $\tilde{\boldsymbol{\eta}} = \left[\tilde{\boldsymbol{\eta}}_0^{\mathrm{T}}, \ldots, \tilde{\boldsymbol{\eta}}_K^{\mathrm{T}}\right]^{\mathrm{T}}$, where $\tilde{\boldsymbol{\eta}}_k = \left[\mathbf{s}_k^{\mathrm{T}}, \tilde{\mathbf{h}}_k^{\mathrm{T}}\right]^{\mathrm{T}}$ with $\mathbf{s}_k = [s_{k,x}, s_{k,y}]^{\mathrm{T}} \in \mathbb{R}^2$ denoting the location of the k-th scatterer shown in Fig. 4.1 for $k \neq 0$ and $\tilde{\boldsymbol{\eta}}_0 = \left[\mathbf{p}^{\mathrm{T}}, \alpha, \tilde{\mathbf{h}}_0^{\mathrm{T}}\right]^{\mathrm{T}}$. The FIM of $\tilde{\boldsymbol{\eta}}$ is obtained by means of the $(4K+5) \times 5(K+1)$ transformation matrix $\mathbf{T}$ as

$$\mathbf{J}_{\tilde{\boldsymbol{\eta}}} = \mathbf{T}\mathbf{J}_{\boldsymbol{\eta}}\mathbf{T}^{\mathrm{T}}, \tag{4.3.10}$$

where

$$\mathbf{T} \triangleq \frac{\partial \boldsymbol{\eta}}{\partial \tilde{\boldsymbol{\eta}}}. \tag{4.3.11}$$

The entries of $\mathbf{T}$ can be obtained by the relations between the parameters in $\boldsymbol{\eta}$ and $\tilde{\boldsymbol{\eta}}$ from the geometry of the problem shown in Fig. 4.1 as:

$$\begin{aligned}
\tau_0 &= \|\mathbf{p} - \mathbf{q}\|/c, \\
\tau_k &= \|\mathbf{q} - \mathbf{s}_k\|/c + \|\mathbf{p} - \mathbf{s}_k\|/c, \\
\cos(\theta_{\mathrm{Tx},0}) &= (p_x - q_x)/\|\mathbf{p} - \mathbf{q}\|, \\
\cos(\theta_{\mathrm{Tx},k}) &= (s_{k,x} - q_x)/\|\mathbf{s}_k - \mathbf{q}\|, \\
\cos(\pi - (\theta_{\mathrm{Rx},k} + \alpha)) &= (p_x - s_{k,x})/\|\mathbf{p} - \mathbf{s}_k\|, \\
\alpha &= \pi + \theta_{\mathrm{Tx},0} - \theta_{\mathrm{Rx},0},
\end{aligned}$$

Consequently, we obtain

$$\mathbf{T} = \begin{bmatrix} \mathbf{T}_{0,0} & \ldots & \mathbf{T}_{K,0} \\ \vdots & \ddots & \vdots \\ \mathbf{T}_{0,K} & \ldots & \mathbf{T}_{K,K} \end{bmatrix}, \tag{4.3.12}$$

in which $\mathbf{T}_{r,s}$ is defined as

$$\mathbf{T}_{r,s} \triangleq \frac{\partial \boldsymbol{\eta}_r^{\mathrm{T}}}{\partial \tilde{\boldsymbol{\eta}}_s}. \tag{4.3.13}$$

For $s \neq 0$, $\mathbf{T}_{r,s}$ is obtained as

$$\mathbf{T}_{r,s} = \begin{bmatrix} \partial\tau_r/\partial\mathbf{s}_s & \partial\boldsymbol{\theta}_r^{\mathrm{T}}/\partial\mathbf{s}_s & \partial\tilde{\mathbf{h}}_r^{\mathrm{T}}/\partial\mathbf{s}_s \\ \partial\tau_r/\partial\tilde{\mathbf{h}}_s & \partial\boldsymbol{\theta}_r^{\mathrm{T}}/\partial\tilde{\mathbf{h}}_s & \partial\tilde{\mathbf{h}}_r^{\mathrm{T}}/\partial\tilde{\mathbf{h}}_s \end{bmatrix}, \tag{4.3.14}$$

and $\mathbf{T}_{r,0}$ is obtained as

$$\mathbf{T}_{r,0} = \begin{bmatrix} \partial\tau_r/\partial\mathbf{p} & \partial\boldsymbol{\theta}_r^{\mathrm{T}}/\partial\mathbf{p} & \partial\tilde{\mathbf{h}}_r^{\mathrm{T}}/\partial\mathbf{p} \\ \partial\tau_r/\partial\alpha & \partial\boldsymbol{\theta}_r^{\mathrm{T}}/\partial\alpha & \partial\tilde{\mathbf{h}}_r^{\mathrm{T}}/\partial\alpha \\ \partial\tau_r/\partial\tilde{\mathbf{h}}_0 & \partial\boldsymbol{\theta}_r^{\mathrm{T}}/\partial\tilde{\mathbf{h}}_0 & \partial\tilde{\mathbf{h}}_r^{\mathrm{T}}/\partial\tilde{\mathbf{h}}_0 \end{bmatrix}, \tag{4.3.15}$$

where

$$\begin{aligned}
\partial\tau_0/\partial\mathbf{p} &= \frac{1}{c}\Big[\cos(\theta_{\mathrm{Tx},0}), \sin(\theta_{\mathrm{Tx},0})\Big]^{\mathrm{T}}, \\
\partial\theta_{\mathrm{Tx},0}/\partial\mathbf{p} &= \frac{1}{\|\mathbf{p}-\mathbf{q}\|}\Big[-\sin(\theta_{\mathrm{Tx},0}), \cos(\theta_{\mathrm{Tx},0})\Big]^{\mathrm{T}}, \\
\partial\theta_{\mathrm{Rx},0}/\partial\alpha &= -1, \\
\partial\tau_r/\partial\mathbf{p} &= \frac{1}{c}\Big[\cos(\pi-\theta_{\mathrm{Rx},r}), -\sin(\pi-\theta_{\mathrm{Rx},r})\Big]^{\mathrm{T}}, \ r \neq 0 \\
\partial\tau_r/\partial\mathbf{s}_r &= \frac{1}{c}\Big[\cos(\theta_{\mathrm{Tx},r}) + \cos(\theta_{\mathrm{Rx},r}), \sin(\theta_{\mathrm{Tx},r}) + \sin(\theta_{\mathrm{Rx},r})\Big]^{\mathrm{T}}, \ r \neq 0 \\
\partial\theta_{\mathrm{Tx},r}/\partial\mathbf{s}_r &= \frac{1}{\|\mathbf{s}_r-\mathbf{q}\|}\Big[-\sin(\theta_{\mathrm{Tx},r}), \cos(\theta_{\mathrm{Tx},r})\Big]^{\mathrm{T}} \\
\partial\theta_{\mathrm{Rx},r}/\partial\mathbf{p} &= \frac{1}{\|\mathbf{p}-\mathbf{s}_r\|}\Big[\sin(\pi-\theta_{\mathrm{Rx},r}), \cos(\pi-\theta_{\mathrm{Rx},r})\Big]^{\mathrm{T}}, \ r \neq 0 \\
\partial\theta_{\mathrm{Rx},r}/\partial\alpha &= -1, \ r \neq 0 \\
\partial\theta_{\mathrm{Rx},r}/\partial\mathbf{s}_r &= -\frac{1}{\|\mathbf{p}-\mathbf{s}_r\|}\Big[\sin(\pi-\theta_{\mathrm{Rx},r}), \cos(\pi-\theta_{\mathrm{Rx},r})\Big]^{\mathrm{T}}, \ r \neq 0
\end{aligned}$$

and $\partial\tilde{\mathbf{h}}_r^{\mathrm{T}}/\tilde{\mathbf{h}}_r = \mathbf{I}_2$ for $r = 0, \ldots, K$. The rest of terms in $\mathbf{T}$ are zero, and $\mathbf{T}$ is of full row rank.

4.3.4 Localization Bounds

The PEB is obtained by inverting $\mathbf{J}_{\tilde{\boldsymbol{\eta}}}$, summation over the diagonal entries of the 2×2 sub-matrix, and taking the root square as:

$$\mathrm{PEB} = \sqrt{\mathrm{tr}\left\{[\mathbf{J}_{\tilde{\boldsymbol{\eta}}}^{-1}]_{1:2,1:2}\right\}}, \tag{4.3.16}$$

and the rotation error bound (REB) is obtained as:

$$\text{REB} = \sqrt{[\mathbf{J}_{\tilde{\boldsymbol{\eta}}}^{-1}]_{3,3}}, \tag{4.3.17}$$

where the operations $[.]_{1:2,1:2}$ and $[.]_{3,3}$ denote the selection of the first 2×2 sub-matrix and the third diagonal entry of $\mathbf{J}_{\tilde{\boldsymbol{\eta}}}^{-1}$, respectively.

4.4 Position and Orientation Estimation

In this section, we propose a beamspace transceiver model that can be used to implement the proposed signal model in (4.2.4). The main advantage of the proposed beamspace transceiver is reducing the complexity using the sparsity of the mm-wave MIMO channel [Bra13, Bra15]. We assume that the channel dispersion factor for $\phi_{\max} = \max\{|\sin(\theta_{\text{Tx},k})|, |\sin(\theta_{\text{Rx},k})|\}$ and $N_{\max} = \max\{N_t, N_r\}$ defined as

$$\Delta_{\text{ch}} = N_{\max}\text{FB}(d/\lambda_c)\phi_{\max},$$

is not affecting the performance, i.e.,$\Delta_{\text{ch}} \ll (|f/f_c| \ll 0.02$ over the bandwidth) for $-B/2 \leq f \leq B/2$, see [Bra15] for a multi-beam solution for the case that this condition is violated. Then, a two stage algorithm including detection and estimation is proposed for the estimation of AOA/AOD and TOA that are used for position and orientation estimation using the EXIP.

4.4.1 Beamspace Transceiver

Prior to sector beam search to choose the strongest link between the BS and MS, the number of required beams for estimation of the position of the MS is not known. The wideband beamformer $\mathbf{F}[n]$ uses $M_t = N_t$ orthogonal beams in the transmitter to cover the angle span $[0, 2\pi)$. However, this is costly to implement considering the large antenna arrays in the transmitter and receiver. Therefore, we resort to the beamspace transceiver to obtain the dominant beams and design the wideband beamformer only for those beams. Beamspace transceiver exploits the sparsity of the mm-wave MIMO channel $\mathbf{H}[n]$ by

introducing the discrete Fourier transform (DFT) matrix[4]

$$\mathbf{U}_{\mathrm{Tx}} \triangleq \left[\mathbf{u}_{\mathrm{Tx}}(\widetilde{\phi}_{\mathrm{Tx},-L_t}), \ldots, \mathbf{u}_{\mathrm{Tx}}(\widetilde{\phi}_{\mathrm{Tx},L_t})\right],$$
$$\mathbf{u}_{\mathrm{Tx}}(\widetilde{\phi}_{\mathrm{Tx},p}) \triangleq \frac{1}{\sqrt{N_t}}\left[1, \ldots, e^{j2\pi(N_t-1)\widetilde{\phi}_{\mathrm{Tx},p}}\right],$$

where L_t is defined such that p is ranging from $-(N_t-1)/2$ to $(N_t-1)/2$ and from $-N_t/2$ to $N_t/2-1$ for odd and even values of N_t, respectively, and $\widetilde{\phi}_{\mathrm{Tx},p} = p\Delta\widetilde{\phi}_{\mathrm{Tx}}$ for $-L_t \leq p \leq L_t$ denotes the uniform sampling of the principal ϕ period for virtual spatial angles$\Delta\ \widetilde{\phi}_{\mathrm{Tx}} = 1/N_t$, and L_r is defined similarly by replacing the subscript t by r[Say02]. Similarly, $\mathbf{U}_{\mathrm{Rx}}$ is defined by replacing the subscript Tx by Rx and N_t by N_r. The partial virtual representation of the channel with respect to space can be written as [Bra15]

$$\mathbf{H}_{\mathrm{v}}[n] = \mathbf{U}_{\mathrm{Rx}}^{\mathrm{H}}\mathbf{H}[n]\mathbf{U}_{\mathrm{Tx}} = \left[H_{v,i,m}[n]\right]_{i\in\mathcal{I}(N_r),m\in\mathcal{I}(N_t)}, \tag{4.4.1}$$

$$H_{v,i,m}[n] = \sum_{k=0}^{K}\gamma_n(h_k,\tau_k)\varsigma_{N_r}(\phi_{\mathrm{Rx},k,n}-\widetilde{\phi}_{\mathrm{Rx},i})\varsigma_{N_t}(\phi_{\mathrm{Tx},k,n}-\widetilde{\phi}_{\mathrm{Tx},m}), \tag{4.4.2}$$

where $\mathcal{I}(M) = \{l : l = 0, \ldots, M-1\}$ is the set of indices,

$$\varsigma_{N_t}(\phi_{\mathrm{Tx},k,n}-\widetilde{\phi}_{\mathrm{Tx},m}) = \frac{\sin(\pi N_t(\phi_{\mathrm{Tx},k,n}-\widetilde{\phi}_{\mathrm{Tx},m}))}{\sqrt{N_t}\sin(\pi(\phi_{\mathrm{Tx},k,n}-\widetilde{\phi}_{\mathrm{Tx},m}))},$$

and $\phi_{\mathrm{Tx},k,n} = (d/\lambda_n)\sin(\theta_{\mathrm{Tx},k})$ and $\varsigma_{N_r}(\phi_{\mathrm{Rx},k,n}-\widetilde{\phi}_{\mathrm{Rx},i})$ is defined similarly by replacing the subscript Tx by Rx and N_t by N_r. From (4.4.1)-(4.4.2), it is observed that $\mathbf{H}_{\mathrm{v}}[n]$ is approximately sparse in the angular domain, since 'strong' components are generated only in the directions of $\{\theta_{\mathrm{Tx},k}\}$ and $\{\theta_{\mathrm{Rx},k}\}$. However, since the AOAs/AODs are actually continuous, different off-grid based algorithms can be used to reduce the quantization error [Zhu10, Eka11]. This is the main reason that the proposed algorithm includes the detection phase and estimation phase to compensate for quantization error.

For the training phase, we consider sequential transmission of G signals

$$\{\mathbf{x}^{(1)}[n], \ldots, \mathbf{x}^{(G)}[n]\},$$

where $\mathbf{x}^{(g)}[n]$ is an $M_t \times 1$ vector. Consequently, the g-th received signal would be

$$\mathbf{y}^{(g)}[n] = \mathbf{H}[n]\mathbf{F}^{(g)}[n]\mathbf{x}^{(g)}[n] + \mathbf{n}^{(g)}[n]. \tag{4.4.3}$$

[4]This can be achieved approximately using the lens-based analog multi-beamforming proposed in [Bra13].

Replacing $\mathbf{H}[n]$ from (4.4.1) in (4.4.3), vectorization, and stacking $\mathbf{y}^{(g)}[n]$ on top of each other, we obtain

$$\bar{\mathbf{y}}[n] = \boldsymbol{\Omega}[n]\bar{\mathbf{h}}_{\mathrm{v}}[n] + \bar{\mathbf{n}}[n], \tag{4.4.4}$$

where[5]

$$\begin{aligned}
\boldsymbol{\Omega}[n] &= \begin{bmatrix} \boldsymbol{\Omega}^{(1)}[n] \\ \vdots \\ \boldsymbol{\Omega}^{(G)}[n] \end{bmatrix}, \\
\boldsymbol{\Omega}^{(g)}[n] &= (\mathbf{Z}_{\mathrm{Tx}}^{(g)}[n])^{\mathrm{T}} \otimes \mathbf{U}_{\mathrm{Rx}}, \\
\mathbf{Z}_{\mathrm{Tx}}^{(g)}[n] &= \mathbf{U}_{\mathrm{Tx}}^{\mathrm{H}} \mathbf{F}^{(g)}[n] \mathbf{x}^{(g)}[n],
\end{aligned}$$

and $\bar{\mathbf{h}}_{\mathrm{v}}[n]$ denotes the $N_r N_t \times 1$ vector formed by vectorizing $\mathbf{H}_{\mathrm{v}}[n]$ defined in (4.4.1). Due to the sparsity of $\bar{\mathbf{h}}_{\mathrm{v}}[n]$, (4.4.4) is seen to be a sparse reconstruction problem and a compressed sensing (CS) based estimation method can be used for the estimation of $\bar{\mathbf{h}}_{\mathrm{v}}[n]$ with much reduced pilot overhead. Moreover, detecting the columns of DFT matrices $\mathbf{U}_{\mathrm{Tx}}$ and $\mathbf{U}_{\mathrm{Rx}}$ corresponding to non-zero entries of the sparse vector $\bar{\mathbf{h}}_{\mathrm{v}}[n]$ leads to the estimation of AOA/AOD with a quantization error due to the limited grid size that is compensated in the estimation phase. Next, we explain the estimation of channel parameters: $\{\theta_{\mathrm{Tx},k}, \theta_{\mathrm{Rx},k}, \tau_k, \tilde{h}_k\}$ in a two-stage procedure including detection phase and estimation phase.

4.4.2 Sparse Estimation of Channel Parameters

In this section, first we explain the detection of the non-zero entries of the $(K+1)$-sparse vector $\bar{\mathbf{h}}_{\mathrm{v}}[n]$ with *unknown* $K+1$. Then, a method for the estimation of corresponding channel parameters to the detected non-zero entries of $\bar{\mathbf{h}}_{\mathrm{v}}[n]$ is proposed. Since the collection of vectors $\bar{\mathbf{h}}_{\mathrm{v}}[n] \in \mathbb{C}^{N_r N_t \times 1}$, for $i = 1, \ldots, N$, corresponding to the sensing matrix $\boldsymbol{\Omega}[n]$ in (4.4.4) is approximately joint $(K+1)$-sparse, i.e., $|\cup_n \quad \mathrm{supp}(\bar{\mathbf{h}}_{\mathrm{v}}[n])| \leq S$

[5]For the special case when one beam is transmitted in the sequential transmission of G signals (i.e., $M_t = 1$), we obtain

$$\mathbf{Y}[n] = \mathbf{H}[n]\bar{\mathbf{F}}[n]\mathbf{X}[n] + \mathbf{N}[n], \tag{4.4.5}$$

where $\mathbf{Y}[n]$ denotes the $N_r \times G$ received matrix, $\bar{\mathbf{F}}[n]$ is the $N_t \times G$ beamforming matrix with the g-th column $\mathbf{f}^{(g)}[n]$, $\mathbf{X}[n]$ denotes the $G \times G$ diagonal matrix of the input signal with the g-th entry of $x^{(g)}[n]$, and $\mathbf{N}[n]$ denotes the $N_r \times G$ zero mean Gaussian noise matrix. The expression (4.4.5) can be written in the form of sparse reconstruction problem as in (4.4.4) by replacing $\mathbf{H}[n]$ from (4.4.1) in (4.4.3) and vectorization. To accurately estimate $\bar{\mathbf{h}}_{\mathrm{v}}[n]$ from (4.4.4), it is required to have $G \geq N_t$ in conventional algorithms (e.g., minimum mean square error (MMSE)). This leads G to be much larger than the channel coherence time and results in pilot overhead [Alk14].

Algorithm 2 Detection Phase

Input: Recieved signals $\bar{\mathbf{y}}[n]$, sensing matrix $\mathbf{\Omega}[n]$, and the threshold δ.
Output: The detected channel parameters for $k = 0, \ldots, K$.

$$\hat{\theta}^{(0)}_{\mathrm{Tx},k} = \arcsin\left((\lambda_c/d)(n_{\mathrm{Tx},k} - L_t - 1)\Delta\widetilde{\phi}_{\mathrm{Tx}}\right), \tag{4.4.6}$$

$$\hat{\theta}^{(0)}_{\mathrm{Rx},k} = \arcsin\left((\lambda_c/d)(n_{\mathrm{Rx},k} - L_r - 1)\Delta\widetilde{\phi}_{\mathrm{Rx}}\right), \tag{4.4.7}$$

gains in (4.4.19), and $\hat{\tau}^{(0)}_k$ in (4.4.20).

1: For $n = 0, \ldots, N-1$, the residual vectors are set to $\mathbf{r}_{-1}[n] = \mathbf{0}$ and $\mathbf{r}_0[n] = \bar{\mathbf{y}}[n]$, the orthogonalized coefficient vector $\hat{\boldsymbol{\beta}}_n = \mathbf{0}$, $\mathcal{K}_0$ is chosen to be an empty set, and $t = 1$.
2: **while** (4.4.12) **do**
3: Find AOA/AOD pair using (4.4.8).
4: Update AOA/AOD set of indices $\mathcal{K}_t = \mathcal{K}_{t-1} \cup \{\tilde{n}\}$.
5: Orthogonalize the selected basis vector as (4.4.9).
6: Update the residual vector $\mathbf{r}_t[n]$ as (4.4.10).
7: $t = t + 1$.
8: **end while**
9: Find $\mathbf{h}_{\mathrm{v},t}[n]$ for $n = 0, \ldots, N-1$ based on (4.4.13).
10: Find gains using (4.4.19), and TOA using (4.4.20).

with $\mathrm{supp}(\bar{\mathbf{h}}_{\mathrm{v}}[n]) \triangleq \{m \in \{1, \ldots, N_r N_t\} | [|\bar{\mathbf{h}}_{\mathrm{v}}[n]]_m| \geq \gamma_{\mathrm{th}}\}$ where γ_{th} is a threshold on the non-zero entries of $\bar{\mathbf{h}}_{\mathrm{v}}[n]$ and $[\bar{\mathbf{h}}_{\mathrm{v}}[n]]_m$ denotes the m-th entry of $\bar{\mathbf{h}}_{\mathrm{v}}[n]$, one can use the compressed sensing tools for the estimation of channel parameters, e.g., distributed compressed sensing-simultaneous OMP (DCS-SOMP) [Dua05], compressive sampling matched pursuit (CoSOMP) [Dua09], and group sparse compressed sensing (GCS) [Eld10a]. For the special case when the sparsity pattern of the sensing matrix is the same for all the measurement vectors for MMV one can apply group basis pursuit denoising (G-BPDN) or simultaneous OMP (SOMP) [Tro06, Che06, Cot05, Eld10b]. If the FB and the number of antennas are not violating the condition for the small array dispersion, there exists a common sparse support among the N signals $\bar{\mathbf{h}}_v[n]$. Consequently, a DCS-SOMP method can be applied for the detection of channel parameters. In the estimation phase, the channel parameters in the detection phase are refined by numerically determining the maximum likelihood estimation (MLE) using an iterative procedure.

Detection Phase

During the detection phase we focus on getting coarse estimates of the parameters: AOA/AOD, delays, and gains for each path. In the estimation phase, these estimates are

then refined. The following sets of parameters are defined in the detection phase: $\boldsymbol{\omega}_m[n]$ denotes the m-th column of measurement matrix $\boldsymbol{\Omega}[n]$, $\mathbf{r}_t[n]$ is the residual of the measurement $\bar{\mathbf{y}}[n]$ remaining after the first t iterations, $\hat{\boldsymbol{\beta}}_n \in \mathbb{C}^{K+1}$ denotes the orthogonalized coefficient vector with the t-th entry of $\hat{\beta}_n(t)$, and $\mathcal{K}_t$ is the set of indices after the first t iterations. The detection phase in Algorithm 2 summarizes the detection of AOA/AOD, TOA, and the corresponding gains. In the step 1 of the detection phase, the iteration counter is set to $t = 1$, the residual vectors are set to $\mathbf{r}_{t-2}[n] = \mathbf{0}$ and $\mathbf{r}_{t-1}[n] = \bar{\mathbf{y}}[n]$ for $n = 0, \ldots, N-1$, the orthogonalized coefficient vector is set to $\hat{\boldsymbol{\beta}}_n = \mathbf{0}$, the set of indices $\mathcal{K}_{t-1}$ is an empty set, and error threshold δ. In step 3, the AOA/AOD is obtained by choosing the column of $\boldsymbol{\Omega}[n]$ denoted by $\boldsymbol{\omega}_m[n]$ with the strongest correlation with the residual vector $\mathbf{r}_{t-1}[n]$ as

$$\tilde{n}_t = \underset{m=1,\ldots,N_rN_t}{\operatorname{argmax}} \sum_{n=0}^{N-1} \frac{|\boldsymbol{\omega}_m^{\mathrm{H}}[n]\mathbf{r}_{t-1}[n]|}{\|\boldsymbol{\omega}_m[n]\|_2}. \tag{4.4.8}$$

The index of AOD and AOA is obtained from the uniform N_t and N_r points grids as $n_{\mathrm{Tx},t} = \lceil \tilde{n}_t/N_r \rceil$ and $n_{\mathrm{Rx},t} = \mathrm{mod}(\tilde{n}_t - 1, N_r) + 1$, respectively, where $\lceil . \rceil$ is the ceiling operator and $\mathrm{mod}(\tilde{n}_t - 1, N_r)$ denotes the reminder of $\tilde{n}_t - 1$ when divided by N_r. In step 4, the set of indices $\mathcal{K}_t$ is updated from the step 3 corresponding to the column of $\boldsymbol{\Omega}[n]$ with the highest correlation with the residual vector $\mathbf{r}_{t-1}[n]$. In step 5, we orthogonalize the selected basis vector $\boldsymbol{\omega}_{\tilde{n}_t}[n]$ against the orthogonalized set of previously selected dictionary vectors

$$\boldsymbol{\rho}_t[n] = \boldsymbol{\omega}_{\tilde{n}_t}[n] - \sum_{\tilde{t}=0}^{t-1} \frac{\boldsymbol{\omega}_{\tilde{n}_t}^{\mathrm{H}}[n]\boldsymbol{\rho}_{\tilde{t}}[n]}{\|\boldsymbol{\rho}_{\tilde{t}}[n]\|_2} \boldsymbol{\rho}_{\tilde{t}}[n]. \tag{4.4.9}$$

In step 6, the residual vector $\mathbf{r}_t[n]$ is updated by subtracting the effect of chosen columns from $\mathbf{r}_{t-1}[n]$ as:

$$\mathbf{r}_t[n] = \mathbf{r}_{t-1}[n] - \hat{\beta}_n(t)\boldsymbol{\rho}_t[n], \tag{4.4.10}$$

where

$$\hat{\beta}_n(t) = \frac{\boldsymbol{\rho}_t^{\mathrm{H}}[n]\mathbf{r}_{t-1}[n]}{\|\boldsymbol{\rho}_t[n]\|_2^2}. \tag{4.4.11}$$

In step 7, the iteration counter is updated and the detection phase continues as long as:

$$\sum_{n=0}^{N-1} \|\mathbf{r}_{t-1}[n] - \mathbf{r}_{t-2}[n]\|_2^2 > \delta \ . \tag{4.4.12}$$

In step 9, the mutilated version of the sparse vector $\bar{\mathbf{h}}_{\mathrm{v}}[n]$ assosiated with $\mathcal{K}_t$,

$$\mathbf{h}_{\mathrm{v},t}[n] = \Big[h_{\mathrm{v},1}[n], \ldots, h_{\mathrm{v},K+1}[n]\Big]^{\mathrm{T}},$$

is recovered using the QR factorization of the mutilated basis $\mathbf{\Omega}_{\mathcal{K}_t}[n] = [\boldsymbol{\omega}_{\tilde{n}_1}[n], \ldots, \boldsymbol{\omega}_{\tilde{n}_{K+1}}[n]]$ as $\mathbf{\Omega}_{\mathcal{K}_t}[n] = \mathbf{\Upsilon}[n]\mathbf{R}[n]$ where $\mathbf{\Upsilon}[n] = [\boldsymbol{\rho}_1[n], \ldots, \boldsymbol{\rho}_{K+1}[n]]$. Since

$$\mathbf{\Omega}_{\mathcal{K}_t}[n]\mathbf{h}_{\mathrm{v},t}[n] = \mathbf{\Upsilon}[n]\mathbf{R}[n]\mathbf{h}_{\mathrm{v},t}[n] = \mathbf{\Upsilon}[n]\hat{\boldsymbol{\beta}}_n,$$

we obtain

$$\mathbf{h}_{\mathrm{v},t}[n] = \mathbf{R}^{-1}[n]\hat{\boldsymbol{\beta}}_n. \tag{4.4.13}$$

In step 10, after detecting $\mathbf{h}_{\mathrm{v},t}[n]$ for $n = 0, \ldots, N-1$, the TOA can be obtained using the following model for the detected values $\mathbf{h}_{\mathrm{v},t}[n]$ at different subcarriers.

$$\mathbf{H}_{\mathrm{v},t} = \mathbf{\Gamma}(\boldsymbol{\tau})\mathbf{H}_{d,x} + \mathbf{V}, \tag{4.4.14}$$

where $\mathbf{H}_{\mathrm{v},t} = \mathrm{diag}\{\mathbf{h}_{\mathrm{v},t}^{(0)}, \ldots, \mathbf{h}_{\mathrm{v},t}^{(K)}\}$ denotes[6] an $N(K+1) \times (K+1)$ block diagonal matrix with $\mathbf{h}_{\mathrm{v},t}^{(k)} = [h_{\mathrm{v},t}^{(k)}[0], \ldots, h_{\mathrm{v},t}^{(k)}[N-1]]^{\mathrm{T}}$ where $h_{\mathrm{v},t}^{(k)}[n]$ is the n-th element of $\mathbf{h}_{\mathrm{v},t}^{(k)}$ for $n = 0, \ldots, N-1$, $\mathbf{H}_{d,x} = \mathrm{diag}\{\tilde{h}_0\mathbf{x}_{\mathrm{TR}}(\boldsymbol{\theta}_0), \ldots, \tilde{h}_K\mathbf{x}_{\mathrm{TR}}(\boldsymbol{\theta}_K)\}$ where $\mathbf{x}_{\mathrm{TR}}(\boldsymbol{\theta}_k)$ denotes an $N \times 1$ vector with the n-th entry $x_{\mathrm{TR},n}(\boldsymbol{\theta}_k)$ defined as

$$x_{\mathrm{TR},n}(\boldsymbol{\theta}_k) \triangleq \mathbf{u}_{\mathrm{Rx}}^{\mathrm{H}}(\widetilde{\phi}_{\mathrm{Rx},n_{\mathrm{Rx},t}-L_r-1})\mathbf{a}_{\mathrm{Rx},n}(\theta_{\mathrm{Rx},k})\mathbf{a}_{\mathrm{Tx},n}^{\mathrm{H}}(\theta_{\mathrm{Tx},k})\mathbf{u}_{\mathrm{Tx}}(\widetilde{\phi}_{\mathrm{Tx},n_{\mathrm{Tx},t}-L_t-1}). \tag{4.4.15}$$

The expression in (4.4.15) is simplified as

$$|x_{\mathrm{TR},n}(\boldsymbol{\theta}_k)| = \varsigma_{N_t}(\phi_{\mathrm{Tx},k,n} - \widetilde{\phi}_{\mathrm{Tx},n_{\mathrm{Tx},k}-L_t-1})\varsigma_{N_r}(\phi_{\mathrm{Rx},k,n} - \widetilde{\phi}_{\mathrm{Rx},n_{\mathrm{Rx},k}-L_r-1}),$$

where $\mathbf{V}$ denotes the noise matrix that is formed identically to $\mathbf{H}_{\mathrm{v},t}$, $\boldsymbol{\tau} = [\tau_0, \ldots, \tau_K]^{\mathrm{T}}$, and $\mathbf{\Gamma}(\boldsymbol{\tau}) = \mathrm{diag}\{\mathbf{\Gamma}(\tau_0), \ldots, \mathbf{\Gamma}(\tau_K)\}$ where

$$\mathbf{\Gamma}(\tau_k) = \mathrm{diag}\{1, \ldots, e^{-j2\pi(N-1)\tau_k/(NT_s)}\}.$$

Assuming that the channel dispersion factor due to beam squint is not affecting the

[6]The proposed matching pursuit algorithm is rank-blind and it is not assumed that the number of the detected paths (i.e., $K+1$) is known [Dav12]. Since $K+1$ is unknown, we use the change of residual fitting error in (4.4.12) at each iteration to thresholds based on the noise power to determine the termination of the algorithm.

performance, it is observed that $x_{\mathrm{TR},n}(\boldsymbol{\theta}_k) \approx x_{\mathrm{TR}}(\boldsymbol{\theta}_k)$ and (4.4.14) is simplified as:

$$\mathbf{H}_{\mathrm{v},t} = \widetilde{\boldsymbol{\Gamma}}(\boldsymbol{\tau})\widetilde{\mathbf{H}}_{d,x} + \mathbf{V}, \tag{4.4.16}$$

where $\widetilde{\boldsymbol{\Gamma}}(\boldsymbol{\tau}) = \mathrm{diag}\{\boldsymbol{\gamma}(\tau_0), \ldots, \boldsymbol{\gamma}(\tau_K)\}$ in which $\boldsymbol{\gamma}(\tau_k) = [1, \ldots, e^{-j2\pi(N-1)\tau_k/(NT_s)}]^{\mathrm{T}}$ and $\widetilde{\mathbf{H}}_{d,x} = \mathrm{diag}\{\widetilde{\varsigma}_0, \ldots, \widetilde{\varsigma}_K\}$ where $\widetilde{\varsigma}_k = \tilde{h}_k x_{\mathrm{TR}}(\boldsymbol{\theta}_k)$. The MLE solution for (4.4.16) can be found as

$$\hat{\boldsymbol{\tau}}, \hat{\widetilde{\mathbf{H}}}_{d,x} = \underset{\boldsymbol{\tau}, \widetilde{\mathbf{H}}_{d,x}}{\mathrm{argmin}} \ \|\mathbf{H}_{\mathrm{v},t} - \widetilde{\boldsymbol{\Gamma}}(\boldsymbol{\tau})\widetilde{\mathbf{H}}_{d,x}\|_{\mathrm{F}}^2. \tag{4.4.17}$$

The expression (4.4.17) is simplified as

$$\{\hat{\tau}_k, \hat{\widetilde{\varsigma}}_k\} = \underset{\{\tau_k\},\{\widetilde{\varsigma}_k\}}{\mathrm{argmin}} \ \sum_{k=0}^{K} \left(N|\widetilde{\varsigma}_k|^2 - 2\Re\left\{ \widetilde{\varsigma}_k^* \boldsymbol{\gamma}^{\mathrm{H}}(\tau_k)\mathbf{h}_{\mathrm{v},t}^{(k)} \right\} \right). \tag{4.4.18}$$

Taking the derivative of (4.4.18) with respect to $\widetilde{\varsigma}_k^*$ for $k = 0, \ldots, K$ we obtain

$$\hat{\widetilde{\varsigma}}_k = \frac{1}{N}\boldsymbol{\gamma}^{\mathrm{H}}(\tau_k)\mathbf{h}_{\mathrm{v},t}^{(k)}. \tag{4.4.19}$$

Replacing (4.4.19) in (4.4.18), $\hat{\tau}_k$ for $k = 0, \ldots, K$ is obtained as

$$\hat{\tau}_k = \underset{\tau_k}{\mathrm{argmax}} \ |\boldsymbol{\gamma}^{\mathrm{H}}(\tau_k)\mathbf{h}_{\mathrm{v},t}^{(k)}|^2. \tag{4.4.20}$$

Once $\hat{\tau}_k$ is obtained from (4.4.20), $\hat{\widetilde{\varsigma}}_k$ is obtained by replacing $\hat{\tau}_k$ in (4.4.19). It is worth mentioning that the term $x_{\mathrm{TR}}(\boldsymbol{\theta}_k)$ in the expression of $\widetilde{\varsigma}_k$ is ideally equal to one. However, due to the limited grid size for the detection of continuous AOAs/AODs, $x_{\mathrm{TR}}(\boldsymbol{\theta}_k)$ leads to some errors in the detection of channel coefficients. This effect will be compensated in the estimation phase. Note that (4.4.20), require a one-dimensional search and the maximum can be obtained by solving the function with a sufficiently fine grid of points. Using the fact that all arriving paths fall into the interval T_{CP}, we choose a sufficiently fine grid of points with the time resolution as a multiple, δ_τ, of the baseband sampling T/N to obtain $K_\tau = \delta_\tau N T_{\mathrm{CP}}/T$ grid of points

$$\tau_k \in \left\{ \frac{T}{\delta_\tau N}, \frac{2T}{\delta_\tau N}, \ldots, T_{\mathrm{CP}} \right\}.$$

Consequently, there is no need to apply more complex algorithms for multi-dimensional search, e.g., iterative quadratic maximum likelihood (IQML) algorithm for ULAs [Bre86].

Estimation Phase

After the detection phase, channel parameters are estimated in an iterative procedure that is initialized by the detected values. Given that we have initial estimates of all parameters, one can perform an iterative ascent algorithm directly on the log likelihood function associated with the model (4.4.4). However, this requires a multi-dimensional minimization and computationally complex solutions. A more practical approach would be to use the EM algorithm with the incomplete data space in (4.4.4) as the superposition of $K+1$ complete data space $\bar{\mathbf{y}}_k[n]$ as:

$$\bar{\mathbf{y}}[n] = \sum_{k=0}^{K} \underbrace{\boldsymbol{\Omega}[n]\bar{\mathbf{h}}_{\mathrm{v},k}[n] + \bar{\mathbf{n}}_k[n]}_{\bar{\mathbf{y}}_k[n]}, \tag{4.4.21}$$

where $\bar{\mathbf{h}}_{\mathrm{v},k}[n]$ denotes the vectorized form of $\mathbf{H}_{\mathrm{v},k}[n]$ defined as $\mathbf{U}_{\mathrm{Rx}}^{\mathrm{H}}\mathbf{H}_k[n]\mathbf{U}_{\mathrm{Tx}}$ with $\mathbf{H}_k[n]$ being the corresponding term for the k-th path in the channel frequency response $\mathbf{H}[n]$ in (4.2.1). In (4.4.21), it is assumed that $\bar{\mathbf{n}}[n] = \sum_{k=0}^{K} \bar{\mathbf{n}}_k[n]$. This requires the noise processes $\bar{\mathbf{n}}_k[n]$ to be independent of each other and have the total power spectral density of $N_0/2$. Writing (4.4.21) for all the subcarriers results:

$$\bar{\mathbf{y}} = \sum_{k=0}^{K} \underbrace{\bar{\boldsymbol{\Omega}}\bar{\mathbf{h}}_{\mathrm{v},k} + \bar{\mathbf{n}}_k}_{\bar{\mathbf{y}}_k}, \tag{4.4.22}$$

where

$$\begin{aligned}
\bar{\boldsymbol{\Omega}} &= \mathrm{diag}\left\{\boldsymbol{\Omega}[0], \ldots, \boldsymbol{\Omega}[N-1]\right\}, \\
\bar{\mathbf{y}} &= \left[\bar{\mathbf{y}}^{\mathrm{T}}[0], \ldots, \bar{\mathbf{y}}^{\mathrm{T}}[N-1]\right]^{\mathrm{T}}, \\
\bar{\mathbf{h}}_{\mathrm{v},k} &= \left[\bar{\mathbf{h}}_{\mathrm{v},k}^{\mathrm{T}}[0], \ldots, \bar{\mathbf{h}}_{\mathrm{v},k}^{\mathrm{T}}[N-1]\right]^{\mathrm{T}}, \\
\bar{\mathbf{n}}_k &= \left[\bar{\mathbf{n}}_k^{\mathrm{T}}[0], \ldots, \bar{\mathbf{n}}_k^{\mathrm{T}}[N-1]\right]^{\mathrm{T}}.
\end{aligned}$$

In the $(m+1)$-th iteration, the expectation and maximization steps are performed as follows.

Expectation

In the expectation step, we compute the conditional expectation of the hidden data space $\bar{\mathbf{y}}_k$ log-likelihood function based on the previous estimation $\hat{\boldsymbol{\eta}}^{(m)}$ and the incomplete data

Algorithm 3 Estimation Phase

Input: The detected channel parameters $\hat{\boldsymbol{\eta}}^{(0)}$.
Output: The estimated channel parameters $\hat{\boldsymbol{\eta}}$.

1: **Repeat:**
(a) **Expectation:** Determine $Q(\boldsymbol{\eta}_k|\hat{\boldsymbol{\eta}}^{(m)})$ based on (4.4.24).
(b) **Maximization:** Maximize $Q(\boldsymbol{\eta}_k|\hat{\boldsymbol{\eta}}^{(m)})$ with respect to $\boldsymbol{\eta}_k$ sequentially using Gauss-Seidel-type iterations to obtain $\hat{\theta}_{\mathrm{Tx},k}^{(m+1)}$, $\hat{\theta}_{\mathrm{Rx},k}^{(m+1)}$, $\hat{\tau}_k^{(m+1)}$, and $\hat{\tilde{h}}_k^{(m+1)}$, respectively.

2: **Until:** $\hat{\boldsymbol{\eta}}$ converges.

space $\bar{\mathbf{y}}$ as:

$$Q(\boldsymbol{\eta}_k|\hat{\boldsymbol{\eta}}^{(m)}) \triangleq \mathbb{E}\left[\ln f(\bar{\mathbf{y}}_k|\boldsymbol{\eta}_k, \{\hat{\boldsymbol{\eta}}_l^{(m)}\}_{l\neq k})|\bar{\mathbf{y}}, \hat{\boldsymbol{\eta}}^{(m)}\right]. \tag{4.4.23}$$

For $k = 0, \ldots, K$, we obtain

$$Q(\boldsymbol{\eta}_k|\hat{\boldsymbol{\eta}}^{(m)}) \propto -\underbrace{\|\hat{\mathbf{z}}_k^{(m)} - \bar{\boldsymbol{\mu}}(\boldsymbol{\eta}_k)\|^2}_{\widetilde{Q}(\boldsymbol{\eta}_k|\hat{\boldsymbol{\eta}}^{(m)})}, \tag{4.4.24}$$

where $\bar{\boldsymbol{\mu}}(\boldsymbol{\eta}_k) = \bar{\boldsymbol{\Omega}}\bar{\mathbf{h}}_{\mathrm{v},k}$, and

$$\hat{\mathbf{z}}_k^{(m)} = \bar{\mathbf{y}} - \sum_{l\neq k, l=0}^{K} \bar{\boldsymbol{\mu}}(\hat{\boldsymbol{\eta}}_l^{(m)}). \tag{4.4.25}$$

For the initialization of the iterative procedure, we use the AOA/AOD, TOA, and channel coefficients from the detection phase using $\hat{\theta}_{\mathrm{Tx},k}^{(0)}$ and $\hat{\theta}_{\mathrm{Rx},k}^{(0)}$ obtained from (4.4.6) and (4.4.7), respectively, $\hat{\tau}_k^{(0)}$ computed from (4.4.20), and the corresponding coefficient obtained from (4.4.19).

Maximization

In the maximization step, the goal is to find $\boldsymbol{\eta}_k$ such that (4.4.24) is maximized or $\widetilde{Q}(\boldsymbol{\eta}_k|\hat{\boldsymbol{\eta}}^{(m)})$ is minimized. In other words, we have

$$\hat{\boldsymbol{\eta}}_k^{(m+1)} = \underset{\boldsymbol{\eta}_k}{\operatorname{argmin}}\ \widetilde{Q}(\boldsymbol{\eta}_k|\hat{\boldsymbol{\eta}}^{(m)}). \tag{4.4.26}$$

Solving (4.4.26) directly for $\boldsymbol{\eta}_k$ is analytically complex due to the fact that it is hard to compute the gradient and Hessian with respect to $\boldsymbol{\eta}_k$. Instead, we update the parameters $\hat{\theta}_{\mathrm{Tx},k}^{(m+1)}$, $\hat{\theta}_{\mathrm{Rx},k}^{(m+1)}$, $\hat{\tau}_k^{(m+1)}$, and $\hat{\tilde{h}}_k^{(m+1)}$ sequentially using Gauss-Seidel-type iterations [Ort66]. The estimation phase in Algorithm 3 summarizes the procedure of estimating channel parameters.

4.4.3 Conversion to Position and Rotation Angle

Conversion of the estimated channel parameters to position and rotation angle in LOS and NLOS is proposed in this section.

LOS

For the case of LOS, there exists an invertible mapping $\boldsymbol{\varpi}_{\text{los}}(.)$ such that

$$\boldsymbol{\eta}_0 = \boldsymbol{\varpi}_{\text{los}}(\tilde{\boldsymbol{\eta}}_0) \in \mathbb{D}_{\boldsymbol{\eta}_0}, \quad \forall \tilde{\boldsymbol{\eta}}_0 \in \mathbb{D}_{\tilde{\boldsymbol{\eta}}_0} \tag{4.4.27}$$

where $\mathbb{D}_{\boldsymbol{\eta}_0}$ and $\mathbb{D}_{\tilde{\boldsymbol{\eta}}_0}$ represent the domains of the generic parameters $\boldsymbol{\eta}_0$ and $\tilde{\boldsymbol{\eta}}_0$, respectively. The classical invariance principle of estimation theory could be invoked to prove the equivalence of minimizing the maximum likelihood (ML) criterion in terms of either $\boldsymbol{\eta}_0$ or $\tilde{\boldsymbol{\eta}}_0$ [Zac81]. Consequently, the estimated values of $\hat{\mathbf{p}}$ and $\hat{\alpha}$ are obtained directly from

$$\hat{\mathbf{p}} = \mathbf{q} + \hat{d}_0[\cos(\hat{\theta}_{\text{Tx},0}), \sin(\hat{\theta}_{\text{Tx},0})]^{\text{T}}, \tag{4.4.28}$$

and $\hat{\alpha} = \pi + \hat{\theta}_{\text{Tx},0} - \hat{\theta}_{\text{Rx},0}$ where $\hat{d}_0 = c\hat{\tau}_0$ denotes the distance between the MS and the BS in the LOS.

NLOS

For the case of NLOS with K clusters and a LOS path, the EXIP could be used assuming there exists a function $\boldsymbol{\varpi}_{\text{nlos}}(.)$ satisfying

$$\boldsymbol{\eta} = \boldsymbol{\varpi}_{\text{nlos}}(\tilde{\boldsymbol{\eta}}) \in \mathbb{D}_{\boldsymbol{\eta}}, \quad \forall \tilde{\boldsymbol{\eta}} \in \mathbb{D}_{\tilde{\boldsymbol{\eta}}} \tag{4.4.29}$$

where $\mathbb{D}_{\boldsymbol{\eta}}$ and $\mathbb{D}_{\tilde{\boldsymbol{\eta}}}$ represent the domains of the generic parameters $\boldsymbol{\eta}$ and $\tilde{\boldsymbol{\eta}}$, respectively. Consequently, for sufficiently large number of data samples N the estimated $\hat{\tilde{\boldsymbol{\eta}}}$ obtained as

$$\hat{\tilde{\boldsymbol{\eta}}} = \underset{\tilde{\boldsymbol{\eta}}}{\text{argmin}} \ \left(\hat{\boldsymbol{\eta}} - \boldsymbol{\varpi}_{\text{nlos}}(\tilde{\boldsymbol{\eta}})\right)^{\text{T}} \mathbf{J}_{\boldsymbol{\eta}} \left(\hat{\boldsymbol{\eta}} - \boldsymbol{\varpi}_{\text{nlos}}(\tilde{\boldsymbol{\eta}})\right), \tag{4.4.30}$$

is asymptotically equivalent to the estimate of the transformed parameter $\tilde{\boldsymbol{\eta}}$ [Sto89, Swi02]. The Levenberg-Marquardt algorithm (LMA), also known as the damped least-squares (DLS) method, can be used to solve (4.4.30) [Lev44, Mar63]. Unlike Gauss-Newton algorithm (GNA), LMA finds a solution even if it starts very far off the optimal solution. To initialize $\tilde{\boldsymbol{\eta}}$ in (4.4.30) using the LMA algorithm, the estimated $\hat{\mathbf{p}}$,

$\hat{\alpha}$, $\hat{h}_k$ from the LOS and the NLOS links could be used, and $\hat{\mathbf{s}}_k$ can be obtained using $\tan(\pi - (\hat{\theta}_{\mathrm{Rx},k} + \hat{\alpha})) = (\hat{p}_y - s_{1,y})/(\hat{p}_x - s_{1,x})$ and $\tan(\hat{\theta}_{\mathrm{Tx},k}) = (s_{1,y} - q_y)/(s_{1,x} - q_x)$ with $\hat{\theta}_{\mathrm{Rx},k}$, $\hat{\theta}_{\mathrm{Tx},k}$, $\hat{\alpha}$, and $\hat{\mathbf{p}}$ obtained from the LOS and NLOS links.

4.5 Simulation Results

In this section, we present simulation results to demonstrate the performance of the proposed bound and the estimator with respect to different parameters.

4.5.1 Simulation Setup

Performance of the Bounds

Performance is measured in terms of the PEB expressed in meters and the REB expressed in radians in (4.3.16) and (4.3.17), respectively. We compute the PEB for different locations of the MS for the BS located at a fixed position. The comparison between PEB for the case of LOS and in the presence of the clusters is provided. Finally, the localization performance in the presence of clusters (i.e., NLOS) is compared with the performance when the LOS is blocked (i.e., OLOS). To analyze the performance of the localization bounds, we set $f_c = 60$ GHz, $B = 600$ MHz, and $N_0 = 2$W/GHz. The inter-element spacing is assumed to be $d = \lambda_c/2$. The number of transmit and receive antennas for the non-polarized ULAs are set to $N_t = 64$ and $N_r = 8$.

Comparison between the Bounds and the Estimator

We set $f_c = 60$ GHz, $B = 100$ MHz, $c = 0.3$ m/ns, and $N = 20$. The geometry-based statistical path loss [Li14] is used with path length d_k and the number of reflectors in each path is set to one, i.e., it is assumed that there is one cluster in each NLOS path. The number of transmit and receive antennas are set to $N_t = 64$ and $N_r = 64$, respectively. The BS is located at $\mathbf{q}\,[\mathrm{m}] = [0, 0]^{\mathrm{T}}$ and the MS is located at $\mathbf{p}\,[\mathrm{m}] = [4, 0]^{\mathrm{T}}$ with the rotation angle $\alpha = 0.1$ rad. We consider the sequential transmission of $G = 30$ signals $x^{(g)}[n]$. In order to guarantee the good performance for sparse signal recovery based on the compressed sensing theory [Eld12], we choose the m-th entry of $[\mathbf{F}_{\mathrm{BB}}^{(g)}[n]\mathbf{x}^{(g)}[n]]_m$ to be of the form of $e^{j\theta_{m,n,g}}$ where $\theta_{m,n,g}$ follows the i.i.d. uniform distribution $\mathcal{U}[0, 2\pi)$. Moreover, $[\mathbf{F}_{\mathrm{RF}}^{(g)}]_{m_1,m_2} = e^{j\theta_{m_1,m_2,g}}$ where $\theta_{m_1,m_2,g}$ is obtained from the i.i.d. uniform distribution $\mathcal{U}[0, 2\pi)$. The values of the CRB for TOA_k, AOA_k, and AOD_k are defined similar to PEB

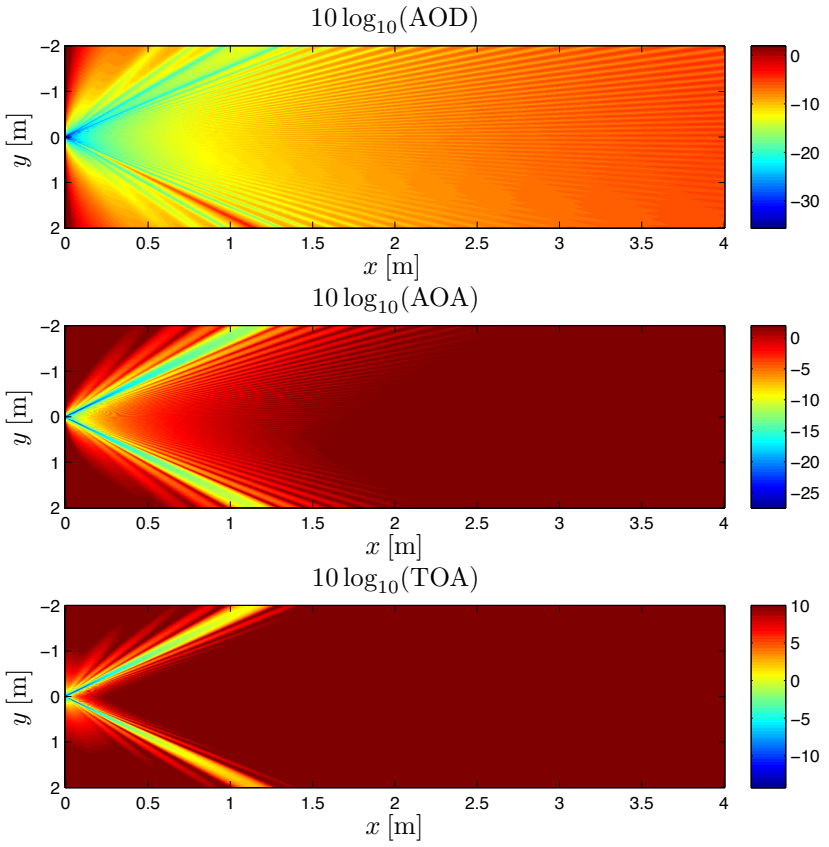

Figure 4.1: Performances of the AOD, AOA, and TOA in the LOS for different locations of the MS and the BS located at $\mathbf{q}$ [m] $= [0, 0]^{\mathrm{T}}$, for a scenario with 3 beams in the directions $[\pm\pi/3, \pi/3 + 0.01]$.

and REB in (4.3.16) and (4.3.17), respectively, by inverting the FIM, choosing the corresponding diagonal entries and taking the root square. Finally, the received signal-to-noise ratio (SNR) is defined as SNR $\triangleq \mathbb{E}[\|\bar{\widetilde{\mathbf{\Omega}}}\bar{\mathbf{h}}\|_2^2]/\mathbb{E}[\|\bar{\mathbf{n}}\|_2^2]$ where $\bar{\mathbf{h}} = [\bar{\mathbf{h}}^{\mathrm{T}}[0], \ldots, \bar{\mathbf{h}}^{\mathrm{T}}[N-1]]^{\mathrm{T}}$ with $\bar{\mathbf{h}}[n]$ denoting the column-wise vector form of $\mathbf{H}[n]$, and $\bar{\widetilde{\mathbf{\Omega}}} = \mathrm{diag}\{\widetilde{\mathbf{\Omega}}[0], \ldots, \widetilde{\mathbf{\Omega}}[N-1]\}$ with

$$\widetilde{\mathbf{\Omega}}[n] = \begin{bmatrix} \widetilde{\mathbf{\Omega}}^{(1)}[n] \\ \vdots \\ \widetilde{\mathbf{\Omega}}^{(G)}[n] \end{bmatrix},$$

and $\widetilde{\mathbf{\Omega}}^{(g)}[n] = (\mathbf{F}^{(g)}[n]\mathbf{x}^{(g)}[n])^{\mathrm{T}} \otimes \mathbf{I}_{N_r}$.

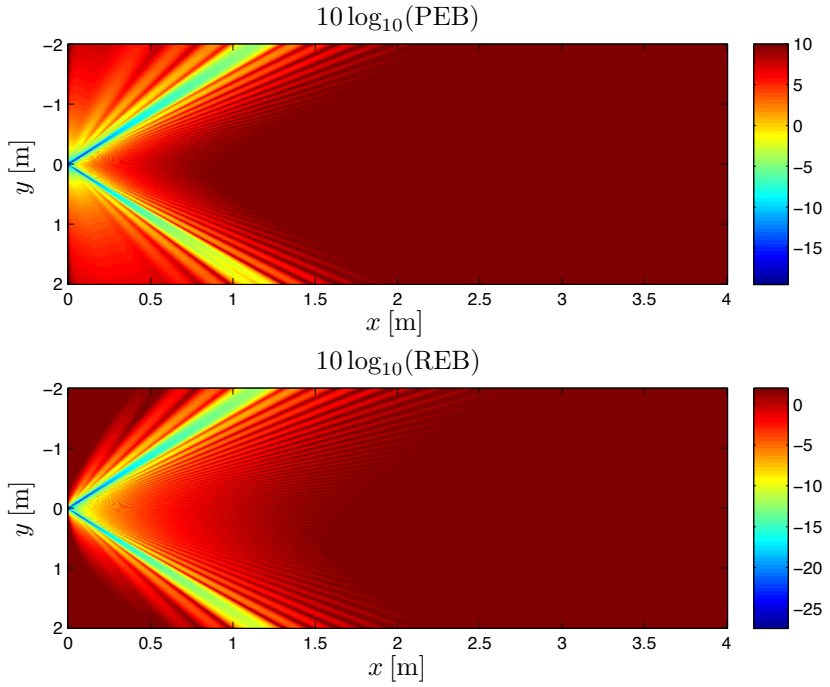

Figure 4.2: Performances of the PEB (top) and REB (bottom) in the LOS for different locations of the MS and the BS located at $\mathbf{q}\,[\mathrm{m}] = [0, 0]^{\mathrm{T}}$, for a scenario with 3 beams in the directions $[\pm\pi/3, \pi/3 + 0.01]$.

4.5.2 Results and Discussion

Performance in LOS

Fig. 4.1-4.2 show the AOD, AOA, and TOA in the LOS and the resulting values of the PEB and REB for different locations of the MS. It is observed that in the directions of the beams, the AOA/AOD and TOA together with the PEB and REB have the lowest values, while in the other locations the values are much higher. More specifically, for a distance of $\|\mathbf{q} - \mathbf{p}\| = 0.5\,\mathrm{m}$, the PEB in the directions of the beams is approximately 5 cm while the highest PEB is approximately 3 m. The REB values range from 0.01 rad in the direction $\pi/3$, over 0.02 rad in the direction $-\pi/3$, up to 0.2 rad outside any of the beams. We observe the impact of the extra beam in the direction of $\pi/3$ that provides increased SNR, leading to better TOA information (in the Fisher sense) and good information regarding AOA/AOD that leads to reducing the PEB and REB. On the other hand, the single beam that is transmitted in the direction of $-\pi/3$ provides good TOA and AOA information but leads to poor AOD information (except for MS locations close to the BS). Hence, the PEB and REB in the direction of $-\pi/3$ are higher.

Fig. 4.3 shows the evolution of the root-mean-square error (RMSE) of TOA and AOA/AOD for 1000 Monte Carlo realizations in the LOS conditions. The corresponding bounds are shown by the red lines with the same markers as the corresponding values of the RMSE for a given received SNR. It is observed that after a few iterations of Algorithm 2 the RMSE of TOA and AOA/AOD converges to the corresponding bounds even for SNR $= -20$ dB, -10 dB, 0 dB. The performance of the RMSE of the estimation algorithm for 1000 Monte Carlo realizations with respect to different values of the received SNR is shown in Fig. 4.4–4.5. It is observed that after SNR ≈ -20 dB the RMSE of the TOA, and AOA/AOD converge to their corresponding bounds (red dashed lines). Moreover, the proposed algorithm performs well even for very low values of the received SNR which is the typical case at mm-wave systems before beamforming.

Performance in NLOS and OLOS

In the presence of LOS, the effect of NLOS paths on position estimation is shown in Fig. 4.6. It can be observed that adding the clusters sequentially reduces the position information (in the Fisher sense) that leads to higher values of the PEB. Moreover, sufficiently good localization accuracy can be obtained even at low SNR.

Fig. 4.7 compares the PEB for the LOS in presence of clusters and OLOS conditions. It can be observed that the PEB for the OLOS is much higher than the LOS condition (around 35 dB at SNR ≈ 1 dB). Moreover, adding the clusters make the performance worse due to reducing the position information in the Fisher sense. Fig. 4.8 shows the evolution of the RMSE of TOA and AOA/AOD for 1000 Monte Carlo realizations in the presence of a cluster located at $\mathbf{s}_k$ [m] $= [1.5, 0.4]^{\mathrm{T}}$. It can be observed that the RMSE of TOA and AOA/AOD converges after a few iterations to the corresponding bounds (shown by the red lines with the same markers as the corresponding values of the RMSE for a given received SNR) for the LOS (left column) and NLOS (right column) paths even at very low received SNR. The performance of the RMSE of the estimation algorithm for 1000 Monte Carlo realizations with respect to the received SNR is shown in Fig. 4.9-4.10. It is observed that after a few iterations the RMSE of TOA, AOA/AOD, rotation angle, and position converge to the corresponding bounds (shown by the red lines) even for very low values of the received SNR. Particularly, at SNR ≈ -10 dB the TOA, AOA/AOD, rotation angle, and position approach the corresponding bounds.

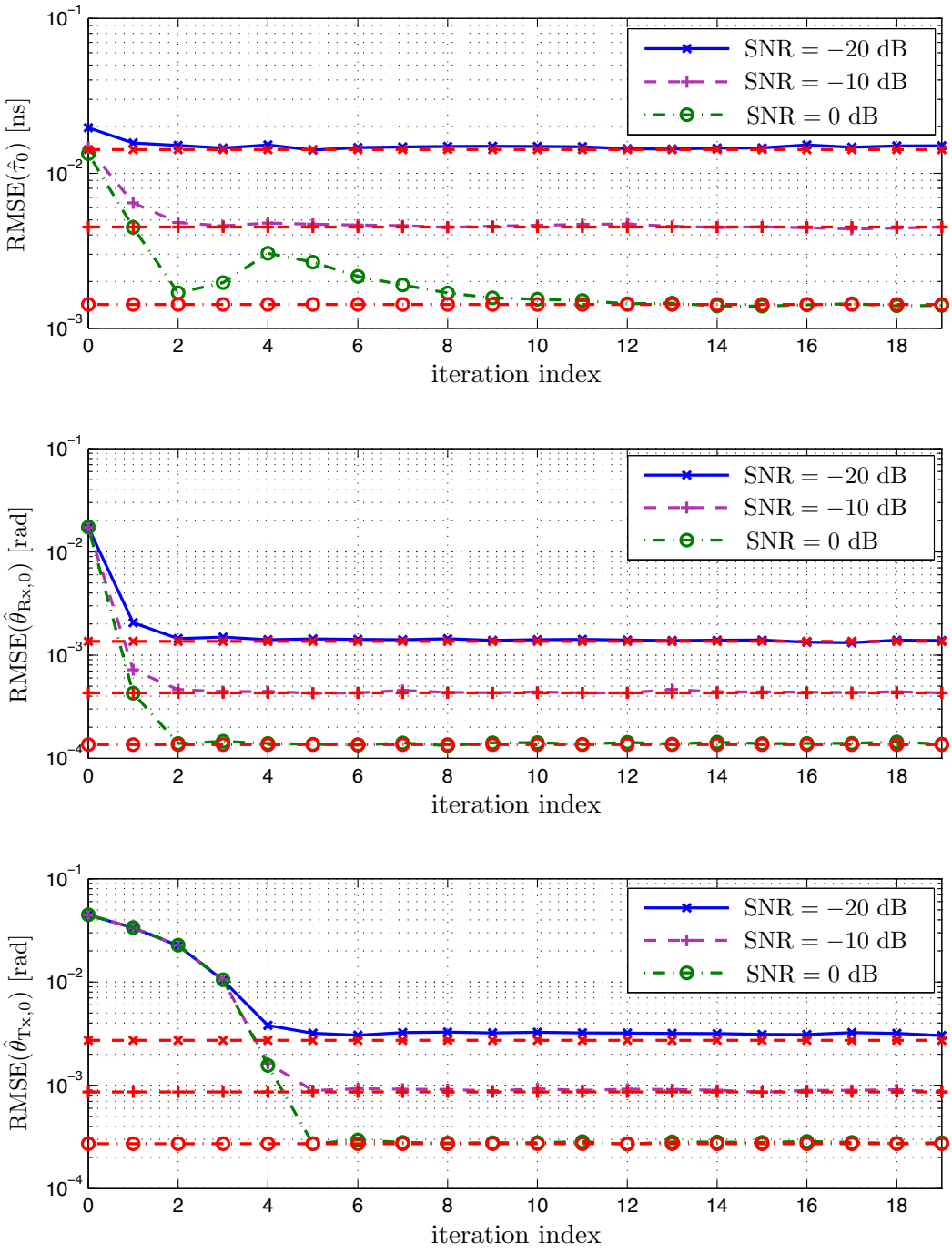

Figure 4.3: The evolution of RMSE of TOA and AOA/AOD for the LOS for SNR $= -20\,\mathrm{dB}, -10\,\mathrm{dB}, 0\,\mathrm{dB}$.

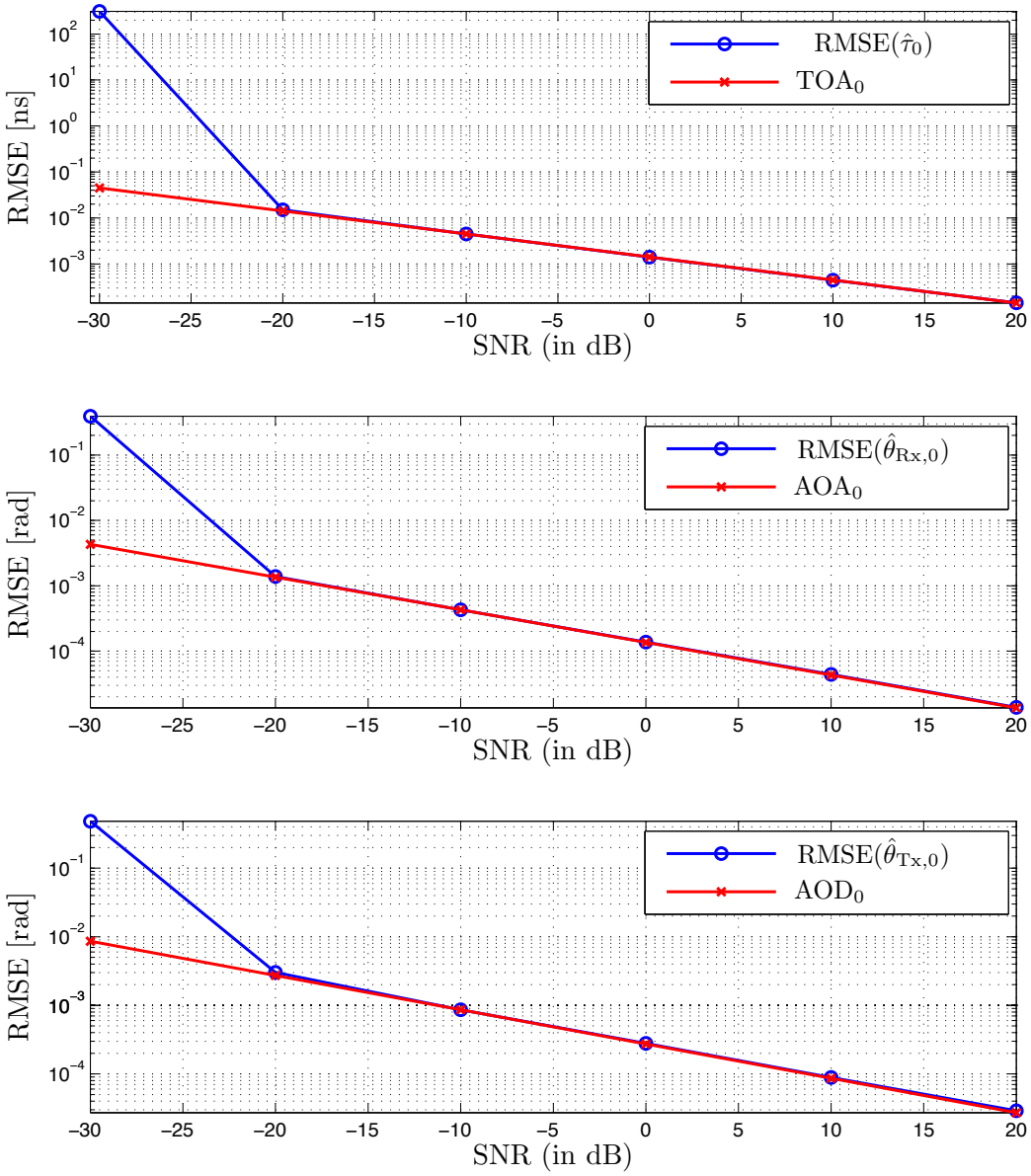

Figure 4.4: RMSE in dB scale plotted against received SNR for TOA and AOA/AOD in the LOS conditions.

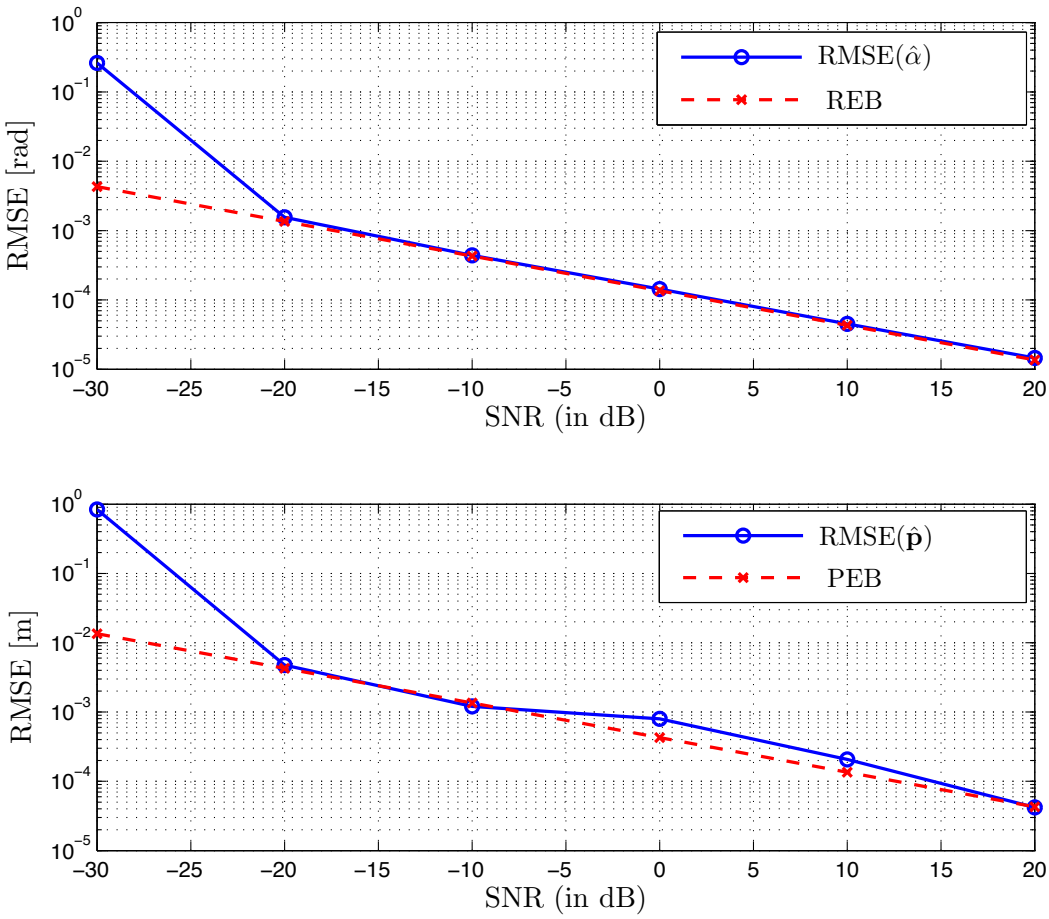

Figure 4.5: RMSE in dB scale plotted against received SNR for rotation angle (top) and position (bottom) in the LOS.

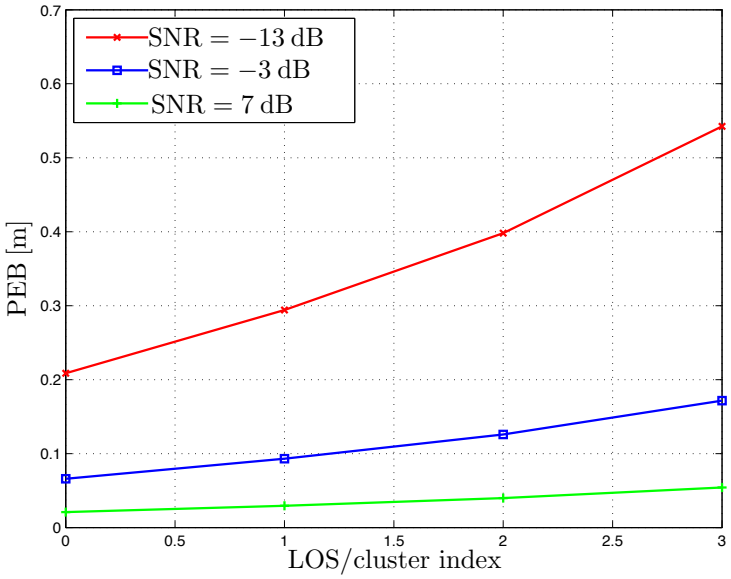

Figure 4.6: The effect of adding NLOS links on the PEB for the case that the beams are transmitted in the LOS and in the directions of the clusters. The clusters are added sequentially by moving away from the LOS link as $\mathbf{s}_k$ [m] $= [1.5, 1 + (k-1) \times 0.1]^{\mathrm{T}}$ for $k = 1, \ldots, 3$, $\mathbf{q}$ [m] $= [0, 0]^{\mathrm{T}}$, and $\mathbf{p}$ [m] $= [0, 4]^{\mathrm{T}}$. The index $k = 0$ denotes the LOS condition.

Comparison with Adaptive CS in [Alk14]

We compare the performance of the proposed detection-estimation approach with the adaptive CS in [Alk14] in terms of training overhead. To make the results comparable with [Alk14], we apply the received beamformer in the proposed algorithm by multiplying the left hand side of the g-th received signal in (4.4.3) with the Hermitian of $\mathbf{W}^{(g)}[n] = \mathbf{W}_{\mathrm{RF}}^{(g)}\mathbf{W}_{\mathrm{BB}}^{(g)}[n]$ where $\mathbf{W}_{\mathrm{RF}}^{(g)}$ denotes the $N_r \times M_r$ RF combining matrix that is similar to the RF precoder and $\mathbf{W}_{\mathrm{BB}}^{(g)}[n]$ denotes the $M_r \times M_r$ digital combining matrix with the (m_1, m_2)-th entry of $e^{j\theta_{m_1,m_2,n,g}}$ where $\theta_{m_1,m_2,n,g}$ follows the i.i.d. uniform distribution $\mathcal{U}[0, 2\pi)$. The rest of development in the proposed algorithm remains unchanged. The parameters for the adaptive CS are adjusted to the simulation setup. Moreover, $K_s = 2$ beamforming vectors are used in 2^{s-1} subsets for the codebook level s, $M_r = 2$, and the AOAs/AODs resolutions are set to $2\pi/N_{\mathrm{res}}$ where $N_{\mathrm{res}} = 2^{N_Q}$ with phase shifters quantization bits $N_Q = 7$. The training overhead for the adaptive CS is $G_{\mathrm{ad}} \triangleq K_s(K+1)^2\lceil K_s(K+1)/M_r \rceil \log_{K_s}^{N_{\mathrm{res}}/(K+1)}$ [Alk14], and the training overhead for the proposed algorithm is $G_{\mathrm{prop}} = G$. Fig. 4.11 shows the root-square error (RSE) and the RMSE of AOA and AOD with blue and red squares, respectively, for 50 realizations in the LOS for the adaptive CS and the proposed

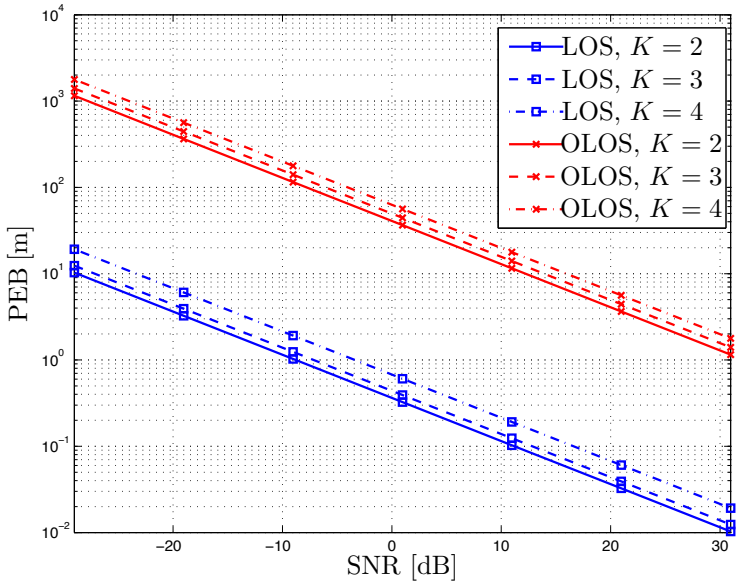

Figure 4.7: Performances of the PEB for the LOS in presence of clusters and OLOS with different number of clusters $\mathbf{s}_k\,[\mathrm{m}] = [1.5, 1+(k-1)\times 0.1]^{\mathrm{T}}$ for $k = 2, \ldots, 4$, $\mathbf{q}[\mathrm{m}] = [0, 0]^{\mathrm{T}}$, and $\mathbf{p}\ [\mathrm{m}] = [0, 4]^{\mathrm{T}}$.

method. The results show that for $G_{\mathrm{prop}} \geq 20$ the variations of RMSE of AOA and AOD is negligible, while the adaptive CS requires $G_{\mathrm{ad}} \geq 32$ to approach the desired resolution that is restricted by phase shifters quantization bits $N_Q = 7$ for the LOS. Fig. 4.12 shows that for $G_{\mathrm{prop}} \geq 24$ the variations of RMSE of AOAs and AODs is negligible, while the adaptive CS requires $G_{\mathrm{ad}} \geq 64$ to approach the desired resolution that is restricted by phase shifters quantization bits $N_Q = 7$ for the NLOS. This can be justified using the fact that the proposed algorithm leverages the angular sparsity of the mm-wave channel, while the adaptive CS does not take into account the angular sparsity in the estimation of AOAs/AODs. Consequently, the relative training overhead$\Delta\ G = (G_{\mathrm{ad}} - G_{\mathrm{prop}})/G_{\mathrm{prop}}$ increases for the adaptive CS compared to the proposed method. More specifically,$\Delta\ G$ is around 0.6 for the LOS and 1.67 for the NLOS. In principle, by increasing the number of channel path the training overhead increases by approximately $(K+1)^3 \log_{K_s}^{N_{\mathrm{res}}/(K+1)}$ for the adaptive CS, while the training overhead is not significantly changing using the proposed method.

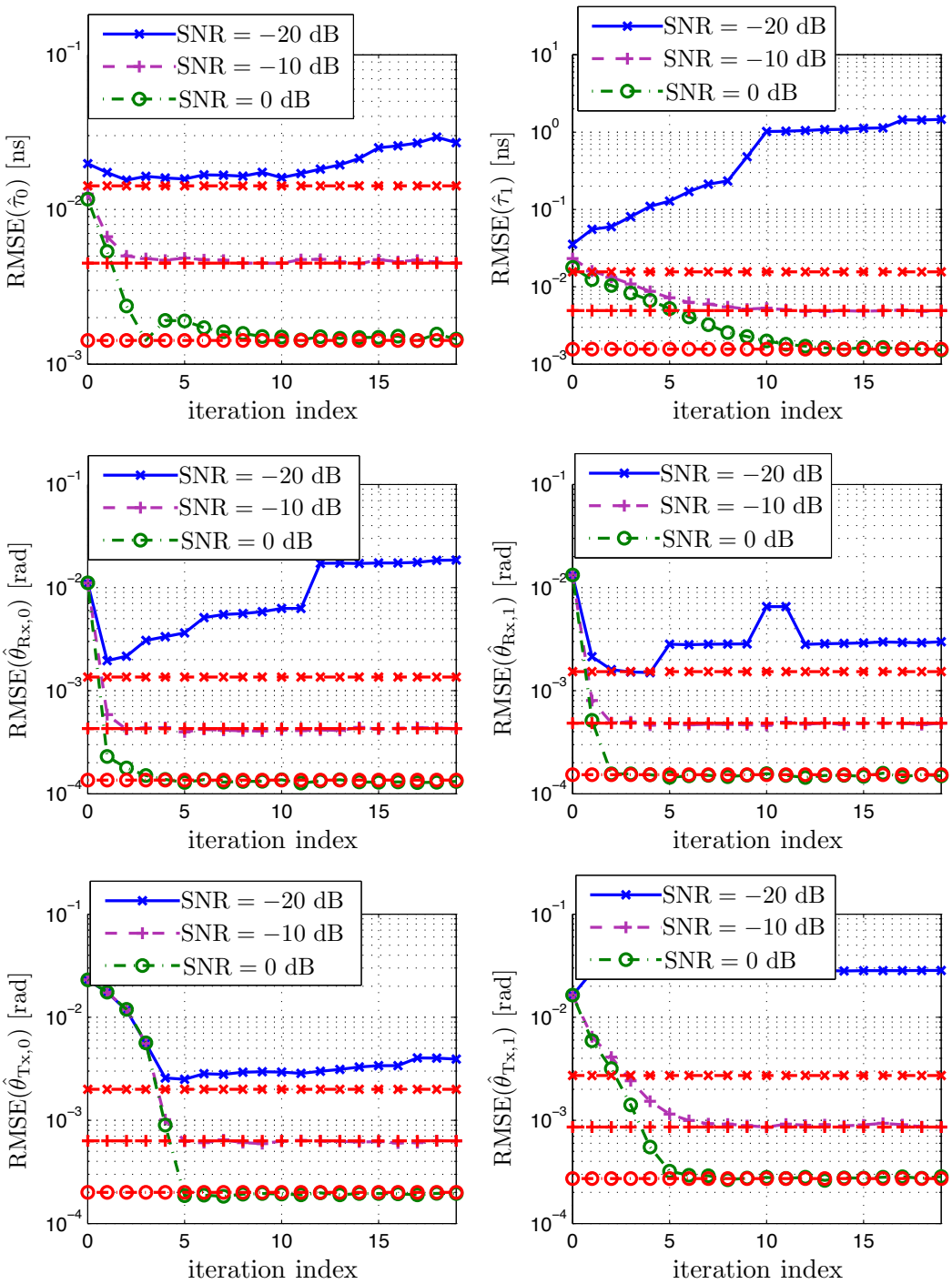

Figure 4.8: The evolution of RMSE of TOA and AOA/AOD for the LOS (left column) and the NLOS (right column) paths at SNR $= -20\,\mathrm{dB}, -10\,\mathrm{dB}, 0\,\mathrm{dB}$.

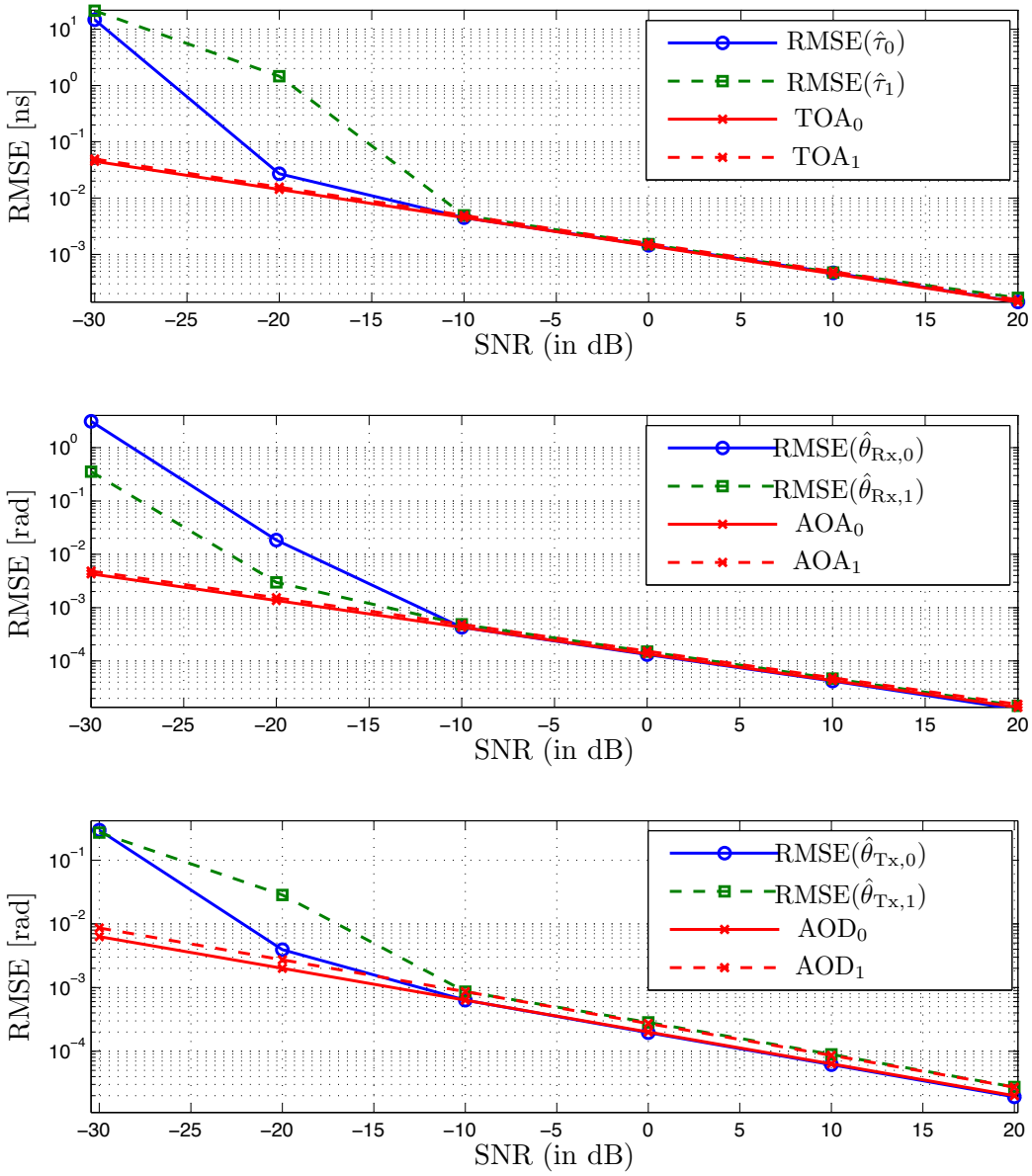

Figure 4.9: RMSE in dB scale plotted against received SNR for TOA and AOA/AOD in the presence of a cluster located at $\mathbf{s}_k$ [m] $= [1.5, 0.4]^{\mathrm{T}}$.

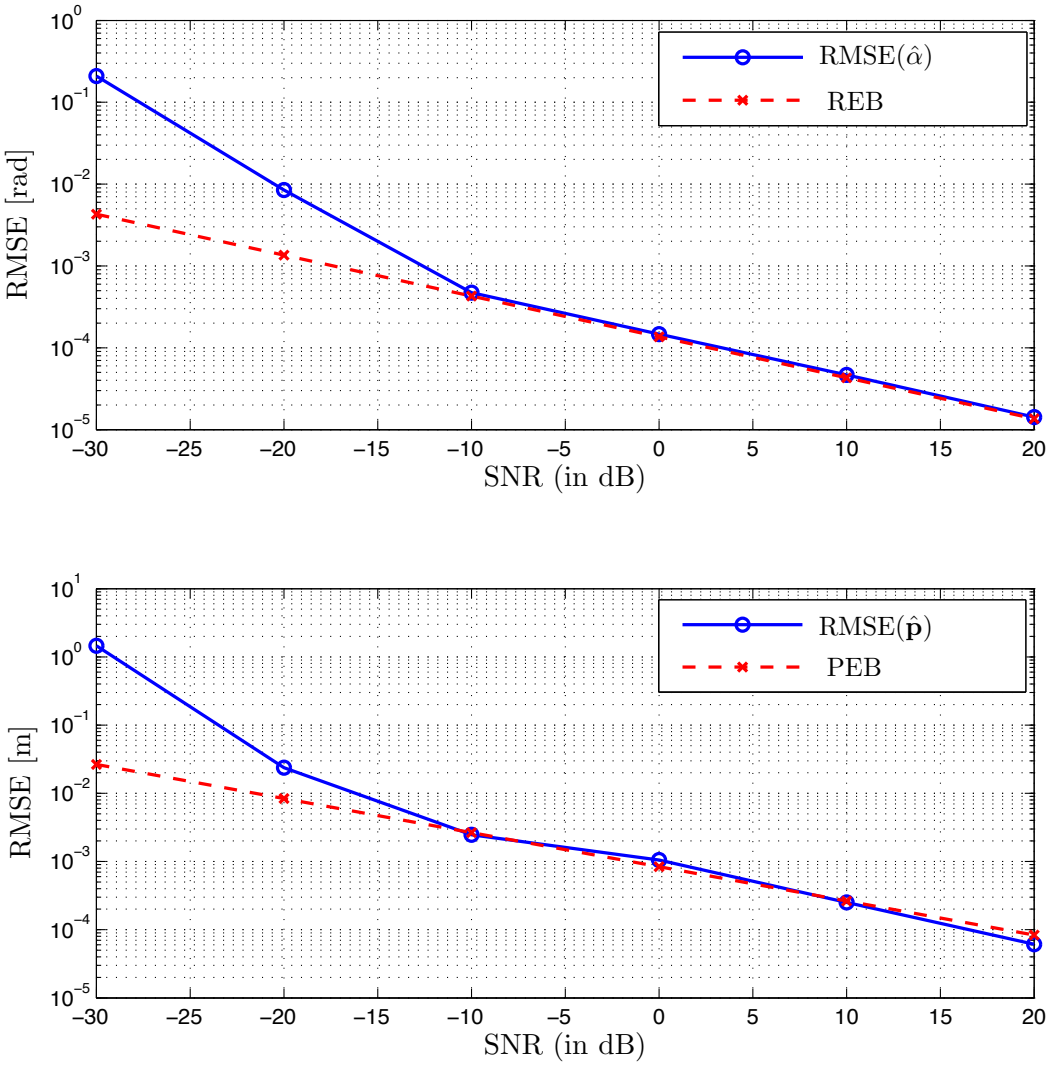

Figure 4.10: RMSE in dB scale plotted against received SNR for rotation angle (top) and position (bottom) in the presence of a cluster located at $\mathbf{s}_k$ [m] $= [1.5, 0.4]^{\mathrm{T}}$.

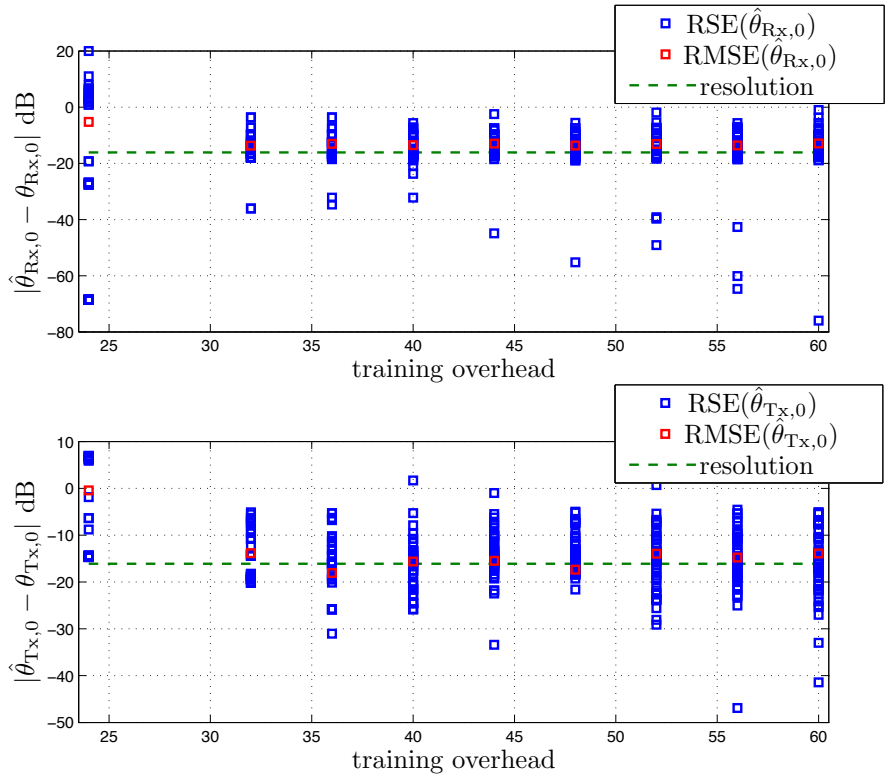

(a) adaptive CS for 50 realizations

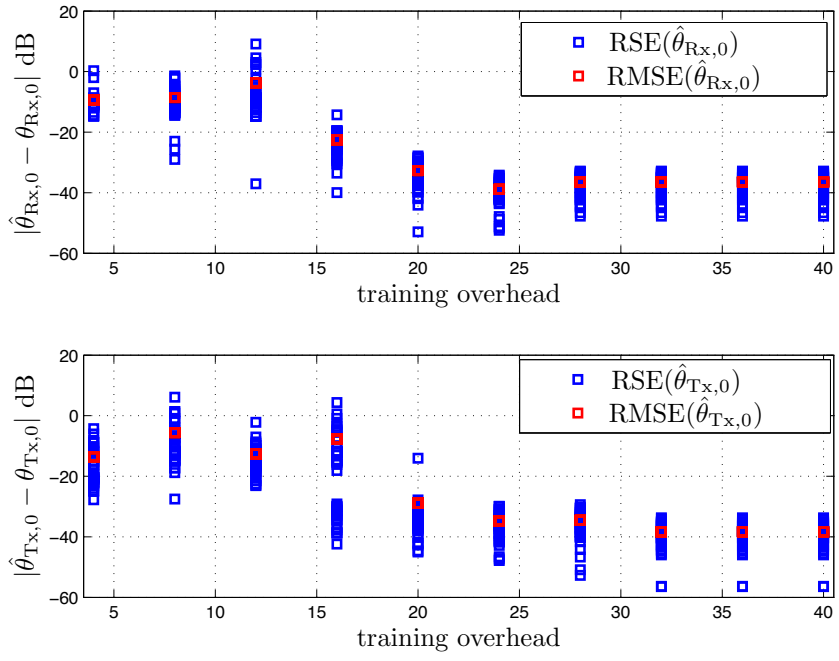

(b) proposed method for 50 realizations

Figure 4.11: Comparison of the RSE/RMSE of AOA/AOD estimation schemes against the training overhead at SNR = 0 dB for the LOS.

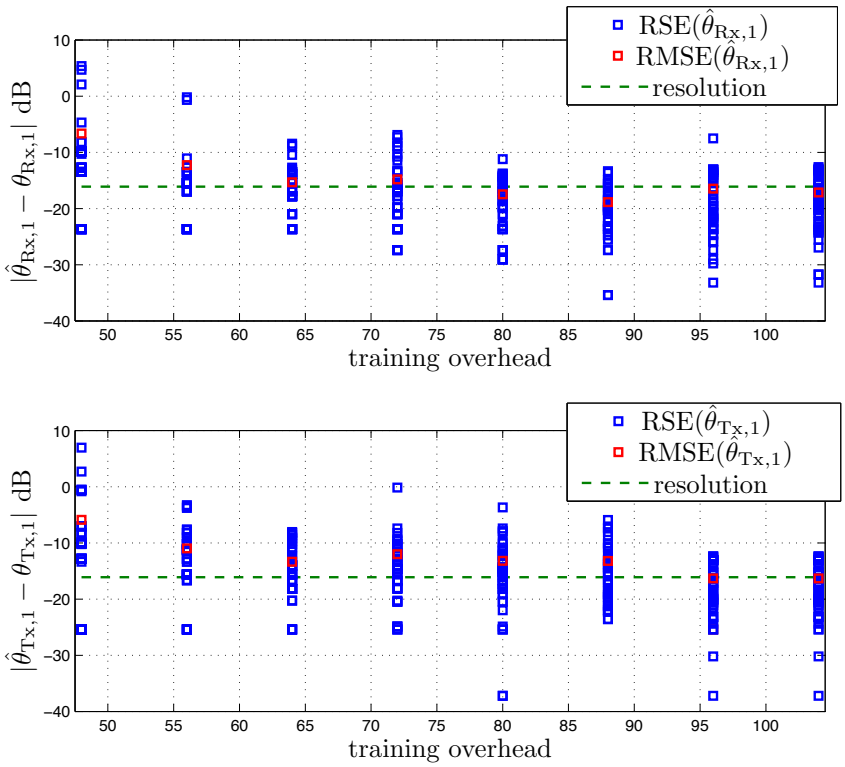

(a) adaptive CS for 50 realizations

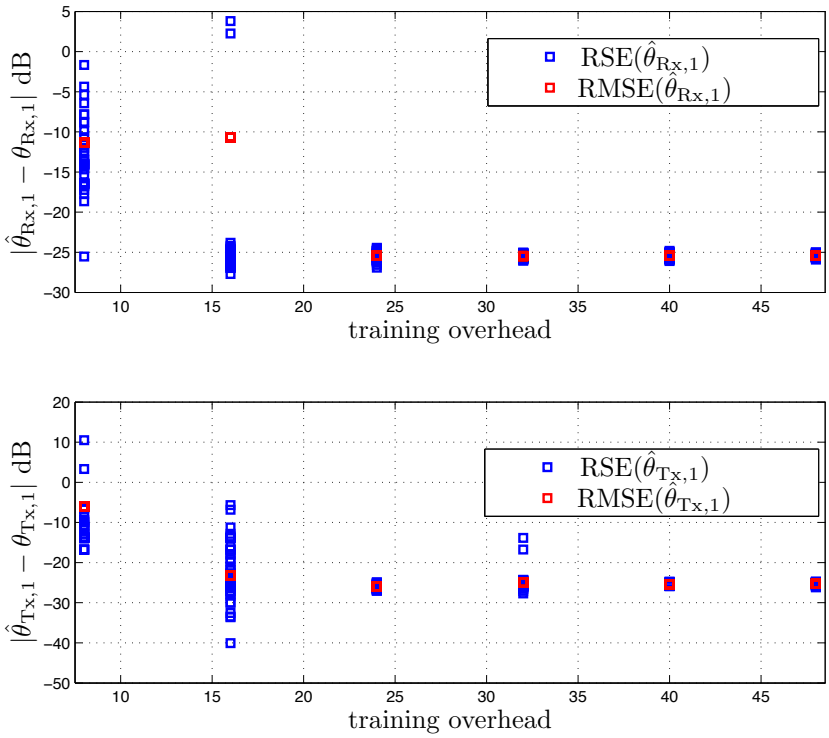

(b) proposed method for 50 realizations

Figure 4.12: Comparison of the RSE/RMSE of AOA/AOD estimation schemes against the training overhead at SNR = 0 dB for the NLOS.

4.6 Conclusion

We have presented a study of the fundamental bounds of a wideband MIMO mm-wave system. Using LOS and NLOS channel models, we have first computed the FIM for delay, AOD, AOA, and channel gain. We have then transformed the FIM to comprise the position and rotation angle of MS. A two stage algorithm including the detection phase and the estimation phase for the sparse estimation of AOA, AOD, and TOA has been developed. The results show that the estimated values of AOA, AOD, and TOA converge to the corresponding values obtained from the inverse of the FIM. Moreover, the estimated values of position and rotation angle converge to the PEB and REB after a few iterations.

Appendix 4.A

Proof for (4.3.9)

Replacing $\mathbf{y}[n]$ from (4.2.4) in (4.3.5), using (4.3.7), and considering $\mathbb{E}_{\mathbf{y}|\boldsymbol{\eta}}[\mathbf{n}[n]] = \mathbf{0}$, we obtain

$$\Psi(x_r, x_s) = \frac{2}{N_0} \sum_{n=0}^{N-1} \Re \left\{ \frac{\partial \boldsymbol{\mu}^{\mathrm{H}}[n]}{\partial x_r} \frac{\partial \boldsymbol{\mu}[n]}{\partial x_s} \right\}. \tag{4.A.1}$$

The elements of the FIM are obtained based on (4.A.1). The terms including $\{\tau_r, \tau_s\}$ and $\{\boldsymbol{\theta}_r, \boldsymbol{\theta}_s\}$ are summarized as:

$$\Psi_n(\tau_r, \tau_s) = \frac{2}{N_0} \Re\{\tilde{h}_r^* \tilde{h}_s A_{\mathrm{Rx},n}(\theta_{\mathrm{Rx,r}}, \theta_{\mathrm{Rx,s}}) A^{(2)}_{\mathrm{Tx},\mathbf{F},n}(\tau_r, \tau_s, \theta_{\mathrm{Tx,s}}, \theta_{\mathrm{Tx,r}})\}, \tag{4.A.2}$$

$$\Psi_n(\tau_r, \theta_{\mathrm{Tx},s}) = \frac{2}{N_0} \Re\{j\tilde{h}_r^* \tilde{h}_s A_{\mathrm{Rx},n}(\theta_{\mathrm{Rx,r}}, \theta_{\mathrm{Rx,s}}) A^{(1)}_{\mathbf{D}_{\mathrm{Tx},s},\mathbf{F},n}(\tau_r, \tau_s, \theta_{\mathrm{Tx,s}}, \theta_{\mathrm{Tx,r}})\}, \tag{4.A.3}$$

$$\Psi_n(\tau_r, \theta_{\mathrm{Rx},s}) = \frac{2}{N_0} \Re\{j\tilde{h}_r^* \tilde{h}_s A_{\mathbf{D}_{\mathrm{Rx},s},n}(\theta_{\mathrm{Rx,r}}, \theta_{\mathrm{Rx,s}}) A^{(1)}_{\mathrm{Tx},\mathbf{F},n}(\tau_r, \tau_s, \theta_{\mathrm{Tx,s}}, \theta_{\mathrm{Tx,r}})\}, \tag{4.A.4}$$

$$\Psi_n(\theta_{\mathrm{Tx},r}, \theta_{\mathrm{Tx},s}) = \frac{2}{N_0} \Re\{\tilde{h}_r^* \tilde{h}_s A_{\mathrm{Rx},n}(\theta_{\mathrm{Rx,r}}, \theta_{\mathrm{Rx,s}}) A_{\mathbf{Dd}_{\mathrm{Tx}},\mathbf{F},n}(\tau_r, \tau_s, \theta_{\mathrm{Tx,s}}, \theta_{\mathrm{Tx,r}})\}, \tag{4.A.5}$$

$$\Psi_n(\theta_{\mathrm{Tx},r}, \theta_{\mathrm{Rx},s}) = \frac{2}{N_0} \Re\{\tilde{h}_r^* \tilde{h}_s A_{\mathbf{D}_{\mathrm{Rx},s},n}(\theta_{\mathrm{Rx,r}}, \theta_{\mathrm{Rx,s}}) A^{(0)}_{\mathbf{D}_{\mathrm{Tx},r},\mathbf{F},n}(\tau_r, \tau_s, \theta_{\mathrm{Tx,s}}, \theta_{\mathrm{Tx,r}})\} \tag{4.A.6}$$

$$\Psi_n(\theta_{\mathrm{Rx},r}, \theta_{\mathrm{Rx},s}) = \frac{2}{N_0} \Re\{\tilde{h}_r^* \tilde{h}_s A_{\mathbf{D}_{\mathrm{Rx},r,s},n}(\theta_{\mathrm{Rx,r}}, \theta_{\mathrm{Rx,s}}) A^{(0)}_{\mathrm{Tx},\mathbf{F},n}(\tau_r, \tau_s, \theta_{\mathrm{Tx,s}}, \theta_{\mathrm{Tx,r}})\}. \tag{4.A.7}$$

The following notations are introduced:

$$A^{(k)}_{\mathrm{Tx},\mathbf{F},n}(\tau_r, \tau_s, \theta_{\mathrm{Tx,s}}, \theta_{\mathrm{Tx,r}}) \triangleq \mathbf{a}^{\mathrm{H}}_{\mathrm{Tx},\mathbf{F},n}(\theta_{\mathrm{Tx,s}}) \mathbf{A}_{k,n}(\tau_r, \tau_s) \mathbf{a}_{\mathrm{Tx},\mathbf{F},n}(\theta_{\mathrm{Tx,r}}), \tag{4.A.8}$$

$$A^{(l)}_{\mathbf{D}_{\mathrm{Tx},s},\mathbf{F},n}(\tau_r, \tau_s, \theta_{\mathrm{Tx,s}}, \theta_{\mathrm{Tx,r}}) \triangleq \mathbf{a}^{\mathrm{H}}_{\mathbf{D}_{\mathrm{Tx}},\mathbf{F},n}(\theta_{\mathrm{Tx,s}}) \mathbf{A}_{l,n}(\tau_r, \tau_s) \mathbf{a}_{\mathrm{Tx},\mathbf{F},n}(\theta_{\mathrm{Tx,r}}), \tag{4.A.9}$$

$$A^{(l)}_{\mathbf{D}_{\mathrm{Tx},r},\mathbf{F},n}(\tau_r, \tau_s, \theta_{\mathrm{Tx,s}}, \theta_{\mathrm{Tx,r}}) \triangleq \mathbf{a}^{\mathrm{H}}_{\mathrm{Tx},\mathbf{F},n}(\theta_{\mathrm{Tx,s}}) \mathbf{A}_{l,n}(\tau_r, \tau_s) \mathbf{a}_{\mathbf{D}_{\mathrm{Tx}},\mathbf{F},n}(\theta_{\mathrm{Tx,r}}), \tag{4.A.10}$$

$$A_{\mathbf{Dd}_{\mathrm{Tx}},\mathbf{F},n}(\tau_r, \tau_s, \theta_{\mathrm{Tx,s}}, \theta_{\mathrm{Tx,r}}) \triangleq \mathbf{a}^{\mathrm{H}}_{\mathbf{D}_{\mathrm{Tx}},\mathbf{F},n}(\theta_{\mathrm{Tx,s}}) \mathbf{A}_{0,n}(\tau_r, \tau_s) \mathbf{a}_{\mathbf{D}_{\mathrm{Tx}},\mathbf{F},n}(\theta_{\mathrm{Tx,r}}), \tag{4.A.11}$$

where $l \in \{0, 1\}$, and $\mathbf{A}_{k,n}(\tau_r, \tau_s), k \in \{0, 1, 2\}$, is given by

$$\mathbf{A}_{k,n}(\tau_r,\tau_s) \triangleq (2\pi n)^k \ \mathbf{x}[n]\mathbf{x}^{\mathrm{H}}[n]e^{-j2\pi n(\tau_n-\tau_m)/(NT_s)}. \tag{4.A.12}$$

The vectors $\mathbf{a}_{\mathrm{Tx},\mathbf{F},n}(\theta_{\mathrm{Tx},r})$ and $\mathbf{a}_{\mathbf{D}_{\mathrm{Tx}},\mathbf{F},n}(\theta_{\mathrm{Tx},r})$ are given by

$$\mathbf{a}_{\mathrm{Tx},\mathbf{F},n}(\theta_{\mathrm{Tx},r}) = \mathbf{F}^{\mathrm{H}}[n]\mathbf{a}_{\mathrm{Tx},n}(\theta_{\mathrm{Tx},r}),$$

and

$$\mathbf{a}_{\mathbf{D}_{\mathrm{Tx}},\mathbf{F},n}(\theta_{\mathrm{Tx},r}) = \mathbf{F}^{\mathrm{H}}[n]\mathbf{D}_{\mathrm{Tx},r}[n]\mathbf{a}_{\mathrm{Tx},n}(\theta_{\mathrm{Tx},r}).$$

The matrix $\mathbf{D}_{\mathrm{Tx},r}[n]$ is defined as

$$\mathbf{D}_{\mathrm{Tx},r}[n] \triangleq j\frac{2\pi}{\lambda_n}d\cos(\theta_{\mathrm{Tx},r})\mathrm{diag}\{0,\ldots,N_{\mathrm{t}}-1\}. \tag{4.A.13}$$

The scalars $A_{\mathrm{Rx},n}(\theta_{\mathrm{Rx,r}},\theta_{\mathrm{Rx,s}})$, $A_{\mathbf{D}_{\mathrm{Rx,s}},n}(\theta_{\mathrm{Rx,r}},\theta_{\mathrm{Rx,s}})$, and $A_{\mathbf{D}_{\mathrm{Rx,r,s}},n}(\theta_{\mathrm{Rx,r}},\theta_{\mathrm{Rx,s}})$ are defined as

$$A_{\mathrm{Rx},n}(\theta_{\mathrm{Rx,r}},\theta_{\mathrm{Rx,s}}) \triangleq \mathbf{a}^{\mathrm{H}}_{\mathrm{Rx},n}(\theta_{\mathrm{Rx},r})\mathbf{a}_{\mathrm{Rx},n}(\theta_{\mathrm{Rx},s}), \tag{4.A.14}$$

$$A_{\mathbf{D}_{\mathrm{Rx,s}},n}(\theta_{\mathrm{Rx,r}},\theta_{\mathrm{Rx,s}}) \triangleq \mathbf{a}^{\mathrm{H}}_{\mathrm{Rx},n}(\theta_{\mathrm{Rx},r})\mathbf{D}_{\mathrm{Rx},s}[n]\mathbf{a}_{\mathrm{Rx},n}(\theta_{\mathrm{Rx},s}), \tag{4.A.15}$$

$$A_{\mathbf{D}_{\mathrm{Rx,r,s}},n}(\theta_{\mathrm{Rx,r}},\theta_{\mathrm{Rx,s}}) \triangleq \mathbf{a}^{\mathrm{H}}_{\mathrm{Rx},n}(\theta_{\mathrm{Rx},r})\mathbf{D}^{\mathrm{H}}_{\mathrm{Rx},r}[n]\mathbf{D}_{\mathrm{Rx},s}[n]\mathbf{a}_{\mathrm{Rx},n}(\theta_{\mathrm{Rx},s}), \tag{4.A.16}$$

where $\mathbf{D}_{\mathrm{Rx},r}[n]$ has the same expression as (4.A.13) by replacing the subscript Tx by Rx and N_t by N_r. The terms including channel coefficients are summarized as:

$$\begin{aligned}\mathbf{\Psi}_n(\tau_r,\tilde{\mathbf{h}}_s) = \frac{2}{N_0}[&\Re\{j\tilde{h}^*_r A_{\mathrm{Rx},n}(\theta_{\mathrm{Rx,r}},\theta_{\mathrm{Rx,s}})A^{(1)}_{\mathrm{Tx},\mathbf{F},n}(\tau_r,\tau_s,\theta_{\mathrm{Tx},s},\theta_{\mathrm{Tx},r})\},\\ &\Re\{-\tilde{h}^*_r A_{\mathrm{Rx},n}(\theta_{\mathrm{Rx,r}},\theta_{\mathrm{Rx,s}})A^{(1)}_{\mathrm{Tx},\mathbf{F},n}(\tau_r,\tau_s,\theta_{\mathrm{Tx},s},\theta_{\mathrm{Tx},r})\}],\end{aligned} \tag{4.A.17}$$

$$\begin{aligned}\mathbf{\Psi}_n(\theta_{\mathrm{Tx},r},\tilde{\mathbf{h}}_s) = \frac{2}{N_0}[&\Re\{\tilde{h}^*_r A_{\mathrm{Rx},n}(\theta_{\mathrm{Rx,r}},\theta_{\mathrm{Rx,s}})A^{(0)}_{\mathbf{D}_{\mathrm{Tx},r},\mathbf{F},n}(\tau_r,\tau_s,\theta_{\mathrm{Tx,s}},\theta_{\mathrm{Tx,r}})\},\\ &\Re\{j\tilde{h}^*_r A_{\mathrm{Rx},n}(\theta_{\mathrm{Rx,r}},\theta_{\mathrm{Rx,s}})A^{(0)}_{\mathbf{D}_{\mathrm{Tx},r},\mathbf{F},n}(\tau_r,\tau_s,\theta_{\mathrm{Tx,s}},\theta_{\mathrm{Tx,r}})\}],\end{aligned} \tag{4.A.18}$$

$$\begin{aligned}\mathbf{\Psi}_n(\theta_{\mathrm{Rx},r},\tilde{\mathbf{h}}_s) = -\frac{2}{N_0}[&\Re\{\tilde{h}^*_r A_{\mathbf{D}_{\mathrm{Rx},r},n}(\theta_{\mathrm{Rx,r}},\theta_{\mathrm{Rx,s}})A^{(0)}_{\mathrm{Tx},\mathbf{F},n}(\tau_r,\tau_s,\theta_{\mathrm{Tx},s},\theta_{\mathrm{Tx},r})\},\\ &\Re\{j\tilde{h}^*_r A_{\mathbf{D}_{\mathrm{Rx},r},n}(\theta_{\mathrm{Rx,r}},\theta_{\mathrm{Rx,s}})A^{(0)}_{\mathrm{Tx},\mathbf{F},n}(\tau_r,\tau_s,\theta_{\mathrm{Tx},s},\theta_{\mathrm{Tx},r})\}],\end{aligned} \tag{4.A.19}$$

$$\Psi_n(\Re\{\tilde{h}_r\},\Re\{\tilde{h}_s\}) = \Psi_n(\Im\{\tilde{h}_r\},\Im\{\tilde{h}_s\}) =$$

$$\frac{2}{N_0}\Re\{A_{\mathrm{Rx},n}(\theta_{\mathrm{Rx,r}},\theta_{\mathrm{Rx,s}})A^{(0)}_{\mathrm{Tx},\mathbf{F},n}(\tau_r,\tau_s,\theta_{\mathrm{Tx},s},\theta_{\mathrm{Tx},r})\}, \quad (4.A.20)$$

$$\Psi_n(\Re\{\tilde{h}_r\},\Im\{\tilde{h}_s\}) = -\Psi_n(\Im\{\tilde{h}_r\},\Re\{\tilde{h}_s\}) =$$
$$\frac{2}{N_0}\Re\{jA_{\mathrm{Rx},n}(\theta_{\mathrm{Rx,r}},\theta_{\mathrm{Rx,s}})A^{(0)}_{\mathrm{Tx},\mathbf{F},n}(\tau_r,\tau_s,\theta_{\mathrm{Tx},s},\theta_{\mathrm{Tx},r})\}. \quad (4.A.21)$$

Chapter 5

Conclusions and Future Work

This dissertation has explored the potential of OFDM signals for localization in 5G systems. In particular, this dissertation has put emphasis on the design of OFDM signals under timing and localization accuracy constraints and sparse estimation of channel parameters for position and orientation estimation in 5G systems. As a result, the proposed design of OFDM signals provides high data rate under timing accuracy constraints and robust performance with respect to network parameter uncertainty with the reduced total power consumption compared to the single-carrier counterparts. Additionally, OFDM signals are used in the mm-wave frequencies due to good capabilities of the mm-wave frequencies for indoor localization in 5G systems. Large number of antenna arrays are used as a solution for the severe effect of path-loss for indoor localization based on OFDM signals in the mm-wave frequencies. The proposed method estimates the channel parameters with the reduced training overhead using the sparsity of mm-wave channels for different subcarriers and finds the position and rotation angle of the MS for indoor localization in 5G systems.

Fig. 5.1 shows the application of OFDM signals for joint localization and communication, WNL, and sparse position and orientation estimation. The topics where contributions have been presented are highlighted in this figure for the sake of clarity. In 5G systems, the information about the location can improve the data rate. This requires the design of signals that provide high data rate and good localization accuracy. To this end, we first consider the topic of joint localization and communication with OFDM signals. This topic has been shown to result in the distinction between time varying and static channels for the design of near optimal OFDM sequences. This is an important issue because, unlike the design of near optimal OFDM sequences for static channels considering the effect of time variations among different OFDM symbols may lead to a more efficient

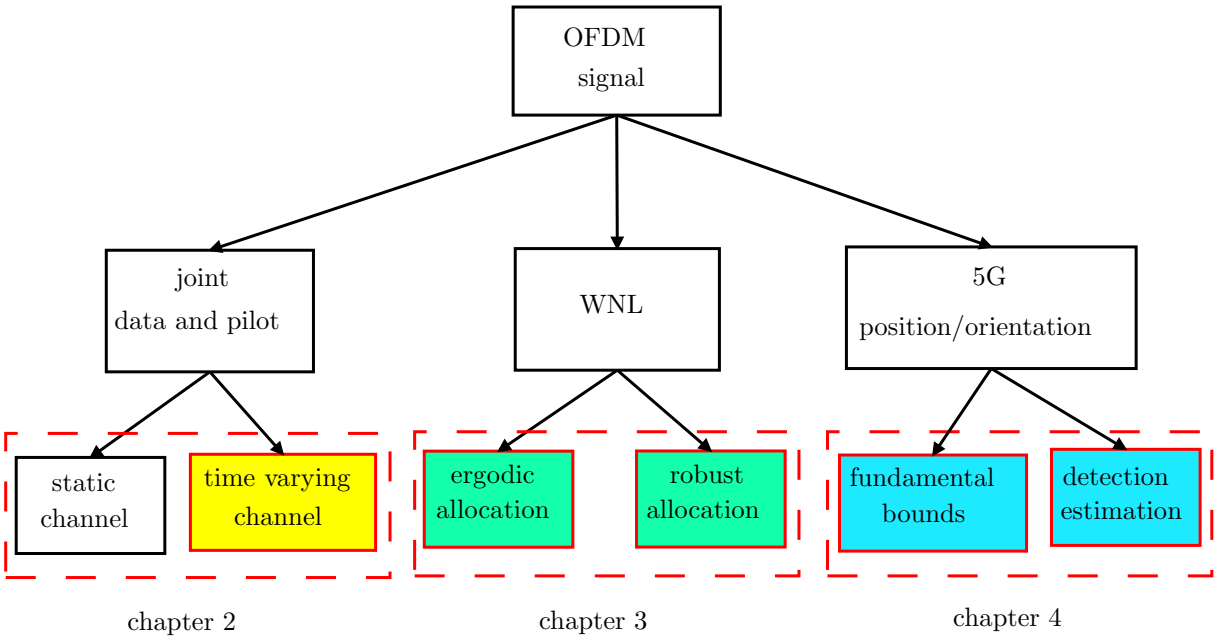

Figure 5.1: Overview of the topics covered within the dissertation.

design for joint localization and communication. In this way, the goal of Chapter 2 has been to design near optimal OFDM sequences in time and frequency for time varying frequency selective channels so that the expected performance loss incurred by applying the near optimal OFDM sequences for static channels can be evaluated. This has constituted the first part of this dissertation.

Once the near optimal OFDM sequences in time and frequency is obtained for time varying and frequency selective channels for single link, the next step has been to move forward into the design of near optimal OFDM sequences for WNL, i.e., subcarrier power allocation. This has constituted the second part of this dissertation. The basic task is the subcarrier power allocation among different BSs in a wireless network for multicast and unicast transmissions. For the case of non-robust subcarrier power allocation, Chapter 3 has shown that the major problem is related with uncertainty on the network parameters. For this reason, ergodic and robust subcarrier allocations have been shown to be essential to compensate the lack of knowledge on the network parameters prior to subcarrier power allocation.

Chapter 4 has dealt with sparse estimation of position and rotation angle of the MS using the OFDM signals in a frequency selective hybrid precoding system for 5G localization.

Next, we summarize the contributions and future research lines for each of the topics addressed in this dissertation.

Joint Localization and Communication

The discussion on the joint data and pilot design has been addressed in Chapter 2 under time varying and frequency selective channels. The main goal has been to design near optimal data and pilot in time and frequency in an analytical manner. To this end, the lower bound on the channel capacity with partially known channel state information (CSI) is considered as the objective function to be maximized under an upper bound on the desired time-delay estimation accuracy. Contrary to the traditional measure of capacity with known CSI and the bound on the time-delay estimation accuracy, the effect of unknown time-delay and channel coefficient are considered in the lower bound of channel capacity and channel statistics (i.e., channel mean and covariance) are used in the formulation of time-delay estimation bound.

In the recent literature, most of the results are dealing with joint data and pilot design for localization and communication for static channels. However, in the real scenarios the time variations in the channel subspace is much faster than the delay subspace and leads to time variations from one OFDM symbol to another OFDM symbol. Thus, considering the effect of time variations between different OFDM symbols may improve the data rate for a given localization accuracy. In this part of the dissertation, one of the most important contributions is that the closed-form expressions are provided for the lower bound of capacity with partially known CSI for time varying frequency selective channels. Moreover, the bounds on the channel coefficients and time-delay for time varying frequency selective channels have been obtained.

In the second step, the design of data and pilot in time and frequency using a relaxed form of the combinatorial optimization problem has led to an important conclusion. Considering the effect of correlation between different OFDM symbols in the design of OFDM sequences in time and frequency led to a semi stair-wise pattern for the joint data and pilot design. Interestingly, this is what we observed in the LTE systems with the PRS in the downlink with the stair-wise pattern. Moreover, ignoring the effect of time variations due to the rapid change in the channel coefficient subspace and applying the joint data and pilot design for static channels led to reducing the channel capacity for the same time-delay accuracy.

When allowing each subcarrier to be used as data and pilot, i.e., the relaxed solution, the capacity is increased by around 31% compared to the solution after masking and limiting each subcarriers to be considered as either data or pilot. Interestingly, in the high SNR regime and after a given threshold on the SNR the time-delay estimation constraint

in the optimization problem for the joint data and pilot design is automatically fulfilled.

The topic that has not been addressed in this dissertation but may be subject to further investigation is the following:

- Extension of the joint data and pilot design for MIMO OFDM is an interesting problem for the case of quasi stationary channels. The main challenge here is to consider the effects of time, frequency, and space in the design of data and pilots (i.e., 3D design of data and pilots) such that the channel capacity with partially known CSI is maximized for a given localization accuracy. In this case, due to antenna arrays in the transmitter and receiver it is possible to use not only the time-delay but also the AOA/AOD for the localization. Using the information provided by the AOA/AOD are useful due to the fact that they are less susceptible to noise. Moreover, the interference cancellation techniques can be applied using the angular information.

Wireless Network Localization

Optimal subcarrier power allocation requires perfect knowledge of the network parameters including the position of the MS that is yet to be estimated and the channel coefficients. However, this leads to the non-robust subcarrier allocations that are susceptible to variations of the network parameters. Consequently, considering the effects of network uncertainty on the design of subcarrier power allocation has been shown to be of critical importance in OFDM WNL. In this dissertation, the uncertainties on the network parameters are treated in the expected and worst case forms using ergodic and robust subcarrier power allocations, respectively. For the case of the ergodic subcarrier power allocation, the total transmitted power in the network is minimized for a given upper bound on the expected value of SPEB. Since the problem is of the form of stochastic optimization, it can be approximated by the corresponding sample average function as the approximate solution for the ergodic subcarrier power allocation. For the case of robust subcarrier power allocation, the worst case SPEB has been obtained using the worst case channel coefficients and positions uncertainties. Then, the robust subcarrier power allocation problem has been formulated by minimizing the total transmitted power subject to an upper bound on the maximum SPEB for given uncertainties on the agents' positions and channel coefficients. The uncertainties on the channel coefficients have been considered as per-tap and vector uncertainties to analyze the effect of different types of uncertainties on the localization accuracy and total power consumption. The simulation

results have led to the following important conclusions:

- It can be observed that the ergodic and robust subcarrier power allocations outperform non-robust solutions with the same total power. This is due to the fact that the proposed subcarrier power allocations use different subcarriers with taking into account the effects of channel coefficients and position uncertainties. Consequently, increasing the total power is not the only factor that affects the ergodic and robust subcarrier power allocations but also the appropriate subcarriers are of critical importance. This can be observed where except the subcarriers at the bandwidth edges the subcarriers used for the non-robust design are different from the subcarriers used for the ergodic and the robust allocations.

- It is observed that increasing the uncertainty on the network parameters leads to increasing the required SNR. Moreover, the required increase of the SNR is affected mainly due to channel uncertainty. The important conclusion from the above discussion is that channel uncertainty is affecting the required SNR for the localization much more than location uncertainty.

- Interestingly, for a given bandwidth the results show that the subcarrier power allocation outperforms the single-carrier counterparts. More specifically, the average relative total power increase in single-carrier design compared to multi-carrier OFDM-based design for a given bandwidth is of the order of 7.8 for non-robust, around 6 for ergodic, and around 2 for the robust allocations for the multicast transmissions, and with an additional 50% for each approach with the unicast transmissions.

Considering the above conclusions from the simulation results and the clear advantage of multi-carrier OFDM-based robust allocations over single-carrier counterparts, there are still some pending issues to be further investigated:

- A natural extension to the proposed model for single antenna OFDM receiver is to obtain the subcarrier power allocations for the case of MIMO systems. In this case not only the locations of the subcarrier play an important role in the localization procedure but also the choice of antenna is of critical importance. Different beamforming techniques may be applied and the design problem for the localization may be reduced to beamformer design.

- The effect of time variations may be considered in the model for OFDM localization. Observing the effect of agent movement and considering prior knowledge on the

channel coefficients and positions in the forms of probability density functions are very exciting extensions in terms of subcarrier power allocation and localization bounds.

- Considering the effect of interference where each BS is transmitting its signal simultaneously on the localization accuracy and subcarrier power allocations is an interesting extension to the proposed approach where we assume sequential transmission of the signals.

Sparse Estimation of Position and Orientation

For the localization in mm-wave massive MIMO systems, there is a clear demand for the estimation of rotation angle of the MS together with the position using one BS. This is due to the fact that only the estimation of the position may lead to ambiguity due to the unknown rotation angle. It has been shown that the LOS path can provide the sufficient information for the rotation angle estimation as indicated in Chapter 4. Moreover, for the case of OLOS it is not possible to estimate the rotation angle as the NLOS links do not provide sufficient information for the estimation of the rotation angle.

There are two main contributions to be highlighted in the topic of position and orientation estimation in 5G systems:

- First, the localization bounds on the position and rotation angle for the wideband systems accounting for the array dispersion have been obtained. The bounds have been obtained for the case of LOS, in the presence of clusters, and for the case when the LOS is blocked.

- To estimate the parameters including AOAs/AODs, TOAs and channel coefficients with the reduced training overhead, the sparsity of the mm-wave channels has been considered using the beamspace transceiver. The sparse estimation of the channel parameters has been organized as a two-stage procedure including detection and estimation steps. In the detection phase, the coarse estimation of channel parameters has been obtained. In the estimation phase, the estimated values from the detection phase have been refined by compensating for the limited grid size effect in the detection phase using an EM like sequential iterative procedure.

Simulation results show that even at very low received SNR that is the case for the mm-wave systems before beamforming the estimated parameters using the proposed

detection-estimation algorithm converge to the proposed bounds. More specifically, at -10 dB all the parameters converge to their corresponding bounds for the LOS and the NLOS. Consequently, the estimated values of the AOAs/AODs and TOAs and position and rotation angle converge to the true values even at very low received SNR. Moreover, the proposed detection-estimation approach for the sparse estimation of channel parameters significantly outperforms the existing contributions in the literature using the adaptive CS in terms of training overhead for the estimation of AOAs/AODs. More specifically, the relative increase of the training overhead is around 0.6 and 1.67 for the LOS and the NLOS, respectively, for the adaptive CS compared to the proposed method.

The performance results of the proposed detection-estimation algorithm for the sparse estimation of the position and rotation angle outperform the adaptive CS in the literature and converge to the corresponding bounds. However, some of the research lines that still remain open are the following:

- The effect of time variations in the channel model and estimation of the parameters of interest for the case that the channel is time varying is an interesting extension of the proposed method.

- Considering the effect of array dispersion and beam squint in the proposed detection-estimation algorithms is a very interesting problem. This is due to the fact the fractional bandwidth (FB) is violating the condition for the common sparse support assumed by the DCS-SOMP in the detection phase of the proposed algorithm. So, it would be interesting to apply a modified form of the proposed DCS-SOMP in the detection phase to account for different angular sparse support among different subcarriers.

Abbreviations

ADC analog-to-digital-converter

AOA angle-of-arrival

AOD angle-of-departure

BF beamforming

BS base station

CoSOMP compressive sampling matched pursuit

CP cyclic prefix

CP-OFDM cyclic prefix OFDM

CRB Cramér-Rao bound

CRS cell-specific reference signal

CS compressed sensing

CSI channel state information

DAC digital-to-analog-converter

DCS distributed compressed sensing

DCS-SOMP distributed compressed sensing-simultaneous OMP

DFT discrete Fourier transform

DLS damped least-squares

DTDOA differential time difference of arrival

ECRB expected CRB

EFIM equivalent Fisher information matrix

EM expectation maximization

EXIP extended invariance principle

FB fractional bandwidth

FBMC filter bank multi-carrier

FFT fast Fourier transform

FIM Fisher information matrix

FDE frequency domain equalization

G-BPDN group basis pursuit denoising

GCS group sparse compressed sensing

GFDM generalized frequency division multiplexing

GMSK Gaussian minimum-shift keying

GNA Gauss-Newton algorithm

GPS global positioning system

GSM global system for mobile communications

ICI intercarrier interference

IFFT inverse fast Fourier transform

IQML iterative quadratic maximum likelihood

ISI intersymbol interference

LMA Levenberg-Marquardt algorithm

LOS line-of-sight

LTE long term evolution

MBSFN multimedia broadcast over single frequency network

ML maximum likelihood

MLE maximum likelihood estimation

MMSE minimum mean square error

MMV multiple measurement vectors

MIMO multiple-input-multiple-output

MISO multiple input single output

MS mobile station

MSK minimum-shift keying

mm-wave millimeter wave

NLOS non-line-of-sight

OFDM orthogonal frequency division multiplexing

OLOS obstructed-line-of-sight

OMP orthogonal matching pursuit

PA power amplifier

PAN personal area network

PAPR peak-to-average power ratio

PBCH physical broadcast channel

PCFICH physical control format indicator channel

PDCCH physical downlink control channel

PDSCH physical downlink shared channel

PEB position error bound

PHICH physical hybrid ARQ indicator channel

PMCH physical multicast channel

PN pseudo noise

PRS positioning reference signal

PSD positive semidefinite

QoS quality-of-service

RA-ORMP rank-aware order recursive matching pursuit

REB rotation error bound

ReMBo reduce MMV and boost

RF radio-frequency

RMS root-mean-square

RMSE root-mean-square error

RSE root-square error

RSS received signal strength

SINR signal-to-interference-plus-noise ratio

SNR signal-to-noise ratio

SPEB squared position error bound

SC-FDE single-carrier frequency domain equalization

SC-FDM single-carrier frequency-division multiplexing

SC-FDMA single-carrier frequency-division multiple access

SC-QAM single-carrier quadrature amplitude modulation

SDL sensor delay line

S/P serial/parallel

SMV single measurement vector

SOMP simultaneous OMP

TDL tapped delay line

TDOA time difference of arrival

TOA time-of-arrival

UE user equipment

UFMC universal-filtered multi-carrier

ULA uniform linear array

UWB ultra-wide bandwidth

WIMAX worldwide interoperability for microwave access

WLAN wireless local area network

WLS weighted least squares

WNL wireless network localization

WOLA weighted overlap and add

Bibliography

[3GP14] "3GPP TS 36.101, evolved universal terrestrial radio access (E-UTRA); user equipment (UE) radio transmission and reception, Rel. 9, V9.18.0", Jan 2014.

[Alk14] A. Alkhateeb, O. E. Ayach, G. Leus, R. W. Heath Jr, "Channel estimation and hybrid precoding for millimeter wave cellular systems", *IEEE Journal of Selected Topics in Signal Processing*, Vol. 8, nº 5, pags. 831–846, 2014.

[Alk15] A. Alkhateeb, R. W. Heath, "Frequency selective hybrid precoding for limited feedback millimeter wave systems", *submitted to IEEE Transactions on Communications (Invited Paper)*, Oct. 2015.

[Alm07] P. Almers, E. Bonek, A. Burr, N. Czink, M. Debbah, V. Degli-Esposti, H. Hofstetter, P. Kyösti, D. Laurenson, G. Matz, A. F. Molisch, C. Oestges, H. Özcelik, "Survey of channel and radio propagation models for wireless MIMO systems", *EURASIP J. Wirel. Commun. Netw.*, Vol. 2007, nº 1, pags. 56–56, 2007.

[Ban14] P. Banelli, S. Buzzi, G. Colavolpe, A. Modenini, F. Rusek, A. Ugolini, "Modulation formats and waveforms for 5G networks: Who will be the heir of OFDM?: An overview of alternative modulation schemes for improved spectral efficiency", *IEEE Signal Processing Magazine*, Vol. 31, nº 6, pags. 80–93, 2014.

[Bar03] I. Barhumi, G. Leus, M. Moonen, "Optimal training design for MIMO OFDM systems in mobile wireless channels", *IEEE Transactions on Signal Processing*, Vol. 51, nº 6, pags. 1615–1624, Jun. 2003.

[Bel10] M. Bellenger, "FBMC physical layer: a primer", *Phydyas report*, 2010.

[Bhu14] N. Bhushan, J. Li, D. Malladi, R. Gilmore, D. Brenner, A. Damnjanovic, R. T. Sukhavasi, C. Patel, S. Geirhofer, "Network densification: the dominant theme

for wireless evolution into 5G", *IEEE Communications Magazine*, Vol. 52, nº 2, pags. 82–89, 2014.

[Boc14] F. Boccardi, R. W. Heath Jr., A. Lozano, T. L. Marzetta, P. Popovski, "Five disruptive technology directions for 5G", *IEEE Communications Magazine*, Vol. 52, nº 2, pags. 74–80, 2014.

[Boy04] S. Boyd, L. Vandenberghe, *Convex Optimization*, Cambridge University Press, New York, NY, USA, 2004.

[Bra13] J. Brady, N. Behdad, A. Sayeed, "Beamspace MIMO for millimeter-wave communications: System architecture, modeling, analysis, and measurements", *IEEE Transactions on Antennas and Propagation*, Vol. 61, nº 7, pags. 3814–3827, 2013.

[Bra15] J. H. Brady, A. Sayeed, "Wideband communication with high-dimensional arrays: New results and transceiver architectures", *IEEE International Conference on Communication (ICC)*, 2015.

[Bre86] Y. Bresler, A. Macovski, "Exact maximum likelihood parameter estimation of superimposed exponential signals in noise", *IEEE Transactions on Acoust., Speech, Signal Processing*, Vol. ASSP-34, pags. 1081–1089, Oct. 1986.

[Cai03] G. Caire, S. Shamai, "On the achievable throughput of a multiantenna gaussian broadcast channel", *IEEE Transactions on Information Theory*, Vol. 49, nº 7, pags. 1691–1706, 2003.

[Cha09] I. Cha, Y. Shah, A. U. Schmidt, A. Leicher, M. V. Meyerstein, "Trust in M2M communication", *IEEE Vehicular Technology Magazine*, Vol. 4, nº 3, pags. 69–75, 2009.

[Che06] J. Chen, X. Huo, "Theoretical results on sparse representations of multiple-measurement vectors", *IEEE Trans. Signal Processing*, Vol. 54, nº 12, pags. 4634–4643, 2006.

[Che14] Z. Chen, C. Yang, "Pilot decontamination in massive MIMO systems: Exploiting channel sparsity with pilot assignment", *IEEE Global conference on Signal and Information Processing (GlobalSIP)*, 2014.

[Cot05] S. F. Cotter, B. D. Rao, K. Engan, K. Kreutz-Delgado, "Sparse solutions to linear inverse problems with multiple measurement vectors", *IEEE Trans. Signal Processing*, Vol. 53, nº 7, pags. 2477–2488, 2005.

[Dai14] W. Dai, Y. Shen, M. Z. Win, "Distributed power allocation for cooperative wireless network localization", *IEEE Journal on Selected Areas in Communications*, Feb. 2014.

[Dam13] A. Dammann, G. Agapiou, J. Bastos, L. Brunel, M. Garcia, J. Guillet, Y. Ma, J. Ma, J. J. Nielsen, L. Ping, R. Raulefs, J. Rodriguez, D. Slock, D. Yang, N. Yi, "WHERE2 location aided communications", *European Wireless Conf.*, 2013.

[Dan12] R. C. Daniels, R. W. Heath, Jr., "Link adaptation with position/motion information in vehicle-to-vehicle networks", *IEEE Transactions on Wireless Communications*, Vol. 11, nº 2, pags. 505–509, 2012.

[Dav12] M. E. Davies, Y. C. Eldar, "Rank awareness in joint sparse recovery", *IEEE Transactions on Information Theory*, Vol. 58, nº 2, pags. 1135–1146, Feb. 2012.

[Den14] H. Deng, A. Sayeed, "Mm-wave MIMO channel modeling and user localization using sparse beamspace signatures", *International Workshop on Signal Processing Advances in Wireless Communications*, pags. 130–134, 2014.

[Dor14] Jean-Baptiste Doré, Vincent Berg, Nicolas Cassiau, Dimitri Kténas, "Fbmc receiver for multi-user asynchronous transmission on fragmented spectrum", *EURASIP Journal on Advances in Signal Processing*, Vol. 2014, nº 1, pags. 41, 2014.

[DPR12] J. A. Del Peral-Rosado, J. A. Lopez-Salcedo, G. Seco-Granados, F. Zanier, M. Crisci, "Achievable localization accuracy of the positioning reference signal of 3GPP LTE", *IEEE Int. Conf. on Localization and GNSS (ICL-GNSS)*, pags. 1–6, 2012.

[DPR14] Jose A. Del Peral-Rosado, *Evaluation of the LTE positioning capabilities in realistic navigation channels*, PhD Thesis, Universitat Autonoma de Barcelona, 2014.

[Dua05] M. F. Duarte, S. Sarvotham, D. Baron, M. B. Wakin, R. G. Baraniuk, "Distributed compressed sensing of jointly sparse signals", *in Proc. 39th Asilomar Conf. Sig., Syst., Comp.*, pags. 3469–3472, 2005.

[Dua09] M. F. Duarte, V. Cevher, R. G. Baraniuk, "Model-based compressive sensing for signal ensembles", *in Proc. 47th Ann. Allerton Conf. Communication, Control, Computing, (Monticello, IL)*, pags. 244–250, 2009.

[Eka11] C. Ekanadham, D. Tranchina, E. P. Simoncelli, "Recovery of sparse translation-invariant signals with continuous basis pursuit", *IEEE Transactions on Signal Processing*, Vol. 59, nº 10, pags. 4735–4744, 2011.

[Eld10a] Y. C. Eldar, P. Kuppinger, Bolcskei, "Block-sparse signals: Uncertainty relations and efficient recovery", *IEEE Trans. Signal Processing*, Vol. 58, nº 6, pags. 3042–3054, 2010.

[Eld10b] Y. C. Eldar, H. Rauhut, "Average case analysis of multichannel sparse recovery using convex relaxation", *IEEE Trans. Info. Theory*, Vol. 6, nº 1, pags. 505–519, 2010.

[Eld12] Y. C. Eldar, G. Kutyniok, *Compressed Sensing: Theory and Applications*, Cambridge Univ. Press, Cambridge, U.K., 2012.

[Fal02] D. Falconer, S. L. Ariyavisitakul, A. Benyamin-Seeyar, D. Eidson, "Frequency domain equalization for single-carrier broadband wireless systems", *IEEE Communications Magazine*, 2002.

[Fan13] J. Fang, Z. You, J. Li, R. Yang, I. T. Lu, "Comparisons of filter bank multicarrier systems", *System, Applications and Technology Conference, IEEE long island*, pags. 1–6, 2013.

[FB11] B. Farhang-Boroujeny, "OFDM versus filter bank multicarrier: development of broadband communication systems", *IEEE Signal Proc. Magazine*, Vol. 29, nº 7, pags. 92–112, 2011.

[Fle99] B. H. Fleury, M. Tschudin, R. Heddergott, D. Dahlhaus, K. I. Pedersen, "Channel parameter estimation in mobile radio environments using the SAGE algorithm", *IEEE Journal on Selected Areas in Communications*, Vol. 17, nº 3, pags. 434–450, 1999.

[Fol13] S. Folea, D. Bordencia, C. Marcu, H. Valean, "Indoor localization based on Wi-Fi parameters influence", *International Conference on Telecommunications and Signal Processing (TSP)*, pags. 190–194, 2013.

[Gha02] M. Ghavami, "Wideband smart antenna theory using rectangular array structures", *IEEE Transactions on Signal Processing*, Vol. 50, nº 9, pags. 2143–2151, Sep. 2002.

[God05] H. Godrich, A. M. Haimovich, R. S. Blum, "Target localization accuracy gain in MIMO radar-based systems", *IEEE Trans. Inf. Theory*, Vol. 56, nº 6, pags. 2783–2803, Jul. 2005.

[GR05] Y. Chang G. Ren, H. Zhang, "Synchronization method based on a new constant envelop preamble for OFDM systems", *IEEE Transactions on Broadcasting*, Vol. 51, nº 1, pags. 139–143, 2005.

[Gra10] M. Grant, S. Boyd, *CVX: Matlab software for disciplined convex programming, version 1.21, http://cvxr.com/cvx,*, Aug. 2010.

[Gue15] A. Guerra, F. Guidi, D. Dardari, "Position and orientation error bound for wideband massive antenna arrays", *ICC Workshop on Advances in Network Localization and Navigation*, 2015.

[Gup15] A. Gupta, R. K. Jha, "A survey of 5G network: Architecture and emerging technologies", *IEEE Access*, Vol. 3, pags. 1206–1232, 2015.

[Gus14] Carl Gustafson, *60 GHz Wireless Propagation Channels: Characterization, Modeling and Evaluation*, PhD Thesis, Lund University, 2014.

[Haj05] A. Hajimiri, H. Hashemi, A. Natarajan, X. Guan, A. Komijani, "Integrated phased array systems in silicon", *Proc. IEEE*, Vol. 93, pags. 1637–1655, 2005.

[Hak15] A. Hakkarainen, J. Werner, M. Costa, K. Leppänen, M. Valkama, "High-efficiency device localization in 5G ultra-dense networks: Prospects and enabling technologies", *IEEE Vehicular Technology Conference (VTC)*, 2015.

[Han15] S. Han, C. L. I, Z. Xu, C. Rowell, "Large-scale antenna systems with hybrid analog and digital beamforming for millimeter wave 5G", *IEEE Commun. Mag.*, Vol. 53, nº 1, pags. 186–194, 2015.

[Has03] B. Hassibi, B. M. Hochwald, "How much training is needed in multiple-antenna wireless links", *IEEE Transactions on Information Theory*, Vol. 49, nº 4, pags. 951–963, Apr. 2003.

[Haw14] M. B. Hawes, W. Liu, "Sparse array design for wideband beamforming with reduced complexity in tapped delay-lines", *IEEE/ACM Transactions on Audio, Speech, and Language Processing*, Vol. 22, nº 8, pags. 1236–1247, Aug. 2014.

[Hu14] Anzhong Hu, Tiejun Lv, Hui Gao, Zhang Zhang, Shaoshi Yang, "An ESPRIT-based approach for 2-D localization of incoherently distributed sources in massive MIMO systems", *IEEE Journal of Selected Topics in Signal Processing*, Vol. 8, nº 5, pags. 996–1011, 2014.

[Hur13] S. Hur, T. Kim, D. Love, J. Krogmeier, T. Thomas, A. Ghosh, "Millimeter wave beamforming for wireless backhaul and accessin small cell networks", *IEEE Trans. Commun.*, Vol. 61, nº 10, pags. 4391–4403, 2013.

[ISO14] "ISO/IEC/IEEE international standard for information technology telecommunications and information exchange between systems–local and metropolitan area networks specific requirements-part 11: Wireless LAN medium access control (MAC) and physical layer (PHY) specifications amendment 3: Enhancements for very high throughput in the 60 GHz band (adoption of IEEE std 802.11ad-2012)", *ISO/IEC/IEEE 8802-11:2012/Amd.3:2014(E)*, Vol. 59, pags. 1–634, 2014.

[Kay10] S. M. Kay, *Fundamentals of Statistical Signal Processing: Estimation Theory*, Prentice Hall, New York, NY, USA, 2010.

[Kim05] J. J. Kim, J. H. Noh, K. H. Chang, "Robust timing and frequency synchronization techniques for OFDM-FDMA systems", *IEEE Workshop on Signal Processing Systems Design and Implementation*, 2005.

[Kle01] A. J. Kleywegt, A. Shapiro, T. Homem-De-Mello, "The sample average approximation method for stochastic discrete optimization", *SIAM Journal of Optimization*, Vol. 12, pags. 479–502, 2001.

[Koi16] M. Koivisto, M. Costa, J. Werner, K. Heiska, J. Talvitie, K. Leppänen, V. Koivunen, M. Valkama, "Joint device positioning and clock synchronization in 5G ultra-dense networks", *submitted for publication*, 2016.

[Kur15] N. P. Kuruvatti, A. Klein, L. Ji, C. Zhou, O. Bulakci, J. Eichinger, R. Sattiraju, H. D. Schotten, "Robustness of location based D2D resource allocation against positioning errors", *IEEE Vehicular Technology Conference*, 2015.

[Lar11] M.D. Larsen, G. Seco-Granados, A.L. Swindlehurst, "Pilot optimization for time-delay and channel estimation in OFDM systems", *IEEE Int. Conf. on Acoustics, Speech and Signal Processing (ICASSP)*, pags. 3564–3567, 2011.

[Lev44] K. Levenberg, "A method for the solution of certain non-linear problems in least squares", *Quarterly of Applied Mathematics*, Vol. 2, pags. 164–168, 1944.

[Li13] W. Li, Y. Shen, Y. J. Zhang, M. Z. Win, "Robust power allocation for energy-efficient location-aware networks", *IEEE/ACM Trans. Netw*, Vol. 21, nº 6, pags. 1918–1930, Dec. 2013.

[Li14] Q. C. Li, G. Wu, T. S. Rappaport, "Channel model for millimeter wave communications based on geometry statistics", *IEEE Globecom Workshop*, pags. 427–432, 2014.

[Li15] Q. C. Li, H. Shirani-Mehr, T. Balercia, A. Papathanassiou, G. Wu, S. Sun, M. K. Samimi, T. S. Rappaport, "Validation of a geometry-based statistical mmwave channel model using ray-tracing simulation", *IEEE Vehicular Technology Conference*, pags. 1–5, 2015.

[Liu09] W. Liu, "Adaptive wideband beamforming with sensor delay-lines", *Signal Processing*, Vol. 89, nº 5, pags. 876–882, May. 2009.

[Mar63] D. Marquardt, "An algorithm for least-squares estimation of nonlinear parameters", *SIAM Journal on Applied Mathematics*, Vol. 11, nº 2, pags. 431–441, 1963.

[Mar09] R. K. Martin, J. S. Velotta, J. F. Raquet, "Bandwidth efficient cooperative TDOA computation for multicarrier signals of opportunity", *IEEE Transactions on Signal Processing*, Vol. 57, nº 6, pags. 2311–2322, 2009.

[Mes07] F. Meshkati, H. V. Poor, S. C. Schwartz, "Energy-efficient resource allocation in wireless networks", *IEEE Signal Process. Mag.*, Vol. 24, nº 3, pags. 58–68, May. 2007.

[Mic14] M. Michailow, M. Matthe, I. S. Gaspar, A. N. Caldevilla, L. L. Mendes, A. Festag, G. Fettweis, "Generalized frequency division multiplexing for 5th generation cellular networks", *IEEE Transaction on Communications*, Vol. 62, nº 9, pags. 3045–3061, 2014.

[Min05] H. Minn, S. Xing, "An optimal training signal structure for frequency-offset estimation", *IEEE Transactions on Communications*, Vol. 53, nº 2, pags. 343–355, Feb. 2005.

[Min06] H. Minn, N. Al-Dhahir, "Optimal training signals for MIMO-OFDM channel estimation", *IEEE Transactions on Wireless Communications*, Vol. 5, nº 5, pags. 1158–1168, May. 2006.

[Mon13] R. Montalban, J. A. Lopez-Salcedo, G. Seco-Granados, A. L. Swindlehurst, "Power allocation method based on the channel statistics for combined positioning and communications OFDM systems", IEEE International Conference on Acoustics, Speech and Signal Processing (ICASSP), 2013.

[Mor09] M. Morelli, L. Sanguinetti, H. V. Poor, "A robust ranging scheme for OFDMA-based networks", *IEEE Transactions on Communications*, Vol. 57, nº 8, pags. 2441–2452, Aug. 2009.

[MR15] R. Méndez-Rial, C. Rusu, A. Alkhateeb, N. González-Prelcic, R. W. Heath, "Channel estimation and hybrid combining for mmwave: Phase shifters or switches?", *Information Theory and Applications Workshop (ITA), 2015*, pags. 90–97, Feb 2015.

[Mur81] K. Murota, K. Hirade, "GMSK modulation for digital mobile radio telephony", *IEEE Trans. Comm.*, Vol. 29, nº 7, 1981.

[Neg98] R. Negi, J. Ciuffi, "Pilot tone selection for channel estimation in a mobile OFDM system", *IEEE Transactions on Consumer Electronics*, Vol. 44, pags. 1122–1128, Aug. 1998.

[Nev12] I. Nevat, G. W. Peters, I. B. Collings, "Location-aware cooperative spectrum sensing via Gaussian processes", *Australian Communications Theory Workshop*, 2012.

[Ort66] J. Ortega, M. Rockoff, "Nonlinear difference equations and gauss-seidel type iterative methods", *SIAM J. Numer. Anal.*, Vol. 3, nº 3, pags. 497–513, 1966.

[Par02] B. Park, H. Cheon, C. Kang, "A simple preamble for OFDM timing offset estimation", *IEEE 56th Vehicular Technology Conference*, 2002.

[Pis14] E. Pisek, S. Abu-Surra, J. Mott, T. Henige, R. Sharma, "High throughput millimeter-wave MIMO beamforming system for short range communication", *IEEE Consumer Communications and Networking Conference (CCNC)*, 2014.

[Piv13] F. Pivit, V. Venkateswaran, "Joint RF-feeder network and digital beamformer design for cellular base-station antennas", *Antennas and Propagation Society International Symposium (APSURSI)*, pags. 1274–1275, 2013.

[Poo94] H. V. Poor, *An Introduction to Signal Detection and Estimation, 2nd ed.*, New York: Springer-Verlag, 1994.

[Poo12] A. Poon, M. Taghivand, "Supporting and enabling circuits for antenna arrays in wireless communications", *Proc. IEEE*, Vol. 100, nº 7, pags. 2207–2218, 2012.

[Rap13] T. Rappaport, S. Sun, R. Mayzus, H. Zhao, Y. Azar, K. Wang, G. Wong, J. Schulz, M. Samimi, F. Gutierrez, "Millimeter wave mobile communications for 5G cellular: It will work!", *IEEE Access*, Vol. 1, pags. 335–349, 2013.

[Ric05] Andreas Richter, *Estimation of Radio Channel Parameters: Models and Algorithms*, PhD Thesis, The Ilmenau University of Technology, 2005.

[Ric06] J. Richter, A. Salmi, V. Koivunen, "An algorithm for estimation and tracking of distributed diffuse scattering in mobile radio channels", *IEEE 7th Workshop on*, 2006.

[Rus13] R. Rusek, D. Persson, B. Lau, E. Larsson, T. Marzetta, O. Edfors, F. Tufvesson, "Scaling up MIMO: Opportunities and challenges with very large arrays", *IEEE Signal Process. Mag.*, Vol. 30, nº 1, pags. 40–60, 2013.

[San02] P Sanchis, JM Martinez, J Herrera, V Polo, JL Corral, J Marti, "A novel simultaneous tracking and direction of arrival estimation algorithm for beam-switched base station antennas in millimeter-wave wireless broadband access networks", *IEEE Antennas and Propagation Society International Symposium*, 2002.

[San09] S. Sand, R. Tanbourgi, C. Mensing, R. Raulefs, "Position aware adaptive communication systems", *Asilomar Conf. Signals, Systems and Computers*, 2009.

[San12] L. Sanguinetti, M. Morelli, "An initial ranging scheme for the IEEE 802.16 OFDMA uplink", *IEEE Transactions on Wireless Communications*, Vol. 11, nº 9, pags. 3204–3215, Sept. 2012.

[Sav15] Vladimir Savic, Erik G Larsson, "Fingerprinting-based positioning in distributed massive MIMO systems", *IEEE Vehicular Technology Conference*, 2015.

[Say02] A. Sayeed, "Deconstructing multiantenna fading channels", *IEEE Transactions on Signal Processing*, Vol. 50, nº 10, pags. 2563–2579, 2002.

[Say05] A. H. Sayed, A. Tarighat, N. Khajehnouri, "Network-based wireless location: Challenges faced in developing techniques for accurate wireless location information", *IEEE Signal Process. Mag.*, Vol. 22, nº 4, pags. 24–40, Jul. 2005.

[Sch97] T. M. Schmidl, D. C. Cox, "Robust frequency and timing synchronization for OFDM", *IEEE Transactions on Communications*, Vol. 45, nº 12, pags. 1613–1621, 1997.

[Ses11] S. Sesia, I. Toufik, M. Baker, *LTE the UMT long term evolution: From theory to practice*, John Wiley and Sons, 2011.

[Sha15] A. Shahmansoori, G. Seco-Granados, H. Wymeersch, "Robust power allocation for OFDM wireless network localization", *IEEE Int. Conf. on Communications (ICC)*, pags. 718–723, 2015.

[She10a] Y. Shen, M. Z. Win, "Fundamental limits of wideband localization part I: A general framework", *IEEE Transactions on Information Theory*, Vol. 56, nº 10, pags. 4956–4980, 2010.

[She10b] Y. Shen, M. Z. Win, "Fundamental limits of wideband localization part I: A general framework", *IEEE Trans. Inf. Theory*, Vol. 56, nº 10, pags. 4956–4980, Oct. 2010.

[She10c] Y. Shen, H. Wymeersch, M. Z. Win, "Fundamental limits of wideband localization part II: Cooperative networks", *IEEE Trans. Inf. Theory*, Vol. 56, nº 10, pags. 4981–4999, Oct. 2010.

[She14] Y. Shen, W. Dai, M. Z. Win, "Power optimization for network localization", *IEEE/ACM Trans. Netw.*, Vol. 22, nº 4, pags. 1337–1350, Aug. 2014.

[Sim04] O. Simeone, Y. Bar-Ness, U. Spagnolini, "Pilot-based channel estimation for OFDM systems by tracking the delay-subspace", *IEEE Transactions on Wireless Communications*, Vol. 3, nº 1, pags. 315 – 325, Jan. 2004.

[Sor06] J. Soriaga, J. Hou, J. Smee, "Network performance of the EV-DO CDMA reverse link with interference cancellation", *IEEE Globecom*, 2006.

[Sto89] P. Stoica, T. Söderström, "On reparametrization of loss functions used in estimation and the invariance principle", *Signal Process.*, Vol. 17, pags. 383–387, 1989.

[Sto03] P. Stoica, O. Besson, "Training sequence design for frequency offset and frequency-selective channel estimation", *IEEE Transactions on Communications*, Vol. 51, nº 11, pags. 1910–1917, Nov. 2003.

[Sud06] P. Sudarshan, N. B. Mehta, A. F. Molisch, J. Zhang, "Channel statistics-based RF pre-processing with antenna selection", *IEEE Trans. Wireless Commun.*, Vol. 5, nº 12, pags. 3501–3511, 2006.

[Swi02] A. L. Swindlehurst, P. Stoica, "Maximum likelihood methods in radar array signal processing", *Proceedings of the IEEE*, Vol. 86, nº 2, pags. 421–441, 2002.

[Swi13] A. L. Swindlehurst, E. Ayanoglu, P. Heydari, F. Capolino, "Millimeter-wave massive MIMO: the next wireless revolution?", *IEEE Communications Magazine*, Vol. 52, nº 9, pags. 56–62, 2013.

[Tar14] R. D. Taranto, S. Muppirisetty, R. Raulefs, D. T. M. Slock, T. Svensson, H. Wymeersch, "Location-aware communications for 5G networks: How location information can improve scalability, latency, and robustness of 5G", *IEEE Signal Processing Magazine*, Vol. 31, nº 6, pags. 102–112, 2014.

[Teh14] M. N. Tehrani, M. Uysal, H. Yanikomeroglu, "Device-to-device communication in 5G cellular networks: Challenges, solutions, and future directions", *IEEE Communications Magazine*, Vol. 52, nº 5, pags. 86–92, 2014.

[Tro06] J. A. Tropp, A. C. Gilbert, M. J. Strauss, "Algorithms for simultaneous sparse approximation. part i: Greedy pursuit", *Signal Processing*, Vol. 86, nº 3, pags. 572–588, 2006.

[Tsa11] Y. Tsang, A. Poon, S. Addepalli, "Coding the beams: Improving beamforming training in mmwave communication system", *Global Telecomm. Conf. (GLOBECOM)*, 2011.

[Var14a] M. Vari, D. Cassioli, "mmWaves RSSI indoor network localization", *IEEE Workshop on Advances in Network Localization and Navigation (ICC)*, 2014.

[Var14b] Marco Vari, Dajana Cassioli, "mmWaves RSSI indoor network localization", *ICC Workshop on Advances in Network Localization and Navigation*, 2014.

[Wan08] X. Wang, T. Wild, F. Schaich, A. Santos, "Contributions to the understanding of the MSK modulation", *REVISTA Telecommunications*, Vol. 11, nº 1, 2008.

[Wan09] J. Wang, "Beam codebook based beamforming protocol for multi-Gbps millimeter-wave WPAN systems", *IEEE J. Sel. Areas Commun.*, Vol. 27, nº 8, pags. 1390–1399, 2009.

[Wan14] X. Wang, T. Wild, F. Schaich, A. Santos, "Universal filtered multi-carrier with leakage-based filter optimization", *European Wireless*, 2014.

[Wer15a] J. Werner, M. Costa, A. Hakkarainen, K. Leppänen, M. Valkama, "Joint user node positioning and clock offset estimation in 5G ultra-dense networks", *IEEE Global Telecommunications (GLOBECOM) Conference*, 2015.

[Wer15b] J. Werner, J. Wang, A. Hakkarainen, D. Cabric, M. Valkama, "Performance and Cramer-Rao bounds for DoA/RSS estimation and transmitter localization using sectorized antennas", *IEEE Trans. Vehicular Technology*, 2015.

[Win06] F. Winkler, E. Fischer, E. Grass, P. Langendorfer, "An indoor localization system based on DTDOA for different wireless LAN systems", *Workshop on positioning, navigation, and communication*, 2006.

[Wym09] H. Wymeersch, J. Lien, M. Z. Win, "Cooperative localization in wireless networks", *Proceedings of the IEEE*, Vol. 97, nº 2, pags. 427–450, 2009.

[YJ10] C. Lott J. Ma R. Gowaikar Y. Jou, R. Attar, "CDMA and SC-FDMA reverse link comparison for cellular voice and data communications", *IEEE VTC*, 2010.

[Yua08] H. Yuan, X. Hu, Y. Ling, "New symbol synchronization algorithms for OFDM systems based on IEEE 802.11 a", *in 6th IEEE International Conference on Industrial Informatics*, 2008.

[Zac81] S. Zacks, *Parametric Statistical Inference: Basic Theory and Modern Approaches*, Oxford, England: Pergamon, 1981.

[Zha05] X. Zhang, A. F. Molisch, S. Kung, "Variable-phase-shift-based RF-baseband codesign for MIMO antenna selection", *IEEE Trans. Signal Process.*, Vol. 53, nº 11, pags. 4091–4103, 2005.

[Zha06] Q. Zhao, J. Li, "Rain attenuation in millimeter wave ranges", *Proc. IEEE Int. Symp. Antennas, Propag. EM Theory*, pags. 1–4, 2006.

[Zho11] P. Zhouyue, F. Khan, "An introduction to millimeter-wave mobile broadband systems", *IEEE Communications Magazine*, Vol. 49, nº 6, pags. 101–107, 2011.

[Zhu10] H. Zhu, G. Leus, G. Giannakis, "Sparse regularized total least squares for sensing applications", *IEEE Eleventh International Workshop on Signal Processing Advances in Wireless Communications (SPAWC)*, 2010.

[Zhu16] D. Zhu, J. Choi, R. W. Heath, Jr, "Auxiliary beam pair design in mmwave cellular systems with hybrid precoding and limited feedback", *IEEE Int. Conf. on Acoustics, Speech, and Signal Proc.*, 2016.